

https://dspace.org/

Analysing ground surface position cGPS and meteorology measurements in southern Africa using signal processing techniques

Gomo, Sikelela

2019

https://hdl.handle.net/10539/29585

Gomo, Sikelela. (2018). Analysing ground surface position cGPS and meteorology measurements in southern Africa using signal processing techniques. University of the Witwatersrand, https://hdl.handle.net/10539/29585

Downloaded from a DSpace repository. https://dspace.org/

Analysing ground surface position cGPS and meteorology measurements in southern Africa using signal processing techniques

Sikelela Gomo

Supervised by

Prof. R. J. Durrheim

Prof. G. R. J. Cooper

A thesis submitted to the Faculty of Science, University of the Witwatersrand, Johannesburg, in fulfilment of the requirements for the degree of

Master of Science

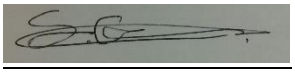
2018



Declaration

I Sikelela Gomo (Student number: 1488846) am a student registered for MSc in Geophysics in the year 2019. I hereby declare the following:

- I am aware that plagiarism (the use of someone else's work without their permission and/or without acknowledging the original source) is wrong.
- I confirm that ALL the work submitted for assessment for the above course is my own unaided work except where I have explicitly indicated otherwise.
- I have followed the required conventions in referencing the thoughts and ideas of others.
- I understand that the University of the Witwatersrand may take disciplinary action against me if there is a belief that this is not my own unaided work or that I have failed to acknowledge the source of the ideas or words in my writing.

Signature:  Date: 30-08-2019

Abstract

The Continuous GPS system (cGPS) is a space geodetic technique used to measure seasonal surface deformation of the outermost solid layer of the Earth, the crust. The crust deforms and translates both in the horizontal and vertical direction due to tectonic and non-tectonic processes, which include meteorological processes. This research focuses on analysing the characteristics of cGPS surface displacement and meteorological (surface air temperature, atmospheric pressure, rainfall and humidity) time series in southern Africa; their relationship; and the use of time series analysis techniques to analyse the time series and their relationship. The analysis of cGPS time series and the processes that affect them is important in Earth science studies because it enables a better understanding, analysis and interpretation of crustal deformation, geodynamics and tectonic plate studies inferred from measurements of geodetic systems. The study is carried out using Fourier Transforms (FT), Wavelet Transforms (WT), Wavelet Semblance (WS), Cross-Spectrum Density (CSD), Coherence, Pearson's and Spearman's methods, which are time, frequency and time-frequency domain analysis techniques. FTs and WTs are frequency and time-frequency decomposition techniques, respectively; while Pearson's, Spearman's, CSD, Coherence and WS methods are time, frequency and time-frequency domain correlation techniques.

Time domain results show that there exists little to no correlation between surface displacement and either pressure, rainfall or humidity time series, while moderate correlation exists between surface displacement and temperature time series. This could be because pressure, rainfall and humidity effects on surface displacement time series measurements are corrected for, while temperature effects are not. Frequency and time-frequency results show that the relationship between temperature, pressure and surface displacement is high and consistent; while correlation between surface displacement, rainfall and humidity time series is small and inconsistent throughout the study area. Implying that temperature (thermal expansion) and pressure (atmospheric pressure induced surface loading) variations have more influence on seasonal surface displacement observed in cGPS time series than rainfall and humidity processes (shrink and swell heave action). This suggests that, like atmospheric pressure corrections, correcting for seasonal annual thermal expansion and thermal noise introduced errors could further reduce the annual seasonal deformation component observed in cGPS position measurements. Furthermore, annual surface displacements are observed to vary systematically from one climatic zone to another.

Dedicated to my parents

uNtomboxolo, Eleanor Gomo

uCwerha, Gxarha, Mlawu, Sibiside, Ihlahla elagawulwa layekwa ngenxa yokuswel'umrhuqi, Ngumqokolo ophephel'amahobe, uMal'ebomvu ethenga phesheya kweGqili, uNjembu, uVambane.

and uGizenga, Alfred Gomo

uNtsikhwe, Dubane, Nqumbe, Mawawa, Ndlebentle zombini, Buhlungu bendlovu, Senzwa, Mkhont'obuthuntu, Philakuzenzela, Mbhalo KaQoshe, Gasel'ethusini, Zihlahla zomnquma bayazigawula kodwa ziyahluma, Mfaz'obelelinye ohleli kumadobo aphesheya komlanjana, angatshiyo nob'umlilo uvuthama dangatye, Ntomntwana ingab'inoboya ifanel'abadala.

Acknowledgements

First and foremost, I would like to thank the Lord for giving me the opportunity to pursue and strength to complete this degree.

I would like to express my sincere gratitude and appreciation to my supervisors, Prof. Raymond Durrheim and Prof. Gordon Cooper for their guidance, willingness and patience to assist me at every step of the research project. I have been extremely lucky and honoured to have worked and learnt from you, it is a privilege I will always cherish.

I would like to extend my gratitude and appreciation to the Council for Geoscience for funding my studies. To acknowledge the Nevada Geodetic Laboratory and the South African Weather Service (SAWS) for providing cGPS and meteorology data used in this project.

I would also like to thank my colleagues and friends for their assistance, for taking their valuable time to peer review some of the work, and for their constructive and insightful comments, I am truly grateful.

Above all, I would like to thank my parents, Nozukile Ntomboxolo Gomo and Gizenga Alfred Gomo for all the sacrifices they made on my behalf, their support, encouragement, love and for crafting a path for me to be able to achieve my goals. My amazing siblings for their support and belief in me. Thank you.

Table of contents

Declaration i

Abstract ii

Acknowledgements iv

Table of contents v

List of figures xi

List of tables xxi

List of abbreviations xxiii

1 Introduction 1

1.1 Background 1

1.2 Project aims 4

1.3 Research objectives 4

1.4 Significance of the study 5

1.5 Hypothesis 5

1.6 Description of the study area 5

1.7 Thesis structure 9

2 Literature review 10

2.1 International Terrestrial Reference Frame (ITRF) 10

2.2 Global Positioning Systems 11

2.3 Global Navigation Satellite Systems segments 12

2.3.1 Space segment 13

2.3.2 Ground segment 14

2.3.3 User segment 14
2.4 Brief overview of GPS errors and their sources 15
2.4.1 Propagation delays 15
2.4.1.1 Ionospheric delay 15
2.4.1.2 Tropospheric delay 18
2.4.2 Multipath errors 20
2.4.3 Satellite geometric errors 21
2.4.4 Orbital path errors 23
2.4.5 Satellite clock errors (atomic clock drift and rounding errors) 24
2.5 How GPS systems measure tectonic and non-tectonic variations 25
2.5.1 GPS for measuring meteorology data 25
2.5.2 GPS for mapping and determining variations in the position of surface features 26
2.5.3 Procedure to measure propagation delays 26
2.5.4 Seasonal variation of GPS position accuracy 27
2.6 Development of Wavelet and Fourier transforms 27
3 Methodology 30
3.1 Sampling criteria 30
3.2 Time domain analysis techniques 31
3.2.1 Pearson's Correlation Coefficient (PCC) 32
3.2.2 Spearman's Correlation coefficient (Rho) 33
3.3 Frequency domain analysis techniques 33

3.3.1 Fourier and fast Fourier transform (FFT) techniques 33

3.3.2 Cross-spectrum 38

3.3.3 Magnitude squared coherence (MSC) 39

3.3.4 Phase difference 40

3.4 Time-frequency domain analysis techniques 41

3.4.1 Computation of wavelet transforms 41

3.4.2 The basis of choosing the complex Morlet wavelet transform. 43

3.4.3 CWT semblance 45

4 Synthetic data 47

4.1 Synthetic time series components 47

4.2 Synthetic data generation 48

4.3 Interpolation 53

4.3.1 Piecewise linear interpolation method 54

4.3.2 Piecewise nearest-neighbour interpolation method 55

4.3.3 Piecewise cubic Hermite interpolation method 56

4.3.4 Piecewise cubic spline interpolation method 56

4.4 Application of the interpolation methods to synthetic data 57

4.4.1 Application of the interpolation techniques on a noise-free synthetic time series 57

4.4.2 Application of the interpolation techniques on a noise contaminated synthetic time series 59

4.5 Decomposition, correlation and phase shift synthetic data tests....63

4.5.1 FFT decomposition....63

4.5.2 Cross-covariance and phase test....64

4.6 Wavelet transforms....66

4.6.1 Decomposition using the continuous wavelet transform....66

4.6.2 Wavelet semblance....70

5 Results and interpretation....73

5.1 Time domain results....73

5.2 Frequency, time-frequency domain decomposition results....76

5.2.1 FFT displacement time series decomposition....76

5.2.2 WT displacement time series decomposition....77

5.2.3 FFT meteorological time series decomposition....81

5.2.3.1 Temperature time series decomposition....81

5.2.3.2 Pressure time series decomposition....81

5.2.3.3 Rainfall time series decomposition....82

5.2.3.4 Humidity time series decomposition....83

5.2.4 WT meteorological time series decomposition....84

5.3 Correlation analysis using Cross-Spectral Density (CSD), coherence, phase and semblance spectral techniques....98

5.3.1 Correlation determination and quantification using CSD and coherence spectral techniques....98

5.3.2 Phase difference determination and quantification using phase spectrum technique 106

5.3.3 Phase correlation determination and visualisation using CWT Semblance spectral technique 109

6 Surface deformation models 114

6.1 Surface deformation model due to thermal expansion 114

6.1.1 Thermal expansion computation 115

6.1.2 Background of thermal expansion of over-consolidated soils 119

6.2 Surface deformation model due to atmospheric loading 121

6.3 Atmospheric pressure computation 123

6.4 Surface deformation due to heaving of expansive soils 127

6.5 Potential heave computation 128

7 Discussion 132

7.1 Surface displacement and meteorological time series decomposition: 132

7.1.1 Surface displacement time series 132

7.1.2 Surface air temperature time series 133

7.1.3 Atmospheric pressure time series 133

7.1.4 Rainfall time series 134

7.1.5 Humidity time series 135

7.2 Relationship between cGPS displacement and meteorological time series components 136

7.2.1 Relation between rainfall, humidity and surface deformation 136

7.2.2 Relation between surface air temperature, atmospheric pressure and surface deformation 137

7.2.3 Relation between annual and semi-annual surface displacement and meteorological process frequency components 138

7.3 Surface air temperature and displacement fluctuations 138

8 Conclusion 142

8.1 Limitations and recommendations 143

9 References 145

Appendices 161

List of figures

Figure 1.1: cGPS daily position time series of station BETH located in Bethlehem, South Africa. BETH represents Bethlehem. (a) Interpolated original time series. (b) Interpolated and detrended original time series; which shows the seasonal displacement of the easting and northing components with respect to that of the up (vertical) component. 2

Figure 1.2: Map of Africa and southern Africa with locations of cGPS stations (http://geodesy.unr.edu/NGLStationPages/gpsnetmap/GPSNetMap.html). 6

Figure 1.3: Climatic zone map of southern Africa (modified after Hepburn and Radloff, 1998). 7

Figure 2.1: Earth-Centred Earth Fixed Coordinates System (modified after Guochang, 2007, p. 7). 11

Figure 2.2: GNSS segments and their relation. 13

Figure 2.3: Tropospheric and ionospheric error sources and zones. 16

Figure 2.4: Variation of the electron density with altitude from the Earth's surface in summer (modified after Pulinets and Boyarchuk, 2004). 17

Figure 2.5: Direct and reflected (Multipath) signals. 20

Figure 2.6: The effect of satellite configuration on position calculations. Evaluating the Geometric Dilution of Precision (GDOP). 22

Figure 2.7: Satellite orbital errors. 24

Figure 3.1: (a) Mexican hat wavelet, (b) Meyer wavelet, (c) Morlet wavelet, and (d) Fourth order Gaussian wavelet. 42

Figure 4.1: Annual (in blue) and semi-annual (in green) signals. Each year is composed of 365.2422 samples which are equivalent to the number of days. The annual signal is defined by a period of 1 year and the semi-annual signal is defined by a period of 6 months. 49

Figure 4.2: Noise-free synthetic time series obtained by adding the annual and semi-annual signals in Figure 4.1. 50

Figure 4.3: (a) Random Gaussian noise with a mean of 0 and a standard deviation of 0.5. (b) Noisy time series obtained by adding the noise time series in (a) and the noise-free-time series in Figure 4.2. 51

Figure 4.4: (a) Trend with a slope of 2 and a y-intercept of zero. (b) Time series obtained by adding the noise contaminated time series in Figure 4.3 and the trend in (a)..... 51

Figure 4.5: Synthetic signal with missing data points. 52

Figure 4.6: The green dots are known points of the original time series and the red dots are interpolation points obtained using different interpolation methods. The plots display how each of the considered interpolation methods interpolate for unknown data points..... 54

Figure 4.7: Response of the interpolation methods when applied to noise-free synthetic time series. (a) Noise-free synthetic time series without gaps (green) and with gaps (blue). (b) Detrended time series. (c) Linear interpolated time series. (d) Nearest neighbour interpolated time series). (e) Piecewise cubic Hermite interpolated time series. (f) Piecewise cubic spline interpolated time series. 58

Figure 4.8: Response of the interpolation methods when applied to a noise-contaminated synthetic time series. (a) Noise-contaminated synthetic time series without gaps (green) and with gaps (blue). (b) Detrended time series. (c) Linear interpolated time series. (d) Nearest neighbour interpolated time series. (e) Piecewise cubic Hermite interpolated time series. (f) Piecewise cubic spline interpolated time series. 60

Figure 4.9: Fast Fourier Transform (FFT) decomposition of a time series without noise, with noise and with a trend. (a) Time series composed of an annual and semi-annual signal (i.e., signals of frequency 1 and 2 cpy), without noise. The annual signal has an amplitude of 3, while the semi-annual signal has an amplitude of 1. (b) Time series in (a)

contaminated by white Gaussian noise with a standard deviation of 3 mm. (c) Time series in (b) with noise and a trend. (d) FFT spectrum of the time series in (a). (e) FFT spectrum of the time series in (b). (f) FFT spectrum of the time series in (c).....63

Figure 4.10: Cross-spectrum and phase tests. (a) Identical time series with a phase difference of 120 degrees (2.1 radians), both (blue and red) time series are composed of an annual and semi-annual signal. The annual signal has an amplitude of 3, while the semi-annual signal has an amplitude of 1. (b) Time series in (a) contaminated by Gaussian noise with a STD of 3. (c) Cross-spectrum of the time series in (a). (d) Cross-spectrum of the time series in (b). (e) Phase spectrum of the time series in (a). f) Phase spectrum of the time series in (d). The phase is given in radians. 64

Figure 4.11: Synthetic data decomposition using the complex continuous wavelet transform (CWT). (a) Noise-free time series composed of an annual and semi-annual signal. The annual signal has an amplitude of 3 mm, while the semi-annual signal has an amplitude of 1 mm. (b) Real part of the complex CWT of the time series in (a). (c) Time series with the same signals as those in (a) but contaminated with a Gaussian noise of standard deviation of 0.5 mm. (d) Real part of the complex CWT of time series in (c). (e) Misfit plot of (b) and (d)The colour bar shows the variation of the CWT coefficients as a function of frequency and time. The colour bar shows the variation of the CWT coefficients as a function of frequency and time. The bright red bands indicate a positive amplitude and the dark blue bands indicates a negative amplitude.....66

Figure 4.12: (a) Time series in Figure 4.11a contaminated with Gaussian noise of higher standard deviation, i.e., 3 mm. (b) Real part of the complex continuous wavelet transform (CWT) of time series in (a). The colour bar shows the variation of the CWT coefficients as a function of frequency and time. The colour bar shows the variation of the CWT

coefficients as a function of frequency and time. The bright red indicates a positive amplitude and the dark blue indicates a negative amplitude. 67

Figure 4.13: Effects of a trend when transforming data into the time-frequency domain using the complex continuous wavelet transform (CWT). (a) Time series with the same properties as that in Figure 4.11c plus a trend with a slope of 2 units. (b) Real part of the complex CWT of time series in (a). The bright red indicates a positive amplitude and the dark blue indicates a negative amplitude. (c) Time series with the same parameters as the time series in (a), but with a trend of higher slope (7 units). (d) Real part of the complex CWT of time series in (c). (e) Misfit plot of (b) and (d). The colour bar shows the variation of the CWT coefficients as a function of frequency and time. The bright red indicates a positive amplitude and the dark blue indicates a negative amplitude. The black boxes at approximately 3.4 to 5 yrs highlight the edge effects, regions of higher than normal CWT coefficients, induced by the presence of a trend. 68

Figure 4.14: Effects of missing data (gaps) on the complex continuous wavelet transform (CWT). (a) Time series with the same properties as that in Figure 4.11c, but with missing values. (b) Real part of the complex CWT of time series in (a). The bright red indicates a positive amplitude and the dark blue indicates a negative amplitude. (c) Linear interpolated time series with the same parameters as the time series in (a). (d) Real part of the complex CWT of time series in (c). The colour bar shows the variation of the CWT coefficients as a function of frequency and time. The bright red indicates a positive amplitude and the dark blue indicates a negative amplitude. 69

Figure 4.15: Morlet wavelet transform of mean shifted time series. (a) Time series in Figure 4.11c with a mean shift, the time series is detrended using a constant mean. (b) Real part of the complex continuous wavelet transform (CWT) of time series in (a). (c) Time series in Figure 4.11c detrended using a first order linear trend. (d) Real part of the complex

CWT of the time series in (c). The colour bar shows the variation of the CWT coefficients as a function of frequency and time. The bright red indicates a positive amplitude and the dark blue indicates a negative amplitude. 70

Figure 4.16: Wavelet transform, phase and semblance correlation spectrums. (a) Time series in Figure 4.11c. (b) Real part of the complex continuous wavelet transform (CWT) of the time series in (a). The bright red indicates a positive amplitude and the dark blue indicates a negative amplitude. (c) Time series in (a) with phase variations between the intervals at 0 - 1.5 yrs, 1.5 – 3.5 yrs and 3.5 - 5 yrs. (d) Real part of the complex CWT of time series in (c). (e) Phase correlation spectrum. (f) Wavelet semblance spectrum. The colour bar shows the variation of the CWT coefficients as a function of frequency and time. The bright red indicates a positive amplitude and the dark blue indicates a negative amplitude. 72

Figure 5.1: On the left-hand side of the black line are displacement and meteorology time series from Worcester (WORC), a town located in the south-western part of southern Africa, a winter rainfall region. On the right are displacement and meteorology time series at in Mafikeng (MFKG). Mafikeng is a summer rainfall region, located in the north-central part of South Africa. The displacement, temperature, pressure and humidity time series are zero centred so as to be able to easily see approximate amplitudes of the different datasets. 74

Figure 5.2: Daily position vertical component cGPS surface displacement time series. The blue points in the cGPS time series plots are the original data points and the red continuous line is the cubic Hermite interpolated time series. 78

Figure 5.3: Daily position cGPS vertical (up) displacement component time series Fast Fourier Transforms (FFT) Power Spectral Density (PSD) spectra of the time series in Figure 5.2. 79

Figure 5.4: Morlet continuous wavelet transform (CWT) spectra of the daily position cGPS vertical displacement component time series in Figure 5.2 The colour bar shows the variation of the CWT coefficients as a function of frequency and time. The bright red indicates a positive amplitude and the dark blue indicates a negative amplitude. 80

Figure 5.5: Average surface air temperature time series. The blue points in the cGPS time series plots are the original data points and the red continuous line is the cubic Hermite interpolated time series. 85

Figure 5.6: Atmospheric pressure time series. The blue points in the cGPS time series plots are the original data points and the red continuous line is the cubic Hermite interpolated time series. 86

Figure 5.7: Rainfall time series. The blue points in the cGPS time series plots are the original data points and the red continuous line is the cubic Hermite interpolated time series. ...87

Figure 5.8: Humidity time series. The blue points in the cGPS time series plots are the original data points and the red continuous line is the cubic Hermite interpolated time series. ...88

Figure 5.9: Surface air temperature Fast Fourier Transforms (FFT) Power Spectral Density (PSD) spectra of the time series in Figure 5.5. 89

Figure 5.10: Atmospheric pressure time series Fast Fourier Transforms (FFT) Power Spectral Density (PSD) spectra of the time series in Figure 5.6. 90

Figure 5.11: Rainfall time series Fast Fourier Transforms (FFT) Power Spectral Density (PSD) spectra of the time series in Figure 5.7. 91

Figure 5.12: Humidity time series Fast Fourier Transforms (FFT) Power Spectral Density (PSD) spectra of the time series in Figure 5.8. 92

Figure 5.13: Surface air temperature time series Morlet continuous wavelet transform (CWT) of the time series in Figure 5.5. The colour bar shows the variation of the CWT coefficients

as a function of frequency and time. The bright red indicates a positive amplitude and the dark blue indicates a negative amplitude. 93

Figure 5.14: Atmospheric pressure time series Morlet continuous wavelet transform (CWT) of the time series in Figure 5.6. The colour bar shows the variation of the CWT coefficients as a function of frequency and time. The bright red indicates a positive amplitude and the dark blue indicates a negative amplitude. 94

Figure 5.15: Rainfall time series Morlet continuous wavelet transform (CWT) of the time series in Figure 5.7. The colour bar shows the variation of the CWT coefficients as a function of frequency and time. The bright red indicates a positive amplitude and the dark blue indicates a negative amplitude. 95

Figure 5.16: Humidity time series Morlet continuous wavelet transform (CWT) of the time series in Figure 5.8. The colour bar shows the variation of the CWT coefficients as a function of frequency and time. The bright red indicates a positive amplitude and the dark blue indicates a negative amplitude. 96

Figure 5.17: Cross-spectrum and coherence correlation plots of cGPS displacement (m) vs average temperature (℃) time series. 101

Figure 5.18: Cross-spectrum and coherence correlation plots of cGPS displacement (m) vs pressure (mbar) time series. 102

Figure 5.19: Cross-spectrum and coherence correlation plots of cGPS displacement (m) vs rainfall (mm) time series. 103

Figure 5.20: Cross-spectrum and coherence correlation plots of cGPS displacement (m) vs humidity (%) time series. 104

Figure 5.21: Phase lag distribution histograms for the considered meteorological processes. 107

Figure 5.22: Semblance correlation plots of cGPS displacement time series (m) vs average temperature time series (℃).....110

Figure 5.23: Semblance correlation plots of cGPS displacement time series (m) vs atmospheric pressure time series (mbar). 111

Figure 5.24: Semblance correlation plots of cGPS displacement time series (m) vs rainfall time series (mm).....112

Figure 5.25: Semblance correlation plots of cGPS displacement time series (m) vs humidity time series (%). 113

Figure 6.1: Thermal expansion curve of expansive Boom clay soil with an OCR of 2 (Delage et al., 2000) 120

Figure 6.2: (a) Local and regional stations used to estimate atmospheric pressure loading inland. (b) Local and regional stations used to estimate atmospheric deformation near the offshore. 124

Figure 6.3: cGPS station locations projected upon regions of swelling clays across South Africa (http://197.96.144.125/jsviewer/Geohazards/index.html, accessed on the 02-03-2019). 130

Figure 7.1: Surface air temperature cycle power vs surface displacement cycle power.....139

Figure 9.1: Synthetic time series T1 (with 2% missing data points), used in the variance test in chapter 4.2 and the response of the interpolation methods when applied to the noise contaminated time series. (a) Noise-contaminated synthetic time series without gaps (green) and with gaps (blue). (b) Detrended time series. (c) Linear interpolated time series. (d) Nearest neighbour interpolated time series). (e) Piecewise cubic Hermite interpolated time series. (f) Piecewise cubic spline interpolated time series. 161

Figure 9.2: Synthetic time series T2 (with 5% missing data points), used in the variance test in chapter 4.2 and the response of the interpolation methods when applied to the noise

contaminated time series. (a) Noise-contaminated synthetic time series without gaps (green) and with gaps (blue). (b) Detrended time series. (c) Linear interpolated time series. (d) Nearest neighbour interpolated time series). (e) Piecewise cubic Hermite interpolated time series. (f) Piecewise cubic spline interpolated time series. 162

Figure 9.3: Synthetic time series T3 (with 10% missing data points), used in the variance test in chapter 4.2 and the response of the interpolation methods when applied to the noise contaminated time series. (a) Noise-contaminated synthetic time series without gaps (green) and with gaps (blue). (b) Detrended time series. (c) Linear interpolated time series. (d) Nearest neighbour interpolated time series). (e) Piecewise cubic Hermite interpolated time series. (f) Piecewise cubic spline interpolated time series. 163

Figure 9.4: Synthetic time series T4 (with 15% missing data points), used in the variance test in chapter 4.2 and the response of the interpolation methods when applied to the noise contaminated time series. (a) Noise-contaminated synthetic time series without gaps (green) and with gaps (blue). (b) Detrended time series. (c) Linear interpolated time series. (d) Nearest neighbour interpolated time series). (e) Piecewise cubic Hermite interpolated time series. (f) Piecewise cubic spline interpolated time series. 164

Figure 9.5: Synthetic time series T5 (with 20% missing data points), used in the variance test in chapter 4.2 and the response of the interpolation methods when applied to the noise contaminated time series. (a) Noise-contaminated synthetic time series without gaps (green) and with gaps (blue). (b) Detrended time series. (c) Linear interpolated time series. (d) Nearest neighbour interpolated time series). (e) Piecewise cubic Hermite interpolated time series. (f) Piecewise cubic spline interpolated time series. 165

Figure 9.6: Additional Cross-spectrum and coherence correlation plots of cGPS displacement (m) vs average temperature (℃) time series. 166

Figure 9.7: Additional cross-spectrum and coherence correlation plots of cGPS displacement (m) vs pressure (mbar) time series. 167

Figure 9.8: Additional cross-spectrum and coherence correlation plots of cGPS displacement (m) vs rainfall (mm) time series. 168

Figure 9.9: Additional cross-spectrum and coherence correlation plots of cGPS displacement (m) vs humidity (%) time series. 169

Figure 9.10: Additional semblance correlation plots of cGPS displacement time series (m) vs average temperature time series (°C). 171

Figure 9.11: Additional semblance correlation plots of cGPS displacement time series (m) vs atmospheric pressure time series (mb). 172

Figure 9.12: Additional semblance correlation plots of cGPS displacement time series (m) vs rainfall time series (mm). 173

Figure 9.13: Additional semblance correlation plots of cGPS displacement time series (m) vs humidity time series (%). 174

Figure 9.14: Time domain plots of the addition displacement time series 175

Figure 9.15: FFT transform of the addition displacement time series 175

Figure 9.16: Morlet wavelet transform of the addition displacement time series. 176

List of tables

Table 1: Rule of thumb for interpreting correlation coefficient strength quantities (After Mukaka, 2012). 32

Table 2: Variance of five similar time series (T1, T2, T3, T4 and T5) with a varying percentage of authentic data points (or missing data points). The values highlighted in blue are the values that were of more significance in choosing the interpolation method that is used in this project. The closer the variance of the interpolated time series to that of the original time series, the better. TS stands for time series. 61

Table 3: Correlation of surface displacement vs meteorological time series using Pearson's (PCC) method. 75

Table 4: Correlation of surface displacement vs meteorological time series using Spearman's (Rho) rank method. 75

Table 5: Quantified power of the annual and semi-annual frequency components present in the cGPS displacement and meteorological time series as obtained from FFT. VC stands for Vertical Component. 97

Table 6: Coherence correlation strength of displacement vs meteorological (average temperature, pressure, rainfall and humidity) processes. 100

Table 7: Phase difference between cGPS displacement time series and meteorological (average temperature, pressure, rainfall and humidity) processes. The annual and semi-annual phase shift averages are computed using absolute phase shift values of the annual and semi-annual phase shift results. 108

Table 8: Average Poisson's ratio and coefficient of thermal expansion values for different types of materials (Wang et al., 2018) 116

Table 9: Average thermal diffusion coefficients for sedimentary, igneous and metamorphic rocks (Wang et al., 2018) 116

Table 10: MFGK station parameters 117

Table 11: Thermal expansion of bedrock parameters (Xu et al., 2017) 118

Table 12: Atmospheric pressure variations in winter, summer, autumn and winter at different stations. 123

Table 13: Distance between the local and regional GPS stations for Model-1 and 2. 124

Table 14: Ocean-less Earth model and Inverted barometer Earth Model displacement summary 127

Table 15: Unit heave strain for soils of varying potential expansiveness. 129

Table 16: Surface expansion depth factor for the first 8 meters of the subsurface. 129

Table 17: Station and site parameters at stations DEAR, SBOK, MFKG, UMTA and ULDI; and annual surface temperature and displacement power at the stations. 139

Table 18: Summary of the relation between surface displacement and meteorology processes. TS, TD, and FD stand for time series, time domain and frequency domain, respectively. 141

Table 19: Additional information about the displacement time series 177

Table 20: Continuous GPS time series processing steps (As taken from the Nevada Geodetic Laboratory site: - http://geodesy.unr.edu/gps/ngl.acn.txt) 178

List of abbreviations

AODC	Altitude and Orbit Determination and Control
BIH	Bureau International de I'Heure
CCF	Cross-Correlation Function
CFT	Continuous Fourier Transform
cGPS	Continuous Global Positioning System
CGCS200	China Geodetic Coordinate System 2000
CLT	Central Limit Theorem
CS	Cross-Spectrum
CSD	Cross Spectral Density
CWT	Continuous Wavelet Transform
DFT	Discrete Fourier Transform
DORIS	Doppler Orbit Determination and Radiopositioning Integrated by Satellite
DWT	Discrete Wavelet Transform
ECEF	Earth-Centred-Earth-Fixed
ENSO	El- Niño-Southern Oscillations
FFT	Fast Fourier Transform
FT	Fourier Transform
GDOP	Geometric Dilution of Precision
GNSS	Global Navigation Satellite System
GPS	Global Positioning System
GTRF	Galileo Terrestrial Reference System
IERS	International Earth Rotation Service
IGS	International GNSS Service

ITCZ	Intertropical Convergence Zone
ITRF	International Terrestrial Reference Frame
LLS	Lunar Laser Ranging
MCS	Master Control Station
MSC	Magnitude Squared Coherence
M-WT	Morlet Wavelet Transform
NAVSTAR	Navigation Satellite Timing And Ranging
OCR	Over-Consolidation Ratio
OCS	Operational Control Segment
PCC	Pearson's Correlation Coefficient
PDMT	Present-Day Surface Mass Trends
PRN	Pseudo-Random Noise
PSD	Power Spectral Density
PVT	Position, Velocity and Time
SAWS	South African Weather Service
SLR	Satellite Laser Ranging
SST	Seas Surface Temperature
STFT	Short Time Fourier Transform
TEB	Thermal Expansion of Bedrock
TEC	Total Electron Content
TEM	Thermal Expansion of the Monument
TS	Time series
TT&C	Tracking, Telemetry and Command
UNR	University of Nevada Reno

VLBL	Very Long Baseline Interferometry
WGS84	World Geodetic System 1984
WS	Wavelet Semblance
WT	Wavelet Transform

1 Introduction

1.1 Background

The outermost solid layer of the Earth, the crust, is always in constant motion; it deforms and translates both in the vertical and horizontal directions as a function of time due to tectonic and non-tectonic processes (Dong et al., 2002; Petrov and Boy, 2004; Min et al., 2005; Rodrigues, 2007; Xu et al., 2017). The continuous Global Positioning System (cGPS) is a space geodetic technique used to measure surface displacement of the crust over time. The measurements are used to study, infer, and monitor crustal deformation, tectonic motion, geodynamic processes and earthquakes (Larson and Agnew, 1991; Rodrigues, 2007; Goudarzi et al., 2012; He et al., 2015; Peng et al., 2017).

Regional and universal cGPS surface displacement measurements from all continents commonly reveal seasonal vertical and horizontal site displacements associated with tectonic and non-tectonic processes (Dong et al., 2002; Min et al., 2005; Rodrigues, 2007; He et al., 2015). Both the vertical and horizontal displacement components usually consist of an annual and semi-annual displacement component (Dong et al. 2002). Dong et al. (2002), van Dam et al. (2001) and van Dam and Wahr. (1998) suggested that the seasonal surface displacement components are a result of atmospheric loading, thermal and hydrodynamics induced variations, seasonal oceanic fluctuations due to tidal and non-tidal forces, variations in surface and subsurface water mass distribution, equipment and systematic processing errors. Surface and groundwater extraction near a cGPS site is also thought to play a significant role in local surface mass loading (van Dam et al., 2001). Surface displacements in the vertical component are often larger than those in the horizontal component; this being partly because 1) GPS systems measure displacement in the vertical direction with less accuracy compared to surface displacement in the horizontal direction (Larson and Agnew, 1991; Dong., et al. 2002; Rodrigues, 2007) and 2) some natural processes have more influence on surface displacement in the vertical direction than in the horizontal direction (Dong et al., 2002; Min et al., 2005; He et al., 2015).

Figure 1.1 shows a daily position surface displacement plot of station BETH, located in Bethlehem (South Africa). The abbreviation BETH represents Bethlehem. The data was collected using the International GNSS Service (IGS) reference frame IGS08. Analysing the easting and northing components in Figure 1.1a, it can be seen that the station is moving

Northeast. In Figure 1.1b, it is observed that at the station seasonal surface displacement in the vertical (up) component is of higher magnitude (±20 mm) compared to that in the horizontal (northing and easting) component (±5 mm), as expected.

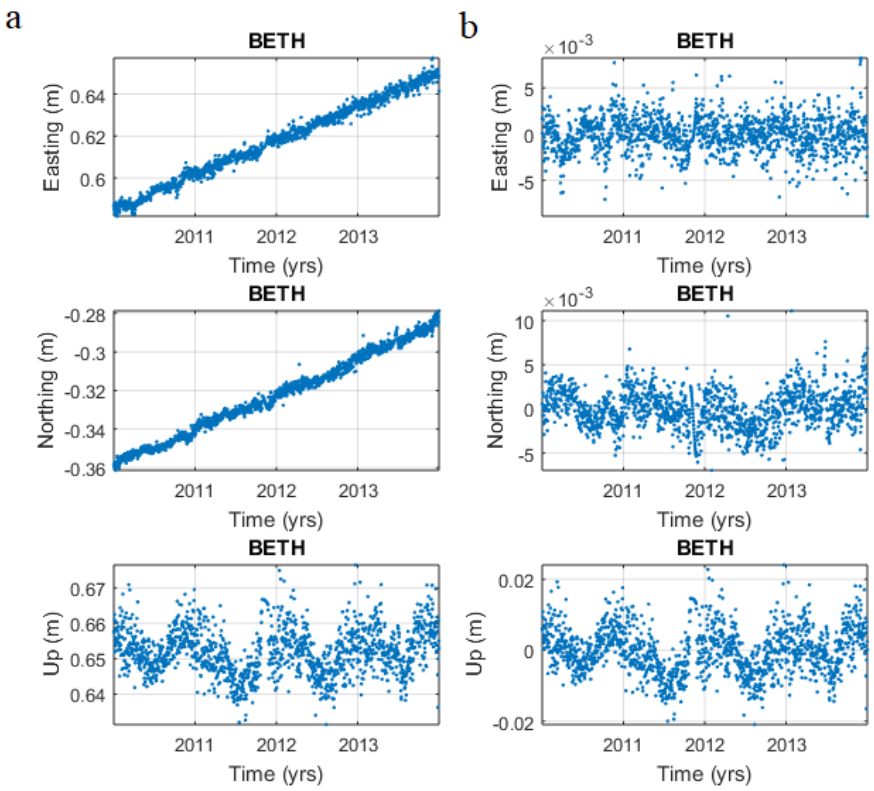


Figure 1.1: cGPS daily position time series of station BETH located in Bethlehem, South Africa. BETH represents Bethlehem. (a) Interpolated original time series. (b) Interpolated and detrended original time series; which shows the seasonal displacement of the easting and northing components with respect to that of the up (vertical) component.

The purpose of this research is to characterise and understand the effects of atmospheric processes (i.e., temperature, rainfall, humidity and pressure) on vertical surface displacement from cGPS time series in southern Africa using time series analysis techniques. To draw inference on the effects of thermal expansion, atmospheric pressure surface loading, and shrink and swell heave action on the displacement time series in southern Africa, since these are not corrected for in the displacement time series. The study focuses on analysing the relationship between the vertical position component of surface displacement with atmospheric processes, because displacement in this component is affected more by non-tectonic processes. Processes such as atmospheric loading, oceanic loading, solid Earth tides, nontidal ocean mass movements, soil moisture, snow depth, and, potentially bedrock thermal expansion and

contraction have more influence on the vertical position measurements than on the horizontal position measurements (Dong et al., 2002; He et al., 2015)

The study does acknowledge that when correcting for tropospheric effects, cGPS uses surface air temperature, atmospheric pressure, and relative humidity or water vapour measurements. These meteorological measurements are either collected by ground meteorological sensors or estimated using standard atmospheric models (El-Rabbany, 2002, p. 39; Kaplan and Hegarty, 2006, p. 314-316; Guochang, 2007, p. 55-57). The measured or estimated meteorological values are used by cGPS to correct for atmospheric effects due to climatic or weather conditions in the troposphere (Shuaggen et al., 2014, p. 19). These correct for atmospheric effects due to both the non-hydrostatic (wet) and hydrostatic (dry) components, which include atmospheric effects due to temperature, pressure, humidity and rainfall. However, thermal expansion and contraction of the cGPS monuments and surrounding bedrock, and near subsurface heave action induced by these processes are usually not taken into account in the conducted corrections (Romagnoli et al., 2003). Thus, in this study, the relationship between surface displacement and surface temperature, atmospheric pressure, rainfall, and humidity processes are studied to infer the effects of 1) thermal expansion and contraction of cGPS monuments and surrounding bedrock, 2) heave action and 3) tropospheric effect residual errors on cGPS surface displacement measurements. The effect of surface loading due to seasonal variations in atmospheric pressure is also inferred, since the used data is not corrected for surface loading due to atmospheric pressure.

Tropospheric effect residual errors are the tropospheric effects that remain behind in cGPS surface displacement measurements after compensating for tropospheric effects using tropospheric models. Since near surface measurements are used to correct for tropospheric effects and atmospheric conditions in the troposphere are not constant but vary with altitude and spatial locations. The models used are weakly correlated to the actual atmospheric conditions at greater altitudes of the troposphere and in between meteorological stations, due to atmospheric distribution uncertainties (El-Rabbany, 2002, p. 39; Kaplan and Hegarty, 2006, p. 315). Thus, the mathematical models leave behind residual errors in cGPS surface displacement measurements. As a result, understanding the influence of the considered atmospheric processes, might benefit the understanding of crustal deformation in southern Africa.

1.2 Project aims

The large number of climatic zones present in southern Africa and the fairly large cGPS spatial coverage, compared to other African regions, provide a good opportunity for investigating the effects of varying climatic conditions on cGPS time series. Thus, the aims of this research are to improve the understanding of seasonal components observed in vertical surface displacement measurements acquired using cGPS. To deduce whether a relation exists between the seasonal components in cGPS time series and the various climatic zones, and if so, does the relationship correlate with known weather information characteristic of the respective climatic zones. The project is carried out with the aim to improve the understanding of both surface displacement and meteorological processes characteristic of southern Africa using time series analysis techniques.

1.3 Research objectives

To achieve the aims of this study, the project will be based on achieving the following objectives:

i. Uncover dominant time series components constituting the cGPS and meteorological (atmospheric pressure, rain, temperature and humidity) time series.
ii. Investigate, understand, and possibly quantify the relationship between the seasonal components in cGPS and meteorological time series in the time, frequency, and time-frequency domains.

The research objective will be achieved through the use of Fourier Transforms (FT), Wavelet Transforms (WT), Wavelet Semblance (WS), Coherence and Cross-Spectrum Density spectral techniques. FT and WT are decomposition methods that enable the determination of dominant frequency components in a time series, in the frequency and time-frequency domain. WT also enable the change of the frequency components constituting a time series to be viewed and studied as a function of time. WS and CSD are frequency domain and time-frequency domain correlation methods that enable the correlation of frequency components of two or more time series. Visual plots will be used to analyse the displacement and meteorological time series in the time domain.

1.4 Significance of the study

The analysis of cGPS position time series is of fundamental importance in Earth science because it provides useful information about the geodynamics, crustal deformation and tectonic plate motion (global plate motion). The study will provide a better understanding of the relationship between rainfall, temperature, atmospheric pressure, humidity and surface displacement time series. It will assist in determining the temporal structure of surface deformation by monitoring transient surface deformation due to the considered meteorological phenomena. It also has the potential to assist in the identification of structural damages that might be associated with surface deformation induced by meteorological related processes; in determining the main meteorological driving forces of vertical surface displacement and better modelling of the process responsible for surface deformation.

1.5 Hypothesis

I will test two hypotheses:

1. Signal processing techniques can be used successfully to gain a better understanding of the processes that drive seasonal surface deformation and how the processes vary with time. Conventionally, cGPS time series components are extracted, estimated and studied using the least-squares and Kalman filter methods; and their relationship with other geophysical processes are studied using well understood geophysical and tectonic models, e.g., Dong et al. (2002) and Davis et al. (2014).
2. Considering that most of the cGPS stations in southern Africa are mounted on concrete slabs and monuments and some of the AfricaArray stations on roof tops, changes in thermal expansion due to seasonal changes in temperature might be more influential in the formation of the seasonal displacement than changes in atmospheric pressure, rainfall, and humidity processes.

1.6 Description of the study area

The study will be conducted on data obtained from cGPS and meteorological stations located in southern Africa, which is the southernmost region of the African continent. It encompasses the following countries: South Africa, Lesotho, Swaziland, Mozambique, Zimbabwe, Zambia, Malawi, Botswana, and Angola (World Meteorological Organization, 2015, p. 5,7, 17) (Figure 1.2). Southern Africa is reasonably well covered by cGPS and meteorological station. It hosts

a large number of cGPS and meteorological stations compared to most regions of the African continent.

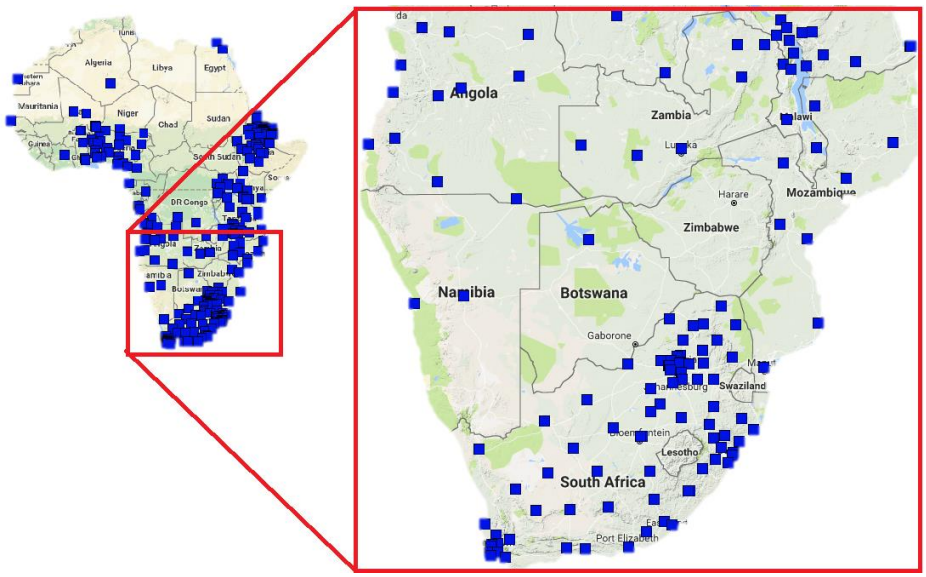


Figure 1.2: Map of Africa and southern Africa with locations of cGPS stations (http://geodesy.unr.edu/NGLStationPages/gpsnetmap/GPSNetMap.html).

Southern Africa is largely a semi-arid region; its western side is covered by desert lands and its general climate varies from dry arid conditions in the west to humid tropical conditions in the north and east side (Hepburn and Radloff, 1998, p. 3; Daron, 2014, p. 7). Southern Africa comprises five climatic zones viz. the Mediterranean, Desert, Sahelian, Dry Tropical and Wet Tropical (Hepburn and Radloff, 1998, p. 3; World Meteorological Organization, 2015, p. 7; Figure 1.3). The Mediterranean climatic zone is a winter rainfall region, with humid winters, and hot and dry summers (Barry and Chorley, 2010, p. 301). It is characterized by an even annual rainfall distribution (Hepburn and Radloff, 1998, p. 294). The Desert climatic zone is a region of high temperature fluctuation and very low rainfall, scattered over time and space (Hepburn and Radloff, 1998, p. 2,11; Barry and Chorley, 2010, p. 298). The Sahelian climatic zone is similar to the Desert climatic zone, however, it is defined by a longer rainfall period and less temperature extremes (fluctuations) compared to the Desert climatic zone. It consists of a distinct extended dry season and a short rainfall season (Hepburn and Radloff, 1998, p. 1,2). The Dry Tropical climatic zone is also characterized by a distinct dry and wet season. It consists of a longer rainfall season and a shorter dry season compared to the Sahelian climatic zone.

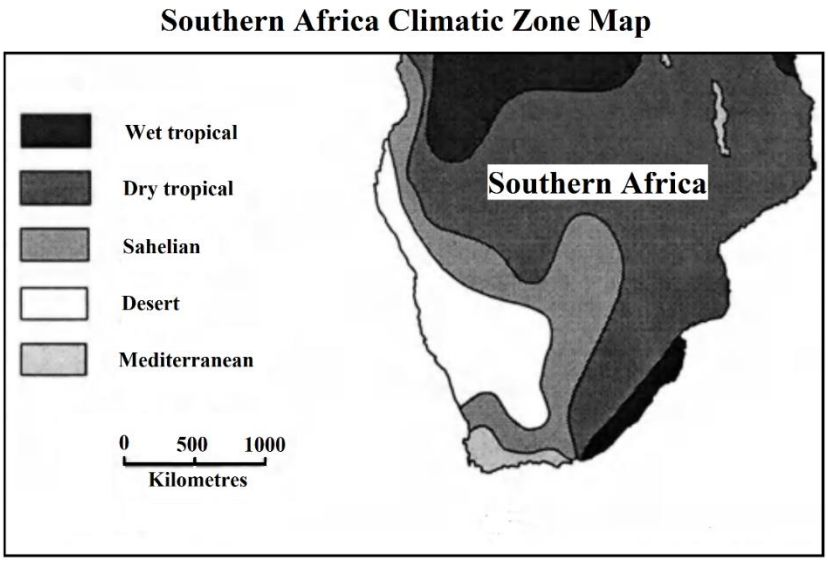


Figure 1.3: Climatic zone map of southern Africa (modified after Hepburn and Radloff, 1998).

The temperature fluctuations in the Dry Tropical climatic zone are less compared to that of the Sahelian and Desert climatic zones (Hepburn and Radloff, 1998, p. 1,2). The Wet Tropical climatic zone is characterized by a longer rainfall season and a shorter dry season. Temperature fluctuations in this climatic zone are less than in the Dry Tropical, Sahelian, Desert and Mediterranean climatic zones (Hepburn and Radloff, 1998, p. 1).

Weather conditions in southern Africa vary due to continental and oceanic interactions. Fluctuations in weather conditions are primarily controlled by the Intertropical Convergence Zone (ITCZ), variation in sea surface temperature (associated with the El-Niño-Southern Oscillations (ENSO) event), tropical cyclones in the warm Indian and cool South Atlantic Oceans, changes in the atmospheric pressure systems, solar radiation and altitude variations (Barry and Chorley, 2010, p. 483; Tadross and Johnston, 2012, p. 2; Jury, 2013; Daron, 2014, p. 7).

The ITCZ is a narrow tropical belt of low atmospheric pressure that occurs where northern and southern hemisphere air masses of contrasting temperature meet (Barry and Chorley, 2010, p. 246, 327; Schneider et al., 2014). The position of the ITCZ shifts seasonally north and south of the equator towards a differentially warmer hemisphere (Barry and Chorley, 2010, p. 246; Daron, 2014, p. 7; Schneider et al., 2014). The interaction (or convergence) of the interhemispheric masses of contrasting temperature at the ITCZ, results in an ascent of moist air mass, cooling, condensation and precipitation from deep convective clouds in the ITCZ (Schneider et al., 2014). Thus, in most parts of southern Africa, excluding the Mediterranean

region, wet spells occur in the presence of the ITCZ during summer, when the ITCZ is at its southernmost location; which as the ITCZ moves towards the north, dry spells prevail (Barry and Chorley, 2010, p. 372). In the Mediterranean region, rainfall is brought by winter cyclones (Barry and Chorley, 2010, p. 484).

The El Niño-Southern Oscillation (ENSO) is a term used to refer to a cyclic phenomenon of above and below average sea surface temperatures (SST) in the Pacific Ocean. The occurrence of the ENSO is associated with the exchange of air mass, subjected to inversely correlated pressure, between the eastern and western hemispheres centred in tropical and subtropical latitudes; and the atmosphere-ocean interactions that results in above (below) normal warming (cooling) sea surface temperatures in the Pacific (Herbert and Dixon, 2002; Stenseth et al., 2003; Barry and Chorley, 2010, p. 8, 187 & 375). The period of the ENSO is irregular, varying from two to ten years. The positive phase (high phase) of the ENSO is called the La Niña and its negative phase (low phase) is called the El Niño. During the positive phase of the ENSO (La Niña) enhanced cooler and wetter conditions prevail in southern Africa and during its negative phase (El Niño) warmer and drier than normal temperatures prevail in southern Africa (Nicholson and Kim, 1997; Barry and Chorley, 2010, p. 376; Tadross and Johnston, 2012, p. 2; Daron, 2014, p. 8). The intensity of the ENSO modulates the position of the ITCZ and the amount of rainfall that southern Africa receives (Nicholson and Kim, 1997; Schneider et al., 2014).

The weather in southern Africa has four seasons, i.e., summer, autumn, winter and spring, the seasonal change mainly reflects seasonal variation in solar radiation and wind distribution. The seasonal changes are mainly associated with variation in the solar radiation, ITCZ, SST and subtropical high-pressure cells (Linacre and Geerts, 1997; Creese et al., 2016; Barry and Chorley, 2010, p. 317). Latitude variations contribute to differences in seasonal maxima and minima of meteorological processes prevalent over southern Africa. Maximum and minimum extremes in temperature, pressure, rainfall and humidity often occur in summer and winter respectively. The difference between summer maxima and winter minima is large over the southern Africa plateau and small near the coasts and in the areas of southern Africa closer to the equator (Linacre and Geerts, 1997; Creese et al., 2016).

Generally, in southern Africa, uniform hot conditions prevail in summer, while low temperatures prevail in winter. Low atmospheric pressure prevails in summer due to the presence of the ITCZ, which is a low-pressure system, and absence of the high-pressure cells

over southern Africa (i.e., the South Atlantic and Indian Ocean high-pressure cells). High atmospheric pressure prevails in winter because of the absence of the ITCZ and merging of the South Atlantic and Indian Ocean pressure cells over southern Africa (Linacre and Geerts, 1997; Sun et al., 2017). The south-western part of southern Africa is characterised by winter rainfall and the central-and north-eastern parts are characterised by summer rainfall. In the summer rainfall regions, heavy and unstable rains associated with the annual fluctuation of the ITCZ occur, while in the winter rainfall regions, rainfall is due to cold fronts (Linacre and Geerts, 1997). In summer, moist air is brought about by easterlies from the Southwest Indian Ocean and warm Agulhas current; while, in winter, dry air is brought about by westerlies from the Southern Atlantic Ocean and Benguela current (Jury, 2013).

1.7 Thesis structure

This thesis is divided into eight chapters, Chapter 1 highlights the project aims, objectives and significance. Chapter 2 gives an overview of GPS systems, their sources of error and application in tectonic and non-tectonic studies. The chapter also gives a brief history about the development of Fourier and wavelet transform techniques. Chapter 3 provides an overview of the sampling procedure and a review of the time, frequency and time-frequency decomposition and correlation time analysis techniques used in carrying out the study. Chapter 4 presents how synthetic data resembling cGPS and meteorology time series is generated. Provides decomposition and correlation tests of the time analysis techniques reviewed in chapter 3 on synthetic data and an analysis of their performance when applied to noise-free and noise contaminated time series. Chapter 5 provides authentic time, frequency and time-frequency decomposition and correlation results of the cGPS and meteorology time series. The chapter also gives a brief interpretation of the obtained decomposition and correlation results. Chapter 6 presents estimates of seasonal surface deformation due to thermal expansion, atmospheric pressure and heave action. Chapter 7 gives a detailed discussion of the decomposition and correlation results of cGPS and meteorology time series in southern Africa and Chapter 8 presents the conclusions and limitations of the research.

2 Literature review

2.1 International Terrestrial Reference Frame (ITRF)

The International Terrestrial Reference Frame (ITRF) is a globally well-defined and stable reference frame used by space geodetic systems (e.g., Global Positioning System) to determine high-precision locations on the Earth's surface. It is the most accurate geodetic reference system of the International Terrestrial Reference Systems (ITRS), on which most reference systems (e.g., the WGS84, CGCS200 and GTRF) are based (Dong et al., 2003; Altamimi et al., 2011; Altamimi, 2012; Blewitt, 2015). The ITRF is essential for high precision navigation, orbit tracking and global change monitoring relative to the rotation motion of the Earth; as well as measurements of the dynamic motion of the tectonic plates relative to the Earth's motion (Wu et al., 2011). It also enables the determination of change in phenomena such as sea level, glacial isostatic adjustments, plate tectonics, plate boundary deformation, regional subsidence, Earth orientation excitation, present-day surface mass trends (PDMT), and geocenter velocity. The ITRF enables position to be determined with a high level of precision (of a few millimetres) so that variations as small as 1 mm/yr can be measured (Altamimi et al, 2001, Dong et al., 2003).

The ITRF was first established in 1988 after the formation of the International Earth Rotation Service (IERS). IERS computed the ITRF using measurements from space geodetic observation techniques, which include the Very Long Baseline Interferometry (VLBI) astrometry, Lunar and satellite laser ranging (LLR, SLR), Doppler Orbit determination and Radiopositioning Integrated by Satellite (DORIS), and GPS tracking (Dong et al., 2003; Altamimi et al., 2011). The ITRF is formed using measurements of the VLBI astrometry, LLR, GPS tracking, SLR and DORIS; linear velocities obtained from a global set of observation sites and a global Cartesian coordinate system (Altamimi et al, 2001). Mathematically and physically, the ITRF is defined by its origin, scale, orientation and its time evolution (Figure 2.1). It is a geocentric datum with its origin at the Earth's centre of mass, which considers its ocean and atmosphere. The scale of the ITRF is taken to be that of the local Earth frame within a relativistic theory of gravitation and its orientation is given by the Bureau International de I'Heure (BIH) orientation (Dong, 2003). The Earth-Centred Earth-Fixed (ECEF) coordinate system is the fundamental basis to which the ITRF is computed (Figure 2.1).

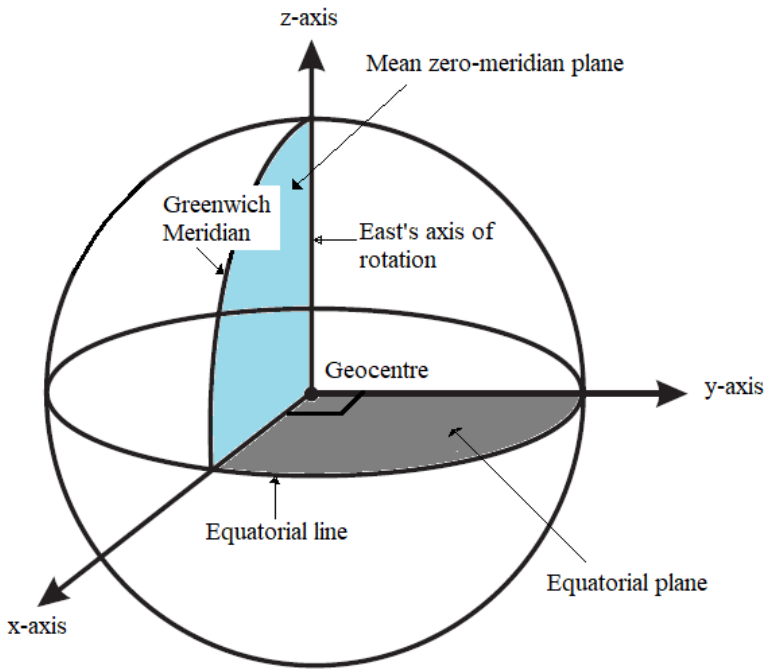


Figure 2.1: Earth-Centred Earth Fixed Coordinates System (modified after Guochang, 2007, p. 7).

The ECEF is a right-handed Cartesian coordinate system (x, y, z). Its origin coincides with the Earth's centre of mass; the x-axis points and extends through the mean Greenwich meridian; and the y-axis is located 90 degrees of the x-axis along the equatorial line. Together, the x-axis and y-axis define the equatorial plane, and the z-axis coincides with the mean rotation axis of the Earth (Figure 2.1, Guochang, 2007, p. 7). Relative to a point on Earth, the ITRF is in static motion, but relative to a point in space, the ITRF is in dynamic motion co-rotating with the Earth. Determination of the Earth's orientation and its variation over time enables the continuous determination of the Earth's rotation (Altamimi et al., 2011). Since the coordinates of the ITRF are arbitrary and are of convenience, the ITFR is considered to be an ideal system. The frame parameters (i.e., scale, origin, and orientation) of the ITFR vary with time as the reference frame is improved through the use of more data and by improving dynamic data (Altamini, 2012; Dong et al., 2003).

2.2 Global Positioning Systems

The Global Positioning System (GPS) is a navigation geodetic system formed by a constellation of 24 satellites distributed in six orbital planes, that orbit the earth twice a day, and several monitoring ground stations. The first space GPS launch was in 1974 and the full

implementation of the GPS constellation was completed in 1994, when it was made available to users globally (El-Rabbany, 2002, p. 1; Guochang, 2007, p. 2; Shuanggen et al., 2014, p. 5). The GPS satellites orbit the earth at a height of about 26560 km from its centre (approximately 20200 km above the Earth) with an orbital plane inclination of about 55 degrees; at a speed of 3.9 km/s and have a circulation Earth time of 11 h 58 min. (Wells et al., 1986, p. 3.8; El-Rabbany, 2002, p. 2; Guochang, 2007, p. 2; Shuanggen et al., 2014, p. 4). The satellites transmit radio signals containing satellite position and time data, which enable the determination of geographical locations.

Over the past two decades, the Global Positioning System (GPS) has been increasingly used to study a wide range of geophysical phenomena, such as the changes in the position of the Earth's tectonic plates, deformations around active areas, and the adjustment of the Earth's surface due to past and present changes. At least three satellites are needed to calculate and observe changes of position and motion in a two-dimensional plane, and at least four satellites are needed to calculate position and motion in three dimensions (McNamara, 2004; Shuanggen et al., 2014, p. 12). The Global Positioning System is used to study atmospheric and surface variations because it provides unparalleled high-accuracy all-weather measurements; it is inexpensive compared to other techniques that are used for the same purpose when used to measure atmospheric or surface variations at a large scale (e.g., tapes, electronic distance measurement (EDM), theodolite, bars etc.); and provides a precise geodetic tool for university scholars and other research groups to use (Shuanggen et al., 2014, p. v, 5; El-Rabbany, 2002, p. 10). In the future, it is thought that GPS systems will play a very important role in atmospheric sounding, meteorology, climatology and space weather studies (Shuanggen et al., 2014, p. v).

2.3 Global Navigation Satellite Systems segments

The Global Navigation Satellite Systems (GNSS) consists of three fundamental segments: viz., the space, control and user segments (Figure 2.2). The segments are linked together into one system by GPS signals that broadcast and carry data from the GPS satellites to both the ground and user segments. Figure 2.2 shows the three GNSS segments and their relationship.

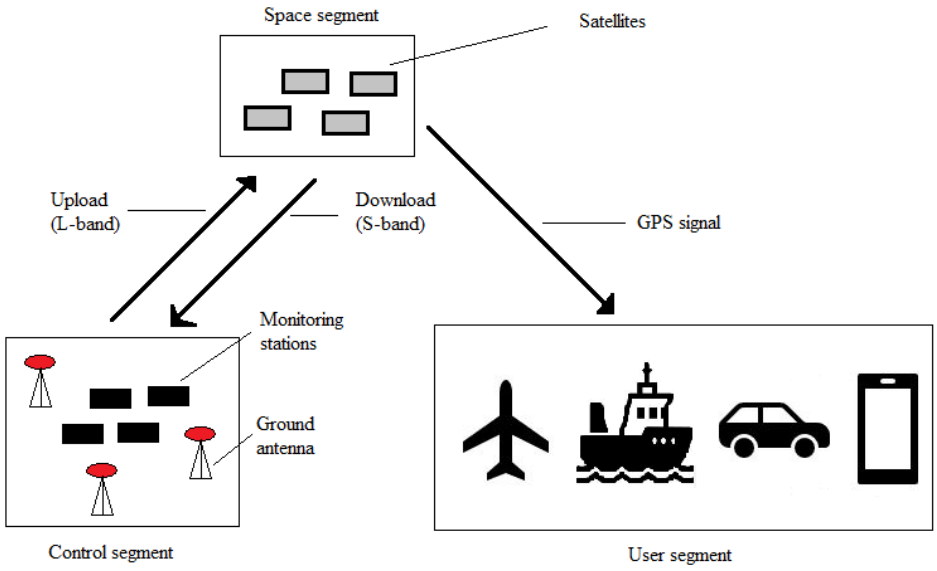


Figure 2.2: GNSS segments and their relation.

2.3.1 Space segment

The space segment is composed of a 24-satellite constellation (plus extra operational spare satellites), that are arranged over six medium Earth orbital planes. The orbits through which the satellites move have an orbital radius of approximately 26 000 km from the Earth's centre of mass (National Research Council, 1995; El-Rabbany, 2002, p. 2; Shuanggen et al., 2014, p. 9). The constellation is designed such that at least four to six satellites are always visible at any point across the globe (Shuanggen et al., 2014, p. 12; McNamara, 2004). The satellites are equipped with navigation antennas, atomic clocks, and other subordinate systems such as Tracking, Telemetry and Command (TT&C); thermal, propulsion, attitude and Orbit Determination and Control (AODC) and power subsystems (Shuanggen et al., 2014, p. 9; El-Rabbany, 2002, p. 3). These control and enable operational flexibility of the satellites to maintain itself without any contact from the Operational Control Segment (OCS) for a prolonged number of days (National Research Council, 1995).

Generally, the signals transmitted by satellites consist of two carrier frequencies (L1 ($f_1 = 1.57542$ GHz) and L2 ($f_2 = 1.2276$ GHz)), a pseudo-random noise (PRN) code and a navigation message (Shuanggen et al., 2014, p. 10). A PRN code is a unique binary number that enables a GPS receiver to distinguish between GPS signals from different satellites, each satellite transmits its own unique PRN code. The carrier frequencies and codes are used to calculate the pseudorange between the GPS satellite and a user receiver; while the navigation

message contains location coordinates that vary as a function of time (El-Rabbany, 2002, p. 2; McNamara, 2004; Shuanggen et al., 2014, p. 11). The signals transmitted by the GPS satellites are controlled by stable atomic clocks. The space segment is also known as the Navigation Satellite Timing And Ranging (NAVSTAR) constellation.

2.3.2 Ground segment

The ground segment is composed of a large worldwide network of tracking stations (Figure 2.2) that track the position of GPS satellites to determine and predict their location (McNamara, 2004; Kaplan and Hegarty, 2006, p. 68; Shuanggen et al., 2014, p. 9). The ground segment is also called the control segment because it is the main controls of the GPS and is used to monitor satellite transmissions, predict satellite ephemeris, to calibrate satellite clocks, and update the navigation message periodically (El-Rabbany, 2002, p. 3; Kaplan and Hegarty, 2006, p. 68; Shuanggen et al., 2014, p. 9). It consists of the master control station (MCS), remote monitoring stations, and uplink antennas (National Research Council, 1995). The MCS is responsible for the overall satellite control and maintenance, which includes maintaining the exact position of all satellite orbits, determining any timing errors, monitoring the signals transmitted by GPS signals, and updating the orbit and clock errors every day. The remote monitoring stations are responsible for tracking the position of all satellite in orbit, monitoring their navigation signal, and for relaying this information to the MCS. The ground antennas are used to update the clock and orbit errors (National Research Council, 1995; Kaplan and Hegarty, 2006, p. 68; Shuanggen et al., 2014, p. 9).

2.3.3 User segment

The last segment is the user segment (Figure 2.2). This segment observes and records the transmissions of several satellites and applies solution algorithms to obtain the position, velocity and time (El-Rabbany, 2002, p. 3; McNamara, 2004). Most user segments consist of a GPS antenna, receiver-processor unit, and a control/display unit. The antenna receives the GPS signal; the receiver-processor unit converts the GPS signal to a usable navigation solution; and the control/display unit provides an interface control and displays the positioning information (National Research Council, 1995; Kaplan and Hegarty, 2006, p. 68).

2.4 Brief overview of GPS errors and their sources

Climate conditions in the atmosphere (upper and lower atmosphere) and geographic features (such as buildings, trees, water, etc) on the Earth's surface induce delays and phase changes in GPS signals that cause retardation of the signal speed and lengthen (curving) the geometric path of the signal.

GPS error sources are commonly classified into satellite errors, propagation errors (errors in transmission medium), and receiver or site errors. Satellite errors are divided into orbital (ephemeris) errors and clock errors, while receiver or site errors are divided into receiver clock errors, antenna phase centre movements, multi-path and imaging errors. Propagation errors are divided into ionospheric and tropospheric refractions. The most significant sources of error are discussed in the following paragraphs.

2.4.1 Propagation delays

As GPS signals propagate through the atmosphere, they are refracted and retarded in the ionosphere (ion- and electron-rich atmospheric layer extending from ~ 60 km to more than 1000 km above the Earth's surface) and tropospheric effect zone (Figure 2.3). The tropospheric effect zone extends from the Earth's surface to approximately 50 km above the surface. The tropospheric effect zone is divided into the troposphere (lowermost layer of the atmosphere, extending from the Earth's surface to roughly 10 km above the surface) and stratosphere (atmospheric layer above the troposphere, extending from 10 km to about 50 km above the Earth's surface). The refraction and retardation of GPS signals as they pass through the atmosphere are a result of the inhomogeneous and complex nature of the atmosphere, which is largely caused by the Earth's magnetic field and solar activities. Refraction of the GPS signal is caused by variations in the air mass, which decreases from the Earth's surface to higher altitudes of the atmosphere. Refraction of the GPS signal is the main cause for ionospheric and tropospheric atmospheric delays in the atmosphere (Shuanggen et al., 2014, p. 17, 78; El-Rabbany, 2002, p. 27).

2.4.1.1 Ionospheric delay

The ionosphere is a complex and fluctuating region within the upper part of the Earth's atmosphere that contains a high concentration of plasma (gas containing positive ions and electrons). It constitutes less than 0.1% of the total mass of the Earth's atmosphere. Its exact

location changes constantly, but generally ranges from 50 km to more than 1000 km above the Earth's surface (Wells et al., 1986, p. 9.5; El-Rabbany, 2002, p. 36; Khan, 2005, p. 14; Kaplan and Hegarty, 2006, p. 310; Guochang, 2007, p. 43, 51; Shuanggen et al., 2014, p. 18, 20, 61, 169).

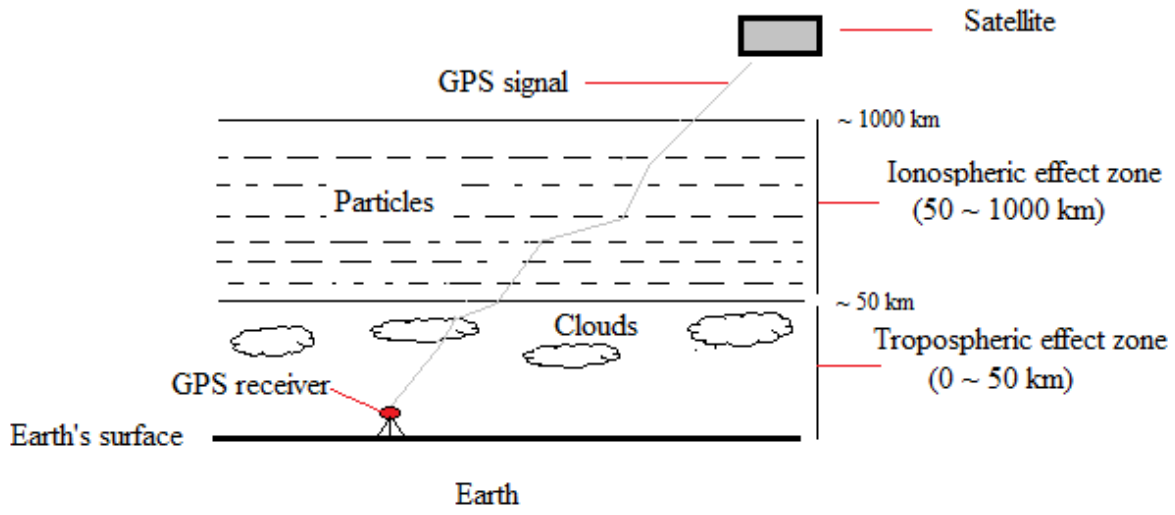


Figure 2.3: Tropospheric and ionospheric error sources and zones.

The charged particles present in the ionosphere are formed when ultraviolet and X-ray radiation emitted by the sun (by solar flares) interacts with atoms and gas molecules present in the ionosphere. The interaction results in gas ionisation in the ionosphere that produces free negatively-charged electrons and positively-charged protons (plasma) (Wells et al., 1986, p. 9.5; El-Rabbany, 2002, p. 36; Kaplan and Hegarty, 2006, p. 310). Within the ionosphere, the plasma is driven by tidal forces, temperature gradients, and Coriolis forces to form an electric current called a ring current that drifts westward from the equatorial region to the poles (Shuanggen et al., 2014, p. 20, 61, 75). Figure 2.4 shows the electron density structure of the atmosphere.

The ionosphere is divided into subregions based on the electron density and variation of the electron density with altitude. The thickness and altitude of these subregions vary depending on the Sun's radiation, Earth's magnetic field, geographic location and time of the year and day (El-Rabbany, 2002, p. 37; Pulinets and Boyarchuk, 2004, p. 19; Khan, 2005, p. 14; Shuanggen et al., 2014, p. 21). These subregions are the D-layer (50-90 km), E-layer (90-140 km), F1-layer (140-210 km), and F2-layer (210-1000 km), as illustrated in Figure 2.4 (El-Rabbany, 2002, p. 37; Pulinets and Boyarchuk, 2004, p. 20; Khan, 2005, p. 14).

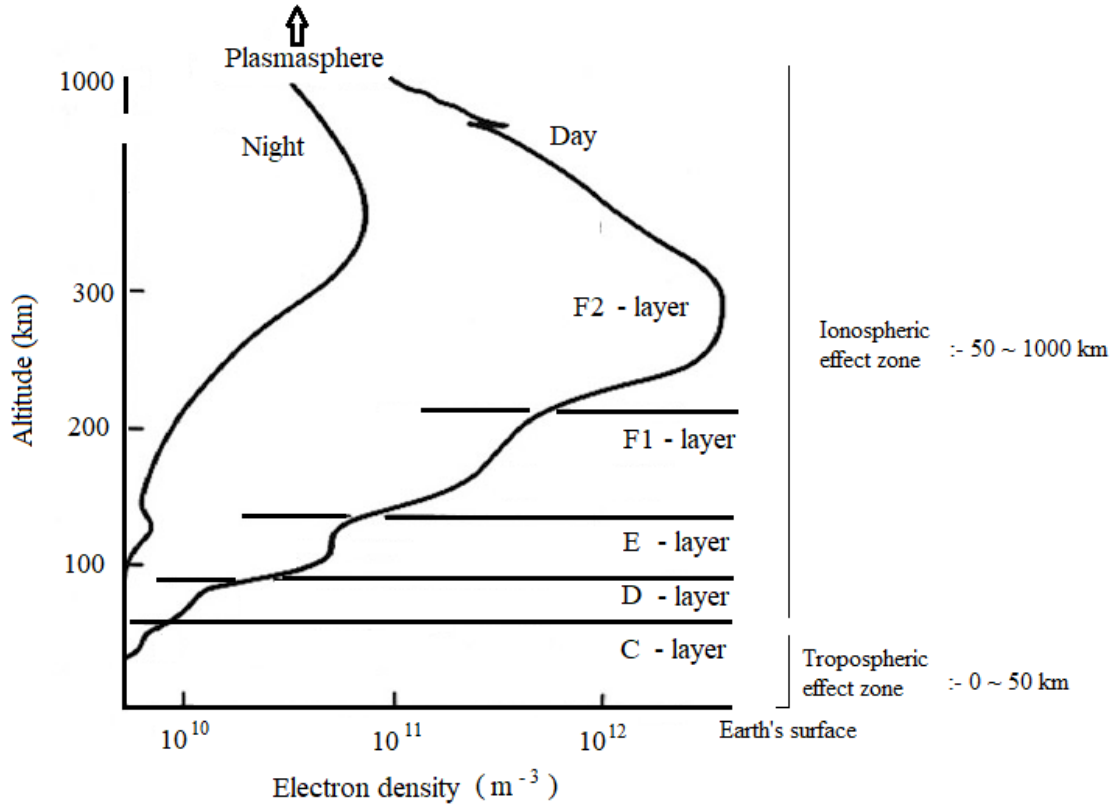


Figure 2.4: Variation of the electron density with altitude from the Earth's surface in summer (modified after Pulinets and Boyarchuk, 2004).

The electron density in the ionosphere is greater during summer than in winter and it reaches its daily maximum in the early afternoon and its minimum around midnight (Shuanggen et al., 2014, p. 87). This is so because the Earth's orbit is closer to the Sun in summer than it is in winter. Thus, the Earth becomes more exposed to the sun's radiation in summertime. Since the Sun's radiation is strongest during daylight, the electron density in the ionosphere is also greatest during the day and smaller at night (Figure 2.4). Electron density levels are also at their lowest (minimum) in mid-latitude regions. Near the poles, auroral, and the equatorial regions, electron density levels are at their highest level and are highly irregular in these regions (El-Rabbany, 2002, p. 37; Shuanggen et al., 2014, p. 87).

Subregion F1 is most likely to appear in summer daylight and is more pronounced in summer than in winter. The Earth's magnetic field is weakest in the F2-layer as compared to the other layers of the ionosphere, consequently the subregion F2 is usually characterized by the greatest electron density (El-Rabbany, 2002, p. 37; Pulinets and Boyarchuk, 2004, p. 22, 23) because less solar flare activity is reflected from it (Shuanggen et al., 2014, p. 21).

When a GPS signal (radio wave) passes through the ionosphere the plasma in the layer acts as a dispersive medium which refracts and bends the GPS radio signals as they pass through it. In the process, the propagation speed of the PRN code and the navigation message becomes slower by approximately the inverse change in the speed of the carrier phase (Wells et al., 1986, p. 9.5; El-Rabbany, 2002, p. 37; Guochang, 2007, p. 43). These changes in the propagation speed of the components of the GPS signal result in a significant delay in the GPS signal, which is proportional to the total electron content present in the ionosphere. The delay introduces significant pseudorange errors in the GPS system that must be accounted for. The pseudorange errors can be of the order of 5 m (at night, sunspot minimum satellites near zenith) to as high as 15 m (at midday, sunspot maximum periods, satellites close to the horizon) (Wells et al., 1986, p. 9.6; El-Rabbany, 2002, p. 37; Guochang, 2007, p. 43). In temperate zones, the behaviour of the ionosphere is much more stable and predictable than near the geographic poles or equator.

2.4.1.2 Tropospheric delay

The troposphere is the lowest layer of the atmosphere; its height varies from the poles (where it is lowest due to the prevalent cold conditions) to the equator (where it is highest due to the prevalent warm conditions). The tropospheric effect zone is an electrically neutral region in the atmosphere where almost all-weather conditions occurs, including wind, rain, thunderstorms, cyclones, etc., occur. It is a non-dispersive medium for frequencies below 30 GHz and only refraction of the carrier frequencies, code and navigation message occurs (Wells et al., 1986, p. 9.7; El-Rabbany, 2002, p. 38; Guochang, 2007, p. 55). Refraction is the main process responsible for GPS radio signal disturbances in the tropospheric effect zone. The refraction in this layer is subdivided into wet and hydrostatic (dry) components. The hydrostatic component is responsible for approximately 90% (only10% is caused by the wet component) of the delay in GPS signals and pseudorange errors that are caused by tropospheric effects (Wells et al., 1986, p. 9.7; El-Rabbany, 2002, p. 39; Kaplan and Hegarty, 2006, p. 310; Guochang, 2007, p. 55; Shuaggen et al., 2014, p. 41, 42). The following equation is usually used to approximate the delays due to refraction by the hydrostatic component in the troposphere (Wells et al, 1986, p. 9.7):

$$\mathrm{DTC} = 2.27 \times 10^{-3}(\mathrm{P}_0) \quad \textbf{(1)}$$

where DTC is the estimated hydrostatic-refraction delay component and P_0 is the surface pressure in mbar.

The wet component delays depend on the atmospheric condition (mainly water vapour) prevalent along the GPS signal path as it travels through the tropospheric effect zone. It is also the hardest tropospheric refraction delay component to predict (Wells et al., 1986, p. 9.7; El-Rabbany, 2002, p. 39; Shuaggen et al 2014, p. 17, 34). Most mathematical models that have been developed to predict the refraction wet component use temperature, atmospheric pressure, humidity and partial water vapour from surface meteorological measurements. These are, however, weakly correlated to the actual atmospheric conditions at greater altitudes of the tropospheric effect zone, rather than the Earth's surface. This is because atmospheric conditions in the tropospheric effect zone are not constant but vary with altitude, which makes it hard to predict the wet component delay of the troposphere with high accuracy (Wells et al., 1986, p. 9.7; El-Rabbany, 2002, p. 39; Kaplan and Hegarty, 2006, p. 314-316; Shuaggen et al., 2014, p. 42).

In general, the amount of delay that the GPS signal attains as it passes through the tropospheric effect zone is dependent on the temperature, humidity, and pressure along the signal path and on the elevation angle (El-Rabbany, 2002, p. 39; Khan, 2005, p. 12; Kaplan and Hegarty, 2006, p. 314; Guochang, 2007, p. 55; Shuaggen et al., 2014, p. 33). At lower elevation angles, satellite signals travel a longer path through the tropospheric effect zone than when travelling through the tropospheric effect zone at angles of high elevation. Thus, the tropospheric delay is maximized at low elevation angles, near the horizon, and minimized at angles of high elevation, at the receiver's zenith (El-Rabbany, 2002, p. 39; Wells et al., 1986, p. 9.06, 9.07).

The delay occurs due to the interaction between the GPS signal with neutral atoms and molecules in the tropospheric effect zone. The delay introduces error in the GPS system's pseudorange calculation, which in turn produces an error in the calculation of position measurements on the Earth's surface. The ionospheric or tropospheric effects have very similar influence on position measurements determined at nearby GPS stations, thus differentiation of the GPS data enables the errors to be cancelled out using the double differential technique (Shuanggen et al., 2014, p. 12, 108-109, 34). For GPS receivers separated by a distance greater than 50 km, the tropospheric conditions above them can be very different, which results in different signal delays and an increase in the influence of tropospheric and ionospheric effects

(Khan, 2005, p. 12). In general, characteristics of this layer alter the travel time of GPS signals, causing their speed to be different from the speed of a GPS signal in space.

2.4.2 Multipath errors

Multipath is the phenomenon where a GPS signal reaches a GPS receiver via two or more propagation paths (Wells et al., 1986, p. 9.11; El-Rabbany. 2002, p. 32; Khan, 2005, p. 16; Guochang, 2007, p. 78). The phenomenon occurs when a GPS satellite signal is disturbed (reflected or diffracted) as it travels through the atmosphere from the GPS satellite to the GPS receiver by, mainly, solid materials in the signal's path (Figure 2.5). GPS signals are reflected by materials such as water (both in the atmosphere and on the surface), soil, walls, mountains, trees, buildings, and flat surfaces (Wells et al., 1986, p. 9.11; Khan, 2005, p. 16; Shuanggen et al., 2014, p. 27). Multipath effects cause an increase in the path length of the GPS signals (from the GPS satellite to the receiver), which in turn, results in the interference of the GPS signals at the receiver and distortion of the original signal (El-Rabbany, 2002, p. 32; Wells et al., 1986, p. 9.11). Multipath effects are a variable of time, satellite position and the environment in which a GPS receiver antenna is situated (Khan, 2005, p. 16; Kaplan and Hegarty, 2006, p. 319; Gouchang, 2007, p. 78; Shuanggen et al., 2014, p. 27).

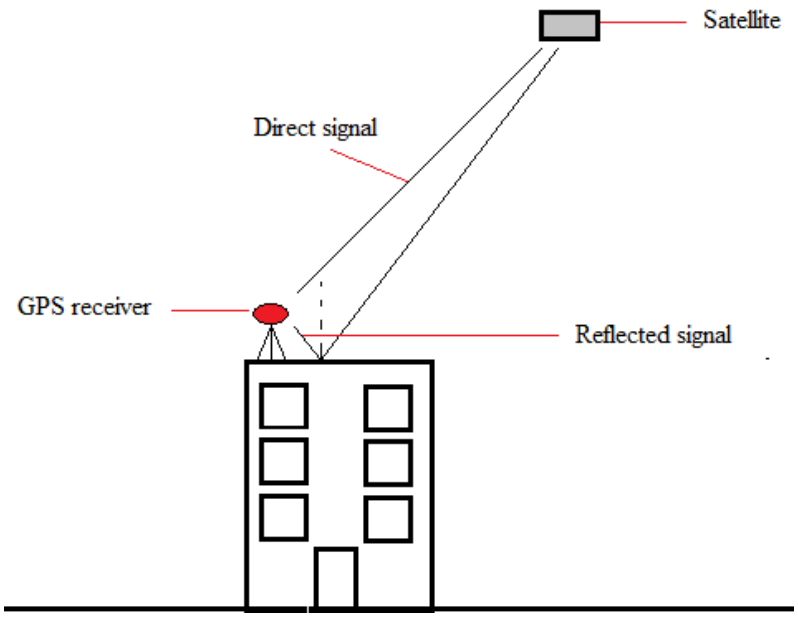


Figure 2.5: Direct and reflected (Multipath) signals.

Consequently, multipath results in erroneous pseudorange estimates (that are much larger than the true value) and introduces a phase shift in the carrier phase. Pseudorange multipath errors can reach a maximum of a few meters (El-Rabbany, 2002, p. 32; Khan, 2005, p. 16; Gouchang, 2007, p. 78). Even though there are techniques to reduce multipath errors, it is difficult to eliminate them with high accuracy because of the variant nature of the geometry of the satellite, reflector and GPS antenna (El-Rabbany, 2002, p. 33; Kaplan and Hegarty, 2006, p. 319). Some of the techniques that are used to reduce multipath errors are to select sites with no reflecting object near the receiver; shaping the antenna to discriminate against signals arriving in certain directions (polarization); use of a chock ring, which attenuates reflected signals; and by using an antenna with a matching polarization with the GPS signal. (Wells et al., 1986, p. 9.12; El-Rabbany, 2002, p. 34).

2.4.3 Satellite geometric errors

Some errors in GPS systems are introduced by the geometry of the satellites used to take GPS position measurements. Satellite geometry is the geometric location of satellites, used to take position measurements, with respect to a GPS receiver (Figure 2.6; El-Rabbany, 2002, p. 39; Dutt et al., 2009). The satellite geometry has a huge influence in the accuracy with which GPS system takes measurements and thus, the margin of error introduced in GPS measurements (Dutt et al., 2009). This is because the satellite geometry alters the measured satellite-receiver distance and thus, the pseudorange measurements, which in turn introduce an uncertainty in the estimated position measurements.

To determine the best satellite configuration, GPS systems use the Geometric Dilution of Precision (GDOP), which is a dimensionless measure of the geometric strength of the satellite configuration (Wells et al., 1986, p. 4. 23, 14.10; El-Rabbany, 2002, p. 40; Dutt et al., 2009). The GDOP calculates the effects of error in the final estimates of GPS position measurements that are introduced in position measurements because of the satellite geometry used to collect the measurements (Dutt et al., 2009; Unogwu et al., 2015). Mathematically, the GDOP is given by the following equation:

$$\text{GDOP} = (\Delta \text{ (Output Location)})/ (\Delta \text{ (Measured Data)}) \quad \textbf{(2)}$$

A low GDOP value represents a good satellite configuration and a high probability of high position accuracy. A high GDOP value represents poor satellite configuration and a low probability of high accuracy (Wells et al., 1986, p. 4. 23; Ferguson, 2000, p. 11; El-Rabbany,

2002, p. 40; Dutt et al., 2009; Unogwu et al., 2015). The GDOP depends only on the position of the GPS satellites relative to the receiver, i.e., the satellite geometry, (Figure 2.6; assuming a 2-D case). The satellite geometry is obtained by determining the position of the satellites in the sky; the distance between the satellite and receiver; orientation of the satellites and the number of satellites visible to the GPS receiver at the time, which should be four or more (Ferguson, 2000, p. 11; Dutt et al., 2009). Ideally, the best satellite geometry is where one satellite lies directly above the GPS receiver and the other satellites, four or more, are evenly spaced above the receiver at wider angles relative to the receiver (Figure 2.6).

When satellites are grouped (clustered) together in the same area of the sky, they produce a high GDOP and, hence, the satellite geometry is classified as weak. However, when they are widely and evenly spread in the sky, they produce a GDOP that is low; this satellite geometry is classified as strong (Figure 2.6). To eliminate satellite geometry problems, GPS receivers are programmed to select the constellation that gives the least uncertainty, i.e., the lowest GDOP (Wells et al., 1986, p. 4.22; Dutt et al., 2009).

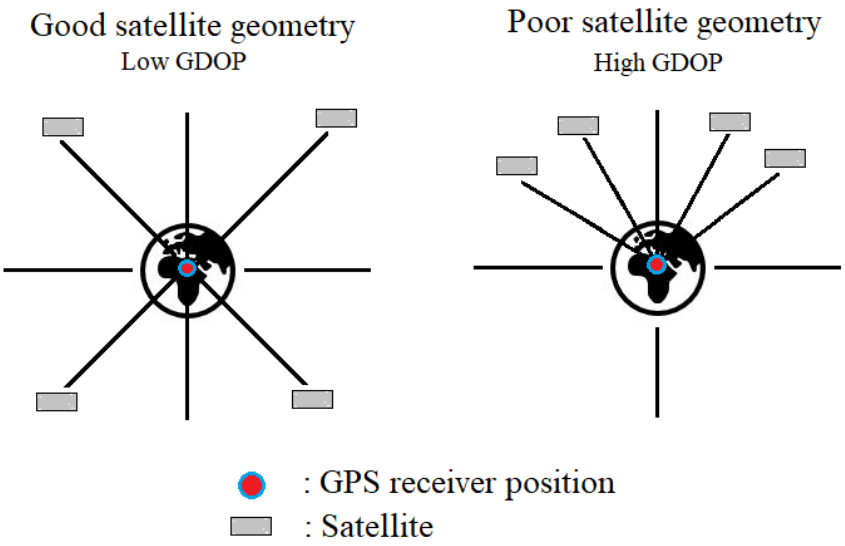


Figure 2.6: The effect of satellite configuration on position calculations. Evaluating the Geometric Dilution of Precision (GDOP).

The satellite geometry is also responsible for the variation in the accuracy precision to which the vertical and horizontal GPS position measurements can be made (Wells et al., 1986, p. 4. 23). When measuring vertical and horizontal position measurements of a point on the Earth's surface, using GPS, the input errors due to other factors (excluding satellite geometry) are always the same in both components. The difference in the accuracy to which the vertical and

horizontal position components are measured arises because the satellite geometry always favours the horizontal position measurements. The satellite geometry enables horizontal surface displacement to be observed and measured symmetrically about a cGPS station, i.e., from both sides of a station (left and right), while vertical surface displacement can only be measured above a station i.e., asymmetrically about the station (Krauter, 1999). The inability to measure vertical surface displacement above and below a station makes surface displacement measurements of the vertical component to be less accurate than horizontal surface displacements. Hence the horizontal position component is always measured with higher accuracy than the vertical position component (El-Rabbany, 2002, p. 41; Dong et al., 2003).

2.4.4 Orbital path errors

To keep up with changes in the position of satellites, GPS receivers use the velocity and the shape of satellite orbits to predict, beforehand, the locations in which the satellites will be at a certain point in time (Figure 2.7). GPS receivers predict new hourly orbital paths using previously measured, overlapping four-hour, GPS observations (Wells et al., 1986, p. 5.17; El-Rabbany, 2002, p. 28; Kaplan and Hegarty, 2006, p. 305). Since neither the velocity nor the shape of the satellite orbits are constant, the prediction of the relative location of satellites is complex. GPS control segments monitor satellite locations at all times, calculate orbit eccentricities, and compile these deviations in documents called ephemerides. Ephemerides are a list of satellite positions that are measured as a function of time (El-Rabbany, 2002, p. 28; Kaplan and Hegarty, 2006, p. 305). The estimates are used by GPS receivers to establish precisely the position of satellites.

Orbital path errors (ephemeris errors) are the difference of the actual orbital satellite location and the predicted orbital satellite location (Ferguson, 2000, p. 22). They slowly increase with the time that has passed since a correction was calculated and vary depending on the location of the GPS receiver. After 24 hours, the magnitude of ephemeris errors is usually of the order of 1 m to 6 m from the last time the values were updated (Kaplan and Hegarty, 2006, p. 382, 384; El-Rabbany, 2002, p. 29). The introduced error is also dependent on the satellite orbit, the smaller the size of the orbit; the smaller the error becomes and vice versa. Receiver stations calculate the precise orbits with an accuracy of 1-6 cm using data collected over several days (Ferguson, 2000, p. 23; Kaplan and Hegarty, 2006, p. 305; Shuanggen et al., 2014, p. 167).

Overall, orbital path errors introduce an error of about 0.8 m (1 σ) in the carrier phase parameters and in pseudorange measurements. The deviation of the predicted orbital paths from the actual satellite paths occurs because satellite orbital paths drift with time (Figure 2.7). The drift is caused by the gravitational force of the Sun and Moon. The errors also result due to the inability to measure the position of the satellite continuously (Kaplan and Hegarty, 2006, p. 305). The deviation is illustrated in Figure 2.7:

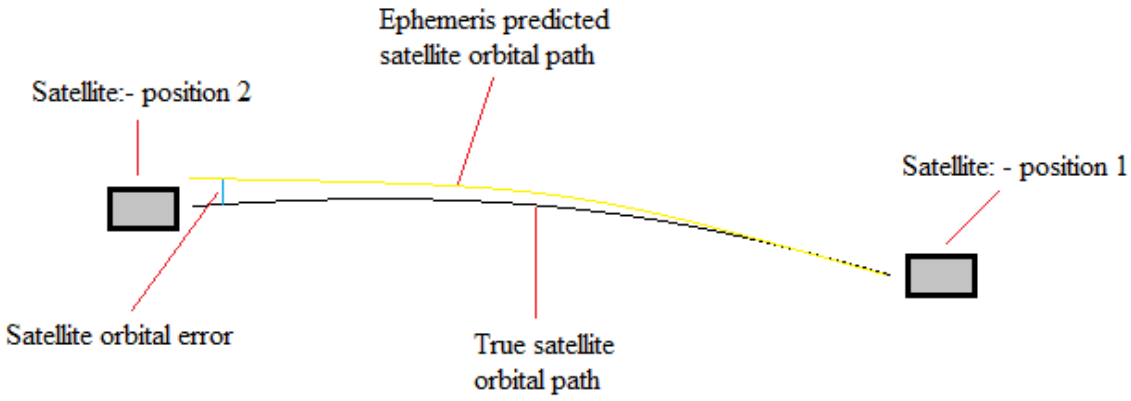


Figure 2.7: Satellite orbital errors.

2.4.5 Satellite clock errors (atomic clock drift and rounding errors)

In satellites, all onboard timing operations and the generation of broadcasting signals are controlled by atomic clocks (Ferguson, 2000, p. 21; Kaplan and Hegarty, 2006, p. 304; Bidikar et al., 2014). Atomic clocks are highly stable and very accurate clocks that determine time to an accuracy of approximately 1 nanosecond. Although atomic clocks are high stable, with passing time they drift from the GPS system time due to the lack of proper synchronisation with true GPS time (Ferguson, 2000, p. 21; Bidikar et al., 2014). The receiver codes used to calculate the pseudorange, i.e., the approximate distance between the satellite and GPS receiver antenna, are derived from the atomic clocks in GPS satellites (Gouchang, 2007, p. 37). GPS receivers use satellite time (contained in the receiver codes) to determine pseudorange and location coordinates. Small deviations in the receiver time can result in huge errors in the estimated position measurements, thus it is important for the time to be determined as accurately as possible. The nanosecond accuracy with which atomic clocks measure the pseudorange and position measurements results in errors of about 3.4 metres per day and can be greater if the satellite time is not reset within a 24-hour period (Ferguson, 2000, p. 21; Kaplan and Hegarty, 2006, p. 305).

Small time deviation errors result in huge position errors because pseudorange and position measurements are calculated using the time it takes for a GPS signals to travel from a satellite to a GPS receiver multiplied by the speed of light (i.e., 299 729 458 m/s) (Kaplan and Hegarty, 2006, p. 24; Guochang, 2007, p. 77). The very high speed of light makes small errors in time very big when converted to position estimates. Satellite clock errors vary depending on the satellite and age of the broadcast data. Like ephemeris errors, clock errors are smallest instantly after the control segment has been uploaded and increase with time after the last upload of the control segment (Kaplan and Hegarty, 2006, p. 305). The deviation of GPS receiver clocks from satellite time is dependent on proper synchronization of GPS receiver time and satellite time, drift, bias, and age parameters of the satellite clock. The satellite time of transmission is computed using the following mathematical expression (Bidikar et al., 2014):

$$t_s = t_{rx} - (P/c) \quad \textbf{(3)}$$

where t_s is the satellite time of transmission in seconds; t_{rx} is the signal reception time at the receiver in seconds; P is the pseudorange in meters; c is the speed of light in meters per second and P/c is the signal propagation time. The time at the instant at which a signal is created in the satellite is obtained by subtracting the signal propagation time of the satellite signal from the signal reception time computed at the receiver. The satellite clock offset (dt) is calculated using the following equation (Wells et al., 1986, p. 8.1; Bidikar et al., 2014):

$$dt = t_s - t_\propto \quad \textbf{(4)}$$

where $t_\propto$ is the time of the satellite clock in seconds. Satellite clock errors can be removed by using two methods: either remove the clock errors through differencing between GPS receivers; or apply the satellite clock error corrections in the navigation message. However, the second method does not remove the errors perfectly; it leaves errors of the order of several nanoseconds, which translate to location errors of a few meters (El-Rabbany, 2002, p. 32).

2.5 How GPS systems measure tectonic and non-tectonic variations

2.5.1 GPS for measuring meteorology data

As signals emitted by GPS satellites travel through the atmosphere from the GPS satellite to the GPS receiver, the atmospheric conditions prevalent in the path of the GPS signal induces a delay and phase change. The induced delay and phase change introduce errors in GPS system that reduces the precision and accuracy of position, velocity and time (PVT) measurements taken using GPS system (Ware et al., 2000; Shuanggen et al., 2014, 12). For a long time, these

delays and phase changes induced in GPS signals by atmospheric conditions (ionospheric and tropospheric effect) were only seen as a source of error. At the end of the 20th century, it was discovered that what was thought to be actually noise can be a source of atmospheric information. Nowadays, atmospheric-induced errors are used to determine both ionospheric and tropospheric parameters (Shuanggen et al., 2014, p. 15). To measure atmospheric conditions, GPS systems measure the delay and phase changes induced in GPS signals by refraction of the GPS signals as they travel through the ionosphere and neutral atmosphere (troposphere and stratosphere). Refraction-induced delays in GPS signals are used to determine tropopause (boundary between the troposphere and stratosphere) parameters; high-resolution tropospheric water vapour, pressure and temperature; total electron content (TEC) in the ionosphere; and the electron density in the atmosphere (Shuanggen et al., 2014, p. 15).

2.5.2 GPS for mapping and determining variations in the position of surface features

Global Positioning Systems are used to perform atmospheric sounding, oceanic sensing, land and hydrology mapping by exploiting the ability of ground-based GPS receiver systems to make precise, continuous, and all-weather (upper and lower atmospheric) delay and phase change measurements (Ware et al., 2000; Shuanggen et al., 2014, p. vi, 3). To determine variations in the ocean height, snow and ice thickness, wind speed, soil moisture and wind direction on and near the Earth's surface, GPS systems use GPS signals reflected from land and oceanic surfaces. Both refraction and reflection induced delays and phase changes in GPS signals are used to image the Earth's surface and near-surface environments (Guochang, 2007, p. 81; Shuanggen et al., 2014, p. 3).

2.5.3 Procedure to measure propagation delays

Propagation delays and phase changes in GPS signals are measured and calculated simultaneously along a GPS signal ray path with high precision using GPS user segments of the GPS system (Ware et al., 2000). The first method that GPS user segments use to compute propagation delays is the pseudorange method, which compares the carrier GPS signals that are received by user segments with a copy of a locally-generated receiver GPS signal. Another method that GPS user segments use to compute transmission delays is the carrier phase observable method, which computes the difference in the phase change between the received carrier signal and the locally-generated receiver signal at the same frequency (Shuanggen et

al., 2014, p. 12). The method produces more precise propagation delay measurements (with a precision of a few millimetres), but its accuracy is less than that of the pseudorange method. This is because, during the tracking stage of the transmitted signal by GPS systems, the phase of the signal can only be known with an ambiguity of an unknown number of times the carrier wavelength (Shuanggen et al., 2014, p. 12). At comparable accuracies, the measurements of the ionospheric and tropospheric parameters obtained with GNSS/GPS systems are consistent with those obtained using traditional methods. The delay and phase changes in the GPS signal are measured simultaneously along a GPS ray path with high precision in the field of view (Ware et al., 2000). Irrespective of the weather conditions characterizing the atmosphere at a given time, the delays and phases changes that occur in GPS signals are measured with a precision of a few millimetres during all weather conditions.

2.5.4 Seasonal variation of GPS position accuracy

Dogan et al. (2014) and others investigated the accuracy of GPS positions during different seasons of the year and found that the accuracy of the GPS system varied in both the horizontal (north-south and east-west directions) and vertical (up-down) directions. They observed that the variations can be of the orders of a few millimetres and are caused primarily by weather and climatic changes. The variations are greater for vertical position measurements since they are more sensitive to tropospheric errors and are less constrained compared to measurements of the horizontal position (Dogan et al., 2014; Dong et al., 2003; Wang and Liou, 2006).

Drouin et al. (2016) observed that unusual weather conditions can cause interannual deviations from the GPS cycles over extended periods of time. Owari et al. (2009) found that GPS positioning accuracy is significantly affected by seasonal variations and that GPS systems give more accurate measurements in winter than in summer time. The results agreed with the findings of Sigrist et al. (1999) but disagreed with the findings of Tachiki et al. (2005) and Dogan et al. (2014), who reported fewer position errors and high position accuracy in summer. However, both Owari et al. (2009) and Dogan et al. (2014) found that the scatter in the position measurements are less in winter than in summer.

2.6 Development of Wavelet and Fourier transforms

The Wavelet Transform (WT) analysis method was first introduced by Haar in 1909 (Owens and Zorin, 1997). It was developed as a solution to the deficiencies of the Short Time Fourier

Transform (STFT) when reconstructing and analysing signals with widely varying frequencies (Heil and Walnut, 1989; Kaiser, 1994). The STFT method is a time-frequency domain transformation technique, a version of the Fourier Transform that simultaneously gives the time and frequency domain response of a series (Kaiser, 1994). The STFT was developed by D. Gabor. It works by dividing a signal into short consecutive segments before computing the Fourier transform of each segment (Heil and Walnut, 1989; Fletcher and Sangwine, 2017). It was developed as an alternative analysis method to Fourier Transforms (FT), to solve the difficulties that Fourier Transforms encounter when applied to non-stationary signals and to also be able to localize a signal in the time and frequency domain simultaneously. The STFT does this by introducing a scale (modulation window), of constant width in the analysis and reconstruction of the signal (Kaiser, 1994; Fletcher and Sangwine, 2017). The window is modulated in time and used to translate the signal in the time and frequency domains.

The STFT works by dividing a signal into several segments that are then analyzed separately to determine the information contained in the signal and is used to reconstruct the signal again (Valens, 1999; Fletcher and Sangwine, 2017). The signal is divided such that no information is lost nor added when the segments are added back together (Kaiser, 1994). However, because the STFT analysis uses a modulation window of constant width, it encounters difficulties when it must decompose, analyze, and reconstruct signals with features that have time intervals that are much shorter or larger than the modulation window used (Heil and Walnut, 1989; Fletcher and Sangwine, 2017; Torrence and Compo, 1998). When decomposing such a feature, the STFT method either underlocalizes or overlocalizes these features in time (Heil and Walnut, 1989; Kaiser, 1994; Fletcher and Sangwine, 2017). Thus, the constant scale imposed by the STFT method causes aliasing of high and low frequencies which makes the method an ineffective method for analyzing signals with very slow or rapid time behaviour (Torrence and Compo, 1998; Fletcher and Sangwine, 2017). The Wavelet Transform (WT) analysis method was developed to solve these deficiencies in Short Time Fourier Transforms.

The Wavelet Transform analysis method is a scale-independent method that reconstructs a signal using multiple wavelets (small waves). Wavelet analysis was developed to overcome localization (resolution) problems related to the STFT when dealing with nonstationary signals with rapidly varying frequencies in time (Kaiser, 1994; Torrence and Compo, 1998). Unlike the STFT, which uses a constant modulation window, wavelet analysis uses a fully scalable modulation window, that enables the analysis of signals characterized by many different time scales or frequencies of a wide variation (Valens, 1999; Kaiser, 1994; Torrence and Compo,

1998). Wavelet Transforms (WT) provide the time-frequency representation of a signal and show which frequencies exist at which time interval in a time series (Kaiser, 1994). Contrary to the STFT, which analyses a signal with a constant resolution, the resolution of wavelet analysis varies in time and is determined by the balance between the width of the modulation window in real space and the width scale in Fourier space (Valens, 1999; Kaiser, 1994). Wavelet transforms are characterized by a good frequency and poor time resolution at low frequencies and a good time and poor frequency resolution at high frequencies (Kaiser, 1994). This variation in resolution of wavelet transforms is possible only because they localize a signal in both time and scale (Torrence and Compo, 1998). Wavelet transforms work by measuring the similarity between the generated wavelets and the time series being analyzed (Kaiser, 1994).

Mathematically, wavelet transforms are a convolution between a wavelet and a function. They localize a segment of a time series in time and frequency by shifting the wavelet in time and varying the scale of the wavelet analysis (Kaiser, 1994). The signal is decomposed into smaller segments by shifting the modulation window across the signal, where, the wavelet spectrum is calculated for each segment. This process is then repeated many times with a slightly shorter (or longer) modulation window for every new cycle. Reconstructing the signal again, the wavelet analysis method returns a collection of a time-frequency representation of the signal being decomposed, all with different resolutions (Valens, 1999). The decomposition of a signal into time and frequency space by using wavelet analysis enables one to determine both the dominant modes of variability in a signal and how these modes vary in time (Torrence and Compo, 1998).

3 Methodology

This chapter outlines the sampling, processing and implementation procedure for the signal processing techniques used in this project to study the cGPS and meteorology time series, and the relationship between them. In this study, time, frequency, and time-frequency domain analysis were carried out using Fourier and wavelet transforms, semblance analysis, cross-spectrum, coherence and phase analysis methods. Fourier and wavelet transforms are used for decomposition purposes. Semblance, cross-spectrum, and coherence methods are used to investigate and quantify the assumed linear relationship between the frequency components of the cGPS and meteorological time series in the frequency and time-frequency domains; while phase analysis is conducted to determine and quantify the phase lag between the cGPS and meteorological time series.

3.1 Sampling criteria

Data from the Nevada Geodetic Laboratory and the South African Weather Service (SAWS) were used to investigate the effects of meteorological processes (i.e., temperature, pressure, rainfall and humidity) on cGPS station data located in Southern Africa. The cGPS data are archived and processed by the geodetic laboratory at the University of Nevada Reno (UNR) (http://geodesy.unr.edu/index.php). The processing procedure of the cGPS data are given at http://geodesy.unr.edu/gps/ngl.acn.txt and in appendix E. The cGPS surface displacement time series are corrected for tropospheric effects (i.e., both hydrostatic and non-hydrostatic delays), first order effects ionospheric effects, solid earth tides, pole tides and oceanic tide loading. However, they are not corrected for non-tidal loading effects (i.e., atmospheric pressure, ocean bottom pressure, surface hydrology, etc.), seasonal thermal expansion and shrink-swell heave effects. See more details of the corrections conducted on the cGPS time series in appendix E. The meteorological time series are taken from ground stations managed by the SAWS. Since we wish to quantify and determine the seasonal influence of atmospheric processes on surface displacement, the raw data provided by the two institutes were used without further processing. The cGPS and meteorological datasets we used were selected based on the following criteria:

1) The cGPS and meteorological stations were selected such that they collectively give coverage for most of southern Africa and all its climatic zones;

2) In most of the climatic zones, excluding the Dry Tropical and Desert climatic zones, at least four cGPS and two meteorological stations were selected. Only three cGPS and

two meteorology datasets were available in the Desert, Dry tropical and Mediterranean climatic zones; and only one meteorological dataset was available in the Dry Tropical climatic zone;

3) The stations, excluding those in appendix D (Figure 9.14, with the exception of station GREY), were selected in spatial locations where both cGPS and meteorological stations are available and separated by no more than 4 km. A separation distance of 4 km was chosen to try minimise the variance in atmospheric conditions and ambient effects that affect cGPS and meteorological stations since these processes vary as a function of distance from the point of interest. The distance between cGPS and meteorological stations was determined using Google Earth;

4) Stations with an observation period of four and more years were selected for use in the study because, under normal conditions, stations that have been collecting data for longer periods are more reliable (or statistically stable) and less influenced by noise;

5) Stations with the least missing data points (i.e., less than 10% missing data points) were selected to avoid introducing artefacts in the data when interpolating the data at a later stage.

All the selected cGPS stations and their locations are given in appendix D, Table 19; and all the selected meteorology stations are given in chapter five, Table 5. The cGPS and meteorological time series and their relation are studied over an observation period of four years, starting from the 1 January 2010 to 31 of December 2013. This period was chosen because most cGPS time series had least disturbances (i.e., gaps and mean shifts) during this period, excluding data from stations GEOA and WELK. Data from station GEOA and WELK was analysed for the period starting from the 1 January 2013 to 31 of December 2016, because the stations started recording in 2012. The signal processing techniques used to analyse the cGPS and meteorological datasets and the relationship between them are discussed below.

3.2 Time domain analysis techniques

Correlation is a statistical measure used to quantify a two way linear association between two continuous variables. It is an inference statistical measure that gives a dimensionless quantity describing the relationship strength of two continuous variables $x(t)$ and $y(t)$. It does not define the dependence nor independence of variables (Mukaka, 2012). The correlation strength

between continuous variables is defined using a range of values between $+1$ to -1, where $+1$ indicates perfect positive correlation and -1 indicates perfect negative correlation, while 0 indicates no correlation (Adler and Parmryd, 2010; Mukaka, 2012). In statistical terms, nonlinear relations that exist between two continuous variables are not correlation. Table 1 gives the Rule of Thumb for interpreting correlation coefficients quantities. In this study, Pearson's and Spearman's correlation techniques are used to quantify the relationship between cGPS surface displacement and meteorology time series in the time domain. Pearson's correlation technique is used to correlate the surface displacement and meteorology time series in the time domain because cGPS data are often assumed to be normally distributed (Tiberius and Borre, 2000). However, previously conducted studies have shown that even though this is a reasonable assumption, it is not always true, thus Spearman's correlation technique is also used (Tiberius and Borre, 2000).

Table 1: Rule of thumb for interpreting correlation coefficient strength quantities (After Mukaka, 2012).

Correlation strength ranges	Correlation strength Interpretation
0.90 to 1.00 (-0.90 to -1.00)	Very high positive (negative) correlation
0.70 to 0.90 (-0.70 to -0.90)	High positive (negative correlation)
0.50 to 0.70 (-0.50 to -0.70)	Moderate positive
0.30 to 0.50 (-0.30 to -0.50)	Low positive (negative) correlation
0.00 to .30 (0.00 to -0.30)	Negligible correlation

3.2.1 Pearson's Correlation Coefficient (PCC)

Pearson's correlation coefficient (PCC) is a dimensionless bivariate measure used to quantify the strength of a linear relationship between two continuous variables x(t) and y(t) (Trauth, 2010, p. 80; Mukaka, 2012). The PCC is often denoted by r and is mathematically defined as (Trauth, 2010, p. 82):

$$r_{x,y} = \frac{\sum_{i=1}^{n}(x_i - \bar{x})(y_i - \bar{y})}{(n-1)S_x S_y} \quad \textbf{(5)}$$

Where n is the number of pairs of xy pairs, x_i and y_i are ith x(t) and y(t) values, $\bar{x}$ and $\bar{y}$ are the univariate means of the x and y time series, S_x and S_y are univariate standard deviations of the x and y time series. The technique is based on the assumptions that 1) the relationship between the continuous variables being analysed is linear and 2) the continuous variables being

analysed are normally distributed (Mukaka, 2012). The technique is not suitable for analysing time series with outliers.

3.2.2 Spearman's Correlation coefficient (Rho)

Spearman's correlation coefficient (Rho) is a nonparametric (distribution free) rank correlation technique used to compute the correlation strength of two continuous variables. Contrary to Pearson's correlation technique, Spearman's Correlation coefficient does not assume linearity and normality between the continuous variables being analysed (Gauthier, 2001; Hauke and Kossowski, 2011). Thus, this method is good at quantifying the relationship between skewed continuous variables. Mathematically, Spearman's correlation coefficient is defined as (Gauthier, 2001; Mukaka, 2012):

$$r_s = 1 - \frac{6\sum_{i=1}^{n} d_i^2}{n(n^2-1)} \quad \textbf{(6)}$$

where d_i is the difference in rank for each continuous variables pair $x(t)$ and $y(t)$ and n is the total number of continuous variable pairs. Unlike Pearson's correlation technique, this technique is more robust, it is suitable for analysing the relationship between non-normally distributed continuous variables and continuous variables with outliers (Gauthier, 2001; Mukaka, 2012). The disadvantage of this technique is that some information gets lost when the continuous variables to be analysed are converted into ranks (i.e., when the datasets are ranked or sorted), and when analysing the relationship between normally distributed datasets, it is less accurate compared to Pearson's correlation technique (Gauthier, 2001). Thus, both Pearson's and Spearman's correlation techniques are used in this study.

3.3 Frequency domain analysis techniques

3.3.1 Fourier and fast Fourier transform (FFT) techniques

The Fourier transform (FT) is a reversible complex method used to convert time domain data into the frequency domain using a fixed window (Cooper and Cowan, 2008; Ryan, 2015). It is an extension of the Fourier series, that enables the analysis of infinite and finite non-periodic time series (Shatkay, 1995; Leavey et al., 2003). FTs can be divided into the Continuous Fourier transform (CFT) and Discrete Fourier transform (DFT) (Graps, 1995; Trauth, 2010, p. 14). The CFT is used to convert a continuous time series into the frequency domain using an infinite window. The DFT is an approximation of the CFT (Graps, 1995; Trauth, 2010, p. 14),

it converts a finite time series into the frequency domain using a finite window. Both the CFT and DFT permit the determination of frequencies embedded in a time series and their power at each frequency (Fletcher and Sangwine, 2017). FTs are good for analysing stationary time series, where no time information is required, and give substantially accurate frequency localisation (Liner, 2010). They are also suitable for analysing nonstationary time series, when one wishes only to uncover the spectral components present in a time series, as this information is independent of time (Polikar, 2001, p. 21). FTs are not suitable for analysing non-stationary time series when one wants to recover the spectral components and their time of occurrence. FTs are based on the assumption that whether a function is periodic or nonperiodic, it can be expressed as a sum of cosine and sine functions with varying amplitudes and phase (Graps, 1995; Shatkay, 1995; James, 2011, p. 8). Given a time series $x(t)$, its Fourier transform, $X(f)$ is defined as (Najmi and Sadowsky, 1997; Mallat, 2009, p. 2):

$$X(f) = \int_{-\infty}^{\infty} x(t)e^{-2\pi ift}dt \tag{7}$$

where f is the frequency of the time series $x(t)$ and t is the time. From the equation, it is observed that the FT is the result of integrating the product of a time series $x(t)$ and a complex sine-cosine function. In the frequency domain, the Fourier transform $X(f)$ is expressed as:

$$X(f) = R(f) + I(f) = |X(f)|e^{i\theta(f)} \tag{8}$$

where $R(f)$ and $I(f)$ are the real and imaginary components of the Fourier transform $X(f)$, $|X(f)|e^{i\theta(f)}$ is the polar form of $X(f)$, $|X(f)|$ is the amplitude, expressed as:

$$|X(f)| = \sqrt{R^2(f) + I^2(f)} \tag{9}$$

and θ is the phase angle; given by

$$\theta = \tan^{-1}\left(\frac{I(f)}{R(f)}\right) \tag{10}$$

Its inverse Fourier transform is

$$x(t) = \frac{1}{2\pi}\int_{-\infty}^{\infty} X(f)e^{2\pi ift}df \tag{11}$$

In the study, Fourier analysis is conducted using the Fast Fourier Transform (FFT), which is an efficient technique for implementing DFT (Cochran et al., 1967; Mallat 2009, p. 2; Trauth, 2010, p 114; Ryan, 2015). The DFT is a discretised version of the Fourier transform; it works by assuming that all finite signals can be represented by a linear combination of finite sine and

cosine functions (Mallat, 2009, p. 2). DFT enable the application of Fourier analysis on finite time series defined by a period N, they are mathematically defined as (Cochran et al., 1967; Mallat 2009, p. 77):

$$X(k) = \sum_{n=0}^{N-1} x(n) e^{\frac{-i2\pi kn}{N}}, \qquad k = 0, \dots, N-1 \tag{12}$$

where k is the frequency of the DFT, N is the total number of samples, and n is the n^{th} sample of the time series (Cochran et al., 1967). However, because of the large computational time the DFT requires, they are rarely used. FFTs substantially reduce computational time associated with the computation and implementation of DFTs by a factor of $(\log_2 N)/N$, where N is the total number of samples in the time series x(n), as well as the round off errors (Cochran et al., 1967; Shatkay, 1995, Mallat, 2009, p. 78). In producing the spectrum of the time series x(n), the FFT uses a total number of frequencies that is close to the number of samples in a time series (Trauth, 2010, p 14).

The cGPS and meteorological time series were prepared and transformed into the frequency domain using the following procedure (note: the paragraphs that follow the procedure steps explain interpolation, detrending, zero padding, windowing and the periodogram techniques, references are obtained in the respective paragraph):

1. Missing data points in the time series were interpolated using the piecewise cubic or linear method (Burden and Faires, 2011);
2. Time series were zero centred and detrended using a linear function;
3. Time series were up-sampled using zero padding to 2048, which is the next power of two, for samples collected over a period of four years;
4. Time series were then windowed using the Kaiser-Bessel window (i.e., equation (13)) so as to minimise spectral leakage (Harris, 1976). Spectral leakage is the phenomenon where energy leaks from a frequency of higher power to frequencies of lower power;
5. The periodogram method was used to convert the time series into the frequency domain (Welch, 1967);
6. The above steps were repeated for all cGPS and meteorological time series analysed.

The interpolation is carried out to avoid errors that may result due to transforming unevenly spaced time series when using FFT, such as spurious peaks and frequency shifts. The piecewise

cubic and linear methods were chosen because the methods are observed to introduces less variance and artefacts in a time series compared to the nearest neighbour and cubic spline interpolation methods when used to interpolate a time series with small gaps. For more information on the interpolation, please read Chapter 4, section 4.2.

Time series detrending is done in an attempt to suppress the formation, in the frequency domain, of a dominant low-frequency spectral component that obscures the frequency response of a time series (Singh et al., 2005; Trauth, 2010, p. 22). The removal of the mean, zero centring, is necessary to minimise the formation of a steep gradient (abrupt changes) between the last and first data points of a time series that form when zero padding is carried out. Abrupt changes in the amplitude of a time series, especially if the time series is non-stationary, cause spectral leakage which obscures and distorts the spectral response of the time series (Singh et al., 2005).

FFTs work more efficiently when applied to time series with a total number of 2^n samples. However, most time series don't meet this condition, including the cGPS and meteorology time series analysed in this study. To resolve this problem, the cGPS and meteorological time series are padded to the next higher power of two using zero padding. Zero padding increases the length of a time series by adding zeros either at the being and/or end of a time series (Nagy and Fury, 1990; Elson and Bennett, 1995). Zero padding not only increases the size of a time series but also reduces quantisation errors in the estimation of the spectral response of a time series, enabling the generation of smoother Power Spectral Density (PSD) spectrum by interpolation and assisting in resolving ambiguities (Kay and Marple, 1981; Nagy and Fury, 1990; Williams et al., 2003; Jensen et al., 2014). Zero padding does not add or remove fundamental frequency components embedded in a time series (Kay and Marple, 1981). The disadvantage of zero padding is that it introduces discontinuities at the edges of a time series that causes spectral leakage and reduction of the ability to resolve spectral power (Clayton and Murray, 1993; Torrence and Compo, 1998; Williams et al., 2003).

Windowing, also known as tapering, is a technique used to reduce spectral leakage (Harris, 1978; Trauth, 2010, p. 114). Spectral leakage is a phenomenon where energy at frequencies of high power (main spectral lobes) leak into nearby frequencies of low power (side lobes), in the processes obscuring and distorting spectral power at these frequencies (Kay and Marple, 1981). It occurs when the time series being analysed is finite, non-periodic, and has sharp gradient changes because of a non-zero amplitude changes at the boundaries (Harris, 1978; Nagy and

Fury, 1990; Podder et al., 2014). Windowing creates smooth transitions at boundaries, returns finite non-zero values inside the window boundaries and zero values outside the window boundaries (Elson and Bennett, 1995; Podder et al., 2014). The disadvantage of windowing is that it reduces spectral leakage at the expanse of spectral resolution, i.e., it reduces the total power of a time series PSD (Kay and Marple, 1981; Nagy and Fury, 1990). Examples of windowing techniques include the Hamming window, Hanning window, Kaiser window, Blackman-Harris window, and Rectangular window (Harris, 1976, 1978). In a study carried out by Harris (1976 and 1978), the Kaiser-Bessel and Blackman-Harris windowing functions were found to be the top performing windowing functions compared to other windowing functions. However, the small main lobe and low further side lobes of the Kaiser-Bessel window, compared to those of the Blackman-Harris window, make it better at resolving frequencies with considerably varying amplitudes that are close to each other, like those found in cGPS time series. Also, its lower further side lobes enable the function to resolve frequencies close to the noise floor of a time series; thus, in this study, the Kaiser-Bessel windowing function is used. The window is defined as (Harris, 1976):

$$W(n) = \frac{I_o\left[\pi\alpha\sqrt{1.0-\left(\frac{n}{N/2}\right)^2}\right]}{I_o}, \text{ where } 0 \leq |n| \leq \frac{N}{2}, \quad \textbf{(13)}$$

α is the ratio of the main-lobe level to side-lobe level parameter, N is the number of samples in the window, and I_o is the zeroth-order modified Bessel function of the first kind, defined as:

$$I_o(X) = \sum_{k=0}^{\infty}\left[\frac{\left(\frac{X}{2}\right)^k}{K!}\right]^2 \quad \textbf{(14)}$$

where k is the ordered index of a basis set and x is the functional domain of I_o. The disadvantage of the Kaiser-Bessel windowing function though, is that it introduces a side lobe artefact at low frequencies (Harris, 1978).

The Welch periodogram is a technique used to implement the FFT when estimating the PSD of a time series (Welch, 1967). It involves breaking down a time series into segments, computing a modified periodogram for each segment; and averaging the modified periodograms for all segments to produce an averaged, smoother PSD spectrum with clearly defined spectral responses at both low and high frequencies (Mallat, 1999, p. 512; Welch, 1967; Singh et al., 2005). By averaging the periodograms of all the defined segments, the method

generates a spectrum with an improved signal to noise ratio. However, the disadvantage of spectral averaging is that it reduces the spectral resolution by smoothing. Smoothing reduces the ability to resolve details in a signal spectrum and may distort the signals in a spectrum. Mathematically, the periodogram is defined as:

$$\mathrm{PSD} = \frac{\Delta t}{N}\left|\sum_{n=0}^{N-1} x_n e^{-2\pi f n}\right|^2, \qquad -\frac{1}{2\Delta t} < f \leq \frac{1}{2\Delta t}, \tag{15}$$

where Δt is the sampling interval, N is the sample number and f is the frequency. When a windowing function ($W(n)$) is set to the periodogram, the periodogram equation changes to:

$$\mathrm{PSD} = \frac{\Delta t}{N}\left|\sum_{n=0}^{N-1} W(n) x_n e^{-2\pi f n}\right|^2, \qquad -\frac{1}{2\Delta t} < f \leq \frac{1}{2\Delta t}, \tag{16}$$

where Δt is the sampling interval and $W(n)$ is the windowing function. For a one-sided periodogram, the spectral energy is conserved by multiplying the values at all frequencies by 2, except at 0 and at the Nyquist ($1/2\Delta t$).

The correlation of the cGPS and meteorological time series was determined and quantified in the frequency domain using the cross-spectrum and coherence methods.

3.3.2 Cross-spectrum

The cross-spectrum, also called the cross-spectral density (CSD), is a complex measure used to study linear covariance and correlation relations between two-time series $x(t)$ and $y(t)$ in the frequency domain (Stoica and Moses, 2005, p. 64; Friston et al., 2011). The cross-spectrum gives information about the phase difference between two time series, as its phase is the phase difference of the two time series being analysed (Panofsky et al., 1956; Eriksson, 2000; Friston et al., 2011). If a causal relation is assumed between time series $x(t)$ and $y(t)$, then the cross-spectrum can be considered to be the sum of the two time series (Granger, 1969). The cross-spectrum is defined as (Timmer et al., 1998):

$$\mathrm{CS}(\omega) = \frac{1}{2\pi}\sum_{\tau} \mathrm{CCF}(\tau)\exp(-i\omega\tau) = \langle X(\omega)Y^*(\omega)\rangle = X_{xy} \tag{17}$$

where ω is frequency, τ the shift parameter, and $\mathrm{CCF}(\tau)$ is the cross-correlation function and is defined as:

$$CCF(\tau) = \langle x(t)y(t-\tau)\rangle \quad \textbf{(18)}$$

The cross-spectrum does not only give information about the correlation and phase difference of two time series, but it also gives information about the coherence of the two time series (Panofsky et al., 1956).

Processing and implementation steps of the cross-spectrum technique:

1. The cGPS and meteorological time series to be analysed were interpolated so as to reduce the formation of spurious frequencies and frequency shifts due to missing data points;
2. The time series were detrended and zero centred to reduce the formation of low-frequency variability that obscures the PSD in the frequency domain and spectral leakage;
3. The time series were windowed using the Kaiser-Bessel windowing function. Zero padding and windowing are necessary since the cross-spectrum is calculated using the Welch periodogram;
4. Computation of the cross-spectrum;
5. The above steps were repeated for all cross-spectrum tests.

3.3.3 Magnitude squared coherence (MSC)

Coherence is a complex frequency domain technique used to quantify and determine the relationship strength between two time series $x(t)$ and $y(t)$ (Kristina et al., 1989; Torrence and Compo, 1998; Timmer et al., 1998, Friston et al., 2011). It indicates how well the frequency domain elements of time series $x(t)$ correspond to that of $y(t)$ at each frequency. It is often used to infer the correlation, power transfer, possible cause-effect relation and the influence one system has on the other, assuming a causal relationship between the systems (Granger, 1969; Baselli et al., 1986). Mathematically, the MSC is defined as (Granger, 1969; Ito, 1985; Timmer et al., 1998; Trauth, 2010, p 117):

$$C_{xy} = \frac{\left|X_{xy}(f)\right|^2}{X_{xx}(f)X_{yy}(f)} \quad \textbf{(19)}$$

where X_{xy} is the cross-power spectral density of $x(t)$ and $y(t)$, $X_{xx}(f)$ and $X_{xx}(f)$ are the power spectral densities of $x(t)$ and $y(t)$, and C_{xy} is the coherence. The coherence is a real number between 0 and 1, where 1 indicates perfect correlation (either positive or negative) and 0

indicates no correlation at the frequency f (Granger, 1969; Hayashi, 1981; Torrence and Compo, 1998; Trauth, 2010, p. 17). For two time series to be analysed using spectral coherence, they must retain a substantial degree of stationarity (Granger 1969; Trauth, 2010, p. 17). One advantage of the coherence method is that it can be used to analyse nonstationary time series; its application and interpretation is not dependent on the concept of linearity (Timmer et al., 2000).

Processing and implementation steps for the coherence method.

1. Interpolation of the cGPS and meteorology time series to be analysed;
2. Detrending and zero mean centring of the time series;
3. Zero padding and windowing of the time series;
4. Computation of the coherence spectrum;
5. The above steps were repeated for all coherence spectrum computations.

3.3.4 Phase difference

The phase difference (phase lag) between the surface displacement and meteorological processes is determined by calculating the phase of the cross-spectrum, which is the phase difference between the processes (Eriksson, 2000). Mathematically, the phase difference is given by (Cooper, 2009):

$$\theta_d = \tan^{-1}\left(\frac{I(X_{xy})}{R(X_{xy})}\right) \quad \textbf{(20)}$$

where θ_d is the phase difference of time series $x(t)$ and $y(t)$, and $R(X_{xy})$ and $I(X_{xy})$ are the real and imaginary components of the cross-spectrum X_{xy} respectively. The advantage of the phase difference technique is that it can be used to compute the difference of processes with different units of measurements, since it does not use amplitude information. However, its disadvantage is that, because it does not use amplitude information, it is sensitive to noise (Cooper and Cowan, 2008).

3.4 Time-frequency domain analysis techniques

3.4.1 Computation of wavelet transforms

Wavelets are small packets of waves (daughter wavelets) that enable time-scale analysis of stationary and nonstationary time series (Zhao et al., 2004; Baker, 2007; Kaiser, 2011, p. 64, 70). They can be dilated, compressed and translated in both the frequency and time domain (Terrence and Compo, 1998; Zhao et al., 2004; Fletcher and Sangwine, 2017). They are characterized by a flexible resolution that depends on the size of the transformation window. The resolution flexibility of wavelet transforms enables them to easily map temporal variations in the spectral characteristics of a time series (Terrence and Compo, 1998; Kaiser, 2011, p. 62; Cooper and Cowan, 2008; Fletcher and Sangwine, 2017). Daughter wavelets, also known as time-frequency atoms or basis functions, are generated from a mother wavelet by translation and dilation of the mother wavelet. Mathematically, mother wavelets are defined as (Terrence and Compo, 1998; Baker, 2007; Fletcher and Sangwine, 2017):

$$\psi(t) = |s|^{-p}\psi\left(\frac{t}{s}\right) \tag{21}$$

and daughter wavelets defined as

$$\psi_{u,s}(t) = |s|^{-p}\psi\left(\frac{t-u}{s}\right) \tag{22}$$

where s and p are scaling (dilation and compression) factors and u is the translation (position) factor of the wavelet (Mallat 2009, p. 5, 102; Kaiser, 2011, p. 62-63; Fletcher and Sangwine, 2017). The factor $|s|^{-p}$ scales the amplitude of the wavelet with respect to variations in the horizontal scale s of the wavelet (Kaiser, 2011, p. 62-63). In wavelet analysis, time series are decomposed at multiple scales using a linear combination of translated and dilated daughter wavelets (Graps, 1995; Baker, 2007). Fundamentally, wavelets are small functions localized both in the time and frequency domain; they have a mean of zero, wiggle around the time (or position) axis and are nonlocal functions (Graps, 1995; Torrence and Compo, 1998; Farge, 1992; Baker, 2007; Mallat 2009, p. 102; Kaiser, 2011, p. 70). When a wavelet $\psi_{u,s}$, of scale (s) and translation (u), is convolved with a function f(t) and integrated from negative infinity to positive infinity, a Continuous Wavelet Transform (CWT) is obtained (Baker, 2007; Cooper and Cowan, 2008):

$$\mathrm{CWT}(u,s) = \int_{-\infty}^{\infty} f(t)\frac{1}{|s|^{0.5}}\psi^*\left(\frac{t-u}{s}\right)dt \tag{23}$$

where ψ^* is the complex conjugate of the chosen mother wavelet ψ. The equation works by continuously shifting the continuously scalable wavelet function over the signal $f(t)$ to obtain its CWT (Zhao et al., 2004; Kaiser 2011, p. 70). The CWT is good at analyzing continuous and discrete time series; it produces a lot of redundant information that helps reduce the noise sensitivity of the transformation by improving the shift invariance of the transformation (Valens, 1999; Baker 2007). The disadvantage of the CWT is that it transforms a time series using a large number of wavelets, which produces a redundant amount of information that increases their computation time (Baker, 2007). The three main advantages of wavelet transform over Fourier transform are that they use (Graps, 1995; Torrence and Compo, 1998; Zhao et al., 2004; Cooper and Cowan, 2008):

1. WTs use a window of varying size;
2. WTs are good at mapping variations in nonstationary time series;
3. WTs map variations in a time series as a function of time and frequency.

There are several mother wavelet functions that can be used to decompose a time series. Examples of these include the classic Haar, Morlet, Daubechies, Gaussian, and Mexican Hat wavelets, all of which are suited to particular applications (Torrence and Compo, 1998; Baker, 2007; Fletcher and Sangwine, 2017).

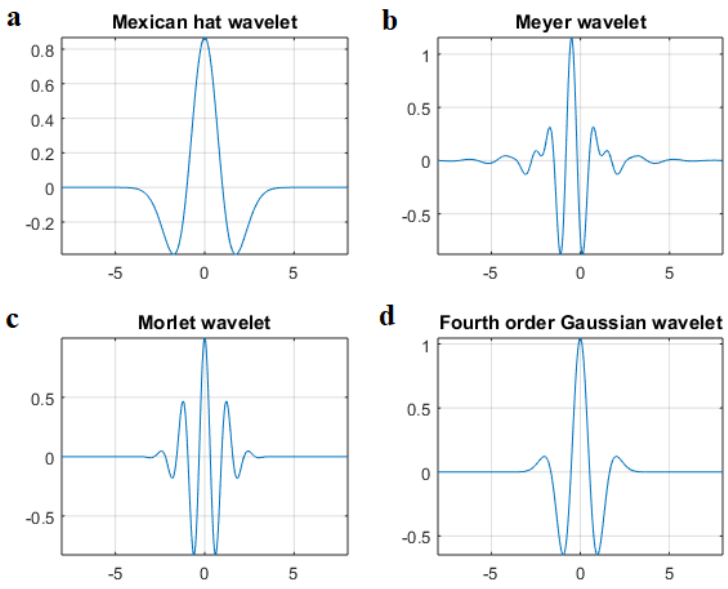


Figure 3.1: (a) Mexican hat wavelet, (b) Meyer wavelet, (c) Morlet wavelet, and (d) Fourth order Gaussian wavelet.

In this study, the Morlet wavelet transform was used to analyse the displacement and meteorological time series. Mathematically, the Morlet wavelet is expressed as (Torrence and Compo, 1998):

$$\psi_o(\eta) = \pi^{-\frac{1}{4}} \exp(i\omega_o \eta) \exp(-\frac{\eta^2}{2}) \quad \textbf{(24)}$$

where η is the time and ω_o is the nondimensional frequency (Torrence and Compo, 1998).

3.4.2 The basis of choosing the complex Morlet wavelet transform.

There are a number of factors to considered when choosing a wavelet transform to use. These include the nature (orthogonal or nonorthogonal), wavelet symmetry (shape and width), and type (complex or real) (Torrence and Compo, 1998; Baker, 2007). In this study, to analyse the cGPS and meteorology time series, the nonorthogonal complex Morlet wavelet transform function was chosen because:

1. The symmetry of the time series data is determined visually, by comparing the symmetry of cosine-sine functions (assumed to exemplify how the time series vary) and that of the Morlet wavelet transform. The similarity in symmetry of the time series and the wavelet function is important because it enables the time series to be decomposed clearly, with higher feature and time-frequency resolution (Torrence and Compo, 1998), and more efficiently using fewer coefficients (Baker, 2007);
2. The nonorthogonal wavelet function, CWT, is better at analysing time series with smooth and continuous amplitude variations, similar to that of cGPS and meteorological time series. When using the nonorthogonal function, the number of scales that can be used is not limited. This enables frequency variations over time to be mapped smoothly (Torrence and Compo, 1998; Baker, 2007). Also, wavelet transform coefficients determined using the nonorthogonal wavelet function do not change when a time series is zero padded at the edges, unlike those obtained using the orthogonal wavelet function, DWT, (Baker, 2007);
3. A complex function of the Morlet wavelet transform was chosen because it is better adapted for capturing oscillatory behaviour compared to the real Morlet wavelet function (Torrence and Compo, 1998). The complex Morlet wavelet transform also returns amplitude and phase information, which are important when applying phase

dependent methods, such as the cross-spectrum and semblance analysis methods (Cooper and Cowan, 2008);

4. It is a high order differential functions with a high number of vanishing moments (Li et al., 2014). Vanishing moments are a property of wavelets that specify the polynomials (i.e., trends) that wavelet functions are orthogonal to and supress (Struzik, 2001; Mallat, 2009, p. 208). They indicate the differential order of the wavelets, i.e., the derivative determined when applying a wavelet function, which is equivalent to the smoothing degree of the wavelets. Wavelets with a high degree of smoothness are well adapted to approximating smooth functions and vice versa. The high number of vanishing moments, n, enables them to supress and disable the visibility of polynomial functions of degrees n-1, n-2, n-3,…, 0 (Struzik, 2001; Mallat, 2009, p. 208). For example, wavelets with one vanishing moment supress polynomials of zero degree, i.e., constants, and wavelets with two vanishing moments supress both constants and linear trends in a time series and so on (Struzik, 2001). The suppression of polynomials by wavelet functions enables the analysis of local or temporal variations in a time series.

A centre frequency and bandwidth value of 1 is used when computing the Morlet wavelet transform, to make the used scales equivalent to the wavelength (Cooper and Cowan, 2008), which is also an inverse of frequency.

Given below are the data preparation and implementation steps used to compute the wavelet transform:

1. Interpolation of time series to reduce the formation of false peaks and spectral response shifts;
2. Detrending and mean subtraction to minimise spectral frequency distortion in the presence of trends and spectral leakage;
3. Implementation of the CWT;
4. Steps 1-3 repeated for all the time series analysed.

In the application of wavelet-based methods, including the semblance method, windowing and padding are not done as Torrence and Compo (1998) indicate that it is unnecessary when using wavelet transforms to convert periodic time series into the time-frequency domain.

3.4.3 CWT semblance

Semblance analysis is a qualitative technique used to correlate and isolate coherent features between two time series x(t) and y(t) based on the variation of their phase angle (Christensen, 2003; Cooper, 2009). It works by calculating how closely aligned the phase angles of the time series being analysed are, in the frequency domain, for each frequency (Christensen, 2003). It returns the correlation results as visual plots that show how the correlation of the time series varies at each frequency over time. Because the method uses phase information, it can also be used to compute the correlation of time series with different units of measure (Christensen, 2003; Cooper and Cowan, 2008; Cooper, 2009). For two time series, x(t) and y(t), Fourier semblance analysis can be conducted in the frequency domain using the following equation (Christensen, 2003; Cooper and Cowan, 2008; Cooper, 2009):

$$S = \cos\theta(f) = \frac{R_x(f)R_y(f) + I_x(f)I_y(f)}{\sqrt{R_x^2(f) + I_x^2(f)} \times \sqrt{R_y^2(f) + I_y^2(f)}} \quad \textbf{(25)}$$

where R_x and R_y are the real components, and I_x and I_y the imaginary components of the time series x(t) and y(t). The CWT semblance (S) of time series x(t) and y(t) is computed using the following equation (Cooper and Cowan, 2008; Cooper, 2009):

$$S = \cos^n(\theta) \quad \textbf{(26)}$$

where n is an odd integer greater than zero and θ is the local phase of the time series given by:

$$\theta = \tan^{-1}(I(CWT_{x,y})/R(CWT_{x,y})) \quad \textbf{(27)}$$

where $CWT_{x,y}$ is the cross-wavelet transform computed using the continuous wavelet transforms of x(t) and y(t) (i.e., CWT_x and CWT_y). The cross-wavelet transform is given by the following equation:

$$CWT_{x,y} = CWT_x \times CWT_y \quad \textbf{(28)}$$

Semblance correlation returns a value between +1 and -1; +1 indicates a perfect positive phase correlation, -1 indicates a perfect negative (or inverse) correlation between the phase angles of the time series; and 0 indicates there is no phase correlation between the two time series x(t) and y(t) (Cooper, 2009; Cooper and Cowan, 2008; Kosek et al., 2014). Fourier-based semblance methods work best with stationary time series (time series whose frequency content is constant over time or position). When dealing with nonstationary time series, Fourier-transform-based semblance methods lose spatial resolution, which results in temporal-spatial variations in the time series to be missed (Cooper and Cowan, 2008). Thus, the CWT

semblance analysis method is used in this study. CWT-based semblance analysis encompasses all the advantages of wavelet transforms over Fourier transforms when analysing nonstationary time series (Cooper and Cowan, 2008). The main disadvantage of semblance methods is that they are sensitive to noise, due to the lack of amplitude information.

Processing and implementation steps:

1. Interpolate both the time series to be correlated to minimise the possible formation of false peaks and spectral response shifts;
2. Detrend and zero centre both time series so as to minimise spectral distortion due to the presences of a trend and non-linearity;
3. Compute the CWT for both time series;
4. Compute the cross-wavelet;
5. Compute the local phase of the cross-wavelet;
6. Compute the semblance spectrum from the local phase.

4 Synthetic data

Synthetic data are artificial data generated to imitate authentic (real) data (Burden and Faires, 2011, p. 93). It is generated so that it contains important properties of the data set being simulated, such as trends, cycles, seasonality and disturbances (Barse et al., 2003; Trauth, 2010, p. 110). The advantage of using synthetic data is that it enables 1) the performance of an analysis algorithm to be tested, knowing the results beforehand, and 2) the effects of distinct features, characteristic of authentic data sets, on an analysis algorithm to be studied, understood and mitigated (Trauth, 2010, p. 82, 110), and 3) it gives control when conducting tests, since one dictates the model properties of the synthetic time series (Barse et al., 2003). The disadvantage of using a synthetic dataset is that it can never produce perfect responses, the same as those obtained from real datasets, since it does not contain all the properties of a real dataset.

In this project, synthetic data are used to test the performance of the decomposition and correlation spectral methods used to analyse the relationship between the cGPS and meteorological datasets; to examine the effects of certain real data features on the decomposition and correlation algorithms; and to determine the best procedure to use when preparing real datasets for Fourier and wavelet transform based analysis.

4.1 Synthetic time series components

Generally, signals collected in Earth sciences are composed of three basic components, 1) a periodic component, 2) a random noise component and 3) a trend component (Trauth, 2010, p. 110).

The periodic component comprises a seasonal and cyclic component. The seasonal component often repeats over a period of about one year and follows roughly the same pattern every year (Arsham and Shao, 1985; Anderson et al., 2011, p. 840). The cyclic component is a nonstationary nonseasonal component of a time series (Bell and Hillmer, 1984; Zhang and Qi, 2005). It is longer than seasonal components (Zhang and Qi, 2005) and follows a pattern that repeats over multiple years, the period of occurrence of the pattern is not fixed (Anderson et al., 2011, p. 837). Not only do cyclic components occur over longer periods of time, but also have different sources to seasonal components (Arsham and Shao, 1985) and are much more difficult to predict (Anderson et al., 2011, p. 837). For a signal to be considered periodic, it must be characterised by at least two or more cycles.

The noise component, also referred to as the erratic, residual, random or error component of a system, is a high frequency (Baxter and King, 1999), unpredictable and non-systematic component of a time series (Anderson et al., 2011, p. 834). The noise component often hides the trend and periodic components of a signal (Hawkins and Stevens, 1950; Trauth, 2010, p. 120) and generates effects that make it hard to decompose or determine the characteristics of a time series using signal processing techniques.

A trend is a low-frequency feature (long-term characteristic) of a time series (Baxter and King, 1999). It is a nonseasonal and, usually, nonstationary long-term upward or downward change in the behaviour of a time series over time (Bell and Hillmer, 1984; Arsham and Shao, 1985; Zhang and Qi, 2005; Anderson et al., 2011, p. 840).

4.2 Synthetic data generation

In this section, a synthetic time series containing an annual and semi-annual frequency component characteristic of cGPS time series, as described by van Dam et al. (2001), Dong et al. (2002) and Peng et al. (2017), is generated. The synthetic time series generation is done in an iterative manner, starting from a simple non-realistic synthetic time series model (Figure 4.1) to a more realistic complex time series model (Figure 4.5) with features observed in real datasets. The time series is generated using a deterministic approach (Brockwell and Davis, 2002, p. 263), which assumes that the properties of time series components are stationary over time (Beveridge and Nelson, 1981). The additive decomposition model is used to generate the synthetic time series because, according to Zhang and Qi (2005) and Anderson et al. (2011, p 830), it is more appropriate for modelling time series with relatively constant seasonal variation. The model assumes the following form:

$$y_t = s_c + t_c + n_c \quad \textbf{(29)}$$

where y_t is the observed time series, s_c, t_c,and n_c are the seasonal, trend and noise components of the time series, y_t, respectively (Brockwell and Davis, 2002, p. 400; Anderson et al., 2011, p. 830). The above time series model representation is also known as the classical decomposition model (Brockwell and Davis, 2002, p. 23, 31; Zhang and Qi 2005).

The following general assumptions are made in generating the synthetic time series:

1. The synthetic time series (y_t) is a summation of seasonal (s_c) and nonseasonal (t_c and n_c) components, i.e., $y_t = s_c + t_c + n_c$;

2. The components s_c, and n_c are independent and stationary;
3. The noise component has zero mean and constant variance;
4. Since the length of the time series analysed is small, i.e., four years, it is assumed that the cyclic component is not present. The chosen real data observation period might be too small to cover a full cycle, as a result, the component of any partially captured cycle is expected to behave more as a trend with slightly varying gradient than a cycle.

Figure 4.1 shows the annual and semi-annual sinusoidal signals used to generate the complex synthetic time series in Figure 4.5 and used to test the analysis algorithms used in this study. In a study carried out by Wang et al. (2017), they observed that seasonal annual GPS components are characterised by a peak to peak amplitude deviation of about 1.2 to 6.3 mm. The magnitude of semi-annual components tends to be about 1/2 to 1/3 times the magnitude of the annual components. Thus, in this study, the annual and semi-annual synthetic signals are generated with an amplitude of 3 mm and 1 mm, respectively.

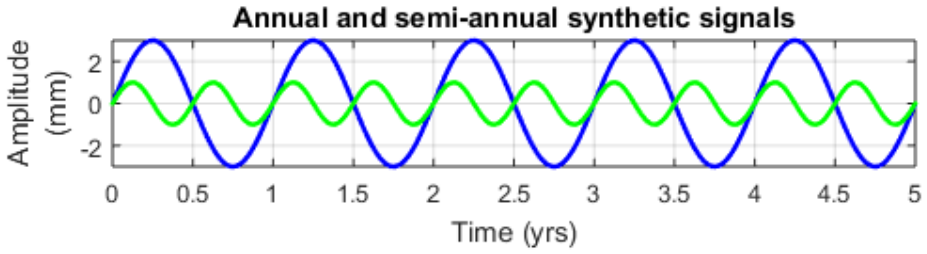


Figure 4.1: Annual (in blue) and semi-annual (in green) signals. Each year is composed of 365.2422 samples which are equivalent to the number of days. The annual signal is defined by a period of 1 year and the semi-annual signal is defined by a period of 6 months.

Taking into consideration that cGPS stations record one observation point a day and the number of days in a year is (365.2422), the sampling frequency (f_s) of the synthetic signals is determined to be $1/365.2242$ a day. Thus, the annual signal has a period of 365.2242 days (i.e., 12 months or 1 year) and the semi-annual signal has a period of 182. 6121 days (i.e., 6 months or $1/2$ a year). Adding the annual and semi-annual signals, a simple estimate of the signal observed in cGPS time series without noise, a trend or any other form of disturbances, is obtained (Figure 4.2).

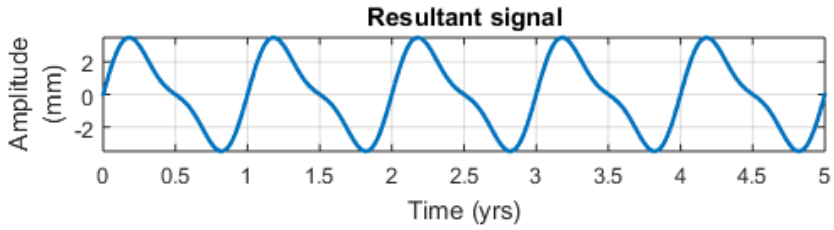


Figure 4.2: Noise-free synthetic time series obtained by adding the annual and semi-annual signals in Figure 4.1.

At this point, the synthetic signal only contains one component of the three main components that generally define an Earth sciences signal (Trauth, 2010, p. 110); hence it is still inadequate to be used as a simulation of a cGPS time series. Signals measured in the real world are never perfectly isolated or measured; a noise component is always associated with them, as correspondingly observed in all GPS time series. Noise is usually a result of multiple sources, which may be related to human and natural activities. Human-related activities usually include ambient motion, underground water withdrawals, etc; while natural-related activities usually include variations in weather patterns (from season to season), volcanic and earthquake activities, and ocean wave vibrations occurring at oceanic margins. These cause fluctuations in authentic time series that must be simulated in the generated synthetic time series.

To make the synthetic time series more realistic, the complexity of the signal is increased by adding Gaussian white noise to the synthetic time series (Figure 4.3b). Gaussian white noise is random noise with a mean of zero, a constant variance (σ^2) and a normal distribution. A Gaussian white noise model is used because, according to the central limit theorem (CLT), the distribution of a random signal formed by a summation of contributions from several sources approaches a normal distribution, regardless of the lone distribution of the sources (Papoulis and Pillai, 2002, p. 278-279; Bendat and Piersol, 2010, p. 57, 60-62, 87). Langbein and Johnson (1997) found that the magnitude of noise in geodetic time series is often less than 0.5 mm, but can be as large as 3 mm. Thus, in this study, the amount of Gaussian white noise introduced in the synthetic time series has a minimum standard deviation of 0.5 mm and a maximum standard deviation of 3 mm. Figure 4.3a shows the Gaussian noise used to generate the noise-contaminated synthetic time series shown in Figure 4.3b.

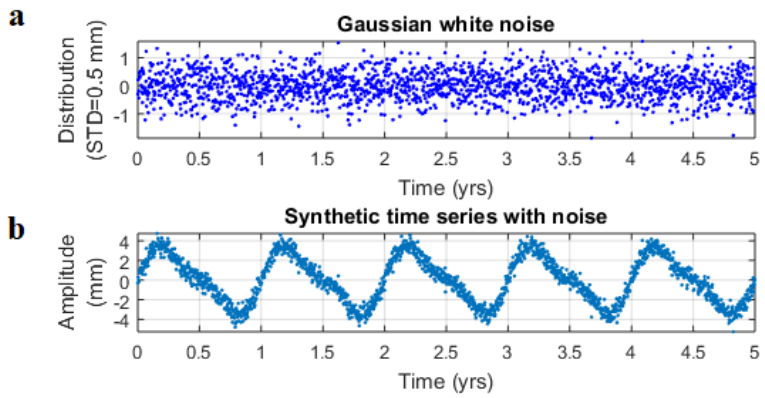


Figure 4.3: (a) Random Gaussian noise with a mean of 0 and a standard deviation of 0.5. (b) Noisy time series obtained by adding the noise time series in (a) and the noise-free-time series in Figure 4.2.

A linear long-term trend component is added to the synthetic time series with noise (Figure 4.4). For this simulation, a simple linear trend is used because 1) of its simplicity, 2) the length of the time series analysed is small and 3) linear trends are common in Earth sciences (Trauth, 2010, p. 112). However, more complex higher-order trends do exist in many Earth sciences systems.

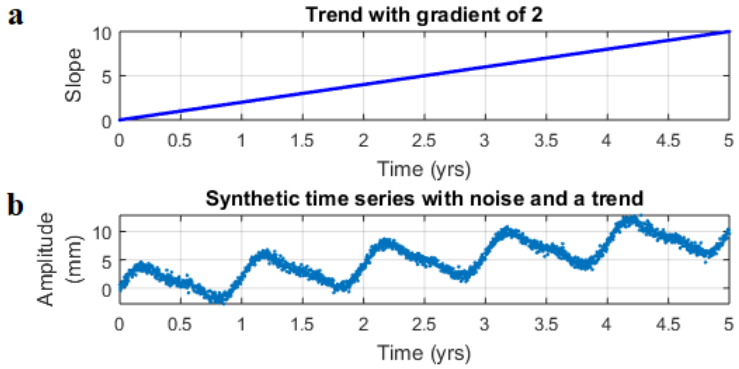


Figure 4.4: (a) Trend with a slope of 2 and a y-intercept of zero. (b) Time series obtained by adding the noise contaminated time series in Figure 4.3 and the trend in (a).

Lastly, a disturbance, in the form of missing data points (gaps), is introduced in the synthetic time series by deleting some values of the time series to create gaps, which represent missing values in authentic GPS datasets (Figure 4.5).

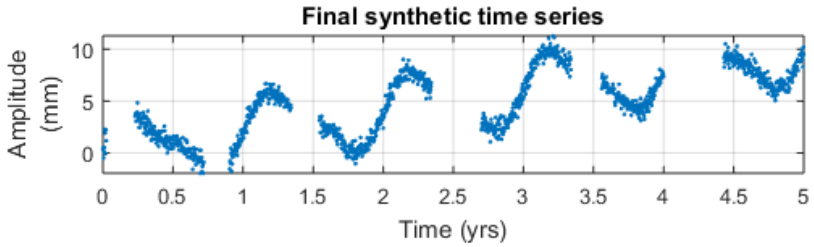


Figure 4.5: Synthetic signal with missing data points.

At this point, the generated synthetic time series contains the fundamental characteristics observed in authentic cGPS time series and can be used to investigate the use of spectral analysis tools. Since the nature of some of the meteorological time series to be analysed (i.e., temperature and pressure) are similar to that of the generated synthetic time series, the generated synthetic time series will be used to represent both cGPS and meteorological time series.

4.3 Interpolation

Time series collected in Earth sciences are usually irregularly sampled, and often characterised by varying sampling intervals due to missing observation points (Trauth, 2010, p. 126). In some cases, irregularities in sampling are caused by equipment failure, change of equipment and reference frame, or periodically-occurring contamination of the data (Baisch and Bokelmann, 1999). Transforming unequally-spaced time series into the frequency domain creates or enhances false peaks (Foster, 1995; Trauth, 2010, p. 126), shifts the frequencies present in the data and introduces errors in the calculated amplitude or magnitudes of the signals embedded in the analysed time series (Kovács, 1981; Foster, 1995, 1996). Thus, to obtain adequate frequency domain results, irregularly-spaced time series should be corrected, and made regularly spaced, before they are converted to the frequency domain (Baisch and Bokelmann, 1999). Unequally sampled time series can be made regularly-spaced by interpolating for missing observation points of the time series. Interpolation is a technique of estimating missing data points, located in between known points, using mathematical functions fitted on the known points of the time series (Akkala et al., 2010; Dumitru et al., 2013). Spatial interpolation assumes that the properties of a time series are continuous and dependent over space (Akkala et al., 2010). Various interpolation functions are generated based on these assumptions.

Many interpolation methods exist, each suitable for use in certain situations, often influenced by factors such as the implementation complexity and speed (Hintzen et al., 2010), nature of the data to be interpolated, and the goal of the interpolation (Li and Heap, 2008, p. 2; Akkala et al., 2010). The is no standard method for interpolating all types of time series (Li and Heap, 2008, p. iii; Dumitru et al., 2013), as all methods have their own advantages and disadvantages that must be considered before the methods are used (Akkala et al., 2010; Trauth, 2010, p. 126). Interpolation methods are commonly used for removing gaps, creating continuous and regularly-spaced grids, and increasing the sampling rate or resolution of a time series (Trauth, 2010 p. 126; Akkala et al., 2010; Dumitru et al., 2013). Since all interpolation methods introduce false and unwanted artefacts, tests to determine which method best estimates the missing data, for the type of time series to be interpolated, need to be done (Akkala et al., 2010).

Irregularly-spaced time series can be interpolated in MATLAB using several interpolation methods. In this study, only the performance of the linear, nearest neighbour, cubic Hermite, and cubic spline piecewise interpolation methods were investigated to find the most suitable interpolation method to use when interpolating the cGPS and meteorology time series.

Theoretical background of interpolation methods

Figure 4.6 shows a quadratic time series interpolated using a linear, nearest neighbour, cubic Hermite and cubic spline interpolant, the figure illustrates how each of these interpolation methods interpolate for missing data points.

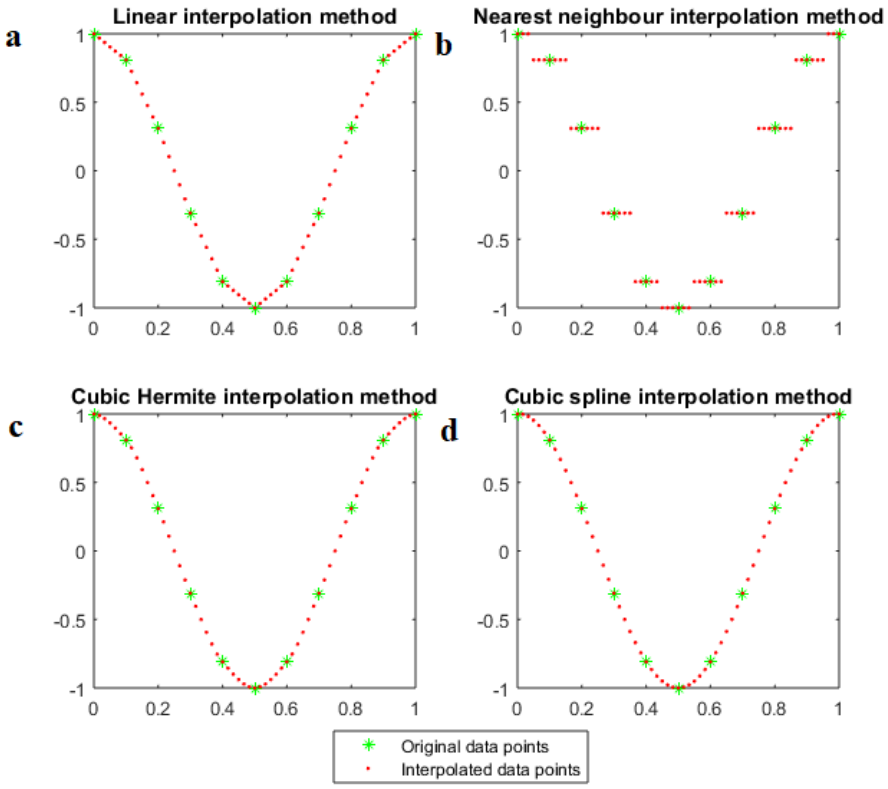


Figure 4.6: The green dots are known points of the original time series and the red dots are interpolation points obtained using different interpolation methods. The plots display how each of the considered interpolation methods interpolate for unknown data points.

4.3.1 Piecewise linear interpolation method

The piecewise linear interpolation method, Figure 4.6a, is a method of estimating unknown data points using a local linear polynomial fitted between successive points of a time series (Hintzen et al. 2010; Burden and Faires, 2011, p. 144). The method assumes that the variation between a neighbouring pair of points $(x_k, f(x_k))$ and $(x_{k+1}, f(x_{k+1}))$ is described by a linear transition (where k = 1, 2, 3, ..,n; n is the number of points constituting the time series of interest; x_k and x_{k+1} are arbitrary adjacent real numbers; and $f(x_k)$ and $f(x_{k+1})$ are function of x_k and x_{k+1} respectively) (Trauth, 2010, p. 126). It interpolates for unmeasured points by fitting a piecewise spline function of degree one through the subinterval $x_k \leq x \leq x_{k+1}$ of a time

series and estimates the missing values at the appropriate point along the line (Unser, 1999; Li and Heap, 2008, p. 8). The method can be applied to data sets with a minimum number of two data points (Hintzen et al., 2010).

The advantages of using a linear interpolant are that it is simple, fast and preserves the variance of a time series (Trauth, 2010, p. 128; Hintzen et al. 2010). Its disadvantage is that it results in the loss of high-frequency components of a time series along unsampled locations (Lehmann et al., 1999; Trauth, 2010, p. 126); its resultant interpolation is usually not smooth at knots (where two piecewise linear segments join); and it fails to interpolate time series characterised by a nonlinear function with high accuracy (Burden and Faires, 2011, p. 144). These disadvantages arise because the method is defined by an interpolation function that is non-differentiable.

4.3.2 Piecewise nearest-neighbour interpolation method

The piecewise nearest-neighbour interpolation method (also known as the proximal interpolation or the maximum proximity method), Figure 4.6b, is a local interpolation method that estimates unsampled or missing data points of a time series based on the distance between the known and unknown points of a time series (Dumitru et al., 2013; Titus and Geroge, 2013). It interpolates for missing data points by assigning the values of known data points, that are nearest to the missing points, to the position of the missing point (Akkala et al., 2010; Titus and Geroge, 2013). The method assumes that adjacent points, closest to each other in a time series, have the same measurable physical properties (Titus and Geroge, 2013). It works by partitioning a time series, using perpendicular bisectors, into subintervals filled with n number of identical data points. The subintervals are constructed based on the sampling interval of the time series to be interpolated (Li and Heap, 2008, p. 6). Data points that are far from the position of the missing value to be interpolated are not taken into consideration in the interpolation calculation (Dumitru et al., 2013).

The advantages of using the nearest neighbour method are that it is fast and easy to implement (Akkala et al., 2010; Dumitru et al., 2013). The disadvantage is that it introduces blurring (Akkala et al., 2010; Titus and Geroge, 2013) and aliasing effects (Lehmann et al., 1999). It can also introduce sharp gradient changes in a time series depending on the x-y positions of the neighbouring points.

4.3.3 Piecewise cubic Hermite interpolation method

The piecewise cubic Hermite interpolation method, Figure 4.6c, is a local interpolant of degree $n = 3$. It interpolates a time series by fitting local polynomials $P(x)$ of degree $n = 3$ into its subintervals, $x_k \leq x \leq x_{k+1}$, and extracts the missing values along the polynomial (Hintzen et al., 2010; Burden and Faires, 2011, p. 166). The fitted piecewise polynomials are local third-degree splines that are in the Hermite form, have continuous first derivatives $P'(x)$ and second derivatives $P''(x)$ that are often non-continuous (Randall et al., 1989; Hintzen et al., 2010; Burden and Faires, 2011, p. 144). The polynomials are computed using at least four points, and the error that exists in each of the fitted polynomials does not affect the neighbouring polynomials (Hintzen et al., 2010; Burden and Faires, 2011, p. 166). The continuously differentiable nature of cubic Hermite interpolation enables the generation of smooth polynomial slopes at knots, where the polynomials meet.

The advantages of using the cubic Hermite interpolation method is that it generates smoother and continuous polynomials compared to the linear and nearest neighbour interpolation methods. Its disadvantage is that, because its second derivative is often not continuous, it exhibits oscillation weaknesses which limit it from performing well when interpolating data sets with many nodes (Burden and Faires, 2011, p. 171).

4.3.4 Piecewise cubic spline interpolation method

The piecewise cubic spline interpolation method, Figure 4.6d, is a local interpolant that interpolates a time series by fitting a gradual and continuous cubic polynomial of degree $n = 3$ between successive pairs of points (Li and Heap, 2008, p. 8; Burden and Faires, 2011, p. 145; Levy, 2010, p. 49). Splines of degree $n = 1$ and $n = 2$ are linear and quadratic polynomials (Li and Heap, 2008, p. 8). Cubic spline and cubic Hermite interpolants are similar in that they are both polynomials of degree $n = 3$ (Burden and Faires, 2011, p. 144-145; Levy, 2010, p. 49-50) and their first derivatives are continuous. They differ in that, while the second derivative of the cubic spline interpolant is always continuous, that of the cubic Hermite interpolant is not. Piecewise cubic spline interpolants can be used to interpolate data sets with a minimum of four data points (Trauth, 2010, p. 126; Hintzen et al., 2010).

The advantages of the cubic spline interpolant over other interpolation methods is that it preserves high-frequency components contained in a time series (Trauth, 2010, p. 126) and

generates smooth continuous piecewise-polynomials (Akkala et al., 2010; Hintzen et al., 2010; Dumitru et al., 2013). Its disadvantage is that it is not suitable for use in time series that have large, rapid, changes within a short distance because it can overshoot the estimated values (Trauth, 2010, p. 126). The method is also complex and can mask uncertainties in a time series (Akkala et al., 2010; Titus and Geroge, 2013).

4.4 Application of the interpolation methods to synthetic data

In this section, the performance of the linear, nearest neighbour, cubic Hermite and cubic spline interpolation methods are examined to determine a suitable interpolant to use when interpolating the cGPS and meteorological time series. A suitable method is considered to be one that will introduce fewer artefacts and variance that is closer to that of the original time series without missing data points (Trauth, 2010, p. 126).

The study is carried out by means of two tests. The first test is conducted on a noise-free time series, in order to verify whether the interpolation algorithm to be used in this study works as expected and to determine which method performs best under ideal conditions when interpolating oscillatory time series with missing data points. The second test is carried out on a noise-contaminated time series, in order to make the study more realistic; to determine the effects of noise on the interpolation methods and the most suitable method to use when interpolating a noise-contaminated periodic time series.

4.4.1 Application of the interpolation techniques on a noise-free synthetic time series

Figure 4.7a shows two similar noise-free synthetic time series composed of an annual and semi-annual signal, the time series in blue has missing data points, while the one in green does not. The time series with gaps is linear detrended and then interpolated using the linear, nearest neighbour, cubic Hermite, and cubic spline interpolation methods to determine the response of each interpolation method when interpolating a noise-free sinusoidal time series. Figure 4.7a shows a noise free synthetic time series with gaps overlaid on top of a version of it that has no missing data points. When detrending the synthetic time series, using a linear trend, it is observed that trends of low gradients are introduced in the time series (Figure 4.7b). The slopes of the introduced trends appear to respond to the absence and presence of missing data points. In this case, the trend introduced in the synthetic dataset with missing data points has a higher

gradient than the one in the gap-free time series (Figure 4.7b). In Figure 4.7c, d, e and f, a third-time series is introduced, the interpolated time series (shown in red).

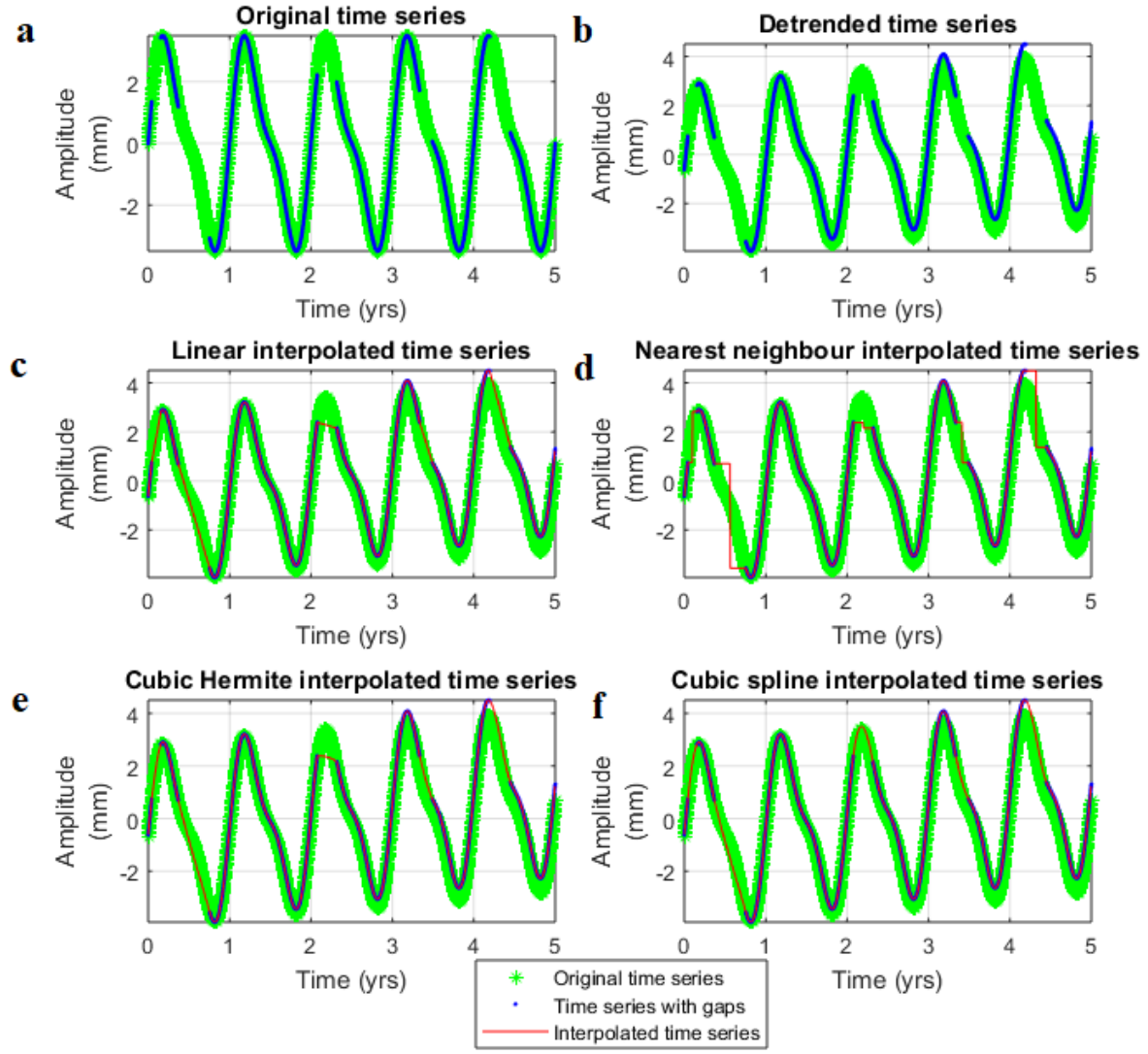


Figure 4.7: Response of the interpolation methods when applied to noise-free synthetic time series. (a) Noise-free synthetic time series without gaps (green) and with gaps (blue). (b) Detrended time series. (c) Linear interpolated time series. (d) Nearest neighbour interpolated time series). (e) Piecewise cubic Hermite interpolated time series. (f) Piecewise cubic spline interpolated time series.

Analysing the linear interpolated time series (Figure 4.7c), it is observed that the linear interpolant does not interpolate well in regions where the time series is characterised by a change in slope along gaps. Although, the method interpolates well along regions of unchanging or slightly varying slopes (Figure 4.7c). When interpolating the time series with gaps using the nearest neighbour interpolation method (Figure 4.7d), it is observed that the method introduces sharp gradient changes in the time series, even in regions of an unchanging

slope. In regions where the is a gradual gradient change, along with small gaps, the gradient change introduced by the nearest neighbour interpolation method is less apparent (Figure 4.7d). When interpolating the time series with gaps using the cubic Hermite interpolation method, it is observed that the method performs similarly to the linear interpolation method (Figure 4.7e). The difference is that the values estimated using the cubic Hermite interpolation method join smoothly in between knots. The cubic spline interpolation method interpolates noise-free time series best (Figure 4.7f). The method interpolates exceptionally well in both regions of high and low gradient changes along small and large gaps using a second order differentiable model. Hence, when interpolating noise-free time series, the cubic spline interpolation method would be the best method to use.

4.4.2 Application of the interpolation techniques on a noise contaminated synthetic time series

Figure 4.8 shows the responses of the linear, nearest neighbour, cubic Hermite and cubic spline interpolation methods when applied to a noise-contaminated dataset. The linear, nearest neighbour and cubic Hermite interpolation methods (Figure 4.8c, d, and e) behave in a same manner as when they are interpolating a noise-free synthetic time series (Figure 4.7c, d, and e). However, the cubic spline interpolation method introduces large artefacts when interpolating a noise contaminated time series. The artefacts cause a large variance in the properties of the synthetic time series, which make it the least suitable method for interpolating a time series with noise, followed by the nearest neighbour method, which introduces sharp gradient changes in a time series (Figure 4.7d). Variance and gradient changes in a time series, introduced by interpolation methods, distort the frequency spectrum of a time series. The linear and cubic Hermite interpolation methods seem to be the most suitable interpolation methods to use when interpolating noisy data. They introduce a small and similar variance in the properties of a time series and interpolate reasonably well along slopes with, almost, constant gradient (Figure 4.8c and e). Thus, from this point onwards, the focus of this section will be on determining a better interpolant, for the time series of interest, between the linear and cubic Hermite interpolation methods.

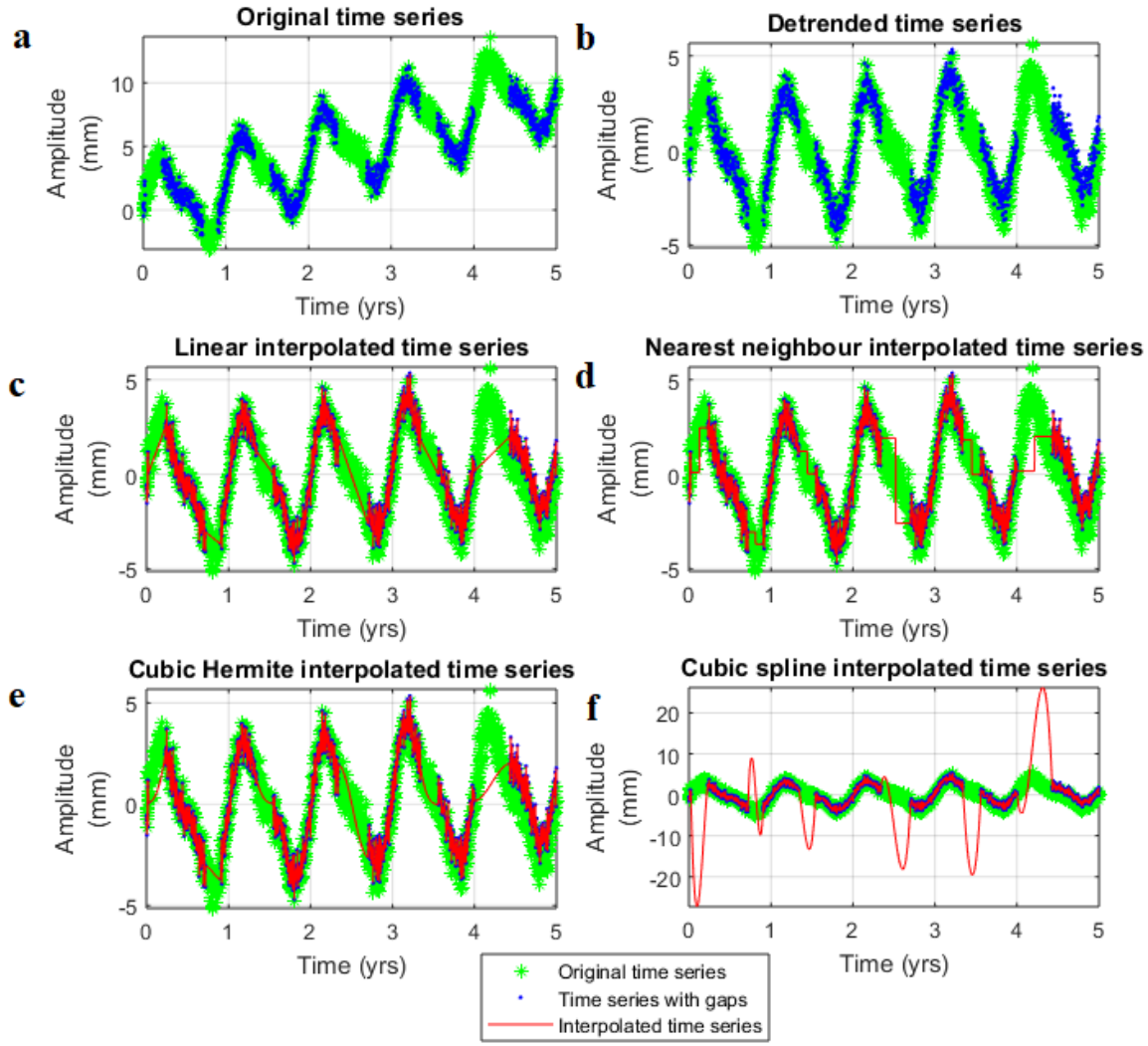


Figure 4.8: Response of the interpolation methods when applied to a noise-contaminated synthetic time series. (a) Noise-contaminated synthetic time series without gaps (green) and with gaps (blue). (b) Detrended time series. (c) Linear interpolated time series. (d) Nearest neighbour interpolated time series. (e) Piecewise cubic Hermite interpolated time series. (f) Piecewise cubic spline interpolated time series.

Table 2 shows the calculated variance of different time series with gaps, without gaps, and after interpolation. Since the use of the un-interpolated, nearest neighbour interpolated, and piecewise spline interpolated time series has been ruled out, the variance considered is that of the linear and cubic Hermite interpolated time series.

From Table 2, it is observed that the linear and cubic interpolation methods introduce relatively similar variance in a time series. The introduced variance is found to be dependent on the number of missing data points in the time series being interpolated. In Table 2, time series T1, it is observed that the variance introduced by the cubic Hermite interpolation method in a time

series with 3% missing data points (i.e., with authentic data points equal to and greater than 97%) is closest to that of the original time series without missing data points.

Table 2: Variance of five similar time series (T1, T2, T3, T4 and T5) with a varying percentage of authentic data points (or missing data points). The values highlighted in blue are the values that were of more significance in choosing the interpolation method that is used in this project. The closer the variance of the interpolated time series to that of the original time series, the better. TS stands for time series.

Interpolation methods	**Variance**				
Time series - % of real data points	T1 – 98%	T2 – 95%	T3 – 90%	T3 – 85%	T5 – 80%
Original (without gaps) TS	5.0559	5.0559	5.0559	5.0559	5.0559
Un-interpolated (with gaps) TS	5.1028	5.2807	5.3439	4.9839	5.0210
Linear interpolated	5.0548	5.0641	5.1267	4.6998	4.0588
Difference of Original TS and Linear interpolated TS	0.0011	-0.0082	-0.0708	0.3561	0.9971
Nearest neighbour interpolated TS	5.0561	5.1386	5.7713	5.6207	4.0832
Cubic Hermite interpolated TS	5.0554	5.0811	5.3226	5.0336	4.0959
Difference of Original TS and Cubic Hermite interpolated TS	0.0005	-0.0252	-0.2667	0.0223	0.96
Spline interpolated TS	5.1177	8.4201	117.7019	227.9904	171.2620

Also, in the time domain plots of time series T1, in appendix A, it is observed that, like the estimates of the linear interpolant, the estimates of the cubic Hermite interpolant do not deviate from the trend of the time series when the number of missing data points is equal to/or less than 5%. These two observations are taken to imply that the cubic Hermite interpolant is the most suitable interpolation method for interpolating a time series with 3% and less missing data points, i.e., for the types of time series taken into consideration in this project.

When interpolating time series with 95% and less authentic data points, the cubic Hermite interpolant performs better or worse than the linear interpolant depending on the type of gap or gaps formed by the missing data points. That is, if the data points form one large gap, like in time series T3, T4 and T5 in appendix A, the method is not desirable because its estimates tend to deviate from the trend of the time series being interpolated, as observed in time domain plots of time series T3 and T4 in appendix A. In this case, it is better to use the linear interpolation method. However, if the missing data points form a series of small gaps, like in Figure 4.8, the

cubic Hermite interpolation method is expected to outperform the linear interpolation method. Thus, in this study, the cubic Hermite interpolant will be used to interpolate time series with less than 5% missing data points and the linear interpolation method will be used to interpolate time series with missing data points equal to 5% and more.

4.5 Decomposition, correlation and phase shift synthetic data tests

In carrying out the decomposition, correlation and phase difference tests, the synthetic time series generated in the above section were used; in some instances, modified versions of the time series were used to meet the aims of the tests carried out. In modulating the synthetic time series, at some points, noise, phase shifts or gaps are introduced in the time series.

4.5.1 FFT decomposition

Figure 4.9 shows the FFT spectra of a stationary time series, composed of an annual and semi-annual signal, when it is noise free (Figure 4.9a), contaminated by white Gaussian noise (Figure 4.9b) and when it contaminated by noise and a trend with a slope of 3 mm/year units (Figure 4.9c). The aim of conducting a frequency domain decomposition test is to determine the performance of the FFT technique when used to decompose a time series with noise and a trend.

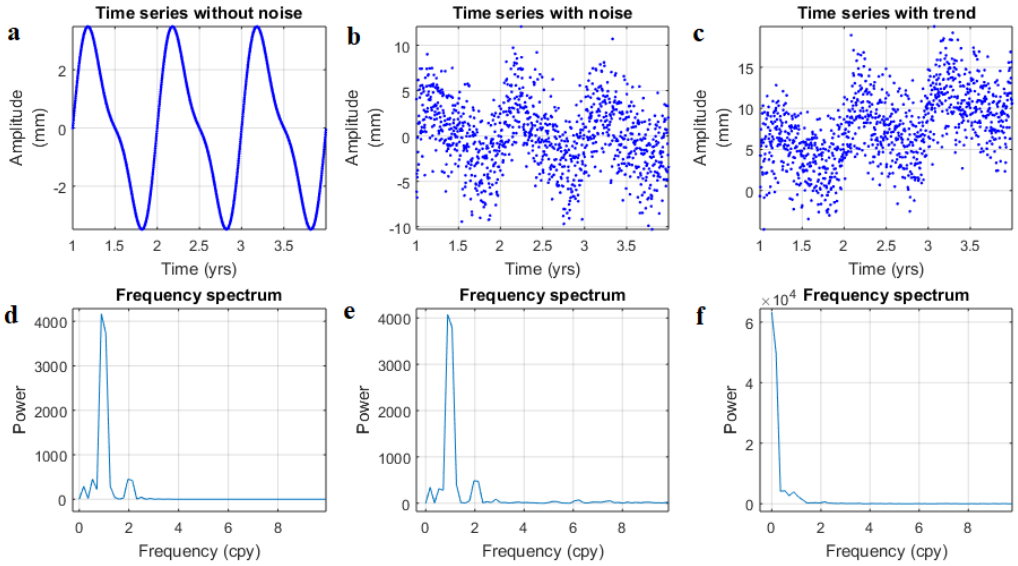


Figure 4.9: Fast Fourier Transform (FFT) decomposition of a time series without noise, with noise and with a trend. (a) Time series composed of an annual and semi-annual signal (i.e., signals of frequency 1 and 2 cpy), without noise. The annual signal has an amplitude of 3 mm, while the semi-annual signal has an amplitude of 1 mm. (b) Time series in (a) contaminated by white Gaussian noise with a standard deviation of 3 mm. (c) Time series in (b) with noise and a trend. (d) FFT spectrum of the time series in (a). (e) FFT spectrum of the time series in (b). (f) FFT spectrum of the time series in (c).

In Figure 4.9d and e, it is observed that the FFT technique recovers the frequency components of a times series well, in both the presence and absence of noise. However, in the presence of

a trend, the FFT technique does not perform well (Figure 4.9c and f), the power at each frequency becomes obscured. The trend appears, in the FFT spectrum, as a long-period cycle (or low-frequency cycle) of high power and obscures power in the whole FFT spectrum. Thus, when computing the FFT spectrum, trends must be removed beforehand, to enhance the visibility of periodic components fully captured in the time series being analysed.

4.5.2 Cross-covariance and phase test

The aim of this test is to investigate how correlation and phase spectrum methods are affected by the presence of noise. Figure 4.10 shows the correlation and phase difference results for two noise-free and noise-contaminated time series with a phase difference of 120 degrees (2.1 radians) when cross-covariance and phase extraction techniques are applied.

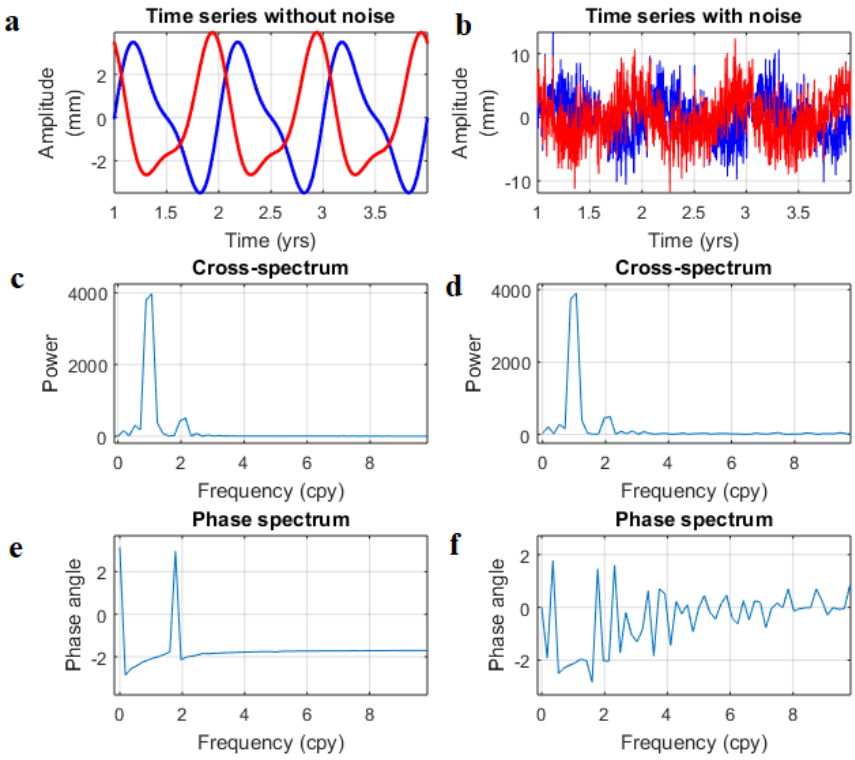


Figure 4.10: Cross-spectrum and phase tests. (a) Identical time series with a phase difference of 120 degrees (2.1 radians), both (blue and red) time series are composed of an annual and semi-annual signal. The annual signal has an amplitude of 3 mm, while the semi-annual signal has an amplitude of 1 mm. (b) Time series in (a) contaminated by Gaussian noise with a STD of 3 mm. (c) Cross-spectrum of the time series in (a). (d) Cross-spectrum of the time series in (b). (e) Phase spectrum of the time series in (a). f) Phase spectrum of the time series in (d). The phase is given in radians.

The time series in Figure 4.10a (in blue and red), are both made up of an annual and semi-annual time series. In Figure 4.10b, the time series in Figure 4.10a are contaminated with Gaussian noise, with a standard deviation of 3 mm and zero mean, so as to study the effect of noise on the cross-spectrum and phase spectrum techniques. In Figure 4.10c and d, it is observed that the cross-spectrum recovers the covariant components of the time series in Figure 4.10a and b well in the presence and absence of noise. Phase shift effects on the power of the frequency component are not visible, because the real component of the cross-spectrum is shown (Figure 4.10c and d). When the complex component of the cross-spectrum is taken into consideration, the interference between the frequency components constituting the two time series becomes apparent in the presence of a phase shift. Correspondingly, the phase technique also performs well in the presence and absence of noise, although the phase results are altered a bit by the presence of noise (Figure 4.10f). For the noise-free time series (Figure 4.10a), the phase spectrum returns an accurate phase difference value of 2.1 radians between the annual and semi-annual components embedded the time series (Figure 4.10e). When applied to the noise contaminated time series, the phase technique retuned a phase difference of -2.13 and -2.02 radians, respectively, between the annual and semi-annual signal constituting the time series (Figure 4.10f). This demonstrates that the presence of noise does affect the phase difference results.

4.6 Wavelet transforms

This section looks at the effect of the presence of noise, gaps and a trend on wavelet and wavelet-based semblance methods. The wavelet and wavelet-based semblance methods are used in this study to decompose and correlate surface displacement and meteorological time series in the time and frequency domain.

4.6.1 Decomposition using the continuous wavelet transform

In most cases, a real-time series is composed of two or more non-stationary signals generated by different processes. In this study, time-frequency decomposition was carried out to determine the dominant signals forming the analysed cGPS and meteorological time series, their frequency of occurrence, and variance over time. The time series were decomposed using the Morlet Continuous Wavelet Transform (CWT) technique. Figure 4.11a and c show a noise free and noise contaminated time series, both composed of an annual and semi-annual signal.

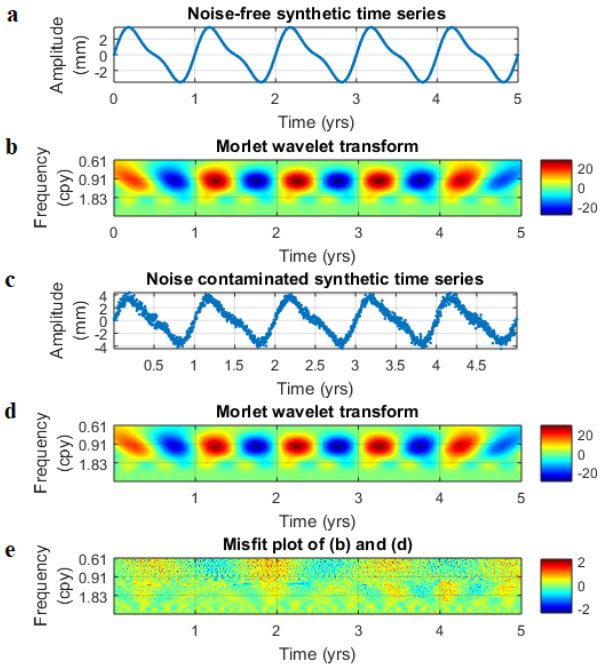


Figure 4.11: Synthetic data decomposition using the complex continuous wavelet transform (CWT). (a) Noise-free time series composed of an annual and semi-annual signal. The annual signal has an amplitude of 3 mm, while the semi-annual signal has an amplitude of 1 mm. (b) Real part of the complex CWT of the time series in (a). (c) Time series with the same signals as those in (a) but contaminated with a Gaussian noise of standard deviation of 0.5 mm. (d) Real part of the complex CWT of time series in (c). (e) Misfit plot of (b) and (d). The colour bar shows the variation of the CWT coefficients as a function of frequency and time. The colour bar shows the variation of the CWT coefficients as a function of frequency and time. The bright red bands indicate a positive amplitude and the dark blue bands indicates a negative amplitude.

Figure 4.11b and d show the real part of the complex CWT of the time series in Figure 4.11a and c, in which, both the signals embedded in the time series and their variance over time can be seen. Figure 4.11d illustrates that a small amount of Gaussian noise has little to negligible effect on the performance of the CWT algorithm, its ability to resolve frequencies contained in a time series is reduced by a very small to negligible amount. The misfit plot, Figure 4.11e, illustrates the effect of a small amount of noise. Next, the standard deviation of the Gaussian noise was increased to be the same as the amplitude of the time series with the highest value, i.e. 3 mm, (Figure 4.12). The resolution at which the seasonality is detected does not get reduced by much, as the frequency and phase variation of the signals are still clearly visible (Figure 4.12).

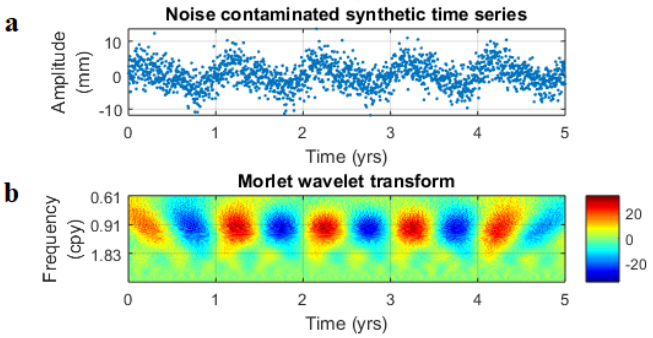


Figure 4.12: (a) Time series in Figure 4.11a contaminated with Gaussian noise of higher standard deviation, i.e., 3 mm. (b) Real part of the complex continuous wavelet transform (CWT) of time series in (a). The colour bar shows the variation of the CWT coefficients as a function of frequency and time. The colour bar shows the variation of the CWT coefficients as a function of frequency and time. The bright red indicates a positive amplitude and the dark blue indicates a negative amplitude.

The cyclicity generated by the signal with an amplitude of 1 mm, at a frequency of 2 cpy, is still well detectable in the presence of noise with a standard deviation three times greater than its amplitude (i.e., 3 mm). This implies that even if the noise standard deviation is greater than the amplitude of the signals constituting a time series, the signals can still be detected adequately using the CWT technique.

In most cases, it is important for trends present in time domain datasets to be identified and removed before the datasets are transformed into the frequency domain. When using certain frequency domain techniques (e.g., Fourier transforms) to convert time domain data to the frequency domain, the presence of a trend distorts the frequency spectrum of the time series and enhances long-term features at the expense of short-term (seasonal and cyclic) features

embedded in the data. Figure 4.13 illustrates the effect of a trend when decomposing a time series using the complex CWT. The synthetic time series in Figure 4.13a and c have trends with a slope of 2 and 7 mm/year.

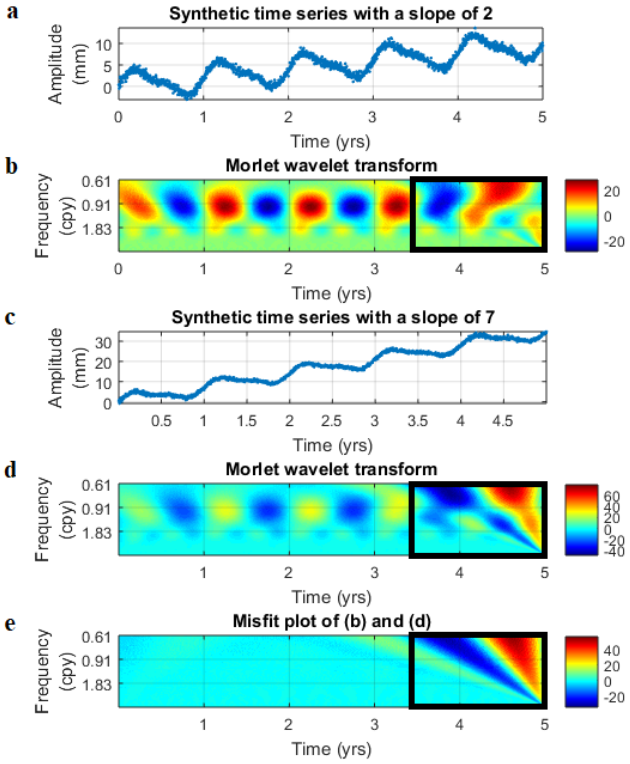


Figure 4.13: Effects of a trend when transforming data into the time-frequency domain using the complex continuous wavelet transform (CWT). (a) Time series with the same properties as that in Figure 4.11c plus a trend with a slope of 2 units. (b) Real part of the complex CWT of time series in (a). The bright red indicates a positive amplitude and the dark blue indicates a negative amplitude. (c) Time series with the same parameters as the time series in (a), but with a trend of higher slope (7 units). (d) Real part of the complex CWT of time series in (c). (e) Misfit plot of (b) and (d). The colour bar shows the variation of the CWT coefficients as a function of frequency and time. The bright red indicates a positive amplitude and the dark blue indicates a negative amplitude. The black boxes at approximately 3.4 to 5 yrs highlight the edge effects, regions of higher than normal CWT coefficients, induced by the presence of a trend.

In both the complex CWT spectrums (Figure 4.13b and d), it is observed that the presence of a trend does not distort the dominant frequencies in the time series and their wavelengths. This is largely due to the use of a high order differential wavelet function with a large number of vanishing moments. Although, the presence of a trend does enhance edge effects. Edge effects are distortions of the CWT spectrum at the edges (Figure 4.13e). CWT coefficients at the far edge of the CWT spectra, starting from roughly 3.4 to 5 yrs, that align with the side of the trend that is greatest, are enhanced and distorted. Conversely, the resolution of the CWT is decreased

at the edges. In Figure 4.13b, d and e, it is observed that as the values of the time series in Figure 4.13a and c increase due to the presence of a trend, the values of the CWT coefficients of the wavelet transform also increase. Thus, it is noted that to avoid or minimise edge effects, and to increase the resolution of the complex CWT decomposition spectrum, trends must be removed or reduced.

Figure 4.14 shows the effects of missing data points and interpolation on the complex CWT. In Figure 4.14b it is observed that the presence of missing data points causes a shift in the determined frequencies and wavelength values of the signals embedded in the time series. In Figure 4.14d it is seen that interpolating a time series with missing data points, before it is decomposed using wavelet transforms (WT), reduces the distortion of the detected frequencies and their waveleghts caused by missing data points.

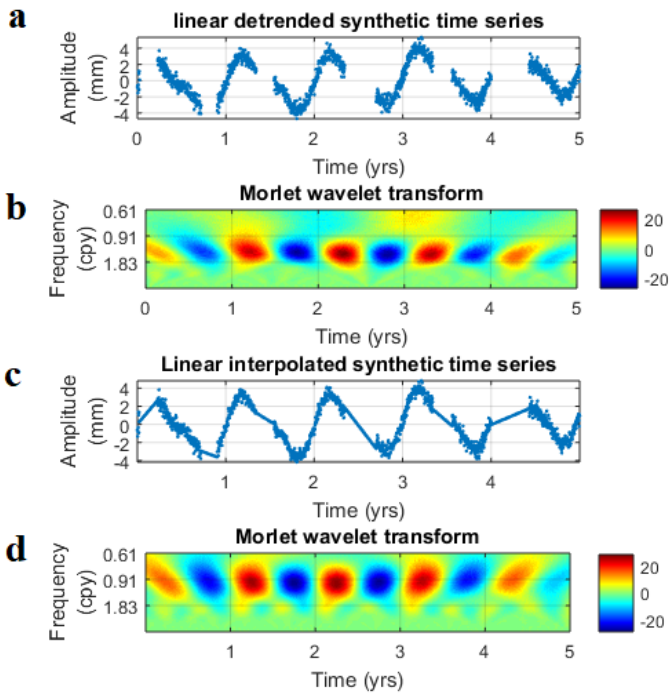


Figure 4.14: Effects of missing data (gaps) on the complex continuous wavelet transform (CWT). (a) Time series with the same properties as that in Figure 4.11c, but with missing values. (b) Real part of the complex CWT of time series in (a). The bright red indicates a positive amplitude and the dark blue indicates a negative amplitude. (c) Linear interpolated time series with the same parameters as the time series in (a). (d) Real part of the complex CWT of time series in (c). The colour bar shows the variation of the CWT coefficients as a function of frequency and time. The bright red indicates a positive amplitude and the dark blue indicates a negative amplitude.

Figure 4.15 shows the effects of detrending and decomposing a time series with a mean offset. CGPS time series commonly display such behaviour, which is often caused by a change in equipment, geodetic reference frame or faulting associated with earthquakes. In Figure 4.15b and d, it is observed that a mean offset is a huge disturbance. It causes large spectral distortion, all over the CWT spectrum, which makes it hard to determine the frequencies embedded in a time series. It is also observed that centring the mean shifted time series using a linear trend slightly reduces the distortion of the mapped frequencies compared to centring the time series by subtracting a constant mean. However, its disadvantage is that it introduces a trend in both the side of the time series with different means, which is not a problem as such (i.e., if the trends have a small gradient), since a trend causes a minimal effect in the resolution of the spectrum, as seen in Figure 4.15d.

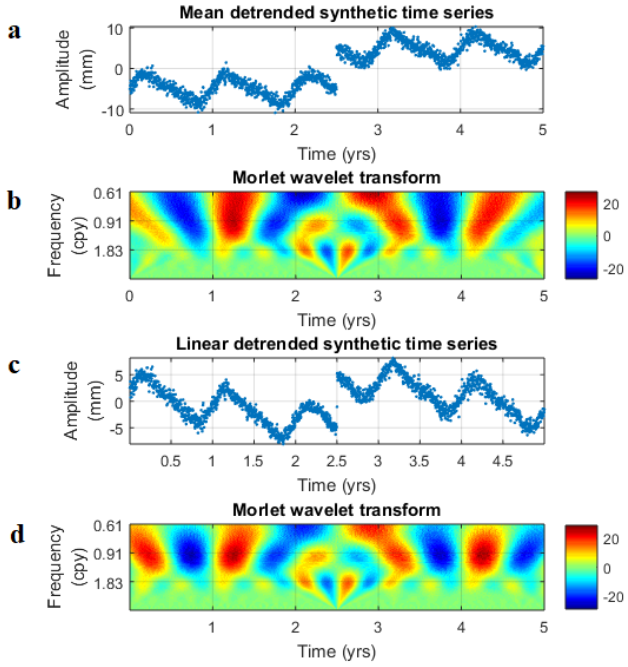


Figure 4.15: Morlet wavelet transform of mean shifted time series. (a) Time series in Figure 4.11c with a mean shift, the time series is detrended using a constant mean. (b) Real part of the complex continuous wavelet transform (CWT) of time series in (a). (c) Time series in Figure 4.11c detrended using a first order linear trend. (d) Real part of the complex CWT of the time series in (c). The colour bar shows the variation of the CWT coefficients as a function of frequency and time. The bright red indicates a positive amplitude and the dark blue indicates a negative amplitude.

4.6.2 Wavelet semblance

Wavelet semblance is a method used to correlate two time series based on their phase information. It produces a visual correlation response that is easy to interpret and enables the

variance in correlation to be observed simultaneously in the time and frequency domain, as seen in Figure 4.16. Figure 4.16 shows a wavelet transform, local phase and wavelet semblance response spectrums for two time series composed of an annual and semi-annual sinusoidal signal. Figure 4.16b illustrates the wavelet transform spectrum of the time series in Figure 4.16a, both the annual and semi-annual signals embedded in the time series are observed to exist throughout the duration of the time series. The time series in Figure 4.16c is composed of annual and semi-annual sinusoidal signals that have phase shifts at 1.5 and 3.5 yrs, Figure 4.16e shows the local phase (ϑ) variance between the frequency components of the time series in Figure 4.16a and c. Figure 4.16f shows the wavelet semblance correlation of the time series in Figure 4.16a and c. Based on the prior knowledge of both the time series, that is:

1. between 0 and 1.5 yrs, the annual components in the time series are perfectly in phase and the semi-annual signals are perfectly out of phase;
2. between 1.5 and 3.5 yrs, no phase correlation exists between the annual components and semi-annual components constituting the time series;
3. between 3.5 and 5 yrs, the phase of both the annual components and semi-annual components constituting the time series are perfectly out of phase with each other.

Analysing the local phase results in Figure 4.16e, it is observed that the local phase correlation spectrum does not give good correlation results to the known phase properties of the signals listed above. Figure 4.16f gives the wavelet semblance correlation spectrum of the two-time series. The semblance spectrum is observed to give good correlation results based on the three known properties of the signals listed above. The red indicates a positive correlation, blue indicates anticorrelation and green indicate no correlation between the time series. The variance observed in the semblance spectrum (Figure 4.16f) almost perfectly corresponds with the known phase variance of the time series. However, the variance observed in the phase spectrum, to a large degree, does not correspond to the prior known phase information of the signals embedded in the time series (Figure 4.16e). Hence, in this study, phase correlation plots will not be used when investigating the relationship between the cGPS and meteorological time series.

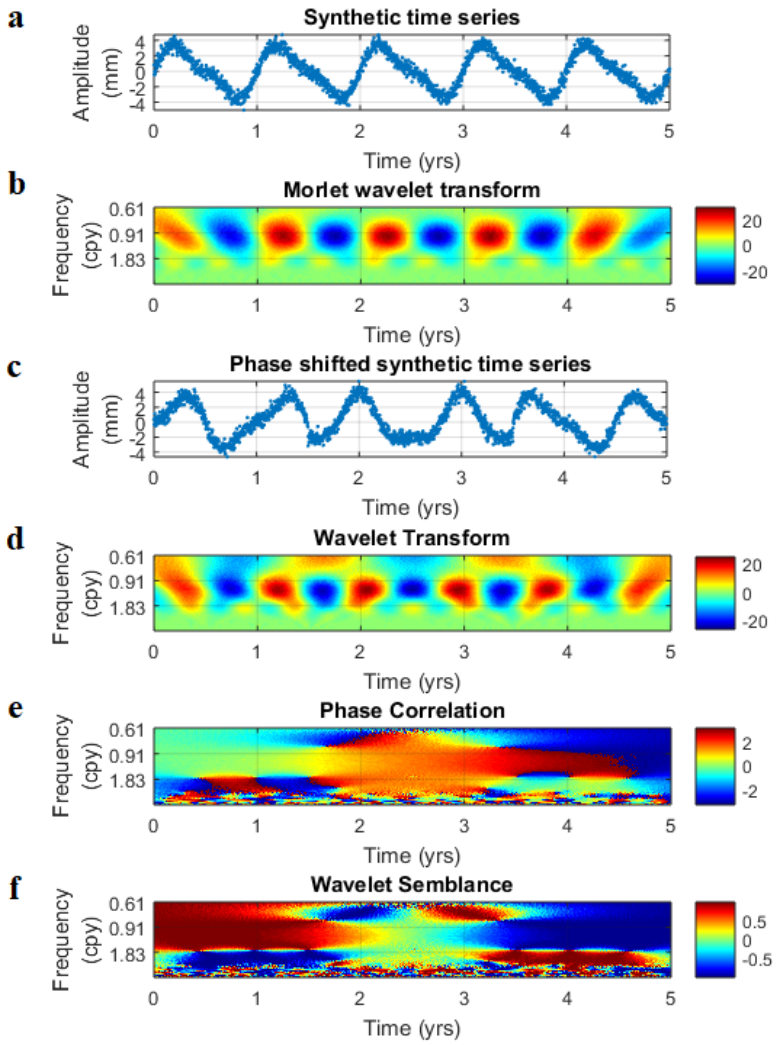


Figure 4.16: Wavelet transform, phase and semblance correlation spectrums. (a) Time series in Figure 4.11c. (b) Real part of the complex continuous wavelet transform (CWT) of the time series in (a). The bright red indicates a positive amplitude and the dark blue indicates a negative amplitude. (c) Time series in (a) with phase variations between the intervals at 0 - 1.5 yrs, 1.5 – 3.5 yrs and 3.5 - 5 yrs. (d) Real part of the complex CWT of time series in (c). (e) Phase correlation spectrum. (f) Wavelet semblance spectrum. The colour bar shows the variation of the CWT coefficients as a function of frequency and time. The bright red indicates a positive amplitude and the dark blue indicates a negative amplitud

5 Results and interpretation

This chapter presents the results of the decomposition and correlation of cGPS displacement and meteorological (surface air temperature, atmospheric pressure, rainfall and humidity) time series obtained using time series analysis techniques. Fast Fourier transforms (FFT) and Wavelet transforms (WT) are used to decompose the time series in the frequency and time-frequency domain, respectively. Cross Spectral Density (CSD), Coherence, Phase, and Semblance techniques are used to determine and quantify the correlation of signals in the frequency and time-frequency domains. The decomposition and correlation techniques are used to study the vertical (up) cGPS displacement component and its relationship with variations in temperature, pressure, rainfall, and humidity.

NB: for the convenience of writing, some figures in this chapter are grouped based on domains, i.e., time, frequency and time-frequency domains. Figures of results from different domains are separated from each other, which can make it a bit hard to follow. Figure 5.5 to Figure 5.8 contain meteorological data time series plots; Figure 5.9 to Figure 5.12 contain fast Fourier transform (FFT) spectra of the meteorology time series; and Figure 5.13 to Figure 5.16 contain wavelet transform (WT) plots of the meteorology time series.

5.1 Time domain results

Visual plots of surface displacement and meteorological time series show that, in all the climatic zones, annual surface displacement and surface air temperature time series are positively in phase with each other (Figure 5.2 and Figure 5.5). The processes reach their maximum positive amplitude in summer and the minimum negative amplitude in winter. Annual atmospheric pressure variations are negatively in phase with surface displacement and temperature time series; they reach their maximum amplitude in winter and minimum in summer (Figure 5.6). As an example, Figure 5.1, illustrates displacement, temperature, pressure, rainfall and humidity time series from cGPS and meteorological stations in Worcester (WORC) and Mafikeng (MFKG). In both regions, the fluctuation amplitude in surface displacement, temperature and pressure time series are ~ 5 mm, ~ 10 ℃ and ~ 20 mbar, respectively, while the fluctuation amplitudes of the humidity time series are ~ 10% in WORC and ~ 20% in MFKG (Figure 5.1).

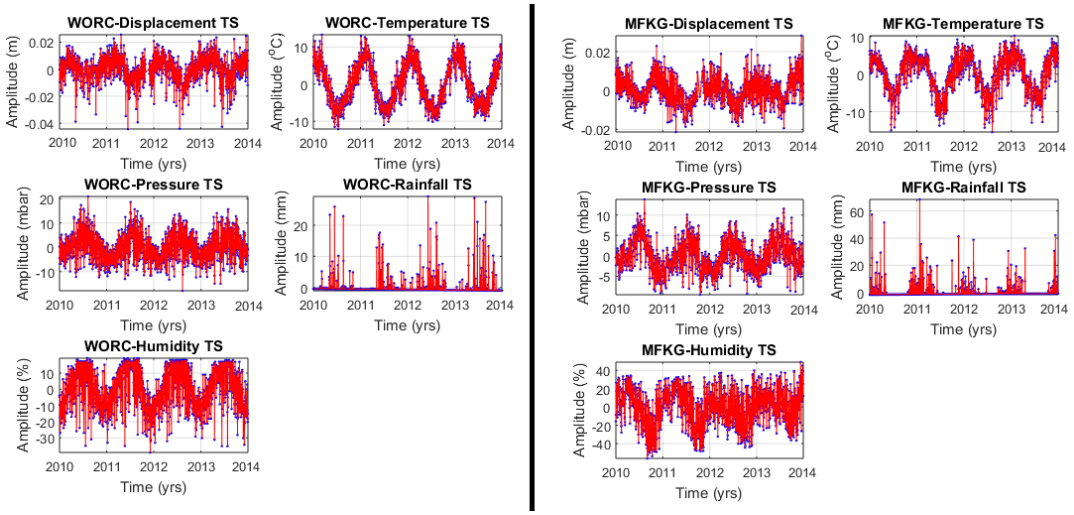


Figure 5.1: On the left-hand side of the black line are displacement and meteorology time series from Worcester (WORC), a town located in the south-western part of southern Africa, a winter rainfall region. On the right are displacement and meteorology time series at in Mafikeng (MFKG). Mafikeng is a summer rainfall region, located in the north-central part of South Africa. The displacement, temperature, pressure and humidity time series are zero centred so as to be able to easily see approximate amplitudes of the different datasets.

In all the climatic zones, annual rainfall and humidity time series are positively in phase with each other, however, their phase is not the same throughout southern Africa (Figure 5.7 and Figure 5.8). In areas defined by a winter rainfall season (south-western parts of southern Africa), e.g, WORC in Figure 5.1, annual rainfall and humidity time series peak in winter and reach their minimum in summer. In areas defined by a summer rainfall season (central and north-eastern parts of southern Africa), e.g., MFKG in Figure 5.1, the time series peak in summer and reach their minimum in winter. Thus, in the south-western parts of southern Africa, annual rainfall and humidity variations are inversely proportional to annual surface displacement and surface air temperature variations, and directly proportional to annual atmospheric pressure variations. In the central and north-eastern parts of southern Africa, annual rainfall and humidity processes are directly proportional to annual surface displacement and surface air temperature variations, and inversely proportional to annual atmospheric pressure variations.

Pearson's and Spearman's correlation results show that there exists a moderate correlation between surface displacement and surface air temperature variations; and a negligible correlation between surface displacement, atmospheric pressure, rainfall and humidity variation (Table 3 and Table 4).

Table 3: Correlation of surface displacement vs meteorological time series using Pearson's (PCC) method.

	GPS Station name	PCC (displacement vs meteorological time series)			
Climatic Zones		Temperature	Pressure	Rainfall	Humidity
Desert	PSKA	0.60	-0.38	0.13	-0.35
	SBOK	0.66	-0.27	-0.13	-0.46
Wet Tropical	GREY	0.39	-0.20	0.05	-0.05
	UMTA	0.34	-0.31		-0.19
	IXOP	0.41	-0.11	-0.04	0.02
	ULDI	0.30	-0.26	0.11	-0.01
Sahelian	DEAR	0.63		0.07	-0.35
	MFKG	0.58	-0.39	0.13	-0.11
Dry Tropical	EMLO	0.44	-0.32	0.11	
	BETH	0.52	-0.27	0.15	
Mediterranean	MALM	0.45	-0.22	-0.16	-0.27
	GEOA	0.48	-0.22	-0.05	-0.04
	WORC	0.47	0.07	-0.37	-0.11

Table 4: Correlation of surface displacement vs meteorological time series using Spearman's (Rho) rank method.

	GPS Station name	Rho (displacement vs meteorological time series)			
Climatic Zones		Temperature	Pressure	Rainfall	Humidity
Desert	PSKA	0.59	-0.40	0.09	-0.35
	SBOK	0.65	-0.27	-0.16	-0.44
Wet Tropical	GREY	0.38	-0.19	0.11	-0.09
	UMTA	0.33	-0.31		-0.19
	IXOP	0.41	-0.10	-0.02	0.00
	ULDI	0.30	-0.26	0.10	-0.03
Sahelian	DEAR	0.61		0.05	-0.34
	MFKG	0.57	-0.39	0.17	-0.10
Dry Tropical	EMLO	0.43	-0.32	0.12	
	BETH	0.51	-0.28	0.22	
Mediterranean	MALM	0.59	-0.28	-0.42	-0.34
	GEOA	0.47	-0.22	-0.05	-0.01
	WORC	0.50	0.02	-0.21	-0.16

5.2 Frequency, time-frequency domain decomposition results

5.2.1 FFT displacement time series decomposition

Decomposing the vertical component displacement time series of cGPS stations in southern Africa using the FFT, it is observed that most of the displacement time series are dominantly composed of an annual and a semi-annual displacement component (Figure 5.3 and appendix D). The annual frequency component is of higher power compared to the semi-annual frequency component, it is often one order of magnitude greater than the semi-annual component. For example, the average annual displacement component power in the Desert, Sahelian and Mediterranean climatic zones are 0.0185, 0.0133, and 0.0191 respectively. The corresponding semi-annual component power values are 0.0032, 0.0035, and 0.0034 respectively. Although, at cGPS stations EMLO, GEOA, UMTA, CPNT, WELK, and NSPT, the order of magnitude of the annual component is the same as that of the semi-annual component, this being largely because the power of the annual component is low at these stations (Table 5). In time series from stations MALM, ULDI, UMTA, and GREY (cGPS station GREY is in appendix D) the semi-annual component appears to be embedded in noise, i.e., have equal spectral power as noise in the time series, or non-existent.

The power of the displacement time series is observed to vary systematically moving from one climatic zone to another (Figure 5.3; Table 5). The power of the annual displacement component is higher in time series from stations located in the Desert climatic zone (SBOK, PSKA and KMAN); lower in time series from stations located in the Wet and Dry Tropical climatic zones (GREY, UMTA, ULDI, EMLO, NSPT and NYLS); and varies a lot in cGPS stations located in the Mediterranean climatic zone (Table 5). This implies that seasonal annual displacement is greater in cGPS stations located in the Desert climatic zone than those in the Sahelian, Wet and Dry Tropical climatic zones. The power of the semi-annual component is higher in time series from cGPS stations located in the Desert, Sahelian, Dry Tropical climatic zones (SBOK, PSKA, MFKG, BETH, and DEAR); low in time series from stations located in the Wet Tropical climatic zone (GEOA, GREY, ULDI, UMTA, and EMLO) and highly variable in stations located in the Mediterranean climatic zone (Figure 5.3; Table 5).

Spectral averaging is also a common feature of the displacement time series, more so in time series from cGPS stations GREY, MALM, IXOP and ULDI (Figure 5.3). Spectral averaging is often an indicator of non-stationarity (i.e., varying frequency) in a time series; it may be an

indication of non-stationarity in the processes responsible for the seasonal deformation observed in the cGPS time series.

5.2.2 WT displacement time series decomposition

Wavelet transform (WT) analysis is conducted to map transient features, and the fluctuating energy and phase of the seasonal deformation cycles observed in the cGPS time series. Plotting the real part of the Continuous Wavelet Transform (CWT) of the displacement time series shows the frequencies embedded in the time series, and how their phase and power vary over the observation period (Figure 5.4 and appendix D). Some of the characteristic CWT features observed in the plots are the exaggeration of low frequencies, suppression of high frequencies, and component frequency overlap.

Like the FFT decomposition displacement spectra, the CWT spectra reveal the presence of dominant seasonal annual and semi-annual components in most of the displacement time series. The observed deformation components are characterised by good time localisation, spectral distortion (mainly at cGPS stations MALM, IXOP, GREY, ULDI, NSPT, CPNT and EMLO), frequency and energy variation over the observation period (mainly at cGPS station BETH, DEAR, EMLO, GREY, KLEY and KMAN) (Figure 5.4 and appendix D). The large frequency overlap, especially at low frequencies (e.g., the annual seasonal cycle at most of the stations overlaps over a frequency range of greater than 0.61 to less than 1.8 cpy), is due to the very good cycle time localisation characteristic of the CWT spectra. It is important to note that, according to the uncertainty principle, it is impossible to obtain precise frequency and time measurements when frequency and time parameters are measured simultaneously. When the time localisation is good, the frequency localisation will be poor and vice versa.

In some of the time series (e.g., EMLO, PSKA, MALM, ULDI, and WORC), the semi-annual cycle is not clearly delineated partly because 1) the component has low energy, and 2) merging of the semi-annual component with the annual cycle through spectral averaging. In most of the decomposed time series, the frequency and power of the annual and semi-annual cycles vary slightly over the observation period (e.g., BETH, DEAR, GEOA, EMLO, GREY, PSKA, MFKG, SBOK), which is expected for real signals, and most of the variation occurs in the annual signal (Figure 5.4 and appendix D).

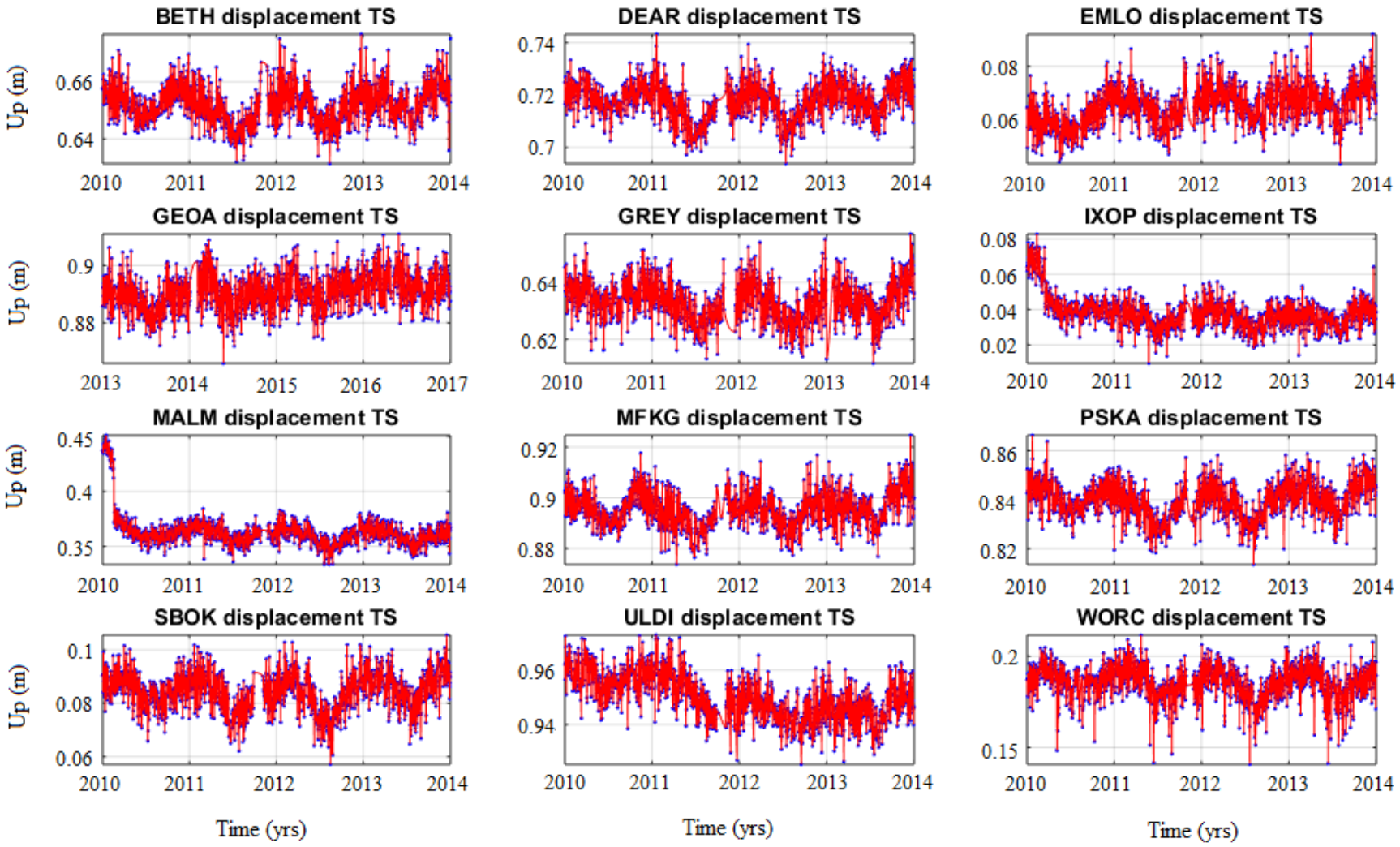


Figure 5.2: Daily position vertical component cGPS surface displacement time series. The blue points in the cGPS time series plots are the original data points and the red continuous line is the cubic Hermite interpolated time series.

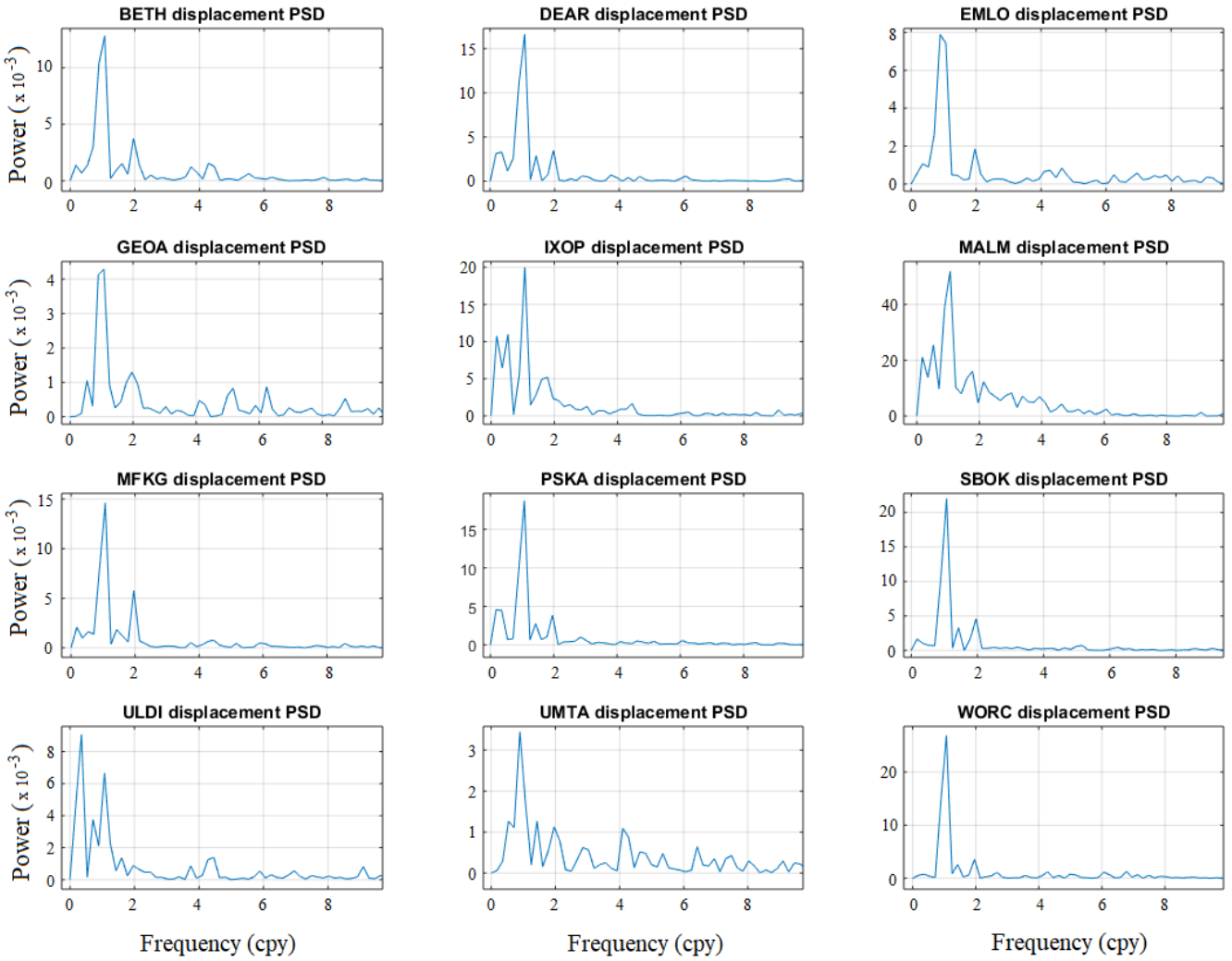


Figure 5.3: Daily position cGPS vertical (up) displacement component time series Fast Fourier Transforms (FFT) Power Spectral Density (PSD) spectra of the time series in Figure 5.2.

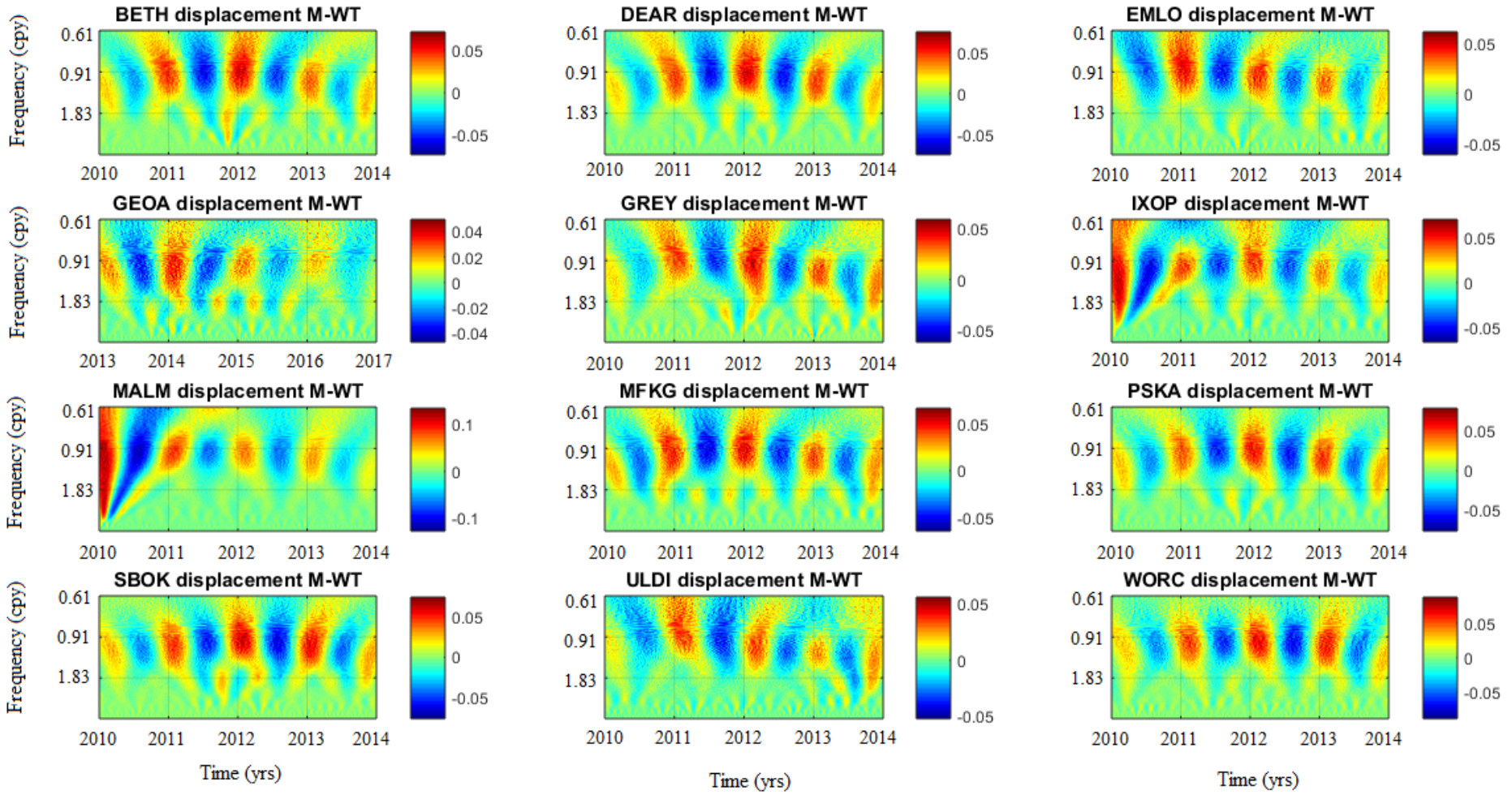


Figure 5.4: Morlet continuous wavelet transform (CWT) spectra of the daily position cGPS vertical displacement component time series in Figure 5.2. The colour bar shows the variation of the CWT coefficients as a function of frequency and time. The bright red indicates a positive amplitude and the dark blue indicates a negative amplitude.

5.2.3 FFT meteorological time series decomposition

5.2.3.1 Temperature time series decomposition

Converting surface air temperature time series into the frequency domain using the FFT reveals that, like the displacement time series, most of the temperature time series are composed of a dominant seasonal annual and semi-annual component (Figure 5.5 and Figure 5.9). The annual temperature component is two to three orders of magnitude greater than the semi-annual temperature component. The energy of the annual and semi-annual seasonal components also varies geographically, from one climatic zone to another (Table 5). Annual surface air temperature fluctuations are observed to be higher in time series located in the Desert and Sahelian climatic zones (PSKA, SBOK, DEAR, and MFKG) and low in time series located in the Mediterranean, Dry and Wet tropical climatic zones (GEOA, ULDI, UMTA, EMLO, and GREY). The average annual surface air temperature fluctuation power in time series located in the Desert, Sahelian, Dry tropical, Mediterranean, and Wet tropical climatic zones are 26780, 21203, 15358, 13042, and 11933 respectively (Table 5).

This means that annual seasonal surface air temperature variation is more definite in the Desert and Sahelian climatic zones than in the Mediterranean, Dry Tropical, and Wet Tropical climatic zones. Which is consistent with known information, i.e., subtropical desert climatic regions experience large temperature fluctuations, usually extreme hot summer and cold winter periods (Walsberg, 2000; Rutherford et al., 2006; Barry and Chorley, 2010, p. 484), and Tropical climatic regions generally experience moderate to small temperature fluctuations, except during tropical storms (Barry and Chorley, 2010, p. 327). The observed geographical dependent temperature variations are analogous to those of the cGPS surface displacement time series (Table 5). Most of the temperature FFT spectra are characterised by low levels of noise (largely clean frequency spectra) and low to no spectral averaging (Figure 5.9). However, the semi-annual temperature component is observed to be non-existent in temperature time series from stations located in the Mediterranean climatic zone (GEOA, MALM, and WORC).

5.2.3.2 Pressure time series decomposition

Unlike the displacement and temperature time series, most of the pressure FFT spectra show that the pressure time series are composed of one dominant frequency component, i.e., the annual component (Figure 5.6 and Figure 5.10). Like the displacement and temperature time

series, the annual pressure component also varies geographically, from one climatic zone to another (Table 5). Annual atmospheric pressure fluctuations are observed to be higher in time series from stations located in the Desert and Mediterranean climatic zones (PSKA, SBOK, MALM, and GEOA), and low in time series from stations located in the Wet Tropical and Dry Tropical climatic zones (GREY, UMTA, ULDI, and EMLO). The average annual atmospheric pressure fluctuation power in the Desert, Mediterranean, Wet Tropical, and Dry Tropical climatic zones are 7329, 6854, 4196, and 1804 respectively (Table 5).

This means that annual seasonal atmospheric pressure fluctuations are higher in the Desert and Mediterranean climatic zones than in the Sahelian, Dry, and Wet Tropical climatic zones. The findings are consistent with known atmospheric pressure variation information for different climatic zones. That is, generally subtropical deserts are high atmospheric pressure zones caused by seasonal descending of hot and dry subtropical atmospheric air mass cells known as Hadley cells (Nicholson and Flohn, 1980; Bollasina and Nigam, 2010). Thus, the shift in atmospheric pressure corresponds with the presence and absence of the Intertropical Convergence Zone (ITCZ). Atmospheric pressure fluctuations are generally low in tropical climate regions, except during tropical storms (Barry and Chorley, 2010, p. 327). Furthermore, most of the pressure time series are characterised by low levels of noise (i.e. low variance at higher frequencies) and spectral averaging (Figure 5.10), except for time series from stations BETH, EMLO, and UMTA, which have small to moderate levels of noise at higher frequencies and spectral averaging. The spectral averaging at these stations might be associated with several processes, which might include thermally-induced pressure lows that often introduce a minor variance in seasonal processes in regions of high temperatures.

5.2.3.3 Rainfall time series decomposition

Decomposing rainfall time series using the FFT, it is observed that most of the rainfall time series are composed of one dominant seasonal component, i.e., the annual seasonal component (Figure 5.7 and Figure 5.11). The only exceptions are time series from stations BETH and MALM. In time series from these stations, the semi-annual component seems to be present but embedded in noise (Figure 5.11). The energy in the rainfall time series is also observed to vary geographically, from one climatic zone to another. Annual rainfall fluctuations are observed to be higher in time series from cGPS stations located in the Dry Tropical and Wet Tropical climatic zones (EMLO, BETH, GREY, IXOP, and ULDI), and low in time series from stations

located in the Desert climate (PSKA and SBOK). The average annual rainfall fluctuation power of the time series located in the Dry and Wet tropical climatic zones, and the Desert climatic zone are 2292, 1369, and 204 respectively (Table 5).

This means that annual seasonal rainfall fluctuation is higher in the Dry and Wet Tropical and the Sahelian climatic zone than in the Mediterranean and Desert climatic zones. This is consistent with known information, i.e., continental dry and wet tropical climatic zones are characterised by well-defined alternating high rainfall and dry seasons (Hepburn and Radloff, 1998, p. 273 & 276; Barry and Chorley, 2010, p. 387). The rainfall FFT spectra are also observed to be characterised by high levels of noise and spectral averaging (Figure 5.11).

5.2.3.4 Humidity time series decomposition

FFT spectra of humidity time series reveal that most of the humidity time series are composed of an annual and semi-annual frequency component, excluding time series from cGPS stations in the Wet Tropical climatic zone (GREY, IXOP, UMTA, and ULDI) (Figure 5.8 and Figure 5.12). The semi-annual component is observed to be non-existent in time series from stations located in the Wet Tropical climatic zone. The power of the humidity time series is also observed to vary geographically. Annual humidity fluctuations are observed to be higher in time series from stations located in the Sahelian, Desert, and Mediterranean climatic zones (DEAR, MFKG, PSKA, SBOK, MALM, and WORC) and low in time series from stations located in the Wet Tropical climatic zone (GREY, UMTA, IXOP, and ULDI). The average annual humidity fluctuation power of time series located in the Sahelian, Desert, Mediterranean, and Wet Tropical climatic zones are 99578, 91690, 53683, and 13479, respectively (Table 5).

This means that annual humidity fluctuations are higher in the Sahelian, Desert and Mediterranean climatic zones than in the Wet Tropical climatic zone. Well-defined seasonal humidity fluctuations in the Mediterranean climatic zone result from the prevalence of alternating seasonal hot, dry summer periods, and mild, wet winter periods (Hepburn and Radloff, 1998, p. 146 & 294; Barry and Chorley, 2010, p. 301). Generally, deserts are perceived as dry zones of low rainfall and humidity (Johnson, 2003; Wang and Jenkins, 2003). However, in a study conducted by Walsberg (2000) it was found that humidity fluctuation varies from one desert type to another and many subtropical deserts are characterised by high seasonal humidity fluctuation due to the seasonal influx of moist air from tropical regions. Considering

that southern Africa consists of subtropical deserts and the humidity fluctuations observed in the FFT spectra is high, it is also possible that the high seasonal humidity fluctuation is caused by a seasonal influx of moist air associated with the ITCZ. The humidity FFT spectra are also observed to be characterised by high levels of noise and spectral averaging, and the humidity fluctuation intensity in Desert and Mediterranean located stations is observed to vary a lot more (Figure 5.12).

5.2.4 WT meteorological time series decomposition

Similar to the FFT spectra, the CWT spectra of the meteorological processes (i.e., temperature, pressure, humidity, and rainfall) show that most of the analysed temperature and humidity time series are composed dominantly of a seasonal annual and semi-annual component (Figure 5.13 and Figure 5.16). Pressure and rainfall time series are composed dominantly of an annual component only (Figure 5.14 and Figure 5.15). In some of the pressure time series the semi-annual component seems to be present but is not continuous over the observation period, while in the rainfall time series, the semi-annual component seems to be non-existent at all (Figure 5.14). Over the duration of the observation period, the frequency and power of the meteorological time series are observed to have a considerably high degree of stationarity. Although, slight variations in the power and frequency of the seasonal components constituting the meteorological time series are observed. In some of the meteorological time series, the cyclic power variation is associated with spectral distortion (Figure 5.12, 5.13, 5.4 and 5.15). Spectral distortion and frequency variation are an indication of non-stationarity, i.e., change, in the meteorological processes over the observation period.

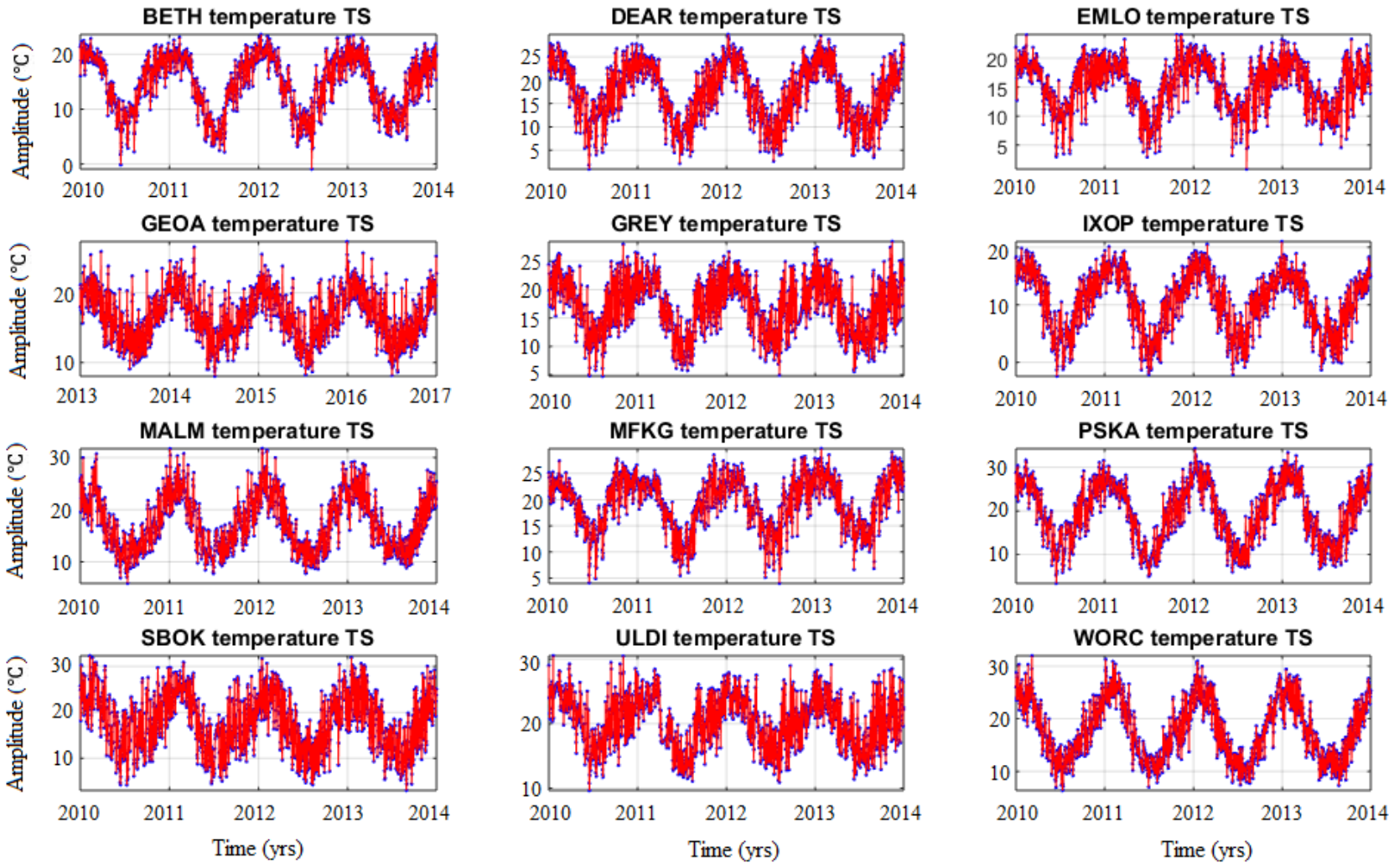


Figure 5.5: Average surface air temperature time series. The blue points in the cGPS time series plots are the original data points and the red continuous line is the cubic Hermite interpolated time series.

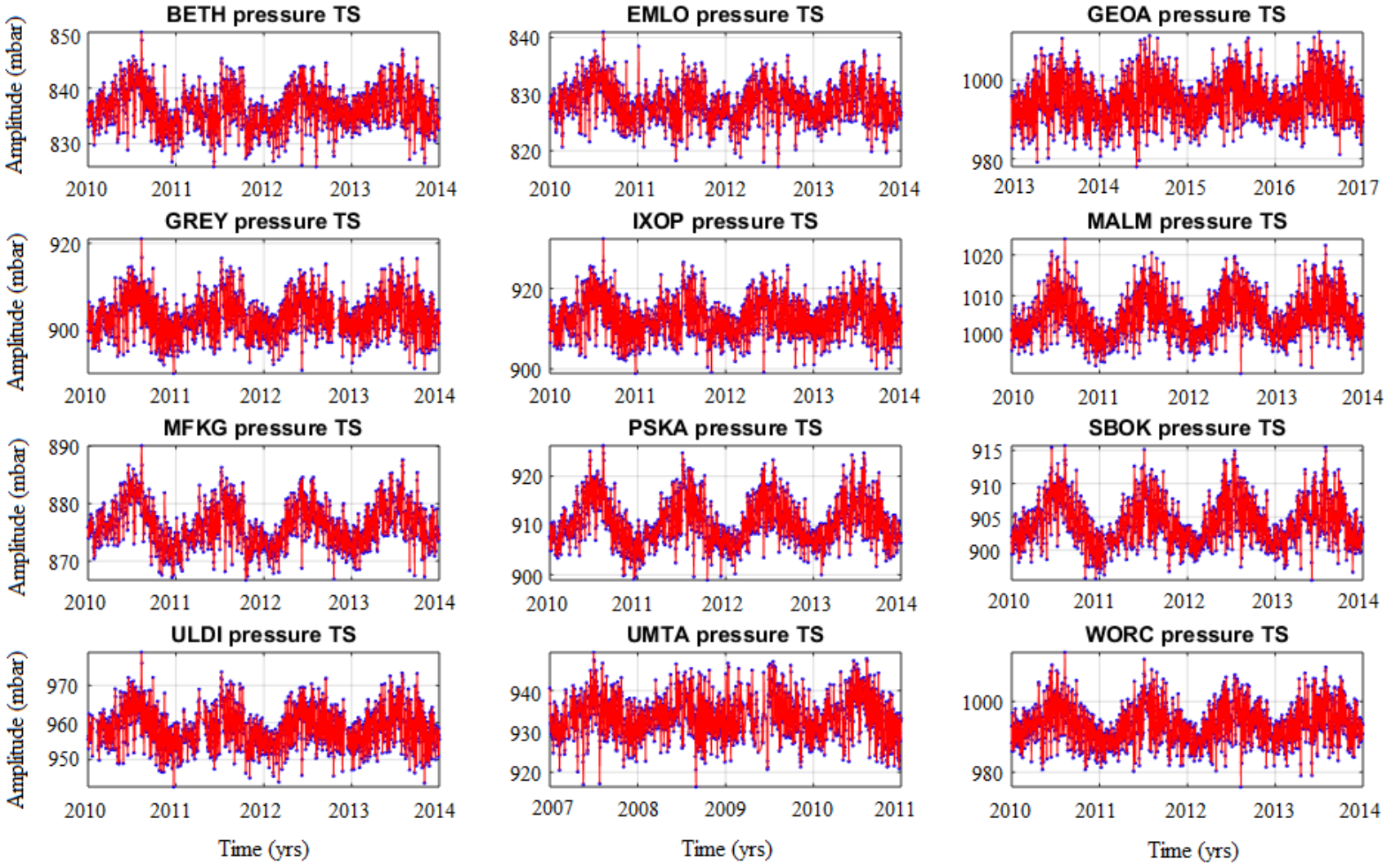


Figure 5.6: Atmospheric pressure time series. The blue points in the cGPS time series plots are the original data points and the red continuous line is the cubic Hermite interpolated time series.

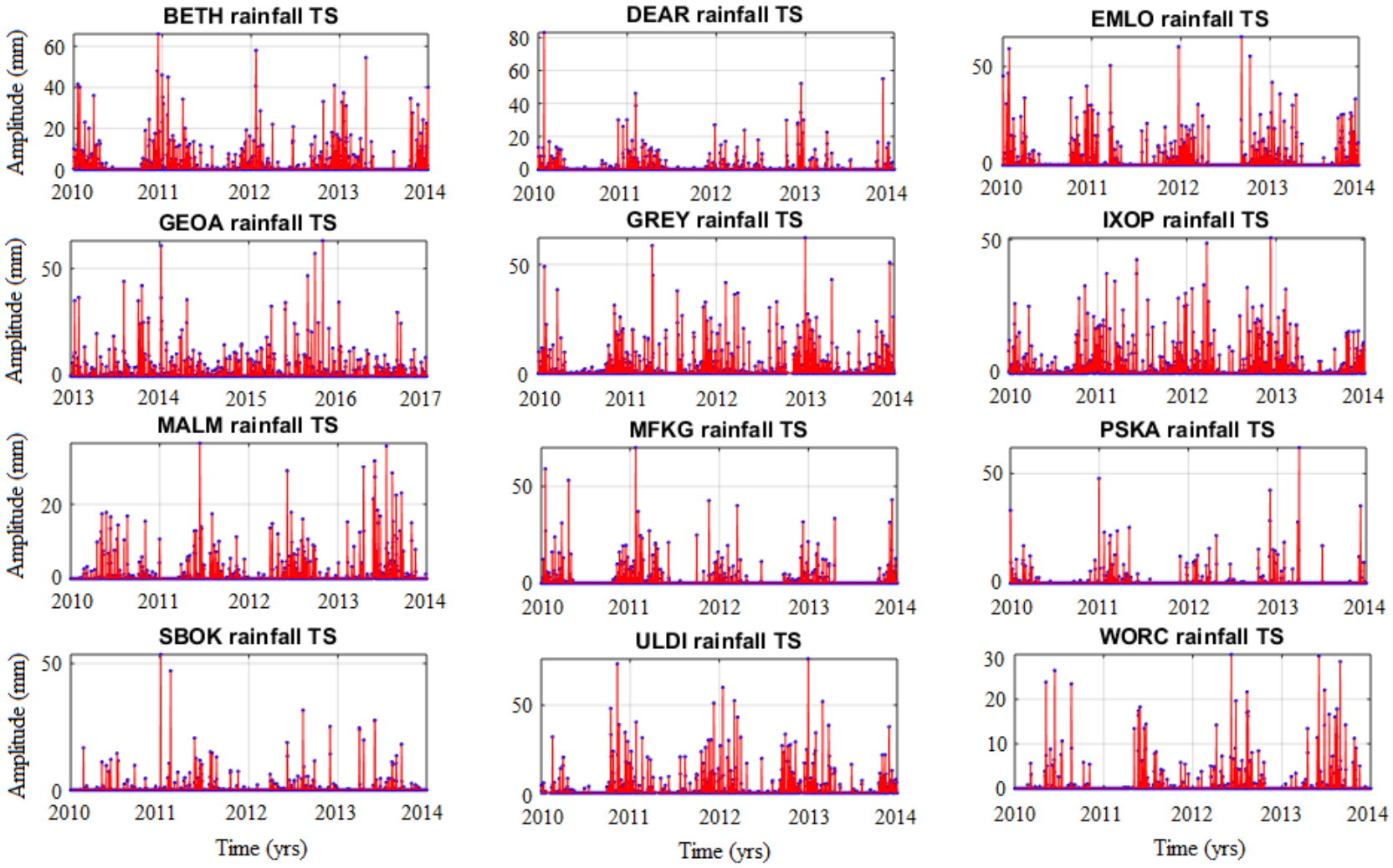


Figure 5.7: Rainfall time series. The blue points in the cGPS time series plots are the original data points and the red continuous line is the cubic Hermite interpolated time series.

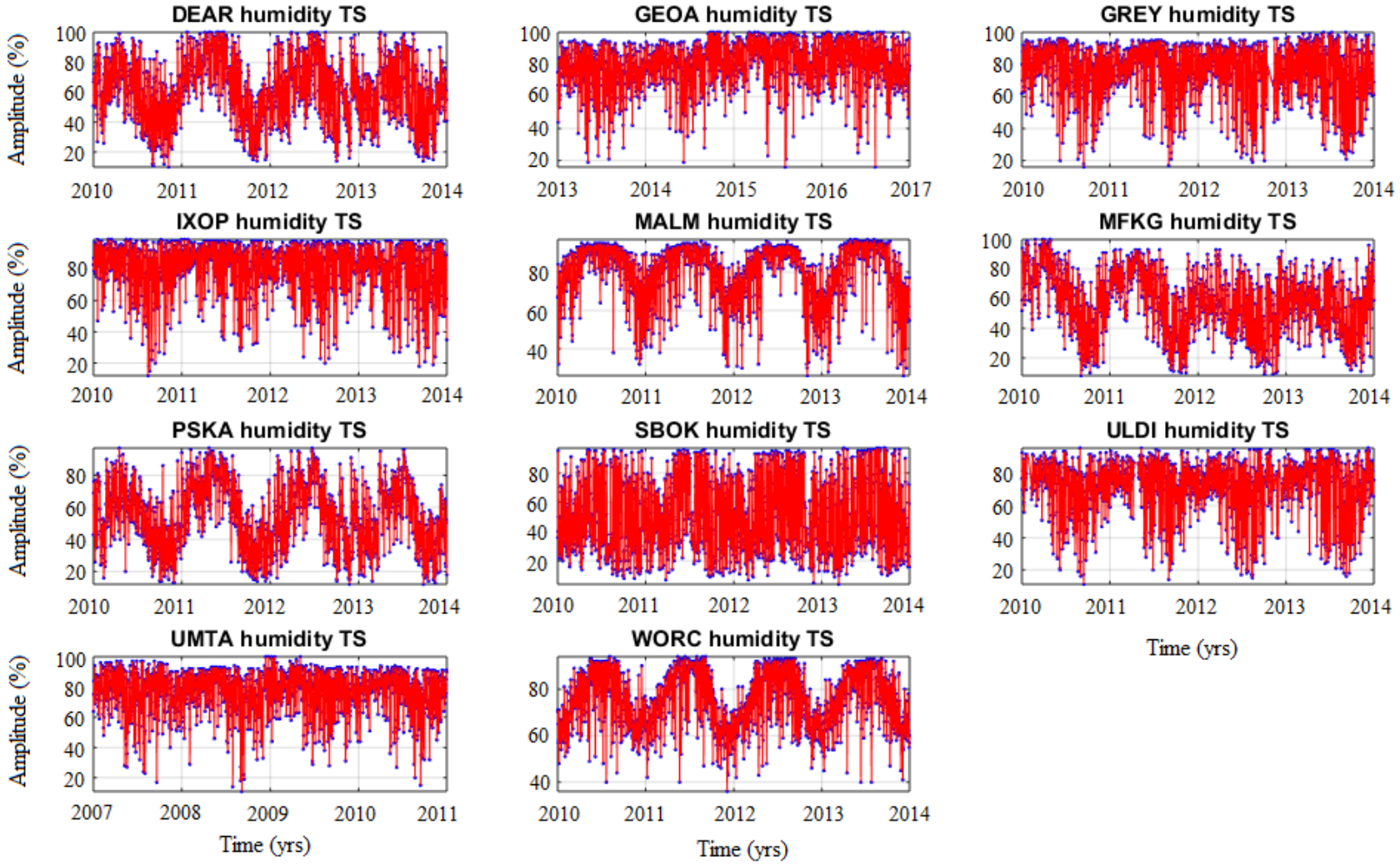


Figure 5.8: Humidity time series. The blue points in the cGPS time series plots are the original data points and the red continuous line is the cubic Hermite interpolated time series.

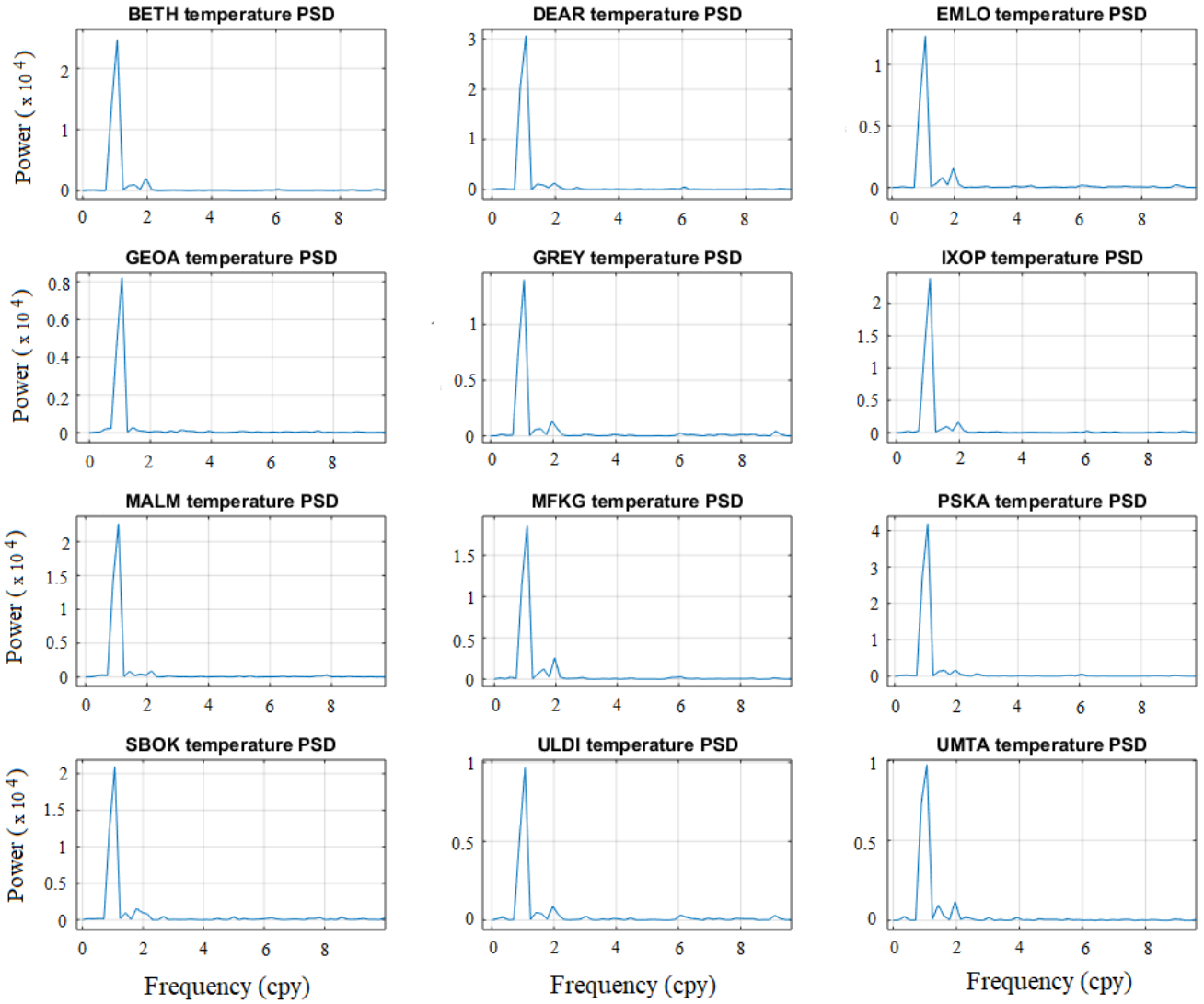


Figure 5.9: Surface air temperature Fast Fourier Transforms (FFT) Power Spectral Density (PSD) spectra of the time series in Figure 5.5.

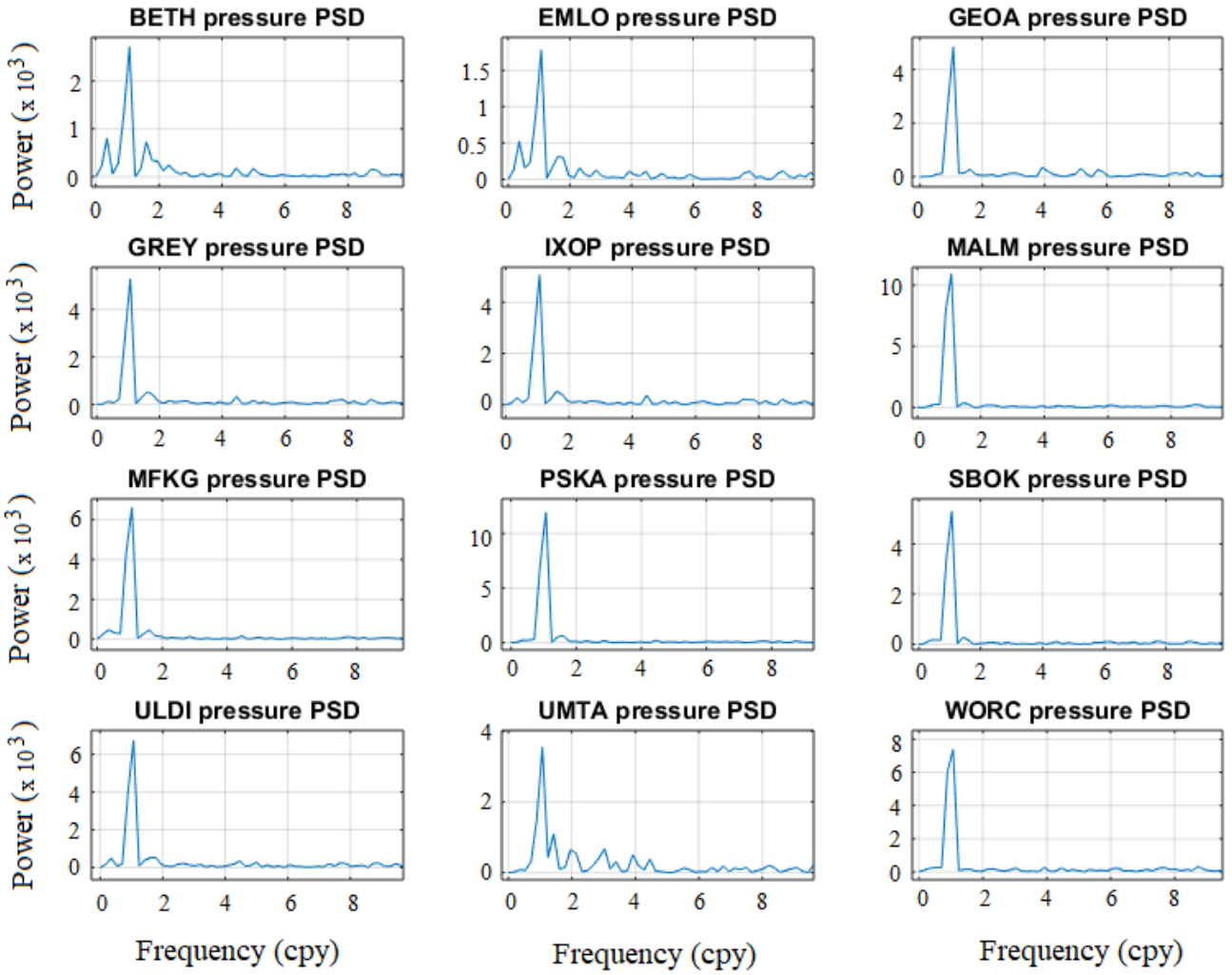


Figure 5.10: Atmospheric pressure time series Fast Fourier Transforms (FFT) Power Spectral Density (PSD) spectra of the time series in Figure 5.6.

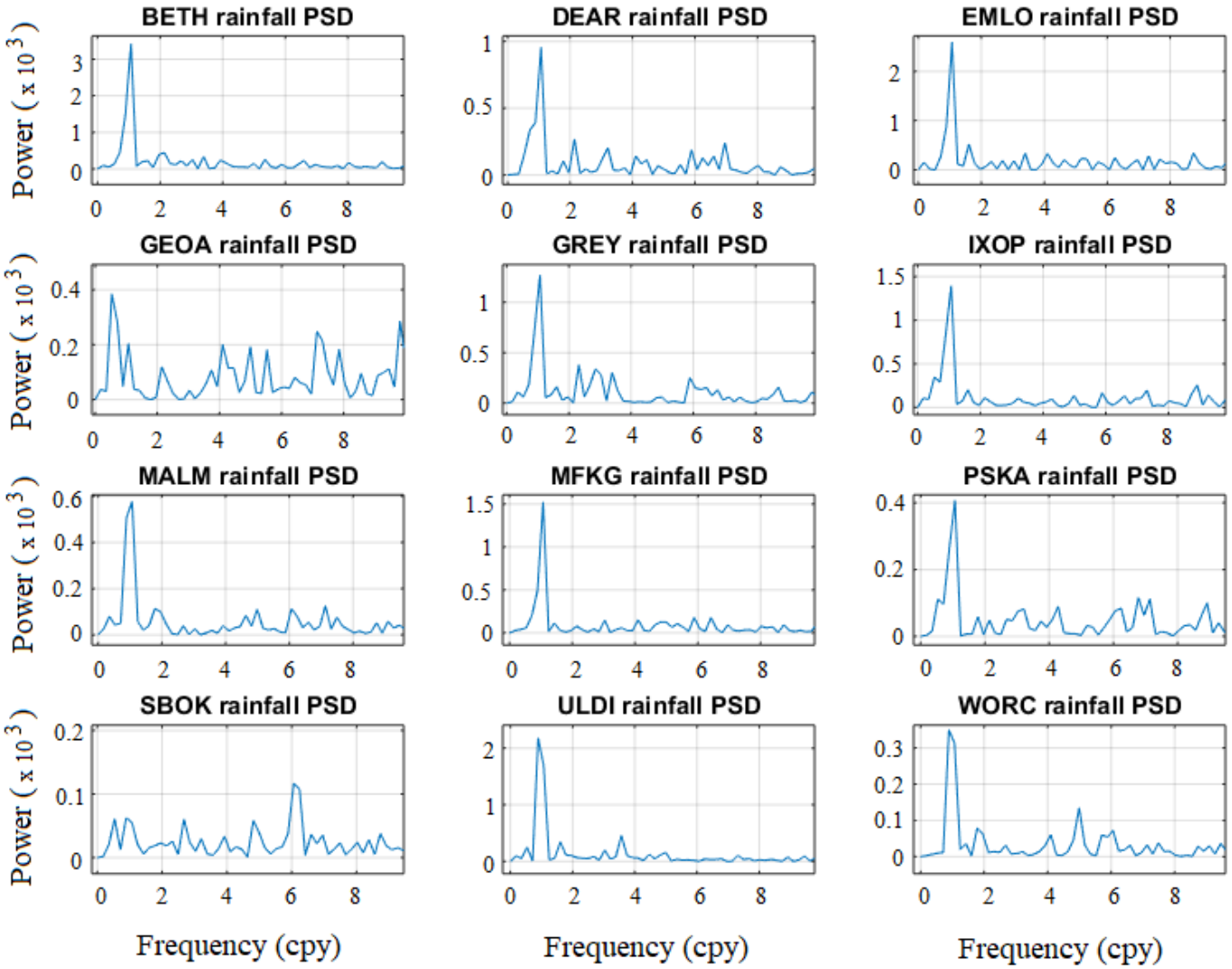


Figure 5.11: Rainfall time series Fast Fourier Transforms (FFT) Power Spectral Density (PSD) spectra of the time series in Figure 5.7.

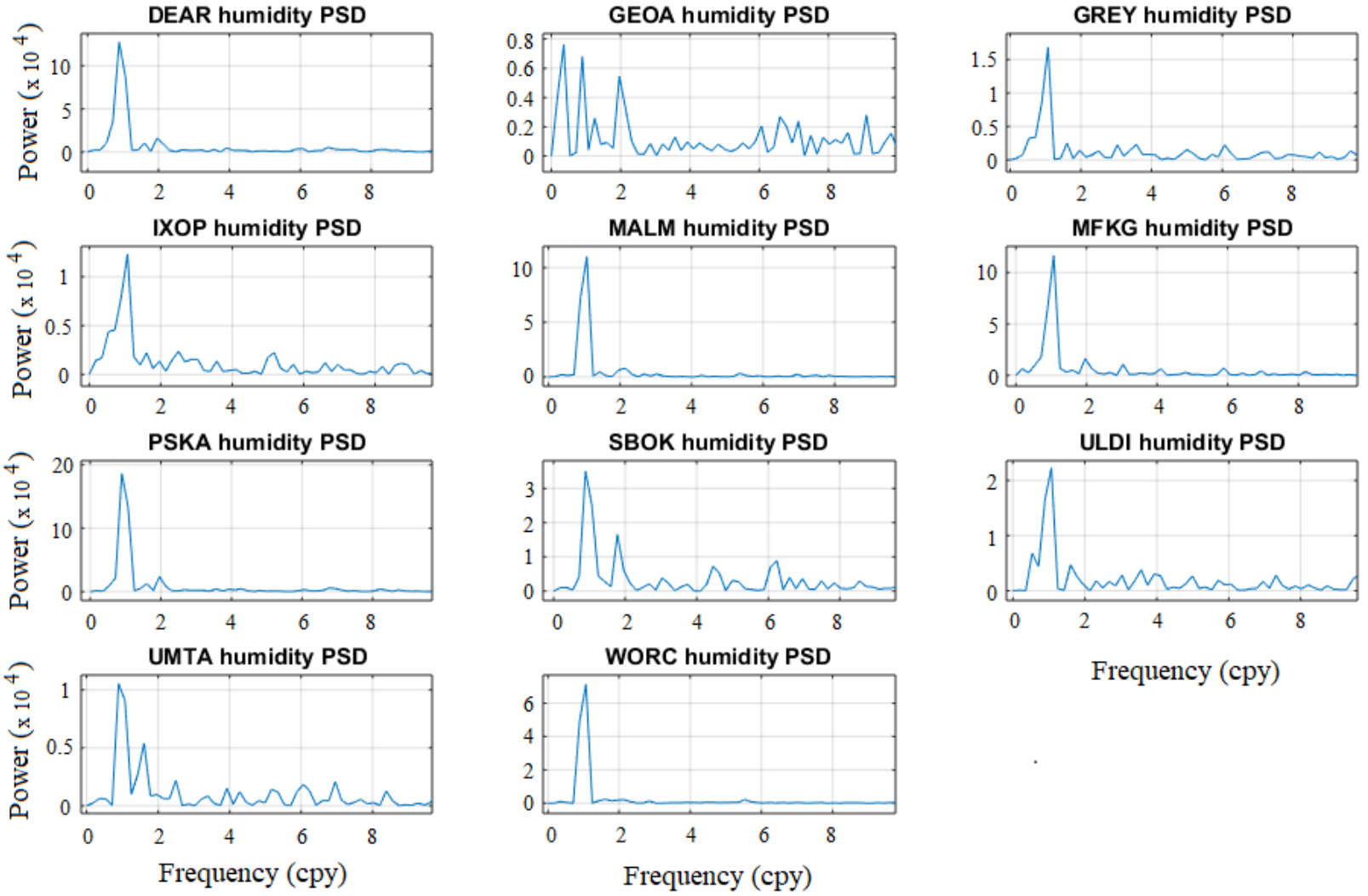


Figure 5.12: Humidity time series Fast Fourier Transforms (FFT) Power Spectral Density (PSD) spectra of the time series in Figure 5.8.

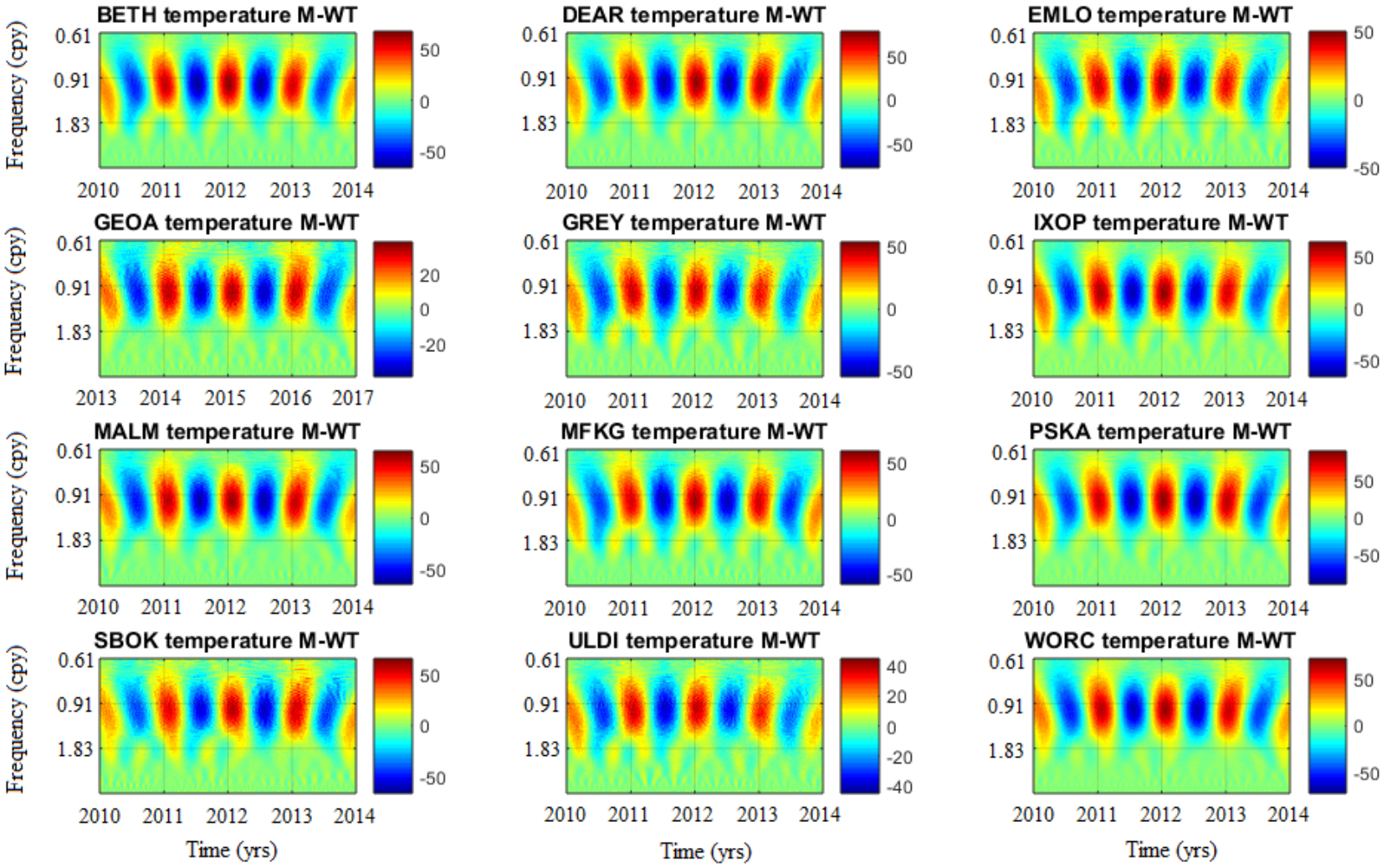


Figure 5.13: Surface air temperature time series Morlet continuous wavelet transform (CWT) of the time series in Figure 5.5. The colour bar shows the variation of the CWT coefficients as a function of frequency and time. The bright red indicates a positive amplitude and the dark blue indicates a negative amplitude.

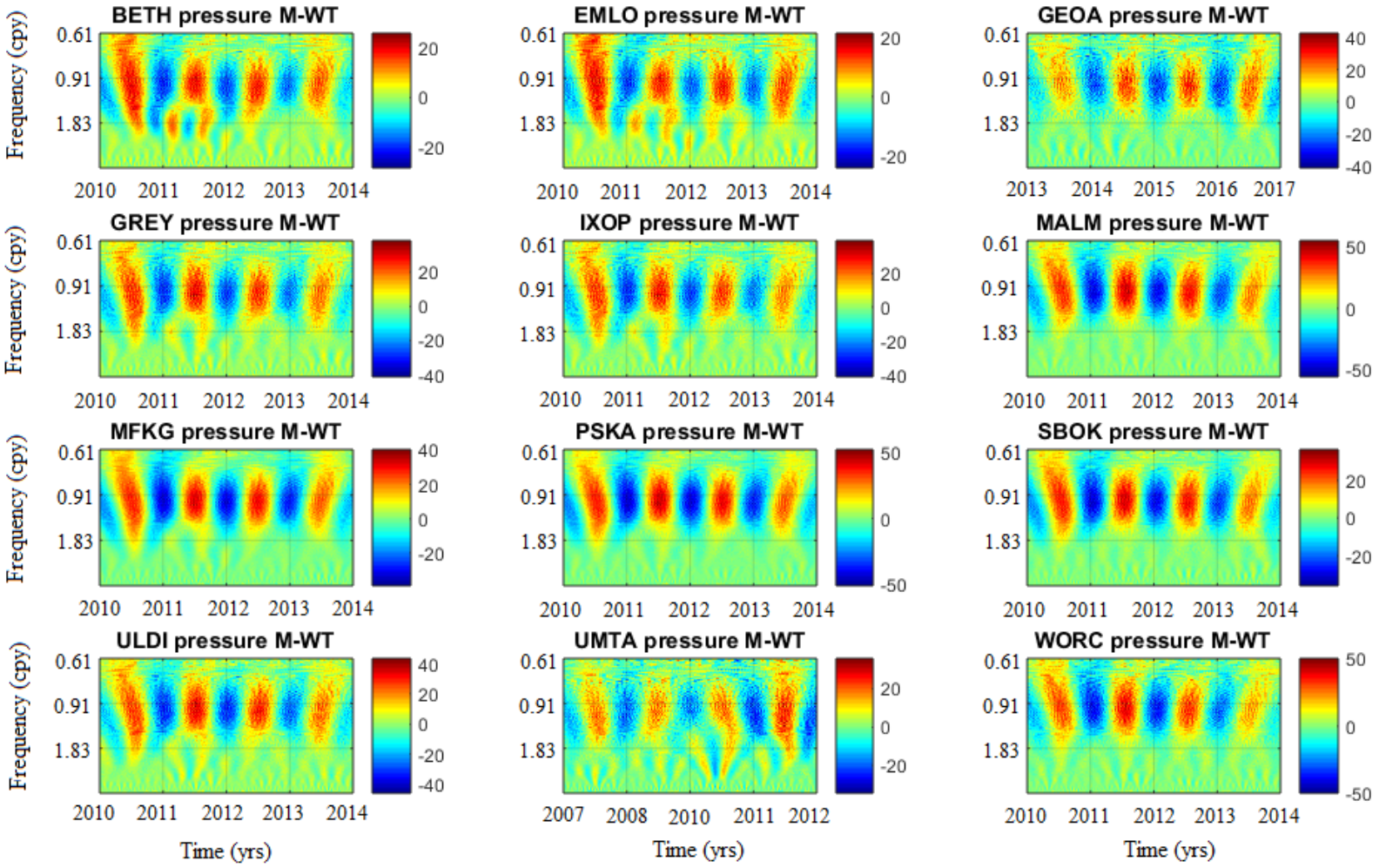


Figure 5.14: Atmospheric pressure time series Morlet continuous wavelet transform (CWT) of the time series in Figure 5.6. The colour bar shows the variation of the CWT coefficients as a function of frequency and time. The bright red indicates a positive amplitude and the dark blue indicates a negative amplitude.

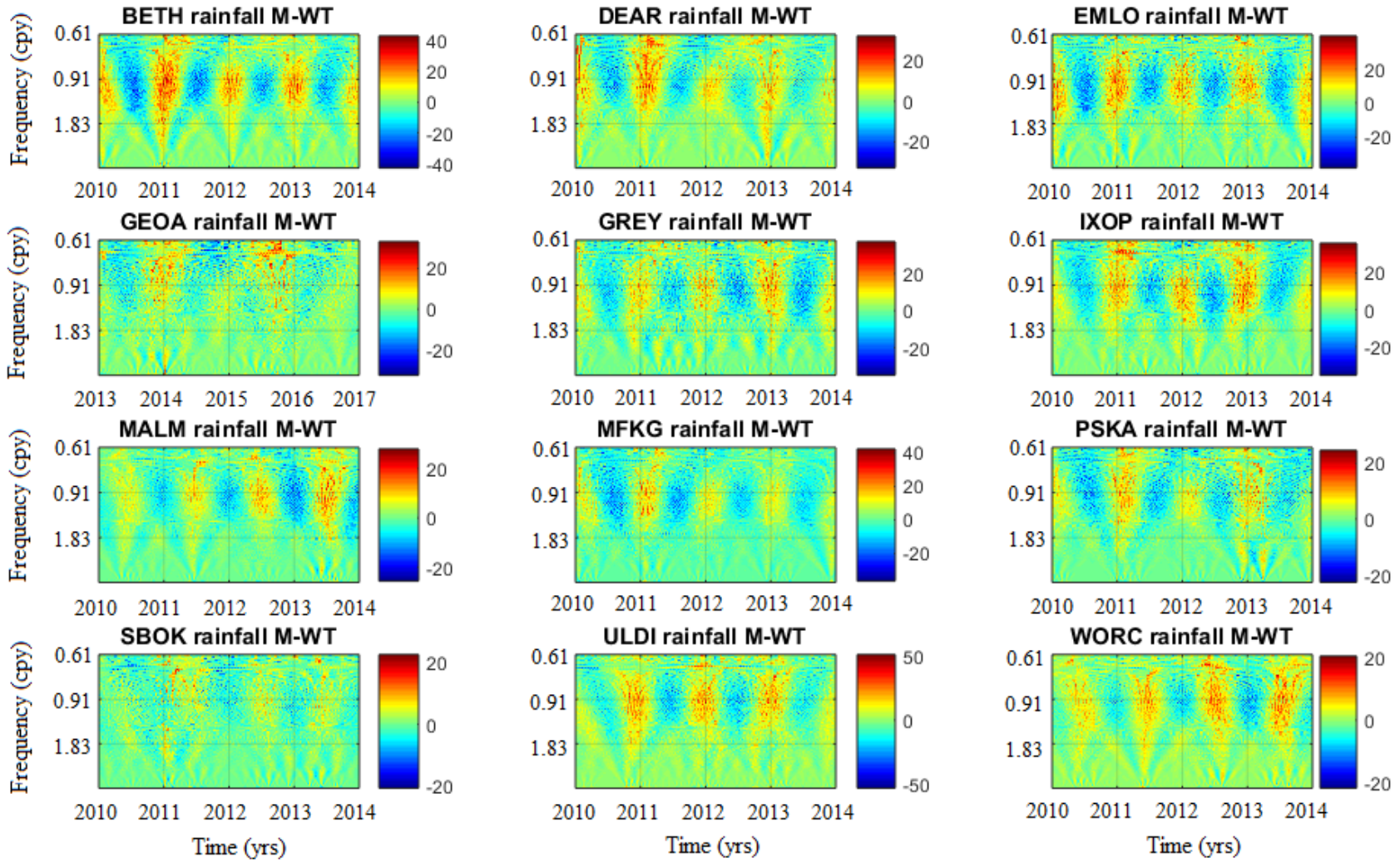


Figure 5.15: Rainfall time series Morlet continuous wavelet transform (CWT) of the time series in Figure 5.7. The colour bar shows the variation of the CWT coefficients as a function of frequency and time. The bright red indicates a positive amplitude and the dark blue indicates a negative amplitude.

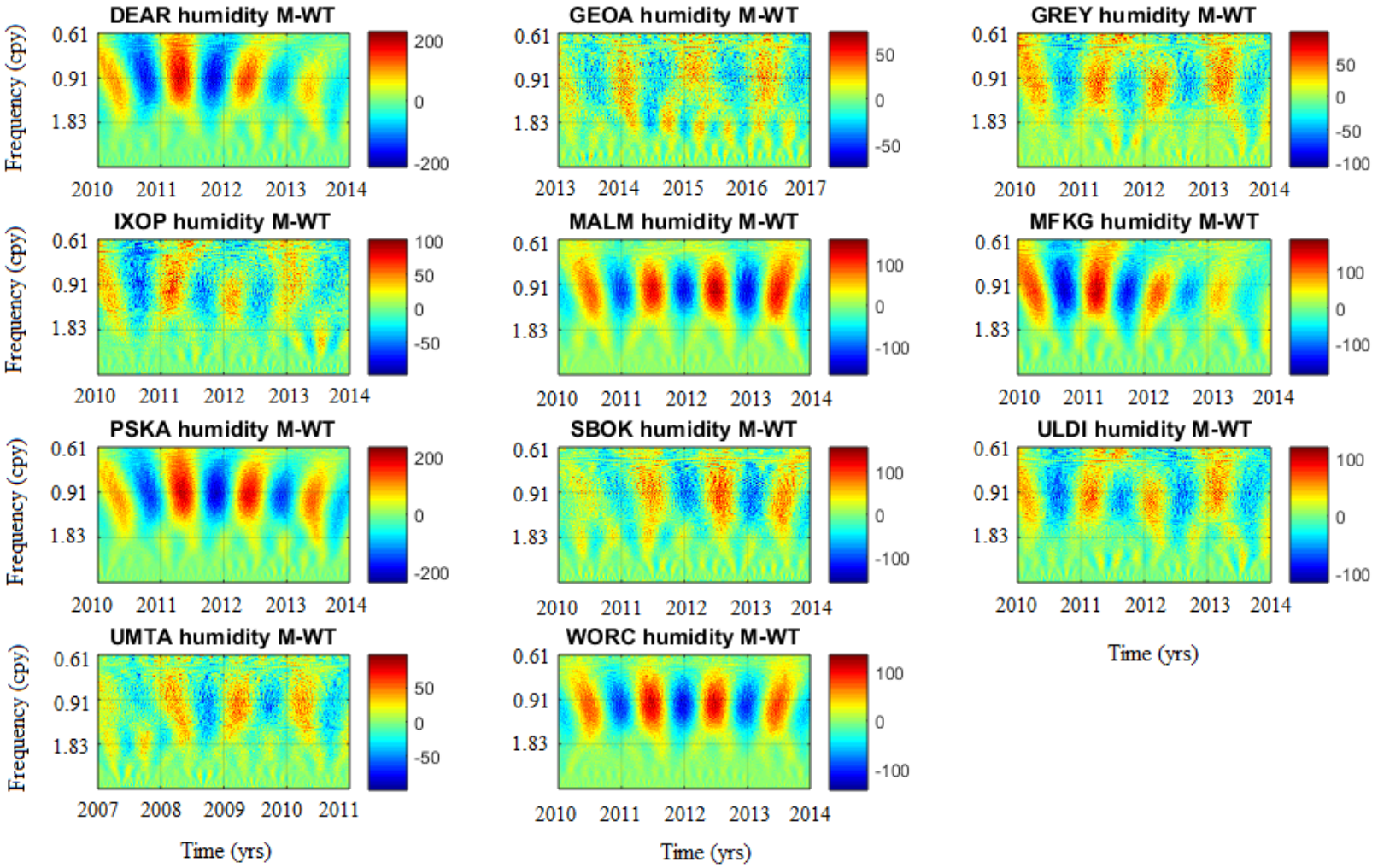


Figure 5.16: Humidity time series Morlet continuous wavelet transform (CWT) of the time series in Figure 5.8. The colour bar shows the variation of the CWT coefficients as a function of frequency and time. The bright red indicates a positive amplitude and the dark blue indicates a negative amplitude.

Table 5: Quantified power of the annual and semi-annual frequency components present in the cGPS displacement and meteorological time series as obtained from FFT. VC stands for Vertical Component.

Climatic Zones	GPS Station name	Annual and semi-annual power of the cGPS vertical component time series									
		Displacement-VC		Temperature		Pressure		Rainfall		Humidity	
		Annual	Semi-annual	Annual	Semi-annual	Annual	Semi-annual	Annual	Semi-annual	Annual	Semi-annual
Desert	PSKA	0.0155	0.0031	36021	1360	10098	101	350.7	14.2	154380	20240
	SBOK	0.0174	0.0036	17539	993	4560.5	29.5	58.1	22.3	29000	5235
	KMAN	0.0225	0.0029	-	-	-	-	-	-	-	-
Wet tropical	GREY	0.0078	0.0014	11577	1174	4281	111.3	1052.5	47.7	13597	1215
	UMTA	0.0025	0.0011	8794	926.4	2740.7	629.2			9656.3	905.3
	IXOP	0.0143	0.0023	19476	1349	4115.8	127.2	1169	43.3	10573	1131
	ULDI	0.0049	0.0008	7886	768	5645	131	1885.5	94.5	20085	845
	PMBG	0.0109	0.0031	-	-	-	-	-	-	-	-
Sahelian	DEAR	0.0146	0.0028	26648	1103			735	69.8	103010	14440
	MFKG	0.0121	0.0047	15758	2063	5709.4	107.9	1120	37.4	96145	14339
	KLEY	0.0189	0.0039	-	-	-	-	-	-	-	-
	WELK	0.0074	0.0026	-	-	-	-	-	-	-	-
Dry tropical	EMLO	0.0077	0.0018	10292	1277	1438.6	46.6	1921.3	22.8	-	-
	BETH	0.0119	0.0033	20424	1581	2169.8	277.7	2661.6	403.7	-	-
	NSPT	0.0066	0.0031	-	-	-	-	-	-	-	-
	NYLS	0.0098	0.0041	-	-	-	-	-	-	-	-
Mediterranean	MALM	0.0468	0.0063	19301	390	9728.5	61	548.5	87.67	95412	6597
	GEOA	0.0042	0.0012	6782	40.7	3989.7	51.4	142.7	31.3	2930.4	4990.3
	WORC	0.022	0.0028			6843.7	47.7	328.1	51.1	62707	1889
	CPNT	0.0035	0.0033	-	-	-	-	-	-	-	-

5.3 Correlation analysis using Cross-Spectral Density (CSD), coherence, phase and semblance spectral techniques

Presented below are quantitative and qualitative cross-spectral analysis results computed using the Cross-Spectral Density (CSD) and coherence methods. This section presents linear relation and correlation strength analysis results of cGPS displacement and meteorological time series computed in the frequency domain.

5.3.1 Correlation determination and quantification using CSD and coherence spectral techniques

Frequency domain spectral coherence and cross-spectrum correlation results of cGPS displacement and meteorological time series show that a correlation exists between the annual and semi-annual frequency components observed in the cGPS surface displacement and meteorological time series. Both the annual and semi-annual frequency components in displacement-temperature time series and displacement-humidity time series are correlated (Figure 5.17, Figure 5.20 and appendix B); whereas, the displacement-pressure time series and displacement-rainfall time series are only correlated at an annual scale (Figure 5.18, Figure 5.19 and appendix B).

The correlation strength of the annual frequency component in the displacement and meteorological time series is observed to be higher than that of the semi-annual frequency component in the time series (Table 6). The correlation strength of the semi-annual frequency component in the displacement-temperature, displacement-pressure, displacement-rainfall and displacement-humidity time series, varies a lot more compared to the correlation strength of the annual frequency component in the time series. The average standard deviation of the semi-annual frequency component spectral correlation strength is 0.20, 0.27, 0.32 and 0.31 for displacement-temperature, displacement-pressure, displacement-rainfall and displacement-humidity time series, respectively. The corresponding average standard deviation correlation strength of the annual frequency component in the cGPS displacement and meteorological time series is 0.07, 0.08, 0.16 and 0.18, respectively (Table 6). It is assumed that there is a relationship between the seasonal surface displacement fluctuations observed in cGPS measurements and the local meteorological measurements. There is a low scatter and high spectral correlation strength between the annual components in the displacement and meteorological time series, compared to the scatter and correlation strength of the semi-annual

components. Indications that there is a stronger dependence relation between annual displacement and annual meteorological cyclic processes than between the semi-annual displacement and semi-annual meteorological cyclic processes.

Table 6: Coherence correlation strength of displacement vs meteorological (average temperature, pressure, rainfall and humidity) processes.

Climatic Zones	GPS Station name	Coherence spectral correlation (vertical component of displacement vs atmospheric processes)							
		Temperature		Pressure		Rainfall		Humidity	
		Annual	Semi-annual	Annual	Semi-annual	Annual	Semi-annual	Annual	Semi-annual
Desert	PSKA	0.92	0.90	0.89	0.24	0.75	0.31	0.99	
	SBOK	0.99	0.56	0.95	0.13	0.42	0.30	0.91	0.36
Wet Tropical	GREY	0.75	0.58	0.70	0.11	0.60	0.24	0.44	0.41
	UMTA	0.95	0.86	0.93	0.73			0.72	0.68
	IXOP	0.84	0.73	0.80	0.39	0.78	0.18	0.59	0.52
	ULDI	0.89	0.65	0.86	0.76	0.92	0.95	0.72	0.40
Sahelian	DEAR	0.91	0.73			0.75	0.35	0.97	0.97
	MFKG	0.92	0.96	0.87	0.42	0.73	0.97	0.78	0.86
Dry Tropical	EMLO	0.89	0.79	0.86	0.13	0.88	0.03		
	BETH	0.90	0.84	0.87	0.28	0.77	0.81		
Mediterranean	MALM	0.99	0.21	0.98	0.59	0.98	0.31	0.99	0.08
	GEOA	0.87	0.85	0.83	0.88	0.77	0.37	0.79	0.94
	WORC	0.99	0.86	0.98	0.19	0.99	0.72	1.00	0.92
Annual average		0.91		0.88		0.76		0.81	
Semi-annual Average			0.72		0.40		0.44		0.61
STD annual		0.07		0.08		0.16		0.18	
STD semi-annual			0.20		0.27		0.32		0.31

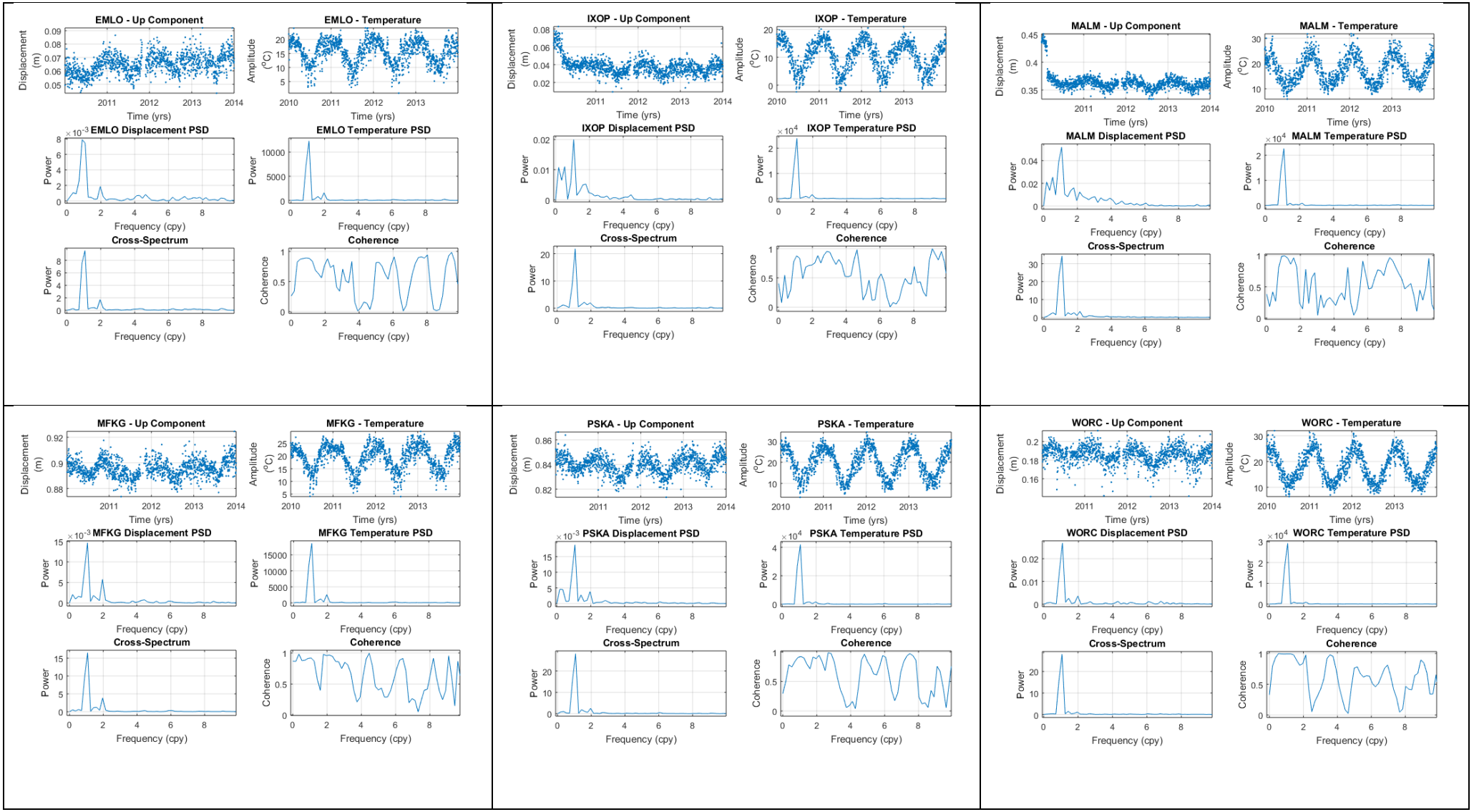


Figure 5.17: Cross-spectrum and coherence correlation plots of cGPS displacement (m) vs average temperature (℃) time series.

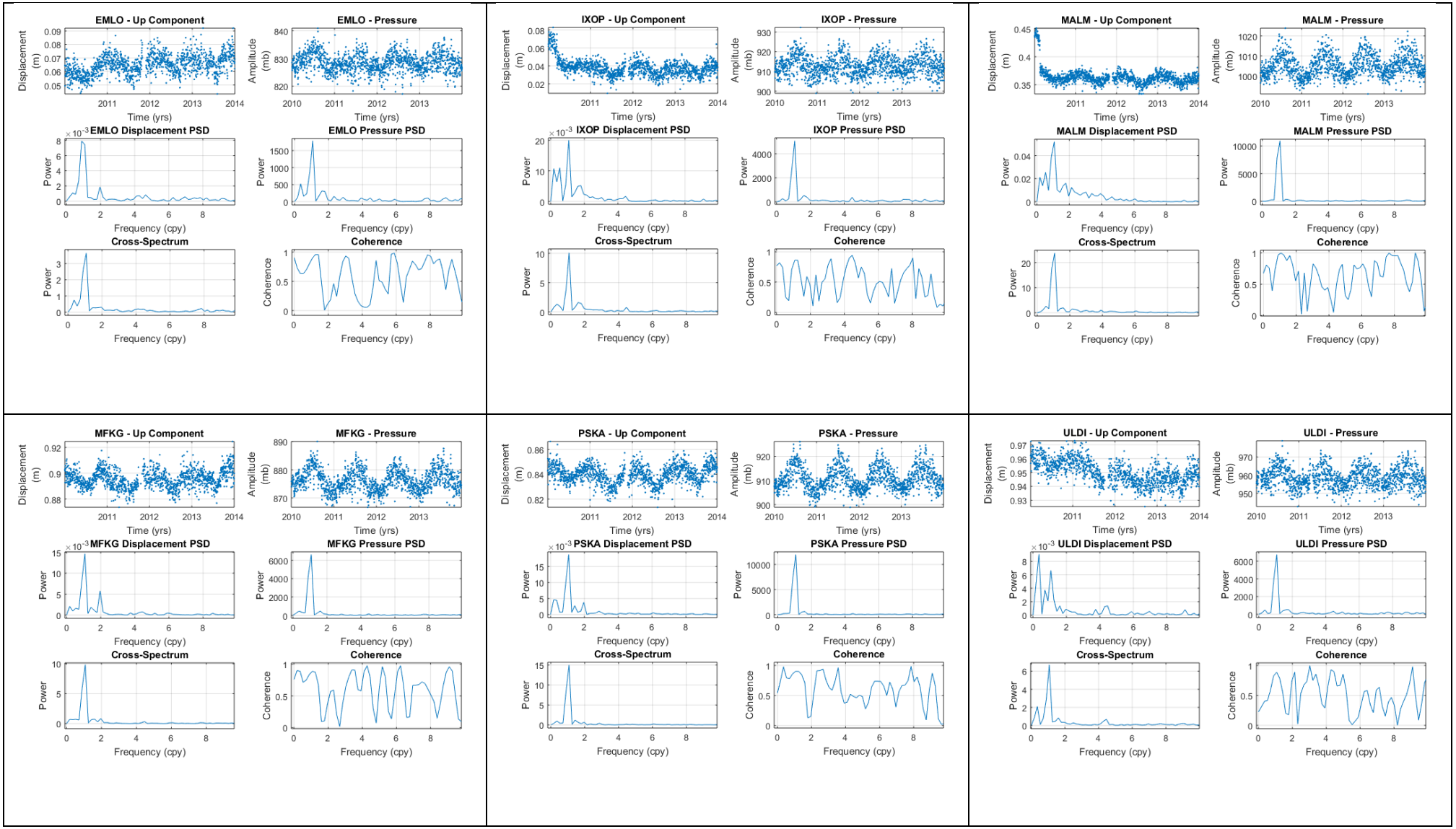


Figure 5.18: Cross-spectrum and coherence correlation plots of cGPS displacement (m) vs pressure (mbar) time series.

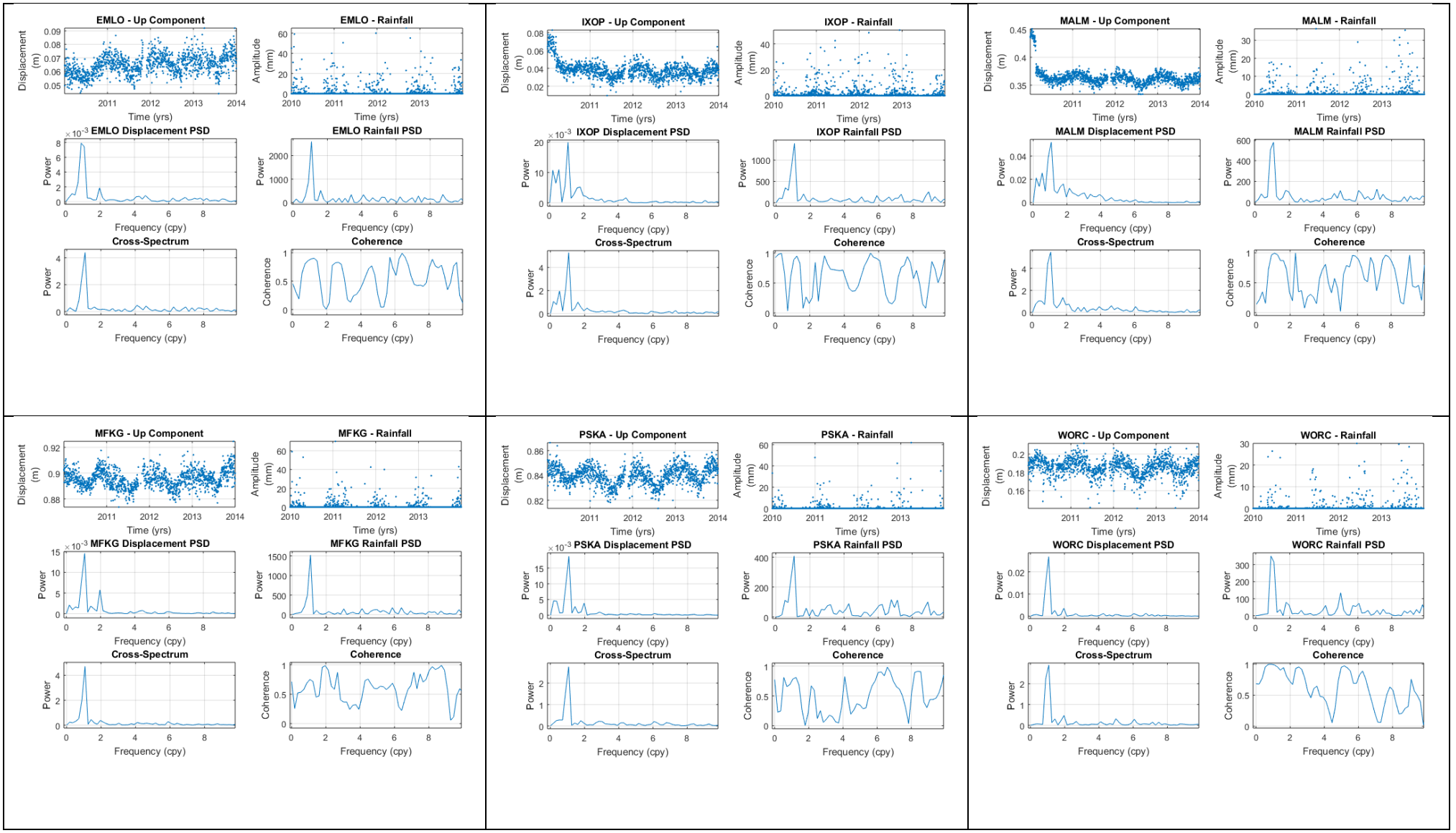


Figure 5.19: Cross-spectrum and coherence correlation plots of cGPS displacement (m) vs rainfall (mm) time series.

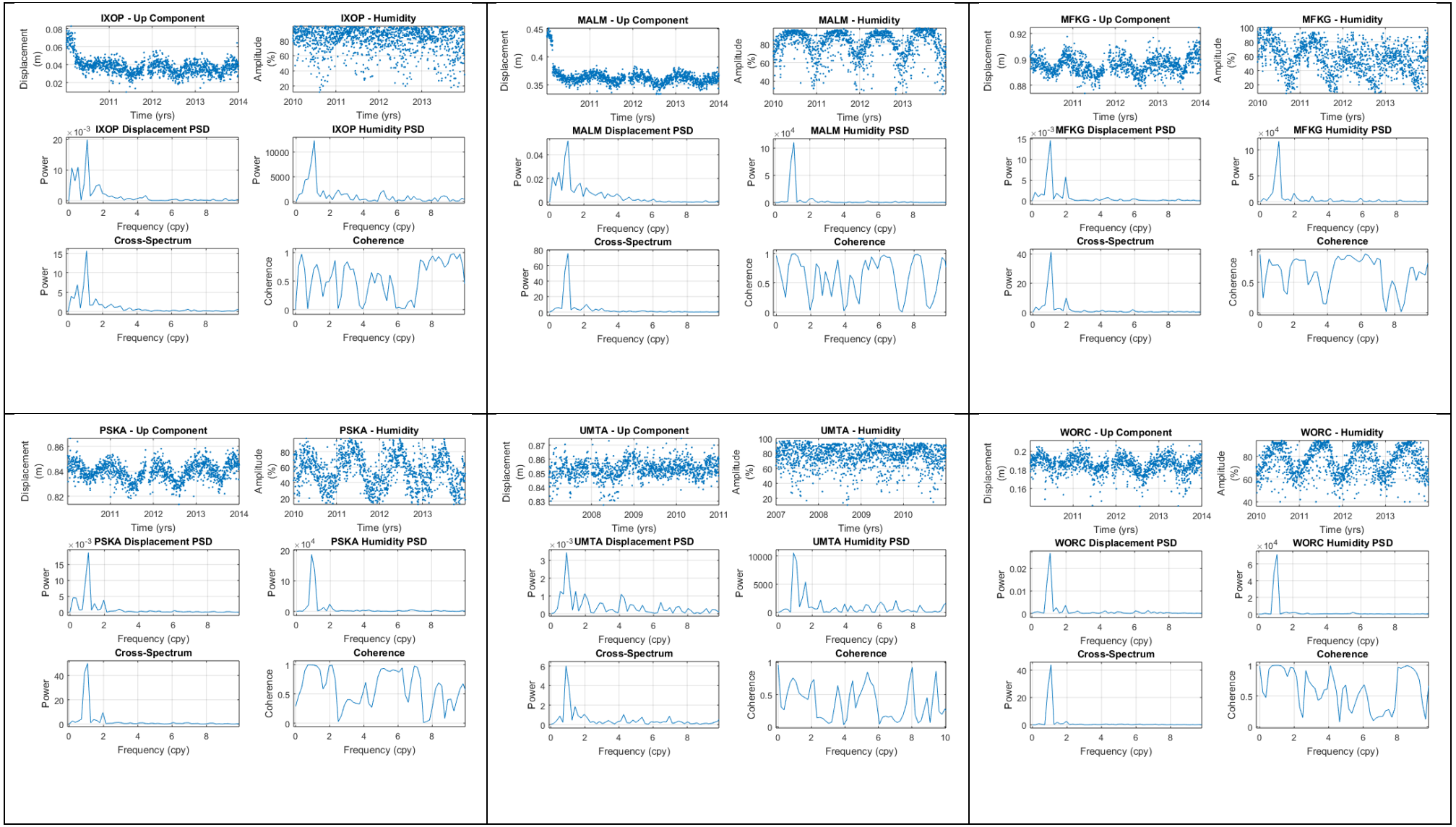


Figure 5.20: Cross-spectrum and coherence correlation plots of cGPS displacement (m) vs humidity (%) time series.

From the cross-spectrum and coherence results, it is frequently observed that the Power Spectral Density (PSD) spectrum of temperature time series is the most similar to that of the cGPS surface displacement time series compared to the PSD spectra of the other meteorological processes (Figure 5.17 and Table 6). Both processes are characterised by annual and semi-annual signal, with low noise levels (low variance at higher frequencies) in most cases and have similar oscillation patterns in the time domain. The coherence spectrum shows a high average linear correlation strength between the annual and semi-annual cycles in the displacement and temperature time series of 0.91 and 0.72 respectively (Figure 5.17 and Table 6); while, slight fluctuations in the correlation strength of the annual and semi-annual cycles are observed to occur moving across the different climatic zones (Table 6).

The correlation between the pressure and displacement time series is observed to exist only at a frequency of 1 cpy (Figure 5.18). The average correlation strength of the annual cycle between these processes is 0.88, second only to that of the displacement-temperature time series (Table 6). The semi-annual cycle average correlation strength between these processes is at a low of 0.40 (Table 6), which is not surprising, considering that the semi-annual cycle is observed to be largely non-existent in the FFT spectra of the pressure time series. The annual cycle correlation strength between these processes is also observed to be roughly the same across all the climatic zones (Table 6).

The correlation between rainfall and surface displacement time series is largely observed to exist at a frequency of 1 cpy (Figure 5.19). The average spectral correlation strength between the annual and semi-annual cycles are 0.76 for the former and 0.44 for the later (Table 6). The moderate annual linear correlation between the two processes is expected since most parts of southern Africa are characterised by one rainfall season in a year. The annual correlation strength of the rainfall-displacement time series varies across the climatic zones. It is highest in the Mediterranean climatic zone, where it is defined by an average values of 0.9, and lowest in the Desert climatic zone, where it is defined by an average value of (0.59) (Table 6).

Similar to the temperature time series, the humidity time series are correlated to the displacement time series at frequencies of 1 and 2 cpy (Figure 5.20). The average spectral correlation strength at these frequencies is 0.81 and 0.61, respectively (Table 6). The correlation strength of the annual cycle is observed to be lower for stations in the Wet Tropical climatic zone (average value of 0.62) and higher for stations in the Desert climatic zone (0.95).

The Semi-annual cycle correlation strength is lower in the Desert climatic zones and higher in the Sahelian and Mediterranean climatic zones (Table 6).

The above findings suggest that all the considered meteorological processes have a direct influence in the seasonal deformation observed in GPS position time series. Because of the high temperature-displacement linear correlation, at both annual and semi-annual periods, and low spectral correlation strength variation, thermal driven processes are thought to have more influence on the observed annual and semi-annual surface deformation compared to processes related to the other meteorological processes.

5.3.2 Phase difference determination and quantification using phase spectrum technique

Table 7 gives the phase difference results between the cGPS displacement and meteorological (average temperature, pressure, rainfall, and humidity) time series. From Table 7, it is observed that the annual cycles in the displacement and meteorological cycles are largely in phase, either positively or negatively in phase. The semi-annual cycles in the cGPS displacement and meteorological time series have moderate to very little phase correlation. The annual phase difference is smallest and more consistent between displacement-temperature time series (average of |16.89| degrees), and largest between displacement-pressure time series (average of |138.69| degrees). The corresponding displacement-temperature and displacement-pressure semi-annual average phase correlations are |59.97| degrees and |65.04| degrees, respectively.

The annual and semi-annual phase difference in the surface displacement-humidity time series and surface displacement-rainfall time series is observed to vary widely, for stations in the same climatic zones and those that are not. The annual phase difference of surface displacement-rainfall time series ranges from |2.35| degrees to |153.84| degrees, and their average phase difference is |60.7| degrees (Table 7). The annual phase difference of surface displacement-humidity time series ranges from |17.45| degrees to |171.48| degrees and has an average phase difference of |87.80| degrees. The corresponding semi-annual average phase difference in the surface displacement-rainfall and displacement-humidity time series is |106.8| degrees and |100.18| degrees, respectively. The variation in both the phase of the annual and semi-annual cycles seems to be independent of the climatic zone. The average annual and semi-annual phase difference of displacement-humidity and displacement-rainfall time series are largely misleading, because of their large variation, hence their ranges are given as well.

The low and more consistent (positive and negative) phase differences between the annual displacement-temperature time series and displacement-pressure time series are taken to indicate high linear dependence between the time series. The large and highly variable annual phase difference between displacement-rainfall and displacement-humidity time series are taken to indicate a low linear dependence between these time series. The results show that temperature and pressure time series have a direct or indirect influence on the annual deformation observed in the vertical component of position cGPS time series; whereas, rainfall and humidity processes have a small influence on the annual deformation observed in the vertical component cGPS time series. The large and highly variable semi-annual phase difference between the displacement and meteorological time series is thought to indicate that meteorological processes have low to no influence on the semi-annual deformation observed in vertical component cGPS displacement time series.

Figure 5.21 shows the phase difference histograms of the displacement-meteorological process phase difference. The histograms visualise and summarise the phase difference characteristics described above. From Figure 5.21 we also observed that the phase of displacement-rainfall and displacement-humidity time series are much more variable than that of the displacement-temperature and displacement-pressure time series.

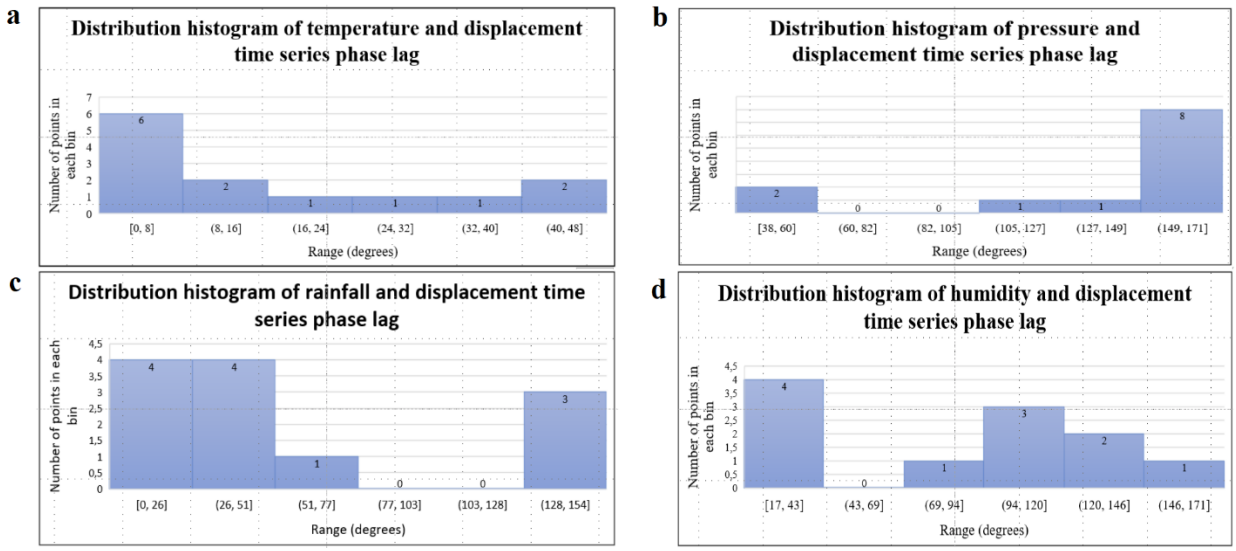


Figure 5.21: Phase lag distribution histograms for the considered meteorological processes.

Table 7: Phase difference between cGPS displacement time series and meteorological (average temperature, pressure, rainfall and humidity) processes. The annual and semi-annual phase shift averages are computed using absolute phase shift values of the annual and semi-annual phase shift results.

Climatic Zones	**GPS Station name**	**Phase shift (in degrees) of the ATM processes with respect to the VC of displacement**							
		Temperature		Pressure		Rainfall		Humidity	
		Annual	Semi-annual	Annual	Semi-annual	Annual	Semi-annual	Annual	Semi-annual
Desert	PSKA	-9.85	-38.43	167.58	-65.44	20.84	-147.02	118.66	94.77
	SBOK	4.21	-69.11	170.93	9.62	153.84	-108.84	171.48	120.32
Wet tropical	GREY	-28.13	-17.36	142.42	-58.83	-46.88	123.15	41.84	171.97
	UMTA	41.14	-123.48	-164.88	90.33			99.73	-59.05
	IXOP	-4.03	-58.43	167.37	-54.97	-17.87	43.09	34.64	112.03
	ULDI	-47.95	-55.77	124.82	-86.22	-76.86	-39.97	-17.45	-80.76
Sahelian	DEAR	-6.02	-63.48			20.62	137.09	107.15	166.43
	MFKG	0.41	-42.68	-38.12	-71.51	25.82	140.94	84.10	134.58
Dry tropical	EMLO	-35.72	-54.91	149.99	-28.85	-43.42	-142.61		
	BETH	-6.06	-78.06	167.36	-56.84	-2.35	117.56		
Mediterranean	MALM	-9.34	-40.52	170.03	78.92	145.82	101.18	144.14	-73.62
	GEOA	-5.00	-43.02	-44.32	63.77	-37.99	49.88	17.71	4.83
	WORC	-21.63	-94.29	156.45	115.19	135.43	129.90	128.87	-83.64
Average (annual cycle)		16.89		138.69		60.65		87.80	
Average (semi-annual cycle)			59.97		65.04		106.77		100.18

5.3.3 Phase correlation determination and visualisation using CWT Semblance spectral technique

In most of the CWT semblance visual plots, the phase correlation between displacement-temperature and displacement-pressure time series is high and consistent over the observation period (Figure 5.22, Figure 5.23, and appendix C). In all the climatic zones, the cGPS displacement time series are positively correlated to temperature time series, Figure 5.22, shown by the red region around 1 cpy. Correspondingly, in all the climatic zones, cGPS displacement time series are inversely correlated to pressure time series, Figure 5.23, shown by the blue region around 1 cpy.

The semblance spectrum of rainfall and humidity time series show that, depending on the spatial location of the meteorological and cGPS stations, displacement-rainfall time series and displacement-humidity time series can either be positively or negatively correlated. The correlation between displacement-rainfall and displacement-pressure time series is often low (60.65) and inconsistent over the observation period (Figure 5.24, Figure 5.25 and appendix C). The time series can either be positively correlated, negatively correlated or not correlated.

At frequencies greater than 1 cpy, no clear and continuous phase correlation is observed between frequency components characteristic of the cGPS displacement and meteorological time series. No clear and continuous phase correlation is observed between the semi-annual cycles in the cGPS displacement and meteorological time series, indicating that the semi-annual components in the cGPS displacement and meteorological time series might be independent of each other. This suggests that rainfall and humidity processes have little, at times, no influence on the annual surface displacements measured by cGPS stations. Thus, it is possible that the effects of rainfall and humidity processes interact constructively and destructively with the effects of processes that drive seasonal surface deformation measured by cGPS stations. That is, in areas where the annual phase of these processes is positively correlated, constructive interference may occur and in areas where they are negatively correlated, destructive interference may occur. The interference may be occurring due to the absorption of water by soils when it rains and increased levels of refraction and reflection of the satellite signals when humidity levels are high.

The observations are taken to imply that thermal- and atmospheric-pressure-related processes contribute more to the surface deformation measured by cGPS systems than rainfall and humidity related processes.

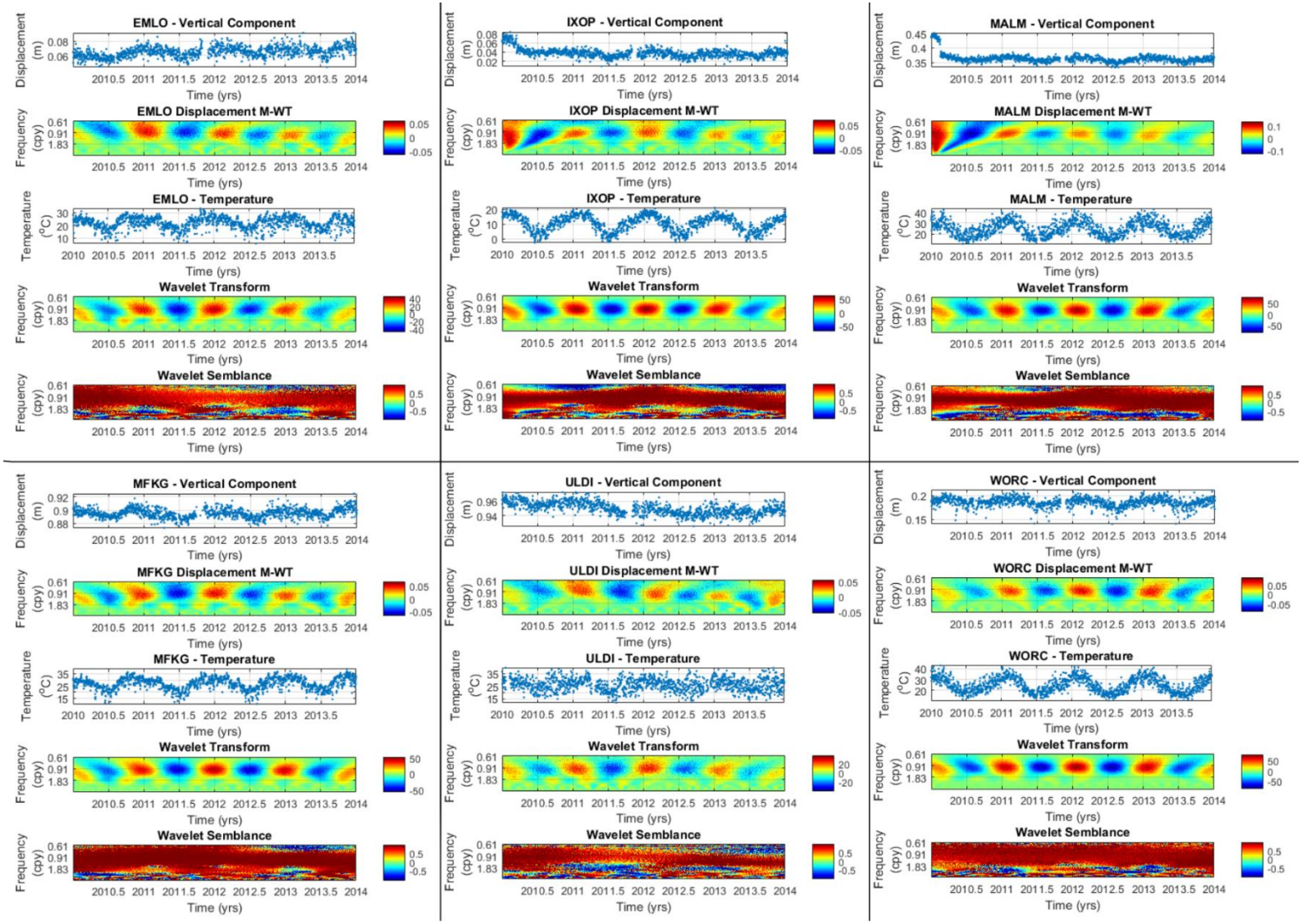


Figure 5.22: Semblance correlation plots of cGPS displacement time series (m) vs average temperature time series (℃)

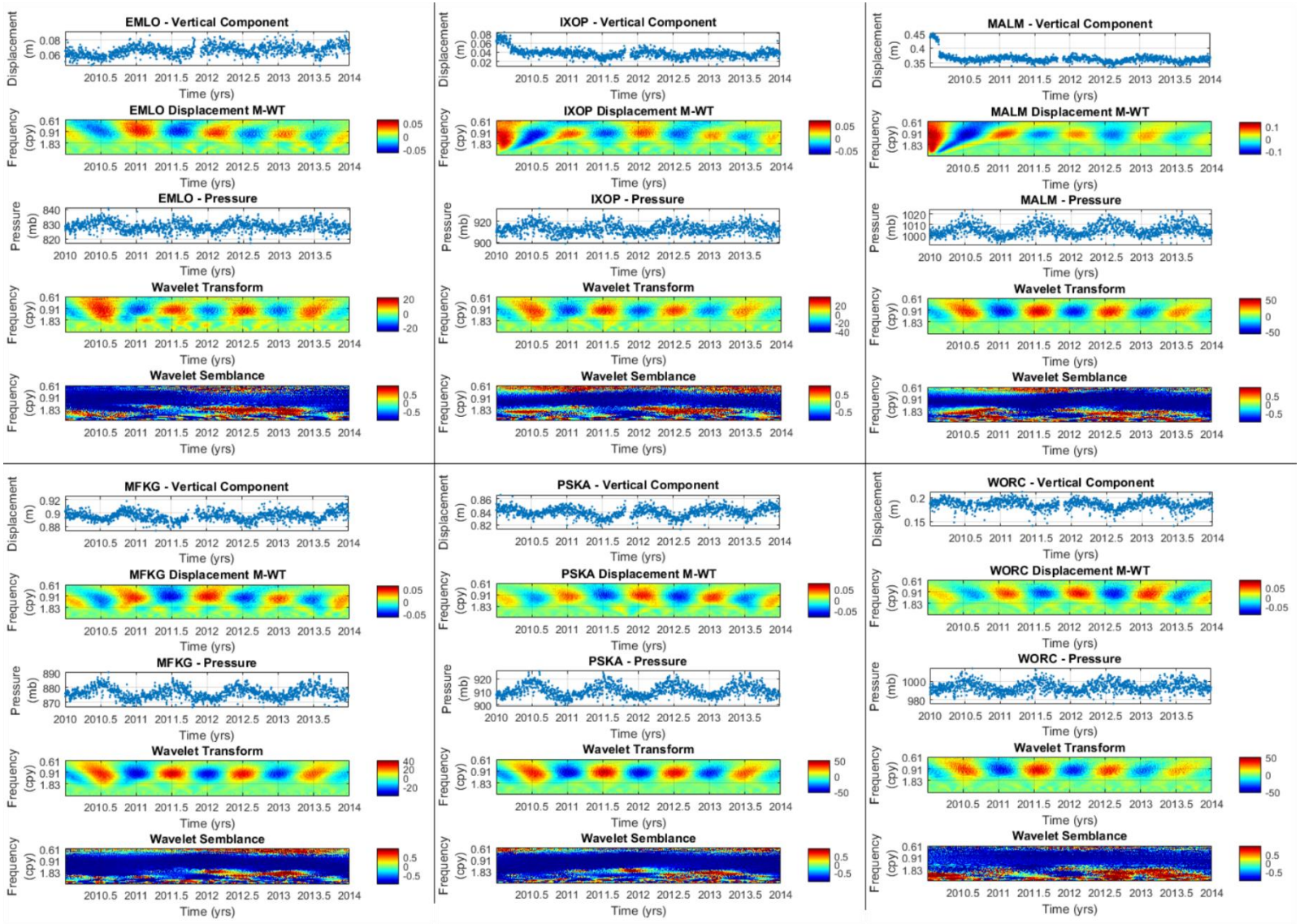


Figure 5.23: Semblance correlation plots of cGPS displacement time series (m) vs atmospheric pressure time series (mbar).

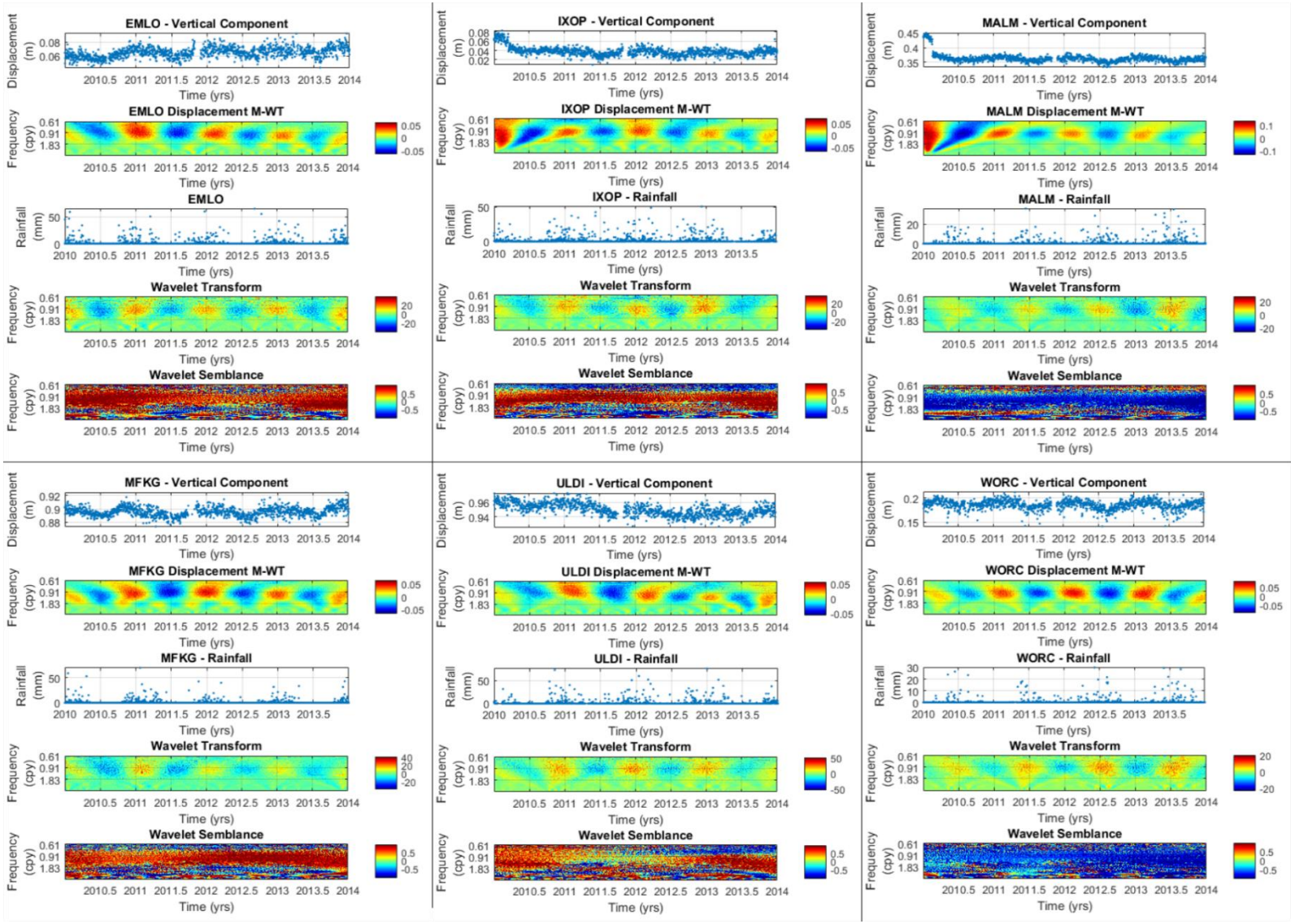


Figure 5.24: Semblance correlation plots of cGPS displacement time series (m) vs rainfall time series (mm).

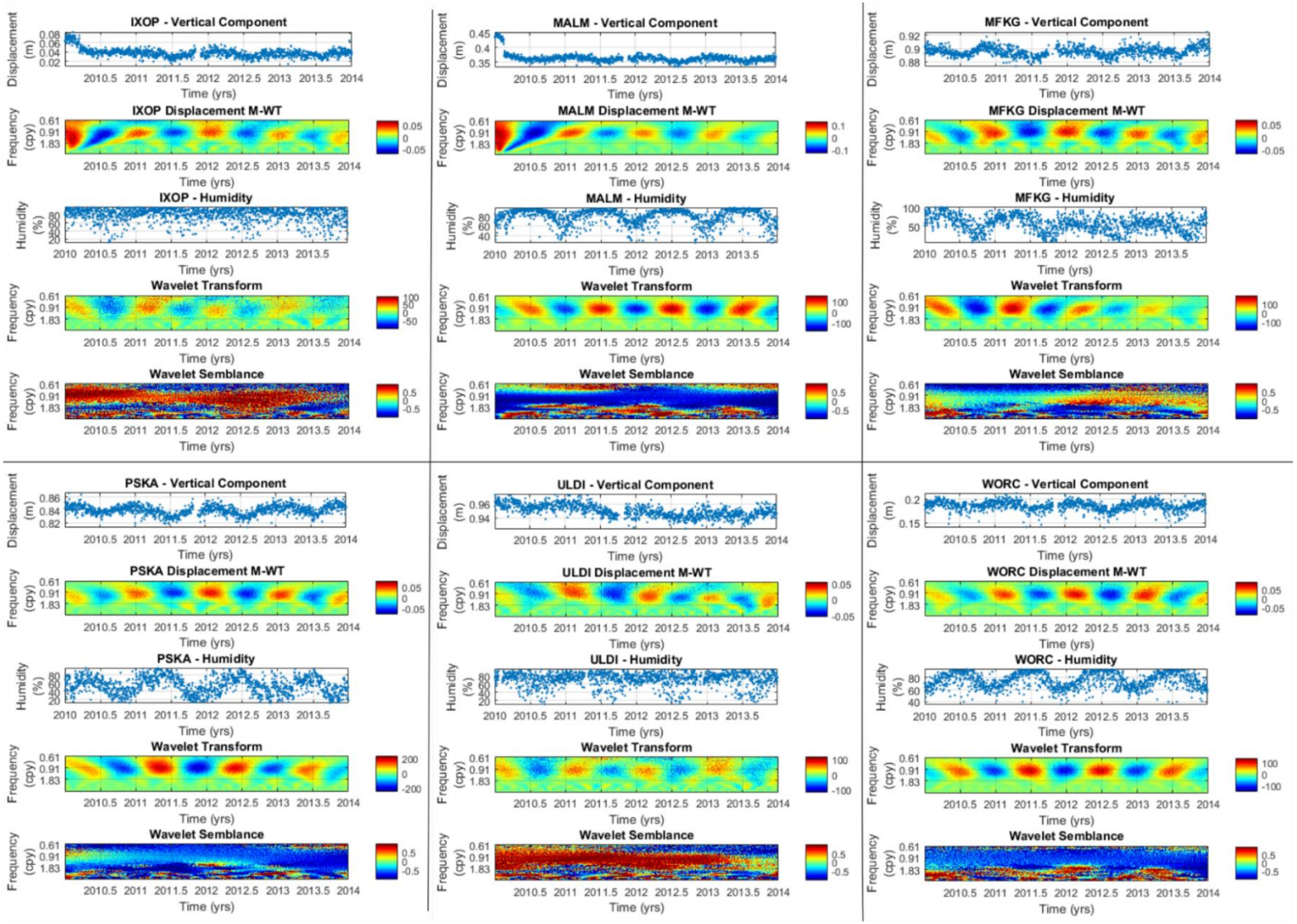


Figure 5.25: Semblance correlation plots of cGPS displacement time series (m) vs humidity time series (%).

6 Surface deformation models

Seasonal temperature, rainfall and atmospheric pressure variations affect the mechanical behaviour of rocks and soils in the near subsurface, e.g., through swelling, collapse, and thermal dilatation and contraction behaviour. In this section, we investigate the amount of surface deformation that is caused by temperature and atmospheric pressure variations, and soil expansivity in near subsurface rocks using surface expansion models.

6.1 Surface deformation model due to thermal expansion

Thermal expansion is a highly seasonal phenomena that affect cGPS datasets and is usually not taken into consideration when correcting cGPS data. However, to obtain high precision position measurements, thermal expansion effects need to be taken into consideration (Romagnoli et al., 2003). The thermal expansion component of GPS stations is subdivided into two components~~,~~ 1) Thermal Expansion of the Monument (TEM) above the Earth's surface and 2) Thermal Expansion of the Bedrock (TEB) beneath the surface (Yan et al., 2009; Wang et al., 2018). The TEM above the surface is mainly due to the variation of the thermal elasticity properties of cGPS components in response to diurnal and seasonal temperature, monument height and type, and direct radiation changes (Yan et al., 2009; Wang et al., 2018). The TEB below the surface is caused by thermal deformation of the bedrock hosting the cGPS stations near the surface of the Earth due to seasonal and diurnal soil (compacted soil) or rock expansion related to temperature variations (Yan et al., 2009). If not accounted for, both the thermal expansion effects can propagate into the horizontal and vertical GPS position measurements and degrade the accuracy of the measurements (Romagnoli et al., 2003; Wang et al., 2018).

Heat transfer in rocks located at depths of about 10 – 15 m is controlled mainly by temperature and rainfall activity in the atmosphere (Márquez et al., 2016). Beyond this depth, the temperature of the Earth is understood to increase by approximately 3℃ every 100 m away from the near subsurface and atmospheric processes have no influence in the Earth's temperature field. The influence of atmospheric processes is greatest at depths of about 1 to 5 m (Florides and Kalogirou, 2007). At a depth of approximately 10 m, the subsurface temperature field is stable and approximates the average annual surface air temperature at a place (Florides and Kalogirou, 2005; Prangnell and McGowan, 2009). Thermal bedrock deformation induced by heat change reduces with depth as temperature fluctuations diminish (Florides and Kalogirou, 2007).

The thermal expansion of soil in the crust is not homogenous. It varies from one area to another, depending on the composition of the soil present in an area, the water content, and depth of burial. The thermal expansion potential differs depending on the thermal diffusivity, thus similar soil types can have different expansion potentials. Thermal diffusivity is the quantity that defines the ability of a material to conduct heat (thermal energy) relative to its ability to store heat (Salazar, 2003; Márquez et al., 2016). It defines the rate of propagation of heat in a rock or in consolidated soils and is dependent on the thermal conductivity, specific heat capacity and density of a material. When computing the thermal expansion of subsurface rocks, an average value for the thermal diffusivity is often assumed, because of its very variable nature.

6.1.1 Thermal expansion computation

The TEM above the surface is estimated using a linear expansion model because a rigorous model that considers all the factors causing thermal expansion of the cGPS monuments has not been developed (Wang et al., 2018). Mathematically, the linear expansion model is defined as (Yan et al, 2009; Wang et al., 2018):

$$\mathrm{TEM} = \propto \cdot \mathrm{h} \cdot [\mathrm{T(t)} - \mathrm{T_m}] = \Delta \mathrm{L} \quad \textbf{(30)}$$

where TEM is the estimated linear monument expansion (m), which is equivalent to the monument length variation (ΔL), due to temperature changes, $\propto$ is the thermal expansion coefficient ($°\mathrm{C}^{-1}$), h is the initial height of the object (m), T(t) is the surface temperature and $\mathrm{T_m}$ is the annual average air temperature (°C). The soil surface temperature near and at the surface of the Earth can be estimated using the following equations (Florides and Kalogirou, 2007; Márquez et al., 2016):

$$\mathrm{T_H} = \mathrm{T_m} + \mathrm{A}\cos(\mathrm{wt} - \varphi) \quad \textbf{(31)}$$

$$\mathrm{T_L} = \mathrm{T_m} - \mathrm{A}\cos(\mathrm{wt} - \varphi) \quad \textbf{(32)}$$

where $\mathrm{T_H}$ and $\mathrm{T_L}$ are the maximum and minimum temperatures (°C) near and at the surface respectively, A is the annual average temperature amplitude from zero, w is the angular frequency (rad/s), t is the time (s), and φ is the phase of the temperature time series (rad). In this study, Fourier transforms are used to determine the amplitude of the temperature time series.

Seasonal thermal expansion of the bedrock (TEB) hosting the cGPS stations is estimated using the following equation (Yan et al., 2009; Wang et al., 2018):

$$TEB = \frac{1+\mu}{1-\mu}\alpha \sum_{i=1}^{N} A_i \sqrt{\frac{k}{w_i}} \cos\left(w_i t - \frac{\pi}{4} - \varphi_i\right) \quad \textbf{(33)}$$

where TEB is the estimated bedrock deformation (m), μ is Poisson's ratio, $\propto$ is the thermal expansion coefficient ($°C^{-1}$), k is the ground thermal diffusivity, N is the number of harmonics constituting the temperature time series, $\pi/4$ is a temperature-surface displacement phase delay, A_i, w_i, φ_i are the amplitude, angular frequency and phase of the different harmonics constituting the temperature time series of interest. The properties of different rock types required to calculate the TEM above the surface and TEB are given in Table 8, Table 9, Table 10 and Table 11 below:

Table 8: Average Poisson's ratio and coefficient of thermal expansion values for different types of materials (Wang et al., 2018)

Monument material	Concrete	Reinforced concrete	Steel	Bronze	Aluminium
Poisson's ratio μ	0.17	0.20	0.27	0.32	0.33
Coefficient of thermal expansion α ($10^{-6}°C^{-1}$)	12	12	13	18	23

Table 9: Average thermal diffusion coefficients for sedimentary, igneous and metamorphic rocks (Wang et al., 2018)

Bedrock type	Igneous	Metamorphic	Sedimentary
Thermal diffusion coefficient k (10^{-6} m^2s^{-1})	1.34	1.25	1.80

Example (Part 1): Estimating the TEM for station MFKG

Analysing the temperature time series for meteorological station MFKG located in Mafikeng, South Africa, we observe that the average temperature (T′) at the place is 19.3 ℃ and the amplitude of the temperature time series (A) is 5.7 ℃. For an annual cycle, the angular frequency defined as:

$$w = \frac{2\pi}{T} \quad \textbf{(34)}$$

where, T is the period and is equal to:

$$T = 365.2422 \text{ days} = 3.16 \times 10^{7} \text{ s}$$

Thus, the angular frequency is:

$$w = \frac{2\pi}{T} = 1.99 \times 10^{-7} \text{ rad/s}$$

For $N = 1$, the maximum surface temperature is given by:

$$T_H = T_m + A\cos(wt - \varphi)$$

When considering the maximum temperature over an annual period, the observation time t is equal to the period of the time series, i.e., $T = t$, thus $wt = 2\pi$ and $\varphi = 0$ (assuming the is no phase delay between temperature and surface displacement variations). Therefore

$$T_H = 19.3\,℃ + (5.7\,℃)\cos(2\pi)$$

$$T_H = 25\,℃$$

The table below gives the parameters of the considered GPS station, i.e., station MFGK, taken from the log file of the station (i.e., at: ftp://igs.org/pub/station/log/ mfkg_20190330.log).

Table 10: MFGK station parameters

Standard Parameters for station MFKG	**Information**
Monument description	Concrete beacon built on gravel sand/ clay (Assumption: sedimentary)
Monument height	2.4 m
Monument foundation	Concrete
Foundation height	0.5 m
Thermal expansion coefficient (α) for concrete	$12 \times 10^{-6}\,℃^{-1}$
Thermal diffusivity coefficient (k)	$1.8 \times 10^{-6}\,m^2s^{-1}$

Substituting the station and calculated parameters in the linear thermal expansion equation to obtain the TEM of station MFKG, we get

$$\mathrm{TEM_s} = (12 \times 10^{-6}\ ^{\circ}\mathrm{C}^{-1})(2.4\ \mathrm{m})(5.7\ ^{\circ}\mathrm{C})$$

$$\mathrm{TEM_s} = 1.6 \times 10^{-4}\mathrm{m} = 0.16\ \mathrm{mm}$$

Thus, the estimated monument thermal expansion above the surface is 0.16 mm.

Part 2: Estimating the TEB in the Mafikeng area

Table 11: Thermal expansion of bedrock parameters (Xu et al., 2017)

Half-space heat conduction model parameters	Information
Coefficient of thermal expansion (α)	$1.6 \times 10^{-5}{}^{\circ}\mathrm{C}^{-1}$
Thermal diffusivity (k)	$1.8 \times 10^{-6}\ \mathrm{m^2 s^{-1}}$
Poisson's ratio (μ)	0.27

Calculating TEB for $\mathrm{N} = 1$, $\mathrm{A} = 5.7\ ^{\circ}\mathrm{C}$, $\mathrm{w} = 1.99 \times 10^{-7}\ \mathrm{rad/s}$, T=t, and $\varphi = 0$, TEB becomes:

$$\mathrm{TEB} = \frac{1+\mu}{1-\mu}\alpha\,\mathrm{A}\sqrt{\frac{\mathrm{k}}{\mathrm{w}}}\cos\left(\mathrm{wt} - \frac{\pi}{4} - \varphi\right)$$

Substituting the station and environmental parameter we get:

$$\mathrm{TEB_s} = \frac{1+0.27}{1-0.27}(1.6 \times 10^{-5}{}^{\circ}\mathrm{C}^{-1})(5.7\ ^{\circ}\mathrm{C})\sqrt{\frac{1.8 \times 10^{-6}\ \mathrm{m^2 s^{-1}}}{1.99 \times 10^{-7}\ \frac{\mathrm{rad}}{\mathrm{s}}}}\cos\left(2\pi - \frac{\pi}{4}\right)$$

$$\mathrm{TEB_s} = 0.0003372\ \mathrm{m} = 0.34\ \mathrm{mm}$$

thus, the estimated total displacement ($\mathrm{D_t}$) induced by thermal expansion is:

$$\mathrm{D_t} = \mathrm{TEM_s} + \mathrm{TEB_s} = 0.16\ \mathrm{mm} + 0.34\ \mathrm{mm} = 0.50\ \mathrm{mm}$$

The TEB value obtained in the above calculation is computed using a thermal expansion coefficient parameter of a uniformly elastic sphere (Xu et al., 2017). However, considering that the concrete beacon foundation only extends to a depth of ~ 0.5 m and is situated in an area consisting of sedimentary rocks, which are consolidated soils. It is possible that the TEB beneath the station is mainly due to the expansion of over-consolidated soils, which have a different thermal expansion coefficient to that of the elastic sphere. Therefore, using the

thermal expansion coefficient of compacted soil, i.e., $\propto_{cs} = 2.0 \times 10^{-4}\ °C^{-1}$ (Romero et al., 2005), to estimate the thermal expansion of the bedrock, TEB_s becomes:

$$TEB_s = \frac{1 + 0.27}{1 - 0.27}(2 \times 10^{-4} °C^{-1})(5.7\ °C)\sqrt{\frac{1.8 \times 10^{-6}\ m^2 s^{-1}}{1.99 \times 10^{-7}\ \frac{rad}{s}}}\cos\left(2\pi - \frac{\pi}{4}\right)$$

$$TEB_s = 0.00422\ m = 4.22\ mm$$

Thus, the displacement (D_t) induced by thermal expansion becomes:

$$D_t = TEM_s + TEB_s = 0.16\ mm + 4.22\ mm = 4.38\ mm$$

when assuming that the thermal expansion is due to the expansion of over-consolidated soils in the subsurface. The obtained thermal expansion value might be overestimated since the weight of the overlaying concrete beacon is not taken into consideration. According to Yan et al. (2009), the highest thermal expansion that can be induced by bedrock thermal expansion is about 1.3 mm, which is much smaller than what we obtained when using the thermal expansion of over-consolidated soil.

6.1.2 Background of thermal expansion of over-consolidated soils

In consolidated soils (i.e., lightly to significantly over-consolidated soils) heat changes induce expansion and contraction (Towhata et al., 1993; Cui et al., 2000; Romero et al., 2005; Tang et al., 2008; Cui and Tang, 2013). Soil expansion is due to thermal expansion of solid mineral phases and absorbed water constituents under low stress; while soil contraction is due to the contraction of solid phases and water constituents as they lose heat, and by the mechanical weakening of the contacts between soil aggregates which causes intra-aggregate water loss as temperatures increase (Towhata, 1993; Cui et al., 2000; Romero et al., 2005; Tang et al., 2008). The thermal mechanical response of soils is extremely dependent on the over-consolidation ratio (OCR) and time. Low OCRs promote the occurrence of irreversible thermal contraction and high OCRs favour the occurrence of reversible thermal expansion (Cui and Tang, 2013). At high OCR, heating at low temperature (20 – 50 °C) induces reversible expansion when allowed to cool (Figure 6.1), continued increase in temperatures (50 °C and more) induces irreversible soil contraction (Delage et al., 2000).

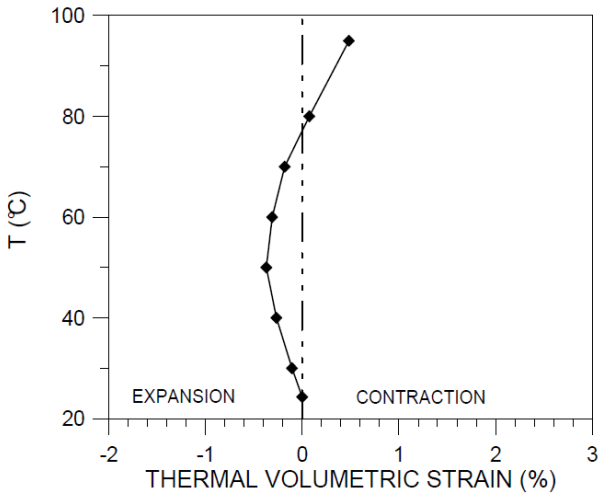


Figure 6.1: Thermal expansion curve of expansive Boom clay soil with an OCR of 2 (Delage et al., 2000)

At low temperatures, the quasi-reversible nature of the thermal volume change behaviour can be considered to be elastic. Plastic contraction of soil occurs at low OCR under high temperatures and stress due to the loss of water (increase in suction) and low shear stress (Towhata, 1993; Romero et al., 2005; Tang et al., 2008; Monfared et al., 2011; Cui and Tang, 2013). It has been observed that (Cui et al., 2000; Romero et al., 2005; Tang et al., 2008; Cui and Tang, 2013):

1. At low OCR irreversible contraction occurs upon heating, pure contraction occurs when OCR is equal to 1 upon heating, and reversible contraction, at high OCR, occurs during cooling.
2. At low temperatures, soil expansion due to heating is reversible, while soil contraction is not.
3. The slope of the expansion curve (i.e., the slope of the volumetric strain, equivalent to the linear thermal expansion coefficient) during heating and contraction curves during cooling were found to be parallel and independent of the applied stress. The slope is observed to be approximately:

$$\propto = 2 \times 10^{-4}\ ^{\circ}\mathrm{C}^{-1}$$

Romero et al. (2005) and Tang et al. (2008) observed that the effect of temperature appears to be dependent on the mechanical expansion properties of soil aggregates. Different soils can have low, medium, high and very high expansion behaviour depending on their clay constituents and content, permeability and intra-aggregate water (moisture content). Test

conducted by Towhata et al. (1993) demonstrated that lightly to over-consolidated soil samples underwent expansion, under room temperature, and the primary stage of expansion was already complete when the temperature was raised through 40 and 60 degrees Celsius to 90 degrees Celsius.

6.2 Surface deformation model due to atmospheric loading

Periodic fluctuations in atmospheric pressure, particularly at long wavelengths, cause seasonal deformation of the Earth's crust that is detectable by space geodetic techniques. The deformations are caused by variations in atmospheric pressure loading at the Earth's surface induced by changes in atmospheric thickness, air mass, and gravitational attraction between the atmosphere and the Earth (van Dam and Wahr, 1987; van Dam et al., 1994). Surface deformation due to atmospheric loading is primarily in the vertical direction of motion of the crust and account for up to 24% of the cGPS height variations observed in the vertical component (van Dam et al., 1994; Petrov and Boy, 2004). Induced atmospheric pressure displacements are larger in winter and at higher latitudes, where pressure variability is greatest and is smaller in summer, coastal areas and at low latitudes where variability is lowest (Rabbel and Zschau, 1985; van Dam and Wahr, 1987; van Dam et al., 1994). The displacements can be estimated using Farrell's theory or the regression equation of Rabbel and Zschau (1985). Rabbel and Zschau (1985) and Zerbini et al. (2001), compared the performance of the two methods and found them to be in good agreement.

Farrell's theory assumes that the atmosphere is a thin homogenous layer located on the Earth's surface and estimates surface displacements by computing the integral convolution of Green's functions with the surface load, expressed by the mean of the surface pressure load (Farrell, 1972; van Dam, 1984; Rabbel and Zschau, 1985; Gladkikh et al., 2011). The Green's functions, together with the Love numbers, describe the response of an elastic Earth to a point mass load. The radial surface displacement due to a point mass load can be computed using the following equation:

$$U(\theta)_r = \frac{rM_l}{M_e} \sum_{n=0}^{\infty} h_n P_n(\cos(\theta)) \quad \textbf{(35)}$$

where $U(\theta)_r$ is the surface radial displacement due to a point mass measured at an angular distance θ, r is the radius of the Earth in metres, M_l is the mass of the surface load in kilograms,

M_e is the mass of the Earth in kilograms, h_n is the Love load number at degree n, and $P_n(\cos(\theta))$ is the Legendre polynomial at degree n.

The method proposed by Rabbel and Zschau (1985), which is also used in this study, estimates surface displacements caused by variations in atmospheric pressure using a regression equation and real surface pressure data. The radial displacement due to atmospheric pressure is estimated using the following equation:

$$U_r = -0.90P_R - 0.35(P_L - P_R) \quad \textbf{(36)}$$

where U_r is the radial displacement in millimetres, P_R is the average regional pressure change in millibars, and P_L is the average local pressure change in millibars. The local pressure measurement is a short wavelength coefficient of the atmospheric variations (at the point of interest) and the regional pressure measurement is a long wavelength coefficient component of the atmospheric variation. The surface displacements can be estimated using an ocean-less Earth model or an inverted barometer Earth model (van Dam and Wahr, 1987). The inverted barometer model considers the oceanic response when subjected to pressure changes, while the ocean-less Earth model does not. The results of the two models are the same for pressure points located inland (i.e., stations located at and more than 500 km from the coast) and different for coastal stations (i.e., stations located less than 500 km from the coast). The definition of coastal and inland stations used in this study follows that of van Dam et al. (1994). At coastal stations, the surface displacement estimates of the ocean-less Earth model are higher and less precise than those of the inverted barometer Earth model (van Dam and Wahr, 1987; van Dam et al., 1994). Surface displacement estimates for pressure points a few kilometres away from the coast are not appreciably affected by the differences of the models. While, for points located near the coastline, the estimates may differ by as much as 50%. The estimates for both an ocean-less and inverted barometer Earth model are computed using equation (36).

In this study, surface pressure displacements are estimated using both the inverted barometer Earth model and the ocean-less earth model. Pressure measurements from stations with a radial displacement of at least 1000 km from the point of interest are used to calculate the average regional pressure measurements, except station MFKG in Model 2 (Figure 6.2b, Table 13). This enables the surface displacements to be estimated with an accuracy of roughly 90% for stations located inland and applies to both the ocean-less and inverted barometer Earth models.

6.3 Atmospheric pressure computation

The results presented below give an indication of the seasonal surface displacements that occur in South Africa during summer and winter time. Surface displacement for a point located inland and near the coastline are estimated using real data collected by the South African Weather Service (SAWS) meteorological stations. Average pressure estimates for summer (December to February), autumn (Match to May), winter (June to August) and spring (September to November) months were computed and are given in Table 12. Table 12 lists the cGPS station coastline distance and the computed annual atmospheric pressure values for the chosen cGPS stations between the period of 2010 – 2014. The pressure values for station GEOA are calculated for the period of 2013 – 2016.

Table 12: Atmospheric pressure variations in winter, summer, autumn and winter at different stations.

Station Name	Station distance from the coastline (km)	Average atmospheric loading (mbar)			
		Winter	Summer	Autumn	Spring
BETH	315	-1.5020	0.9719	0.5288	-0.1012
EMLO	270	-1.7371	0.1869	0.9431	0.6717
GEOA	5	8.0693	-2.5061	0.5315	-4.7236
MALM	26	0.4175	-0.5881	3.2976	-3.1041
MFKG	709	-1.8372	0.3753	2.5543	-1.9250
SBOK	78	-0.4533	0.8714	1.2978	-2.4283

Barometric model surface deformation results are computed from the ocean-less Earth model to the inverted barometer model by reducing the coastal site pressure points by 50%, i.e., data from all the cGPS stations except that from station MFKG (Rabbel and Zschau, 1985; van Dam and Wahr, 1987; van Dam et al., 1994).

Figure 6.2 shows the local and regional pressure stations (points) that were chosen to calculate surface deformation at points EMLO and SBOK induced by atmospheric loading. The separation distance between the local pressure stations and regional pressure stations, for both models, are given in Table 13. The local station EMLO (in model 1) is located more inland while the local station SBOK (in model 2) is located near the coast.

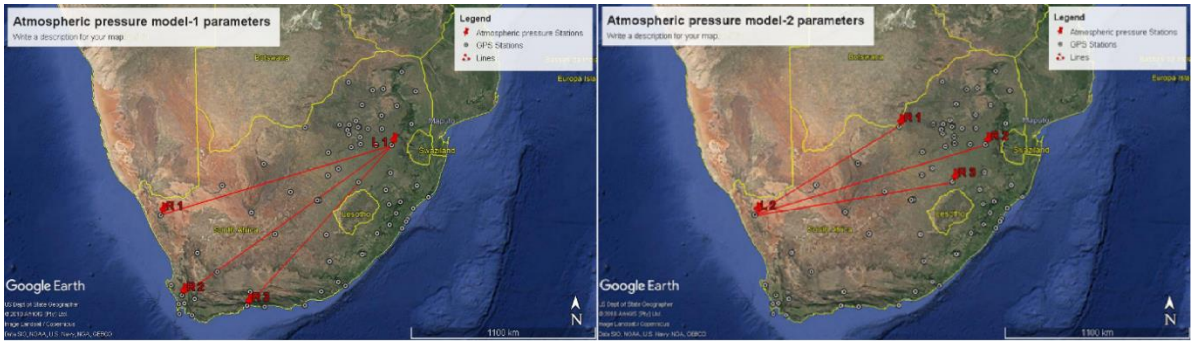


Figure 6.2: (a) Local and regional stations used to estimate atmospheric pressure loading inland. (b) Local and regional stations used to estimate atmospheric deformation near the offshore.

Table 13: Distance between the local and regional GPS stations for Model-1 and 2.

Model-1 Parameters		**Model-2 Parameters**	
Regional Stations	**Distance between the local stations and the regional stations for Model-1 (km)**	**Regional Stations**	**Distance between the local stations and the regional stations for Model-1(km)**
R1	1242	R1	873
R2	1331	R2	1230
R3	1105	R3	1039

Surface deformation at station EMLO (located inland) due to atmospheric pressure variations

Local station: EMLO.

Regional stations: SBOK, MALM and GEOA

Deformation calculation at station EMLO (inland): Summer

The regional atmospheric pressure at station EMLO in summer, calculated using the local pressure at stations SBOK, MALM and GEOA, is:

$$P_R = \frac{(0.87 + (-0.59) + (-2.51))}{3} = -0.74 \text{ mbar}$$

The local atmospheric pressure at this station (EMLO) in summer is:

$$P_L = 0.19 \text{ mbar}$$

Thus, the induced surface atmospheric pressure deformation at station EMLO in summer is:

$$U_r = -0.90P_R - 0.35(P_L - P_R)$$

$$U_{(r,o)} = -0.90(-0.74) - 0.35\big(0.19 - (-0.74)\big) = 0.34 \text{ mm}$$

$$U_{(r,b)} = -0.90(-0.34) - 0.35\big(0.19 - (-0.37)\big) = 0.11 \text{ mm}$$

where $U_{(r,o)}$ is the surface displacement obtained using the ocean-less Earth model and $U_{(r,b)}$ is the surface displacement obtained using the inverted barometric Earth model.

Deformation calculations at station EMLO (inland): Winter

The calculated regional pressure at station EMLO in winter, using atmospheric pressure values at stations SBOK, MALM and GEOA, is:

$$P_R = \frac{(-0.45 + 0.42 + 8.07)}{3} = 2.68 \text{ mbar}$$

The local atmospheric pressure at station EMLO in winter is:

$$P_L = -1.74 \text{ mbar}$$

Thus, the induced surface atmospheric pressure deformation at station EMLO in winter is:

$$U_r = -0.90P_R - 0.35(P_L - P_R)$$

$$U_{(r,o)} = -0.90(2.68) - 0.35\big((-1.74) - (2.68)\big) = -0.87 \text{ mm}$$

$$U_{(r,b)} = -0.90(1.34) - 0.35\big((-0.87) - (1.34)\big) = -0.43 \text{ mm}$$

Surface deformation at station SBOK (located near the coast) due to atmospheric pressure variations

Local station: SBOK.

Regional stations: MFKG, EMLO and BETH.

Deformation calculation at station SBOK (near the coast): Summer

The regional atmospheric pressure at station SBOK in summer, calculated using the local pressure at stations EMLO, MALM and GEOA, is:

$$P_R = \frac{(0.38 + 0.19 + 0.97)}{3} = 0.51 \text{ mbar}$$

The local atmospheric pressure in summer at station SBOK is:

$$P_L = 0.8714 \text{ mbar}$$

Thus, the induced surface atmospheric pressure deformation at station SBOK in summer is:

$$U_r = -0.90P_R - 0.35(P_L - P_R)$$

$$U_{(r,o)} = -0.90(0.51) - 0.35(0.87 - 0.51) = -0.59 \text{ mm}$$

$$U_{(r,b)} = -0.90(0.26) - 0.35(0.44 - 0.26) = -0.30 \text{ mm}$$

Deformation calculation at station SBOK (near the coast): Winter

The calculated regional pressure at station SBOK in winter is:

$$P_R = \frac{(-1.50 - 1.74 - 1.84)}{3} = -1.69 \text{ mbar}$$

The local atmospheric pressure at station SBOK in winter is:

$$P_L = -0.45 \text{ mbar}$$

Thus, the induced surface atmospheric pressure deformation at station SBOK in winter is:

$$U_r = -0.90P_R - 0.35(P_L - P_R)$$

$$U_{(r,o)} = -0.90(-1.69) - 0.35\big(-0.45 - (-1.69)\big) = 1.09 \text{ mm}$$

$$U_{(r,b)} = -0.90(-0.85) - 0.35\big(-0.23 - (-0.85)\big) = 0.55 \text{ mm}$$

The estimated surface displacements are small, possibly because South Africa is situated at mid to low-latitudes and most of the pressure points used are coastal sites.

Table 14: Ocean-less Earth model and Inverted barometer Earth Model displacement summary.

Displacement location	Model 1- Surface displacement (Ocean-less Earth model)		Model 2- Surface displacement (Inverted barometer Earth Model)	
	Summer	Winter	Summer	Winter
EMLO	0.34 mm	−0.87 mm	0.11 mm	−0.43 mm
SBOK	−0.59 mm	1.09 mm	−0.30 mm	0.55 mm

6.4 Surface deformation due to heaving of expansive soils

Heaving (shrinking and swelling) of expansive soils in the near surface can also cause vertical and horizontal ground motion on plan surfaces. Expansive soils are particularly found in regions of high seasonality, characterised by separate prolonged periods of rainfall and drought, mainly arid and semi-arid regions, like southern Africa (Rao, 2000; Vanapalli and Lu, 2012; Khademi and Budiman, 2016). The amount of heave that occurs within a certain region is vastly dependent on the potential expansiveness of the soil and variation of the soil moisture in the region (Van Der Merwe, 1964; Bell and Maud, 1995; Márquez et al., 2016). However, regardless of the total potential expansiveness of soil, in cases of high natural moisture content or in the presence of high-water tables (which prevent drastic variations in moisture content), very little volume change (expansion or contraction) occur over time. Similarly, a considerable soil volume change occurs in regions characterised by high potential expansiveness and high moisture variation over time (Van Der Merwe, 1964). The variation in soil moisture is dependent on the precipitation, evaporation and transpiration rates. Vegetation cover with a high-water demand cause shrinkage in soil by increasing the pore space suction caused by the removal of water in the subsurface soil. Heaving processes are governed by climatic conditions dominant in an area. They often cause damages in infrastructures such as buildings, especially low-rise buildings and roads (Van der Merwe, 1964; Bell and Maud, 1995).

The depth to which heaving extends (active zone) in the dry and wet seasons varies from one region to another. South Africa and most parts of southern Africa are characterised by periods of high soil moisture deficit alternating with short periods of high precipitation, typical of semi-arid climates, which either balances or exceed the evaporation rates (Bell and Maud, 1995). This result in heave active zones that extend from a few centimetres (30 cm) to about 15 meters beneath the subsurface (Rao, 2000). According to Khademi and Budiman (2016) most of the significant heaving occurs at depths less than 3 m, thus in this study, a shrink and swell active zone of 3 meters and less is considered.

The volume change of soils can be predicted using Empirical methods, Soil suction methods and Oedometer methods. In this study, the Van der Merwe (1965) empirical method is used to estimate the expansion of soils related to variations in Soil moisture. The method estimates soil expansion based on the percentage of the plasticity index and clay fraction present in expansive soils (Bell and Maud, 1995; Van der Merwe, 1964). The disadvantage of this method is that it does not consider the initial moisture content or the void ration of the soil. Its advantage is that it enables soil expansion to be expected underneath a building to be estimated without the soil index properties. This method is chosen because:

1. Soil suction and oedometer tests require extensive site investigations, which is beyond the scope of this study.
2. The method provides an easy way for estimating the soil expansion in the absence of field measured soil parameters and accounts for soils with varying potential expansiveness.
3. It is commonly used here in South Africa.

6.5 Potential heave computation

The potential heave is estimated for regions containing 1) highly expansive soils and 2) moderately expansive soils, since South Africa consists of regions of varying expansivity (Figure 6.3). In each region, the potential heave is estimated for a layered hypothetical subsurface-model. In estimating the potential heave, the following assumptions are made: 1) no heaving occurs beyond the active zone due to a lack of moisture change beyond this zone (Lucian, 2011); 2) the potential expansiveness of the layers is different, it progressively decreases moving from one layer to another with depth due to the increase in overburden load, which induces an increase in pressure and compactness, and reduction in moisture intake (Van Der Merwe, 1964; Ito et al., 2014); and 3) the pressure, compactness and moisture intake at each layer is the same.

The subsurface structure of regions consisting of highly expansive soils is modelled using a 3 m layered hypothetical subsurface-model. The hypothetical model consisting of 3 layers (L1 (0 – 1 m), L2 (1 – 2 m), and L1 (2 – 3 m)) of varying expansiveness. The top layer (L1) is made to have very high expansiveness, layer L2 to have high expansiveness and layer L3 to have

medium expansiveness. Table 1 and table 2 give the unit heave strain and depth factor used to estimate heave for soils of vary potential expansiveness, respectively (Jones, 2017).

Table 15: Unit heave strain for soils of varying potential expansiveness.

Potential expansiveness	**Unit heave strain (m/m)**
Very high	0.08
High	0.04
Medium	0.02
Low	0.0

Table 16: Surface expansion depth factor for the first 8 meters of the subsurface.

Depth (m)	0 - 1	1 - 2	2 - 3	3 - 4	5 - 6	6 - 7	7 - 8	8 - 9
Factor F	0.85	0.60	0.40	0.27	0.20	0.12	0.08	0.04

The potential heave at each layer is calculated using the following equation (Van Der Merwe, 1964; Jones, 2017)

$$H_T\,(m) = \sum_{D=1}^{D=N} (P.E)_D \times F_D$$

where H is total heave (m), D is the subsurface depth from the surface (m), $(P.E)_D$ is the potential expansiveness strain (m/m) and F_D is the depth factor. Generally, the potential expansiveness is computed using the plasticity index and percentage clay fraction; the depth factor is the factor by which the heave decreases with depth (Van Der Merwe, 1964). Thus, the estimated potential heave in regions of highly expansive soils is:

$$H_{l1} = 0.08 \times 0.85 = 0.068 \text{ m}$$

$$H_{l2} = 0.04 \times 0.60 = 0.024 \text{ m}$$

$$H_{l2} = 0.02 \times 0.40 = 0.008 \text{ m}$$

$$H_T = H_{l1} + H_{l2} + H_{l2} = 0.100 \text{ m} = 100 \text{ mm}$$

where H_{l1}, H_{l2}, H_{l2}, and H_T are the estimated heave at layer L1, L2, L2 and the combined total heave, respectively.

A shallower 2 m layered hypothetical subsurface-model consisting of 2 layers (L1 (0-1 m) and L2 (1-2 m)) is assumed for modelling regions of moderate expansive soils. In these regions,

the active zone is taken to be 2 m deep and subdivided into 2 layers of high and medium expansiveness. Potential heave calculations for this model are given below:

$$H_{l1} = 0.04 \times 0.85 = 0.034 \text{ m}$$

$$H_{l2} = 0.02 \times 0.60 = 0.012 \text{ m}$$

$$H_T = H_{l1} + H_{l2} = 0.034 + 0.012 = 0.046 \text{ m} = 46 \text{ mm}$$

where H_{l1}, H_{l2}, and H_T are the estimated heave at layers L1, L2 and the total heave at regions of moderately expansive soils. From the calculations, it is observed that the potential heave at both regions of highly expansive and moderately expansive soils is large (i.e., 100 mm and 46 mm, respectively). Thus, assuming that the proposed hypothetical heave models are true at cGPS station in regions of high and moderate expansive soils, then this implies that heave action contributes significantly in the seasonal components observed in cGPS time series.

Projecting locations of the cGPS station used in this study on a geohazard map of swelling clays, Figure 6.3, shows that the selected cGPS stations are in regions of low, very low to non-expansive soils or swelling clays.

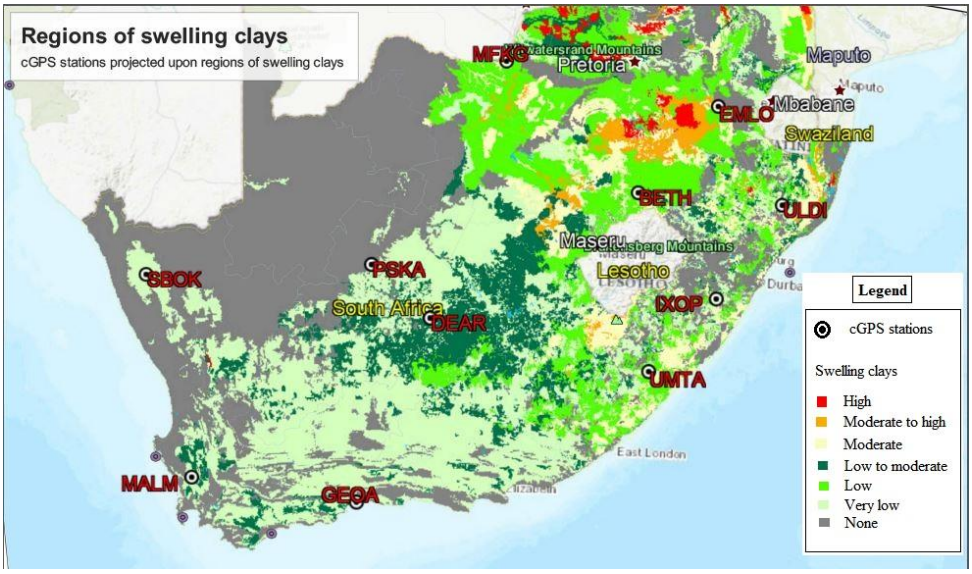


Figure 6.3: cGPS station locations projected upon regions of swelling clays across South Africa (http://197.96.144.125/jsviewer/Geohazards/index.html, accessed on the 02-03-2019).

This suggests that the selected stations are not affected much by heave action. Thus, surface deformation estimated in the heave models above is expected to be irrelevant at the selected cGPS stations. Overall, surface deformation induced by heave action is expected to be small

compared to surface deformation induced by thermal expansion and atmospheric surface loading at the stations.

7 Discussion

The study set out to investigate the effects of varying climatic conditions on cGPS time series and to improve the understanding of cGPS measurement with respect to variations in seasonal surface displacements, surface air temperature, atmospheric pressure and humidity time series. The analyses of these time series were performed in time, frequency and time-frequency domains. The following discussion focuses on interpreting the time series analysis results, justifying the results using known literature and integrating the findings. The implications are drawn and the relationship between surface air temperature, atmospheric pressure, rainfall, humidity and surface displacement are also discussed.

7.1 Surface displacement and meteorological time series decomposition:

This section focuses on interpreting surface deformation, surface air temperature, rainfall, and humidity time series results obtained using Fourier Transform frequency and Wavelet Transform time-frequency (WT) domain decomposition methods.

7.1.1 Surface displacement time series

Surface displacement time series decomposition reveals that the signals consist predominantly of annual and semi-annual components. These deformation components maybe due to gravitational attraction, thermal, hydrodynamical, unmodeled and error-related processes (Dong et al., 2002; Xu et al., 2017). The annual component is larger, often by one order of magnitude, than the semi-annual deformation component. These results coincide with the findings of van Dam and Wahr (1998), van Dam et al. (2001) and Dong et al. (2002). Although not very well delineated, the power of the deformation components is observed to vary in a systematic manner, as a function of the climatic zone in which the cGPS stations are located. The deformation components are larger in cGPS stations located in the Desert climatic zone and lower in time series in the stations located in the Wet and/or Dry Tropical climatic zones. Spectral averaging and spectral distortion are some of the prominent frequency and time-frequency domain features of the time series which imply that the cGPS time series components and the process that drive their formation are non-stationary. The cGPS displacement time series are also observed to be in phase with the annual shift of the ITCZ and seasonal variation of the sun's radiation over southern Africa, suggesting that changes in surface air temperature, atmospheric pressure, rainfall and humidity processes associated with the ITCZ and the Sun's

radiation might have a significant influence on the surface deformation recorded by cGPS stations.

7.1.2 Surface air temperature time series

Temperature time series results, like the displacement time series, are predominantly composed of annual and semi-annual frequency components. Temperatures reach their maximum in summer and minimum in winter. This is because, in midlatitude and subtropical regions, annual surface air temperature fluctuations are primarily controlled by seasonal variations in the sun's radiation (insolation) and the presence of the ITCZ, which vary on an annual basis (Hobbs et al., 1998, p. 9 & 18; Byrne et al., 2018). Summer periods coincide with high insolation and the presence of the ITCZ, while winter periods coincide with low insolation and absence of the ITCZ over southern Africa. According to Hobbs et al. (1998, p. 20) in subtropical regions, like southern Africa, intra-annual temperature fluctuations are caused by the subtropical high-pressure belt and midlatitude disturbances. Thus, it is possible that the observed semi-annual frequency component is caused by the subtropical high-pressure belt and midlatitude disturbances. Over the considered observation period, the temperature time series are also characterised by low levels of noise and a high degree of stationarity.

Furthermore, it is observed that the Wet and Dry Tropical climatic zones (regions that are mostly or normally overlain by the ITCZ in summer) have lower seasonal temperature fluctuations compare to Desert and Saharan climatic zones (regions which or where the ITCZ does not pass over), which is consistent with the findings of Legates and Willmott (1990). This is because low cloudy areas are characterised by high temperatures and extreme temperature fluctuation, while areas of high cloudiness are characterised by low temperatures and low-temperature fluctuation (Hobbs et al., 1998, p. 19).

7.1.3 Atmospheric pressure time series

Atmospheric pressure time series have a dominant and continuous annual frequency component; thus, they dominantly fluctuate on an annual scale. Throughout southern Africa, atmospheric pressure is high in winter and low in summer, which coincides with the variations of anticyclone activities and the shift of the ITCZ over the subcontinent. During the summer-winter transitions, anticyclones over the South Atlantic Ocean and the Indian Ocean weaken and expand towards the southern continents. During winter, the anticyclones merge over

southern Africa and form a high-pressure zonal band (i.e., a high-pressure system) that dominates over southern Africa. In summer, the high-pressure zonal band breaks up, and the South Atlantic Ocean and Indian Ocean high-pressure cell contract and migrate towards their respective oceanic basins (Sun et al., 2017). Also, in summer, the concentration of the southern high-pressure cells over the Atlantic and Indian oceans and the presence of the ITCZ over southern Africa results in the dominance of a low-pressure system over the subcontinent. Most of the time series are characterised by low levels of noise and a high degree of stationarity. This could be because climatic conditions, like the change of anticyclone activities, take a long time to occur and, over most parts of southern Africa, annual anticyclone variability is low. Seasonal atmospheric pressure fluctuations are found to be higher in the Desert and Mediterranean climatic zones and lower in the Wet and Dry tropical climatic zones. This could be because of the higher insolation difference in summer and winter in the Desert climatic zone than in Tropical climatic zones. High seasonal atmospheric pressure fluctuations in the Desert and Mediterranean climatic zones may be due to seasonal insolation fluctuation rates in these climatic zones due to the absence or scarcity of the presence of clouds.

7.1.4 Rainfall time series

Rainfall time series are mainly composed of an annual frequency component, but vary significantly on an annual basis. The phase of the annual component varies spatially and temporally. The central-and north-eastern parts of southern Africa are summer rainfall regions, while the south-western parts of southern Africa are winter rainfall regions. The rainfall seasons across southern Africa vary mainly due to the differences in rainfall sources across the central, north-eastern and south-western parts of southern Africa. In the central and north-eastern parts of southern Africa, the ITCZ is the primary source of rainfall (Hobbs et al., 1998). The rainfall season occurs when the ITCZ passes over southern Africa in summer. In the south-western parts of southern Africa, rainfall is associated with the inflow of low- and high-level westerlies that carry moist air (Ellis and Galvin, 1994; Barry and Chorley, 2010, p. 372). Rainfall during the winter and summer season in southern Africa is highly variable, both on the intra-annual and inter-annual scale due to influences from several processes, such as the ITCZ, solar radiation, ENSO, and variations in atmospheric circulation (Potter and Colman, 2003, p. 837; Jury, 2013; MacKellar et al., 2014). Rainfall seasonality is high in the Wet and Dry Topical climatic zones and low in the Desert climatic zone. This is because of a higher annual rainfall rate in the tropics due to the passing of the ITCZ over the zone and lower annual

insolation rates compared to the desert climatic zones. Low rainfall rates in the Desert climatic zone are related to the ITCZ not passing over the climatic zone and high insolation rates due to the absence of clouds.

7.1.5 Humidity time series

Humidity time series consist of an annual and semi-annual frequency component. They vary as a function of time and spatial geographic location, like the rainfall time series. In the central and north-eastern parts of southern Africa, the moisture content is high during summer and low during winter; while in the south-western parts of southern Africa, humidity levels are high during winter and low during summer. This difference is due to differences in humidity source in the central, north-eastern parts of southern Africa and in the south-western parts of southern Africa. In summer, the moist air in the central and north-eastern parts of southern Africa is brought by inflowing easterlies that carry moist air from the southwest Indian Ocean and warm Agulhas currents; while in winter, the dry air is brought by the westerlies from the south Atlantic Ocean and cool Benguela Currents (Chase and Meadows, 2007; Jury, 2013). In the south-western parts of southern Africa, moist air is brought about by westerlies as they move towards the equator during the winter (Chase and Meadows, 2007). Hobbs et al. (1998, p. 20), reports that because of the influence of the ITCZ in southern Africa, moist air is greatest towards the tropics (Wet and Dry Tropical climatic regions) and diminishes towards the semi-arid regions. However, in this study, we observed that humidity fluctuations are greater in the semi-arid regions than in tropical regions. This could be because annual humidity seasonality is more defined in the semi-arid region than in the tropics. The humidity content across both regions is highly variable and, at times, not continuous at a station over the considered observation period.

Since southern Africa is situated in between the Atlantic Ocean, Indian and Southern oceans; temperature, pressure, rainfall and humidity fluctuation in southern Africa are primarily controlled by the complex interaction between midlatitude, tropical and subtropical climate systems, as well as the development, seasonal positional-shift and interaction of atmospheric and oceanic circulation systems of the Atlantic Ocean, Indian Ocean and Southern oceans (Chase and Meadows, 2007).

7.2 Relationship between cGPS displacement and meteorological time series components

This section focuses on the significance of the results obtained from Cross-spectrum, Coherence, Phase, and Wavelet Transform (WT) Semblance correlation and Phase Difference analyses with the aim of drawing interpretations based on the relationship between surface displacement and the meteorological processes.

7.2.1 Relation between rainfall, humidity and surface deformation

Analysing the relationship between rainfall, humidity and surface displacement reveal that the relationship between these processes varies spatially, moving from the central, and north-eastern parts of southern Africa to the south-western parts of southern Africa. Time, frequency and phase correlation between rainfall-surface displacement and humidity-surface displacement reveal moderate to low and inconsistent frequency component and phase correlation between the time series. These observations are interpreted to imply that i) Rainfall and humidity processes do not have much influence on seasonal surface displacement variations, and ii) the type of interaction, i.e., whether contractive or destructive, rainfall and humidity processes have with surface displacement varies spatially as postulated below.

1. In the central and north-eastern parts of southern Africa, the rainfall-displacement and humidity-displacement time series are directly correlated. Thus, in summer, it is possible that constructive interference occurs between rainfall and humidity induced surface deformation effects, with surface deformation effects induced by variations in surface air temperature and atmospheric pressure. Constructive interference may be occurring between surface deformation effects due to soil absorption of water molecules and seasonal tropospheric error introduced in the cGPS datasets due to high rainfall and humidity levels; with thermal expansion effects caused by thermal expansion of soil particles and water molecules in the near subsurface; and thermal expansion of concrete and metallic components of the cGPS stations in response to the prevalence of high temperatures and low atmospheric pressure.

2. In the south-western parts of southern Africa, the rainfall-displacement and humidity-displacements are anticorrelated. Thus, in winter, it is possible that destructive interference occurs between rainfall and humidity induced surface deformation effects, with surface

deformation effect induced by variations in surface air temperature and atmospheric pressure. Destructive interference may be occurring between surface deformation effects due to soil absorption of water molecules and seasonal tropospheric error introduced in the cGPS datasets due to high rainfall and humidity levels, with thermal contraction effects due to the contraction of soil particles and water molecules in the near subsurface, and thermal contraction of concrete and metallic components of the cGPS stations in response to the prevalence of cold temperatures and high atmospheric pressure.

7.2.2 Relation between surface air temperature, atmospheric pressure and surface deformation

Analysing the relation between surface air temperatures, atmospheric pressure and surface displacement, it was observed that surface displacement is high during the summer, when temperatures are high and atmospheric pressure is low, and low in the winter when temperatures are low and atmospheric pressure is high. This might be partly because high surface air temperatures cause thermal expansion of consolidated soil particles and water molecules in the near subsurface, which instigates thermal expansion of the near subsurface rocks, while low surface air temperatures cause thermal contraction of consolidated soil particles and water molecules, which prompts thermal contraction of near subsurface rocks. Seasonal high and low temperatures also cause thermal expansion and contraction of the concrete and metallic components of the cGPS monument, which could also contribute to the surface deformation measurements recorded by cGPS systems. Furthermore, high and low surface air temperatures cause thermal expansion and contraction of the atmospheric mass, which results in a decrease and an increase in atmospheric air-mass density and atmospheric pressure, respectively. Since low atmospheric pressure favours thermal expansion and high atmospheric pressure favours thermal contraction, this increases the chances of thermal expansion occurring in summer and thermal contraction occurring in winter.

In addition, frequency and phase correlation results between surface displacement-surface air temperature time series and surface displacement-atmospheric pressure time series show a high and consistent frequency and phase correlation between the time series, suggesting that seasonal surface air temperature and atmospheric pressure variations might have a high influence on surface deformation.

7.2.3 Relation between annual and semi-annual surface displacement and meteorological process frequency components

Decomposition results show that, like surface displacement time series, surface air temperature and humidity time series consist of an annual and semi-annual frequency component, while rainfall and atmospheric pressure time series consist predominantly of an annual frequency component only. This indicates that all the considered meteorological processes may contribute to annual surface deformation, while only temperature and humidity processes have the potential to contribute to semi-annual surface deformation. Correlating surface air temperature and humidity time series with surface displacement time series, in the time-frequency domain, shows that correlation between the semi-annual components of the time series is not continuous. The phase lag of the semi-annual component varies a lot over the observation time, suggesting that, even though temperature and humidity processes might contribute to semi-annual surface displacements, they do not contribute much.

7.3 Surface air temperature and displacement fluctuations

Table 17 gives the annual surface air temperature power and surface displacement power values at stations DEAR, SBOK, MFKG, ULDI, and UMTA computed using the fast Fourier transform (FFT) technique. It also gives information about the cGPS monument description, monument height, foundation depth, site geology, International Terrestrial Reference Frame model and whether a station has a temperature stabiliser or not. The descriptive information about the stations was taken from cGPS station log files obtained at (ftp://igs.org/pub/station/log). Data from only five stations are analysed because station log files for the other cGPS station, excluding the ones in Table 17, could not be obtained.

Although the focus of this analysis is on the relationship between annual surface displacement and surface temperature fluctuation, in Table 17, station and site parameters are included because they are also expected to contribute to the annual surface displacement recorded at the stations. In Table 17, the cGPS stations are arranged based on areas of high surface temperature fluctuation to areas of low surface temperature fluctuation, to make it easier to study the relationship between surface displacement and surface temperature fluctuation. Based on the findings of the study obtained so far, it is expected that stations exposed to high annual surface temperature fluctuation are most likely to be characterised by high annual surface displacement and vice versa.

Table 17: Station and site parameters at stations DEAR, SBOK, MFKG, UMTA and ULDI; and annual surface temperature and displacement power at the stations.

Station	Station parameters						Site parameter	Annual temperature cycle power	Annual surface Displacement power
	Monument description	Monument height (m)	Monument foundation	Foundation depth (m)	ITRF	Temperature stabilisers	Site Geology and climatic zone		
DEAR	Concrete beacon built on rock	1.8 m	concrete	0.5 m	ITRF2005	None	Bedrock/gravel (Desert)	26648	0.0146
SBOK	Concrete pillar	2.4 m	-	0.5 m	ITRF2005	None	Bedrock/gravel (Desert)	17539	0.0174
MFKG	Concrete beacon built on gravel sand/clay	2.4 m	concrete	0.5 m	ITRF2005	None	Gravelsand/clay (Sahelian)	15758	0.0121
UMTA	Concrete beacon built on sand/clay	2.4 m	concrete	0.5 m	ITRF2005	None	Sand/clay (Wet tropical)	8794	0.0025
ULDI	Antenna pipe on parapet wall	-	-	-	ITRF2005	None	Sand/clay (Wet tropical)	7886	0.0049

Plotting surface displacement against temperature, Figure 7.1, shows that, generally, stations exposed to high annual surface temperature fluctuation are characterised by high annual surface displacement fluctuation (i.e., DEAR, SBOK and MFKG) and those exposed to low annual surface temperature fluctuations are characterised by low surface displacement fluctuations (i.e., ULDI and UMTA), as expected.

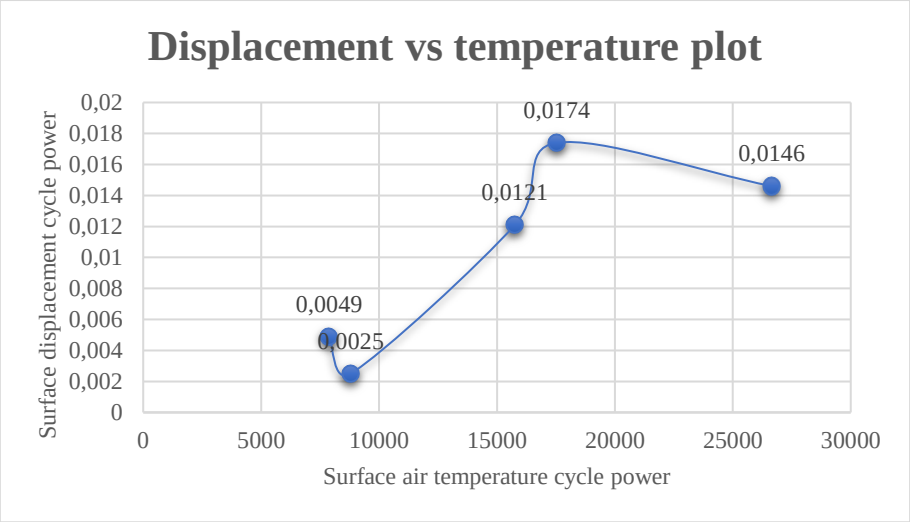


Figure 7.1: Surface air temperature cycle power vs surface displacement cycle power.

However, closely analysing the annual surface displacement and annual surface temperature fluctuation relation at stations ULDI and UMTA; and SBOK and DEAR it is observed that the relationship between annual surface displacement and surface temperature fluctuation is not entirely proportional (Figure 7.1).

It is observed that even though station UMTA is exposed to higher annual surface temperature fluctuation than station ULDI, it is subjected to lower annual surface displacement fluctuation than station ULDI. Considering that the geology, climatic zone and ITRF at the cGPS stations UMTA and ULDI are the same, it might be that the deviation from the expected temperature and surface displacement relation at the stations could be partly because of the parapet wall station ULDI is mounted on (Table 17). On a seasonal basis, it is possible that the parapet wall might be undergoing more thermal expansion and contraction than the concrete beacon station UMTA is mounted on. Although, it is possible that the deviation from the expected temperature-surface displacement might be cause by other station parameter or processes, such as the differences in monument height, foundation depth, and monument foundation of the stations, i.e., if there is any.

Likewise, in Table 17, it is observed that station DEAR is exposed to more annual surface temperature fluctuations than station SBOK, however station SBOK is observed to be subjected to more surface displacement than station DEAR. In this case, considering that the site geology, foundation depth, and the ITRF used to collect the data at stations DEAR and SBOK are the same, it is possible that the observed deviation from the expected temperature and surface displacement relationship, might be partly due to the difference in monument height at the stations (Table 17). The monument height at station DEAR is 1.8 m and at station SBOK, it is 2.4 m, thus station SBOK is most likely subject to greater monument thermal expansion and contraction compared to station DEAR.

In general, the deviation of the temperature and surface displacement fluctuation relationship from the expected is thought to indicate that annual seasonal temperature fluctuation is not the only factor contributing to the annual seasonal surface displacement component observed in cGPS time series. Unfortunately, due to obtaining information for only one station mounted on a building (i.e., station ULDI), the effects of mounting a cGPS station on a building could not be accessed.

Table 18 gives a summary of the relation between surface displacement and meteorology time series.

Table 18: Summary of the relation between surface displacement and meteorology processes. TS, TD, and FD stand for time series, time domain and frequency domain, respectively.

Relationship between variations in surface displacement and meteorological processes				
Regions	**Surface displacement & temperature**	**Surface displacement & pressure**	**Surface displacement & humidity**	**Surface displacement & rainfall**
South-western part of southern Africa	TS are directly correlated	TS are directly correlated	TS are inversely correlated	TS are inversely correlated
	Moderate TD correlation	Low TD correlation	Low TD correlation	Low TD correlation
	High, positive and consistent annual component FD phase correlation	High, negative and consistent annual component FD phase correlation	Moderate to low, negative and inconsistent annual component FD phase correlation	Moderate to low, negative and inconsistent annual component FD phase correlation
	High to moderate and Inconsistent semi-annual component FD phase correlation	Predominantly no semi-annual FD phase correlation	Inconsistent semi-annual component FD phase correlation. Moderate to low phase correlation	Predominantly no semi-annual FD phase correlation
Central, eastern and northern parts of southern Africa	TS are directly correlated	TS are directly correlated	TS are directly correlated	TS are directly correlated
	Moderate TD correlation	Low TD correlation	Low TD correlation	Low TD correlation
	High, positive and consistent annual component FD phase correlation	High, negative and consistent annual component FD phase correlation	Moderate to low, negative and inconsistent annual component FD phase correlation	Moderate to low, negative and inconsistent annual component FD phase correlation
	High to moderate and Inconsistent semi-annual component FD phase correlation	Predominantly no semi-annual FD phase correlation	Inconsistent semi-annual component FD phase correlation. Moderate to low phase correlation	Predominantly no semi-annual FD phase correlation

8 Conclusion

In the study, seasonal surface displacement and meteorological (surface air temperature, atmospheric pressure and humidity) time series are analysed using time series techniques. The main goals of the research are to 1) improve the understanding of the time series, 2) better understand the seasonal effects that surface air temperature, atmospheric pressure, rainfall and humidity processes have on the surface displacement measured by cGPS systems, and 3) find out if time series analysis can be used to analyse surface deformation time series successfully. The time series signals are measured using cGPS and meteorological stations distributed within southern Africa.

The analysis of these time series shows that the annual surface air temperature and atmospheric pressure variations are in phase with surface displacement variations. The power of the time series varies systematically from one climatic zone to another. The phase difference between surface displacement-surface air temperature and surface displacement-atmospheric pressure time series is low and consistent throughout the study area. The annual and semi-annual frequency component correlation between the time series is observed to be high. These findings imply that, at the considered locations, surface air temperature and atmospheric pressure variations have a significant contribution to the observed cGPS surface displacements compared to heave action.

The relationship between surface displacement, rainfall and humidity time series shows that both the phase and frequency component correlation relation between these processes is non-consistent and often low. In winter rainfall regions, the surface displacement-rainfall and surface displacement-humidity time series are anticorrelated. This suggests that, in these regions, rainfall and humidity effects on the surface displacement act against temperature and pressure effects on surface displacement. In summer rainfall regions, surface displacement-rainfall time series and surface displacement-humidity time series are positively correlated, suggesting that, in these regions, rainfall and humidity effects on surface displacement interact constructively with temperature and atmospheric pressure effects on surface displacement.

Additionally, frequency domain component analysis shows that temperature and humidity time series are correlated on an annual and semi-annual, while atmospheric pressure and rainfall time series are correlated with the surface displacement time series on an annual scale only, implying that all the considered meteorological time series have an influence on annual surface displacements, while only temperature and humidity processes are most likely to have an

influence on the semi-annual surface displacement component. Phase correlation between surface displacement, temperature and humidity time series shows that the semi-annual phase of the time series is not consistent, implying that, even though temperature and humidity processes might have an influence on the semi-annual surface displacements, they are not major contributing sources of the semi-annual surface displacements.

Finally, the time series analysis techniques were used successfully to study surface displacement and meteorological time series, and their relationship. The results obtained show that all the considered meteorological processes have a direct or indirect influence on seasonal surface displacement. The extent to which the processes have an influence on surface deformation is partially dependent on the climatic zone in which the cGPS stations are located. Changes in surface air temperature and atmospheric pressure have a greater influence on surface displacement or surface displacement measurements than rainfall and humidity processes.

Furthermore, time domain correlation results show that there is a negligible correlation between atmospheric pressure, rainfall, humidity and surface deformation time series. This could be because seasonal effects due to atmospheric loading, heave action and tropospheric residual errors, in the study area, are small in the surface displacement measurements. This suggests that correcting for thermal expansion and thermal induced errors could further reduce errors in the magnitude of the seasonal surface displacement components.

8.1 Limitations and recommendations

This study has the following limitations.

1. The number of cGPS and meteorological time series used in this study is small. This is due to the lack of data availability and good data for most parts of southern Africa. This forced us to infer results for the most part of southern Africa from results of a smaller part of the subcontinent. Consequently, this limitation reduces the statistical reliability of the results, the analysis and interpretation confidence. Therefore, I recommend installing more cGPS and meteorological stations in each climatic zone, adequate distribution, and better maintenance of the cGPS stations. These recommendations would greatly improve the outcome of future research in the study area.

2. The ambient noise sources affecting the cGPS and meteorological stations are likely to be different, considering that the stations are separated by a few kilometres. Using cGPS and meteorological stations separated by a few meters would be ideal to conduct the study, but unfortunately, this is not possible in our study area, since the cGPS and meteorological stations are far apart. However, this is not a big issue since ambient noise is not expected to affect the data collected by the stations much.

3. The empirical technique used to calculate estimates of potential heave in chapter 6.3.1 is of low accuracy. The used technique does not take into consideration the initial moisture content or the void ratio of the soil, which are two important properties of soil that influence the amount of heaving. A modified and more accurate version of the technique was proposed by Jones (2017); however, it could not be used in this study because of the unavailability of initial moisture content and liquid limit measurements for the expansive soils at the cGPS locations. In order to improve the estimates, soil type, initial moisture content and liquid limit measurements must be collected at the cGPS station location and then used to estimate the potential heave at the locations.

9 References

Adler, J. and Parmryd, I. (2010). Quantifying colocalization by correlation: The Pearson correlation coefficient is superior to the Mander's overlap coefficient. International Society for Advancement of Cytometry, Sweden, 77A, 733-742.

Akkala, A., Devabhaktuni, V. and Kumar, A. (2010). Interpolation techniques and associated software for environmental data. American Institute of Chemical Engineers, 29, 134-141, doi:10.1002/ep.10455.

Altamimi, Z., Angermann, D., Argus, D., Blewitt, G., Boucher, C., Chao, B., Drewes, H., Eanes, R., Feissel, M., Ferland, R., Herring, T., Holt, B., Johannson, J., Larson, K., Ma, C., Manning, J., Meertens, C., Nathnagel, E.P., Petit, G., Ray, J., Ries, J., Scherneck, H., Sillard, P. and Watkins, M. (2001). The Terrestrial Reference Frame and the Dynamic Earth. American Geophysical Union, 82, 278-279.

Altamimi, Z., Collilieux, X. and Metivier, L. (2011). ITRF2008: An improved solution of the International Terrestrial Reference Frame. Journal of Geodesy, 85, 457-473.

Altamimi, Z., Van Dam, T., Kutterer, H. and Rizos, C. (2012). Role and importance of the International Terrestrial Reference Frame for sustainable development, IAG-GGOS-ITRF,100.

Anderson, D.R., Sweeney, D.J. and Williams, T.A. (2011). Statistics for business and economics 11th edition. South-Western Cengage Learning, United State of America.

Arsham, H. and Shao, S.P. (1985). Seasonal and cyclic forecasting for the small firm. American Journal of Small Business, 9, 46-57.

Baisch, S. and Bokelmann, G.H.R. (1999). Spectral analysis with incomplete time series: an example from seismology. Computer & Geosciences, 25, 739-750.

Baker, J.W. (2007). Quantitative classification of near-fault ground motions using wavelet analysis. Bulletin of the Seismological Society of America, 97, 1486-1501, doi:10.1785/0120060255.

Barry, R.G. and Chorley, R.J. (2010). Atmosphere, weather and climate, 9th edition. Routledge Taylor & Francis Group, USA and Canada.

Barse, E.L., Kvarnström, H. and Jonsson, E. (2003). Synthesizing test data for fraud detection systems. Processdings of the 19th Annual Computer Security Applications Conference (ACSAC 2003), 1-11.

Baselli, G., Cerutti, S., Civardi, S., Liberati, D., Lombardi, F., Malliani, A. and Pagani, F. (1985), Spectral and cross-spectral analysis of heart rate and arterial bold pressure variability signals. Computers and Biomedical, 19, 520-534.

Baxter, M. and King, R.G. (1999). Measuring business cycles: Approximate band-pass filters for economic time series. The Review of Economic and Statistics, 81, 575-593.

Bell, F.G. and Maud, R.R. (1995). Expansive clays and construction, especially of low-rise structures: A viewpoint from natal, South Africa. Environmental & Engineering Geoscience, I, 41-59.

Bell, W.R. and Hillmer, S.C. (1984). Issues involved with the seasonal adjustments of economic time series. Journal of Business & Economic Statistics, 2, 291-320.

Bendat, J.S. and Piersol, A.G. (2010). Random data analysis and measurement procedures 4th edition. John Wiley & Sons. United States and Canada.

Beveridge, S. and Nelson, C.R. (1981). A new approach to decomposition of economic time series into permanent and transitory components with particular attention to measurements of the 'business cycle'. Journal of Monetary Economics, 7, 151-174.

Bidikar, B., Rao, G.S., Ganesh, L. and Kumar, M.S. (2014). Satellite clock error and orbital solution error estimation for precise navigation applications. Scientific Research, 5, 22-26.

Blewitt, G. (2015). Terrestrial Reference Frame requirements for studies of geodynamics and climate change. International Association of Geodesy Symposia, University of Nevada, Reno, 1- 8, doi:10.1007/1345_2015_142.

Bollasina, M. and Nigam, S. (2010). The summertime "heat" low over Pakistan/northwestern India: evolution and origin. Climate Dynamics, 37, 957-970, doi:10.1007/s00382-010-0879-y.

Brockwell, P.J. and Davis, R.A. (2002). Introduction to time series and forecasting 2nd edition. Springer, USA, New York.

Burden, R.L. and Faires, J.D. (2011) Numerical Analysis: 9th edition. Brooks/Cole, Cengage learning, United States of America, pp. 144-147.

Byrne, M.P., Pendergrass, A.G., Rapp, A.D. and Wodzicki, K.R. (2018). Response of the Intertropical Convergence Zone to climate change: location, width, and strength. Current Climate Change Reports, 4, 355-370, doi:10.1007/s40641-018-0110-5.

Chase, B.M. and Meadows, M.E. (2007). Late Quaternary dynamics of southern Africa's winter rainfall zone. Earth-Science Reviews, 84, 103-138. doi:10.1016/j.earscirev.2007.06.002.

Christensen, A.N. (2003). Semblance filtering of airborne potential field data. In Extended Abstracts, 16th ASEG Geophysical Conference and Exhibition, Adelaide.

Clayton, R.H. and Murray, R. (1993). Estimation of the ECG signal spectrum during ventricular fibrillation using the fast Fourier transform and maximum entropy methods. Proceedings of Computers in Cardiology Conference IEEE, 867-870, doi: 10.1109/CIC.1993.378299.

Cochran, W.T., Cooley, J.W., Favin, D.L., Helms, H.D., Kaenel, R.A., Lang, W.W., Maling, G.C., Nelson, D.E., Rader, C.M. and Welch, P.D. (1967). What is the Fast Fourier Transform. IEEE Transactions on Audio and Electroacoustics, 55, 1664-1674.

Cooper, G.R.J. (2009). Wavelet-based semblance filtering. Computers & Geosciences, 35, 1988-1991, doi:10.1016/j.cageo.2008.10.017.

Cooper, G.R.J. and Cowan, D.R. (2008). Comparing time series using wavelet-based semblance analysis. Computers & Geosciences, 35, 95-102, doi:10.1016/j.cageo.2007.03.009.

Creese, A., Pokam, W., Washington, R., Hart, N., Blamey, R., Kolusu, S., Desbiolles, F., James, R., Crees, A. and Munday, C. (2016). Africa's climate helping decision-makers make sense of climate sense of climate information. Future Climate for Africa

Cui, Y.J., Sultan, N. and Delage, P. (2000). A thermomechanical model for saturated clays. Canadian Geotechnical Journal, 37, 607-620.

Cui, Y.J. and Tang, A.M. (2013). On the chemo-thermo-hydro-mechanical behaviour of geological and engineered barriers. Journal of Rock Mechanics and Geotechnical Engineering, 5, 169-178, doi:10.1016/j.jrmge.2013.05.001.

Daron, J.D. (2014). Regional climate messages: Southern Africa. Scientific report from the CARIAA Adaptation at Scale in Semi-Arid Regions (ASSAR) Project, December 2014.

Davis, J.L., Wernicke, B.P. and Tamisiea, M.E. (2012). On seasonal signals in geodetic time series. Journal of Geophysical Research, 117, 1-10, doi:10.1029/2011JB008690.

Delage, P., Sultan, N. and Cui, Y.J. (2000). On the thermal consolidation of Boom clay. Canadian Geotechnical Journal, 37, 343-353.

Dogan, U., Uludag, M. and Demir, D.O. (2014). Investigation of GPS positioning accuracy during the seasonal variation. Measurement, 53, 91-100, doi:10.1016/j.measurement.2014.03.034.

Dong, D., Fang, P., Bock, Y., Cheng, K. M. and Miyazaki, S. (2002). Anatomy of apparent seasonal variations from GPS-derived site position time series. Journal of Geophysical Research, 107, 1-17, doi:10.1029/2001JB000573.

Dong, D., Yunck, T. and Heflin, M. (2003). Origin of the International Terrestrial Reference Frame. Journal of Geophysical Research, 108, 1-10, doi:10.1029/2002JB002035.

Drouin, V., Heki, K., Sigmundsson, F., Hreindóttir, S., and Ófeigsson, G. (2016). Constraints on seasonal load variations and regional rigidity from continuous GPS measurements in Iceland, Geophysical Journal International, 205, 1843-1858, doi:10.1093/gji/ggw122.

Dumitru, P.D., Plopeanu, M. and Badea, D. (2013). Comparative study regarding the methods of interpolation. Advances in Geodesy and Geomatics Engineering, 1, 45-52.

Dutt, V.B.S.S.I., Rao, G.S.B., Rani, S.S., Babu, S.R., Goswami, R. and Kumari, C.U. (2009). Investigation of GDOP for precise user position computation with all satellites in view and optimum four satellite configurations. Journal of Indian Geophysical Union, 13, 139-148.

El-Rabbany (2002). Introduction to GPS: The Global Positioning System, Artech House, London.

Ellis, J. and Galvin, K.A. (1994). Climate patterns and land-use practice in the dry zones of Africa. American Institute of Biological Sciences, 44, 340-349.

Elson, J.M. and Bennett, J.M. (1995). Calculation of the power spectral density from surface profile data. Optical Society of America, 34, pp. 201-208.

Eriksson, A. I. (2000) Spectral analysis. Swedish Institute of Space Physics Uppsala, Sweden.

Farge, M. (1992). Wavelet transforms and their applications to turbulence. Annual Review of Fluid Mechanics, 24, 394-457.

Farrell, W.E. (1972). Deformation of the Earth by Surface loads. Reviews of Geophysical and Space Physics, 10, 761-797.

Ferguson, M. (2000). Global Positioning System (GPS) error source prediction. Master's Degree Thesis, Air Force institute of Technology.

Fletcher, P. and Sangwine, S.J. (2017). The development of the quaternion wavelet transform. Signal Processing. 136, 2-15, doi:10.1016/j.sigpro.2016.12.025.

Florides, G. and Kalogirou. S. (2005). Annual ground temperature measurements at various depths. 8th REHVA Wold Congress, Lausanne.

Florides, G. and Kalogirou, S. (2007). Ground heat exchangers – A review of systems models and applications. Renewable Energy, 32, 2461-2478, doi:10.1016/j.renene.2006.12.014.

Foster, G. (1995). The cleanest Fourier spectrum. The Astronomical Journal, 109, 1889-1902.

Foster, G. (1996). Wavelets for period analysis of unevenly sampled time series. The Astronomical Journal, 112, 1709-29, doi:10.1086/118137.

Friston, K. J., Bastos, A., Litval, V., Stephan, K. E., Fries, P. and Moran, R.J. (2011). DCM for complex-valued data: Cross-spectra, coherence and phase delays. Elsevier Inc,59, 439-455. doi:10.1016/j.neuroimage.2011.07.048.

Gauthier, T.D. (2001). Detecting trends using Spearman's correlation coefficient. Environmental Forensics, 2, 359-362, doi:10.1006/enfo.2001.0061.

Gladkikh, V., Tenzer, R. and Denys, P. (2011). Crustal deformation due to atmospheric pressure loading in New Zealand. Journal of Geodetic Science, 1, 271-279, doi:10.2478/v10156-011-0005-z.

Goudarzi, M.A., Cocard, M., Santerre, R. and Woldai, T. (2012). GPS interactive time series analysis software. GPS Solutions, 17, 595-603, doi:10.1007/s10291-012-0296-2.

Granger, C.W.J. (1969). Investigating causal relations by economic models and cross-spectral methods. Econometrica, 37, 424-438.

Graps, A. (1995). An introduction to wavelets. IEEE Computational Science and Engineering, 2, 50- 61.

Guochang, X. (2007). GPS: Theory, Algorithms and Applications 2nd edition. Geodesy and Remote Sensing, Springer, Germany.

Harris, F.J. (1976). Windows, Harmonic analysis, and the discrete Fourier transform. Naval Undersea Center, San Diego, California, 92132.

Harris, F.J. (1978). On the use of windows for harmonic analysis with the discrete Fourier transform. Proceedings of the IEEE, 66, 51-83.

Hauke, J. and Kossowski, T. (2011). Comparison of values of Pearson's and Spearman's correlation coefficients on the same sets of data. Quaestiones Geographicae, Poland, 30, 87-93.

Hawkins, J.E. and Stevens, S.S. (1950). The masking of pure tones and speech by white noise. The Journal of the Acoustical Society of America, 22, 6-13, doi:10.1121/1.1906581.

Hayashi, Y. (1981). Space-time cross spectral analysis using the maximum entropy method. Journal of the Meteorological Society of Japan, 59, 620-623.

He, X., Hua, X., Yu, K., Xuan, W, Lu, T., Zhang, W. and Chen, X. (2015). Accuracy enhancement of GPS time series using principal component analysis and block spatial filtering. Advances in Space Research, 55, 1316-1327, doi:10.1016/j.asr.2014.12.016.

Heil, C.E. and Walnut, D.F. (1989). Continuous and discrete wavelet transforms. Society for Industrial and Applied Mathematics, 31, 628-666.

Hepburn, H.R. and Radloff, S.E. (1998). Honeybees of Africa. Springer-Verlag Berlin Heidelberg GmBH, United States of America, doi:10.1007/978-3-662-03604-4.

Herbert, J.M. and Dixon, W. (2002). Is the ENSO phenomenon changing as a result of Global Warming? Physical Geography, 23, 196-211, doi:10.2747/0272-3646.23.3.196.

Hintzen, N.T., Piet, G.J. and Brunel, T. (2010). Improved estimation of trawling tracks using cubic Hermite spline interpolation of position registration data. Fisheries Research, 101, 108-115.

Hobbs, J.E., Lindesay, L.A. and Bridgman, H.A. (1998). Climate of the southern continents: present, past and future. John Wiley & Sons, New York.

Ito, A. (1985). High resolution relative hypocenters of similar earthquakes by cross-spectral analysis method. Journal of Physics of the Earth, 33, 279-294.

Ito, M., Azam, S. and Hu, Y. (2014). A two stage model for moisture-induced deformations in expansive soils. Environmental Systems Research, 3:19.

James, J.F. (2011). A study's Guide to Fourier transforms 3th ed: with applications in physics and Engineering. United States of America. Cambridge University Press.

Jensen, O., Spaak, E. and Zumer, J.M. (2014). Human brain oscillations: from physiological mechanisms to analysis and cognition. Magnetoencephalography, 359-404, doi:10.1007/978-3-642-33045-2_17.

Johnson, R.H. (2003). Thermal low. Encyclopedia of Atmospheric Sciences, 1, p. 2269-2273.

Jones, G.A. (2017). Am empirical preliminary prediction of heave. Journal of the South African Institution of Civil Engineering, 59, 64-66.

Jury, M.R. (2013). Climate trends in southern Africa. South African Journal of Science, 109, 1-11, doi:10.1590/ sajs.2013/980.

Kaiser, G. (1994). A friendly guide to wavelets. United States of America, Birkhäuser, doi:10.1007/978-0-8176-8111-1.

Kaiser, G. (2011). A friendly guide to wavelets. United States of America, Birkh*ä*user, doi:10.1007/978-0-8176-8111-1.

Kaplan, E.D. and Hegarty, C.J. (2006). Understanding GPS principles and applications, 2nd edition. Artech House, Inc. London.

Kay, S.M and Marple, S.L. (1981). Spectrum analysis-a modern perspective. Proceedings of the IEEE, 69, 1380-1419.

Khademi, F. and Budiman, J. (2016). Expansive soil: causes and treatment. Journal of Civil Engineering, 6, 1-13, doi:10.26634/jce.6.3.8083.

Khan, S.A. (2005). Surface deformation analyzed using GPS time series. Danish National Space Center, Copenhagen.

Kosek, W., Wenk, A., Zbylut-G*ó*rska, M. and Popi*ń*ski, W. (2014). Wavelet analysis of the Earth center of mass time series determined by satellite techniques. Journal of Geodynamics, 253, 30-198, doi:10.1016/j.jog.2014.02.005.

Kovács, G. (1980). Frequency shift in Fourier analysis. Astrophysics and Space Science, 78, 175-188.

Kristina, M.R., Alan, V.S., Jeffrey, M.B. and Swiryn, S. (1989). The coherence spectrum: A quantitative discriminator of fibrillatory and nonfibrillatory cardiac rhythms. American Heart Association, 80, 112-119. doi:10.1161/01.CIR.80.1.112.

Langbein, J. and Johnson, H. (1997). Correlated errors in geodetic time series: Implications for time-dependent deformation. Journal of Geophysical Research, 102, 591-603.

Larson, K.M. and Agnew, D.C. (1991). Application of the Global Positioning System to crustal deformation measurements. Journal of Geophysical Research, 96, 547-565.

Leavey, C.M., James, M.N., Summerscales, J. and Sutton, R. (2003). An introduction to wavelet transforms: a tutorial approach. Insight-non destructive Testing and Condition Monitoring, 45, 344-353.

Legates, D.R. and Willmott, C.J. (1990). Mean seasonal and spatial variability in global surface air temperature. Theoretical and Applied Climatology, 41, 11-21.

Lehmann, M.L., G*ö*nner, C. and Spitzer, K. (1999). Survey: Interpolation methods in medical image processing. IEEE Transactions on medical imaging, 18, 1049-1075.

Levy, D. (2010). Introduction to numerical analysis. Department of Mathematics and Center for Scientific Computation and Mathematical Modeling (CSCAMM), University of Maryland, pp. 25.

Li, H., He, Y. and Sun, Y. (2014). A PSO method foe wavelet approximation. Information Technology Journal, 13, 661-668, doi:10.3923/itj.2014.661.668.

Li, J. and Heap, D. (2008). A review of spatial interpolation methods for environmental scientists. Geoscience Australia.

Linacre, E. and Geerts, B. (1997). Climate and weather explained. Routledge Taylor & Francis Group, London.

Liner, C. (2010). An overview of wavelet transform concepts and applications. Houston, Texas, United States: University of Houston.

Lucia, C. (2011). Geotechnology to determine the depth of active zone in expansive soils in Kibaha, Tanzania. Global Journal of Pure and Applied Sciences, 17., 189-195.

MacKeller, N., New, M. and Jack, C. (2014). Observed and modelled trends in rainfall and temperature for Southern Africa: 1960-2010. South African Journal of Science, 110, 1-13.

Mallat, S. (1999). A wavelet tour of signal processing 2nd edition. USA. Academic Press.

Mallat, S. (2009). A wavelet tour of signal processing 3rd edition. USA. Academic Press Inc.

Márquez, J.M.A., Bohórquez, M.Á.M. and Melgar, S.G. (2016). Ground thermal diffusivity calculation by direct soil temperature measurement: Application to very low Enthalpy Geothermal Energy Systems. Sensors,16, 1-13, doi:10.3390/s16030306.

McCarthy, T. and Rubidge, B. (2005). The story of Earth and life: A southern African perspective on a 4.6-billion-year journey. Struik Nature, South Africa.

McNamara, J. (2004). GPS for Dummies, Wiley Publishing Inc, Indianapolis., Canada.

Min, W., Zheng-Kang, S. and Da-Nan, D. (2005). The effect and correction of non-tectonic crustal deformation and continuous GPS position time series. Chinese Journal of Geophysics, 48, 1121-1129.

Monfared, M., Sulem, J., Delage, P. and Mohajerani, M. (2011). A laboratory investigation on thermal properties of the Opalinus claystone. Rock Mechanics and Rock Engineering, 44, 735-747, doi:10.1007/s00603-011-0171-4.

Mukaka, M.M. (2012). Statistics corner: A guide to appropriate use of correlation coefficient in medical research. Malawi Medical Journal, 24, 69-71.

Nagy, D. and Fury, R.J. (1990). Local geoid computation from gravity using the fast Fourier transform technique. Geological Survey of Canada, 64, 283-294.

Najmi, A.H. and Sadowsky, J. (1997). The continuous wavelet transform and variable resolution time-frequency analysis. John Hopkins APL Technical Digest, 18, 134-140.

National Research Council, (1995). The Global Positioning System: A shared national asset. Washington, DC: The National Academy Press, doi:10.17226/4920.

Nicholson, S.E. and Flohn, H. (1980). African environmental and climatic changes and the general atmospheric circulation in late Pleistocene and Holocene. Climatic Change, 2, 313-348.

Nicholson, S.E. and Kim, J. (1997). The relationship of the El Niño-Southern Oscillation to African rainfall. International Journal of Climatology, 17, 117-135.

Owari, T., Kasahara, H., Oikawa, N. and Fukuoka, S. (2009). Seasonal variation of Global Positionong (GPS) accuracy within the Tokoyo University Forest in Hokkaido. Bull. Tokyo University Forest, 120, 19-28.

Owens, J. and Zorin, D. (1997). Introduction to Wavelets, Mathematical Models for Computer Graphics, Stanford University.

Panofsky, B.A. (1956). Spectrum and cross spectrum analysis of hemispheric westerly index. Pennsylvania State University, USA, 196-200.

Papoulis, A. and Pillai, S.U. (2002). Probability, random variables, and stochastic processes 4th edition. McGraw-Hill. New York, United State of America.

Peng, W., Dai, W., Santerre, R., Cai, C. and Kuang, C. (2017). GNSS vertical coordinate time series analysis using single-channel independent component analysis method. Pure and Applied Geophysics, 174, 723-736, doi:10.1007/s00024-016-1309-9.

Petrov, L. and Boy, L.P. (2004). Study of the atmospheric pressure loading signal in long baseline interferometry observations. Journal of Geophysical Research, 109, 1-14, doi:10.1029/2003JB002500.

Polikar, R. (2001). The engineering ultimate guide to wavelet analysis: the wavelet tutorial. http://users.rowan.edu/~polikar/WAVELETS/WTtutorial.html.

Podder, P., Khan, T.Z. and Khan, M.H. (2014). Comparative Performance Analysis of Hamming, Hanning and Blackman window. International Journal of Computer Applications, 96, 0975-8887.

Potter, T.R. and Colman, B.R. (2003). Handbook of weather, climate, and water: atmospheric chemistry, hydrology and social impacts. John Wiley & Sons, New Jersey.

Prangnell, J. and McGowan, G. (2009). Soil temperature calculation for burial site analysis. Forensic Science International. 191, 104-109, doi:10.1016/j.forsciint.2009.07.002.

Pulinets, S.A. and Boyarchuk, K.A. (2004). Ionospheric precursors of earthquakes. Springer, Berlin.

Rabbel, W. and Zschau, J. (1985). Static deformations and gravity changes at the earth's surface due to atmospheric loading. Journal of Geophysics, 56, 81-99.

Randall, L.D., Edelman, A. and Hyman, J.M. (1989). Nonnegativity-, monotonicity-, or convexity-preserving cubic and quantic Hermite interpolation. American Mathematical Society, 52, 471-4794.

Rao, K.S.S. (2000). Swell-shrink behaviour of expansive soils-geotechnical challenges. Indian Geotechnical Journal, 30, 1-69.

Rodrigues, E.P. (2007). Estimation of crustal vertical movements due to atmospheric loading effects by GPS observations. Revista Brasileira de Geofísica, 25, 45-50.

Romagnoli, C., Zerbini, S., Lago, L., Richter, B., Simon, F., Domenichini, F., Elmi, C. and Ghirotti, M. (2003). Influence of soil consolidation and thermal expansion effects on height and gravity variations. Journal of Geodynamics. 35, 521-539, doi:10.1016/S0264-3707(03)00012-7.

Romero, E., Villar, M. V. and Lloret, A. (2005). Thermo-hydro mechanical behaviour of two heavily overconsolidated clays. Engineering Geology, 81, 255-268, doi:10.1016/j.enggeo.2005.06.011.

Rutherford, M.C., Mucina, L. and Powrie, L.W. (2006). Biomes and Bioregions of Southern Africa. The vegetation of South Africa, Lesotho and Swaziland. Strelitzia, Cape Town, SA. pp. 32-50.

Ryan, Ø. (2015). Linear algebra, signal processing, and wavelets: a unified approach-MATLAB version, https://www.uio.no/studier/emner/matnat/math/nedlagte-emner/MAT-INF2360/v15/kompendium/applinalgmatlab.pdf.

Salazar, A. (2003). On thermal diffusivity. European Journal of Physics, 24, 351-358.

Schneider, T., Bischoff, T. and Haug, G.H. (2014). Migrations and dynamics of the intertropical convergence zone. Nature, 513, 45-53, doi:10.1038/nature13636.

Shatkay, H. (1995). The Fourier transform: a primer. Technical report CS-95-37, Department of Computer Science, Brown University, Providence, R1.

Shuanggen, J., Cardellach, E. and Xie, F. (2014). GNSS Remote Sensing: Theory, Methods, and Applications. Springer, United States of America.

Sigrist, P., Coppin, P. and Hermy, M. (1999). Impact of forest canopy on quality and accuracy of GPS measurements. International Journal of Remote Sensing, 20, 3595-3610, doi:10.1080/014311699211228.

Singh, D., Vinod, K., Saxena, S.C. and Deepak, K.K. (2005). An improved windowing technique for heart rate variability power spectrum estimation. Journal of Medical Engineering & Technology, 29, 95-101, doi:10.1080/03091900412331286378.

Stenseth, N.C., Ottersen, G., Hurrell, J.W., Mysterud, A., Lima, M., Chan, K., Yoccoz, N.G. and *Ȧ*dlandsvik, B. (2003). Studying climate effects on ecology through the use of climate indices: the North Atlantic Oscillation, El Niño Southern Oscillation and beyond. The Royal Society, 270, 2087-2096, doi:10.1098/rspb.2003.2415.

Stoica, P. and Moses, R. (2005). Spectral analysis of signals. USA, Prentice.

Struzik, Z.R. (2001). Wavelet methods in (financial) time-series processing. Physica A, 296, 307-319.

Sun, X., Cook, K.H. and Vizy, E.K. (2017). The South Atlantic subtropical high: Climatology and interannual variability. Journal of Climate, 30, 3279-3296, doi:10.1175/JCLI-D-16-0705.1.

Tachiki, Y., Yoshimura, T., Hasegawa, H., Mita, T., Sakai, T. and Nakamura, F. (2005). GPS positioning accuracy while walking under forest canopy in summer and winter seasons. The Japan Forest Engineering Society, 20, 23-28.

Tadross, M. and Johnston, P. (2012). Climate systems regional report: southern Africa. Cape Town, South Africa: ICLEI-local Governments for sustainability.

Tang, A.M., Cui, Y.J. and Barnel, N. (2008). Thermo-mechanical behaviour of a compacted swelling clay. Geotechnique, 58, 45-54, doi:10.1680/geot.2008.58.1.45.

Tiberius, C.C.J.M. and Borre, K. (2000). Are GPS data normally distributed? International Association of Geodesy Symposia, 121, 243.

Timmer, J., Lauk, M., H*ä*ubler, S. and Radt, V. (2000). Cross-spectral analysis of tremor time series. International Journal of Bifurcation and Chaos, 10, 2595-2610.

Timmer, J., Lauk, M., Pfleger, W. and Deuschl, G. (1998). Cross-spectral analysis of physiological tremor and muscle activity. Biological Cybernetics, 78, 349-357.

Titus, J and Geroge, S. (2013). A comparison study on different interpolation methods based on satellite images. International Journal of Engineering Research & Technology (IJERT), 2, pp. 82-85.

Torrence, C. and Compo, G.P. (1998). A practical guide to wavelet analysis. American Meteorological Society, 79, 61-78.

Towhata, I., Kuntiwattanakul, P. and Kobayashi, H. (1993). A preliminary study on heating of clays to examine possible effects of temperature on soil-mechanical properties. Soils and Foundations, 33, No. 4, 184-190.

Trauth, M.H. (2010). MATLAB recipes for Earth sciences 3rd edition. Springer, Germany.

Unogwu, J.O., Kamal, K.H., Jarikre, A.O. and Prince, J.S. (2015). Enforcing dilution of precision in Global Positioning System (GPS). African Journal of Computing & ICT, 8, 185-196.

Unser, M. (1999). Splines: A perfect fit for signal and image processing. IEEE Signal Processing Magazine, 16, 22-38.

Valens, C. (1999). A really friendly guide to wavelets. [Online]. Available at: http://iar.cs.unm.edu/~williams/cs530/arfgtw.pdf.

van Dam, T.M., Blewitt, G. and Heflin, M.B. (1994). Atmospheric pressure loading effects on Global Positioning System coordinate determination. Journal of Geophysical Research, 99, 939-950.

Van Dam, T.M. and Wahr, J.M. (1987). Displacement of the Earth's Surface due to atmospheric loading: Effects on gravity and baseline measurements. Journal of Geophysical Research. 92, 1281-1286.

van Dam, T.M. and Wahr, J. (1998). Modeling environment loading effects: a review. Physics and Chemistry of the Earth, 23, 1077-1087, doi:10.1016/S0079-1946(98)00147-5.

van Dam, T., Wahr, J., Milly, P.C.D., Shmakin, A.B., Blewitt, G., Lavallée, D. and Larson, K.M. (2001). Crustal displacement due to continental water loading. Geophysical Research Letters, 28, 651-654.

Van Der Merwe, D.H. (1964). The prediction of heave from the plasticity index and percentage clay fraction of soils. The Civil Engineering in South Africa. 6, 103-107.

Vanapalli, S.K. and Lu, L. (2012). A state-of-the art review of 1-D heave prediction methods for expansive soils. International Journal of Geotechnical Engineering. 6, pp 15-41, doi:10.3328/IJGE.2012.06.01.15-41.

Walsberg, G.E. (2000). Small mammals in hot deserts: some generalizations revisited. BioScience, 50, 109-120.

Wang, C. and Liou, Y. (2006). A study of the relationship between seasonal tropospheric variation and positioning accuracy by GPS. Journal of Photogrammetry and Remote Sensing, 11, 191-200.

Wang, G. and Jenkins, G.S. (2003). Deserts and desertification. Encyclopedia of Atmospheric Sciences, 1, p. 633-640.

Wang, K., Chen, H., Jiang, W., Li, Z., Ma, Y. and Deng, L. (2018). Improved vertical displacements induced by a refined thermal expansion model and its quantitative analysis in GPS height time series. Journal of Geophysics and Engineering, 15, 554-567, doi:10.1088/1742-2140/aa93ae.

Wang, L., Chen, C., Du, J. and Wang, T. (2017). Detecting seasonal and long-term vertical displacement in the North China plain using GRACE and GPS. Hydrology and Earth System Sciences, 21, 2905-2922, doi:10.5194/hess-21-2905-2017.

Ware, R.H., Fulker, D.W., Stein, S.A., Anderson, D.N., Avery, S.K., Clark, R.D., Droegemeier, K.K., Kuettner, J.P., Minster, J.B. and Sorooshian, S. (2000). SuomiNet: A real-time national GPS network for atmospheric research and education. American Meteorological Society, 81, 677-694.

Welch, P.D. (1967). The use of fast Fourier transform for the estimation of power spectra: a method based on time averaging over short, modified periodograms. IEEE Transactions on audio and electroacoustics, Au-15, pp. 70-73.

Wells, D., Beck, N., Delikaraoglou, D., Kleusberg, A., Krakiwsky, E.J., Lachapelle, G., Langley, R.B., Nakiboglu, M., Schwarz, K.P., Tranquilla, J.M. and Vanicek, P. (1986). Guide to GPS positioning. Frederic and New Brunswick: Canadian GPS Associates.

Williams, E.G., Houston, B.H and Herdic, P.C. (2003). Fast Fourier transform and singular value decomposition formulations for patch nearfield acoustical holography. Journal of the Acoustical Society of America, 114, 1322-1333, doi: 10.1121/1.1603767.

World Meteorological Organization (WMO). (2015). The climate of Africa: 2013. WMO-No. 1147, Switzerland.

Wu, X., Collilieux, X., Altamimi, Z., Vermeersen, B.L.A., Gross, R.S. and Fukumori, I. (2011). Accuracy of the International Terrestrial Reference Frame origin and Earth expansion. Geophysical Research Letter, 38, 1-5, doi:10.1029/2011GL047450.

Xu, X., Dong, D., Fang, M., Zhou, Y. and Wei, N. (2017). Contributions of thermoelastic deformation to seasonal variations in GPS station position. GPS Solutions, 21, 1265-1274, doi:10.1007/s10291-017-0609-6.

Yan, H., Chen, W., Zhu, Y., Zhang, W. and Zhong. (2009). Contributions of thermal expansion of monuments and nearby bedrock to observed GPS height changes. Geophysical Research Letter. 36, 1-5, doi:10.1029/2009GL038152.

Zhang, P.G. and Qi, M. (2005). Neural network forecasting for seasonal and trend time series. European Journal of Operational Research, 160, 501-514, doi:10.1016/j.ejor.2003.08.037.

Zerbini, S., Richter, B., Negusini, M., Romagnoli, C., Simon, D., Domenichini, F. and Schwahn. W. (2001). Height and gravity variations by continuous GPS, gravity and

environmental parameter observations in the southern Po Plain, near Bologna, Italy. Earth and Planetary Science, 192, 267-279.

Zhao, G., Jiang, D., Diao, J. and Qian, L. (2004). Application of wavelet time-frequency analysis on fault diagnosis for steam turbine. Surveillance 5 CETIM, 11-13 Oct, Senlis, France.

Appendices

Appendix A: Test time series (T1, T2, T3, T4 and T5) used in the interpolation test in chapter 4.2.

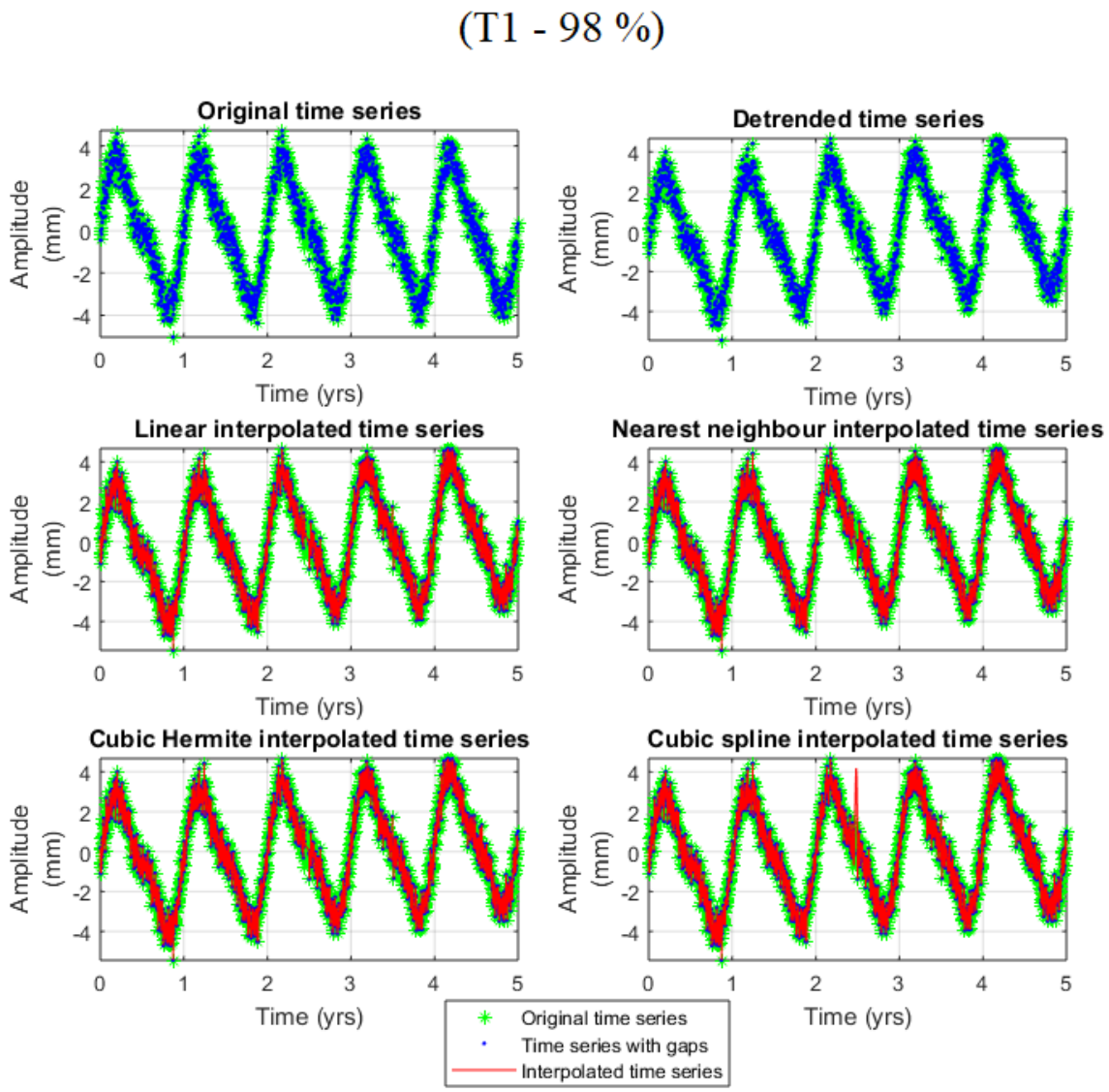


Figure 9.1: Synthetic time series T1 (with 2% missing data points), used in the variance test in chapter 4.2 and the response of the interpolation methods when applied to the noise contaminated time series. (a) Noise-contaminated synthetic time series without gaps (green) and with gaps (blue). (b) Detrended time series. (c) Linear interpolated time series. (d) Nearest neighbour interpolated time series). (e) Piecewise cubic Hermite interpolated time series. (f) Piecewise cubic spline interpolated time series.

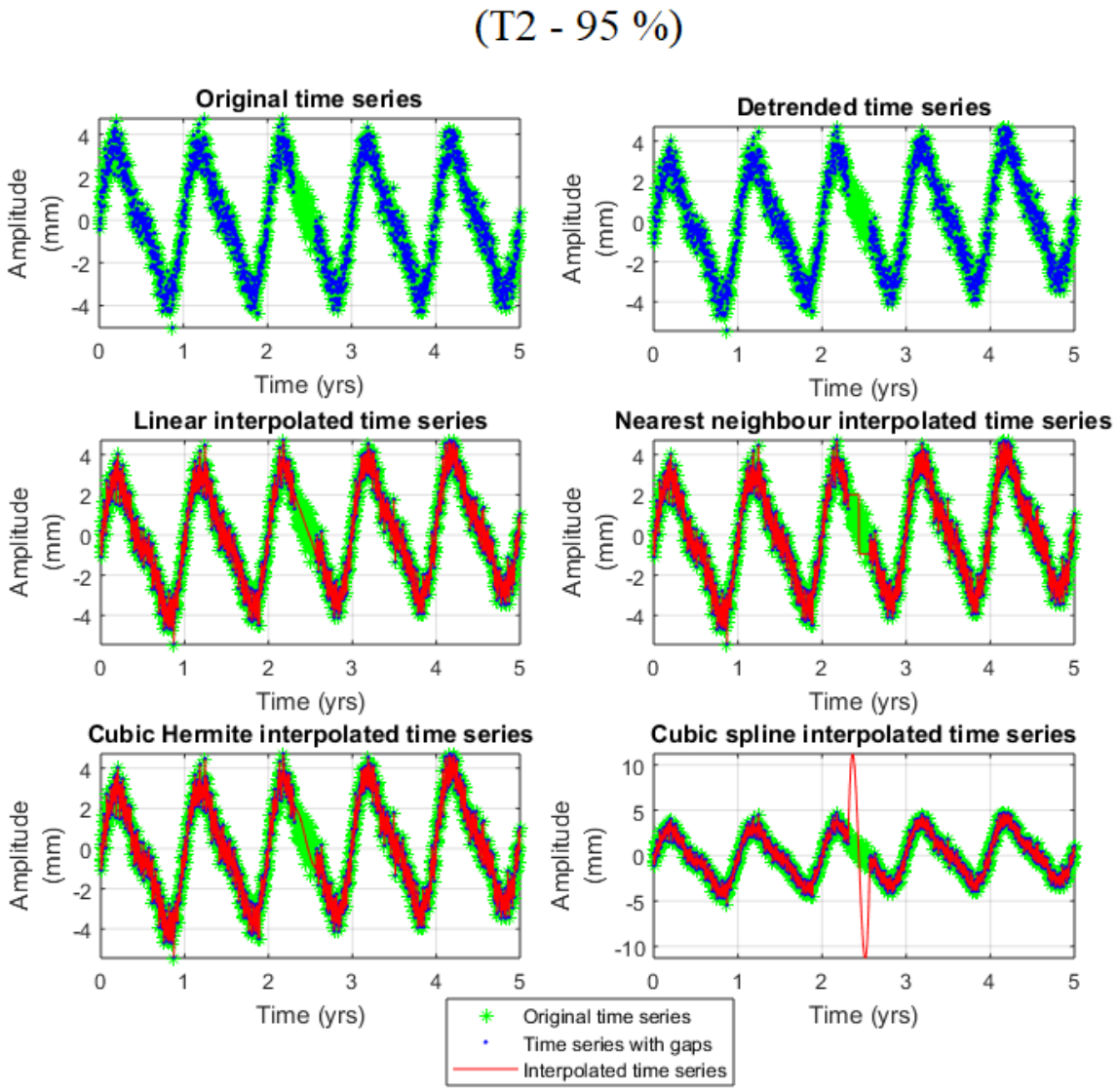


Figure 9.2: Synthetic time series T2 (with 5% missing data points), used in the variance test in chapter 4.2 and the response of the interpolation methods when applied to the noise contaminated time series. (a) Noise-contaminated synthetic time series without gaps (green) and with gaps (blue). (b) Detrended time series. (c) Linear interpolated time series. (d) Nearest neighbour interpolated time series). (e) Piecewise cubic Hermite interpolated time series. (f) Piecewise cubic spline interpolated time series.

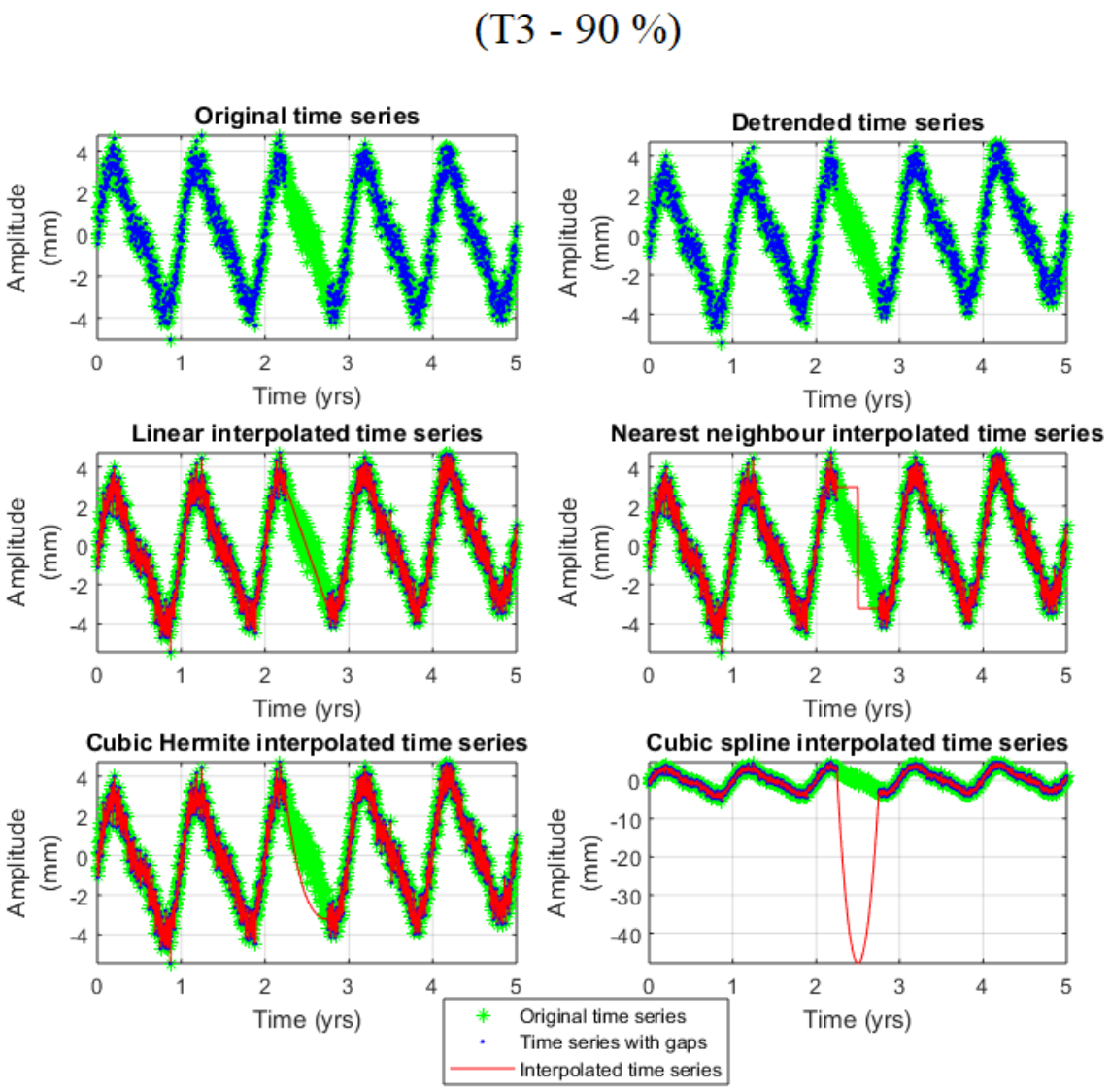


Figure 9.3: Synthetic time series T3 (with 10% missing data points), used in the variance test in chapter 4.2 and the response of the interpolation methods when applied to the noise contaminated time series. (a) Noise-contaminated synthetic time series without gaps (green) and with gaps (blue). (b) Detrended time series. (c) Linear interpolated time series. (d) Nearest neighbour interpolated time series). (e) Piecewise cubic Hermite interpolated time series. (f) Piecewise cubic spline interpolated time series.

(T4 - 85 %)

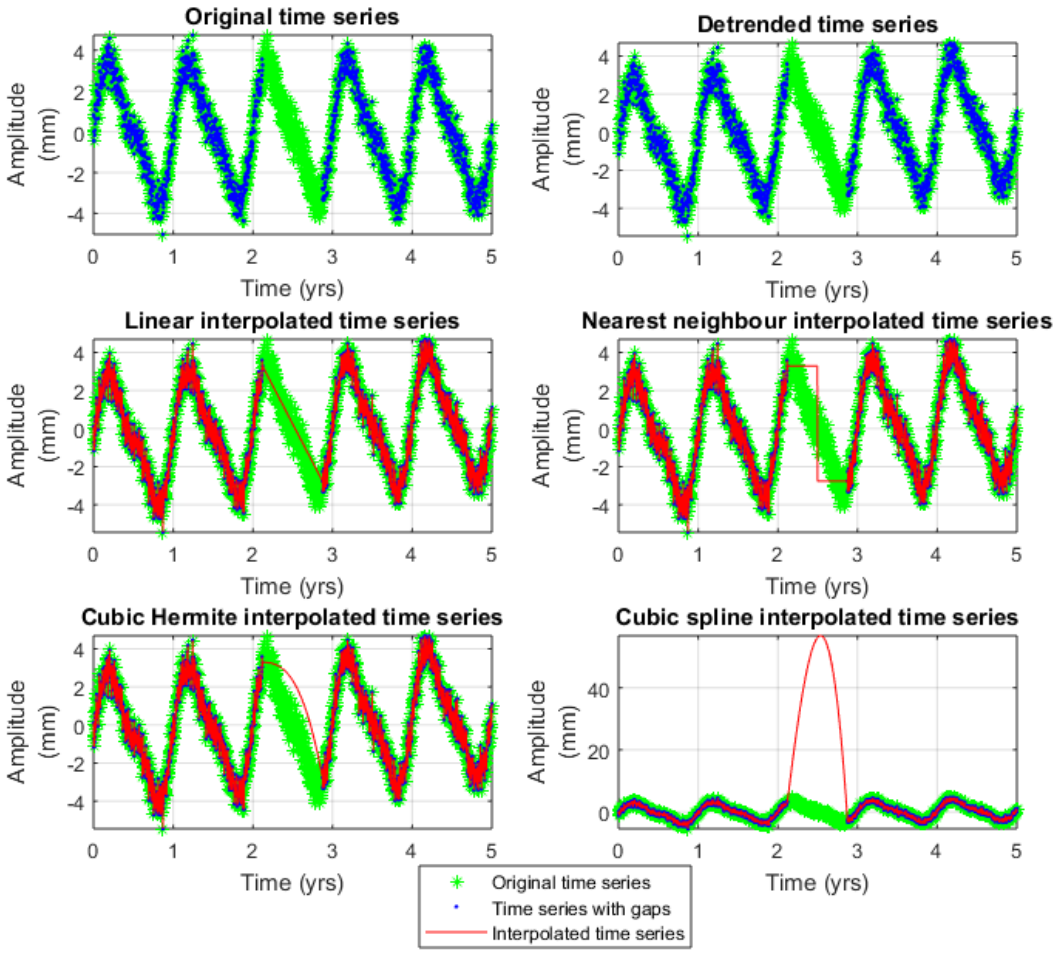


Figure 9.4: Synthetic time series T4 (with 15% missing data points), used in the variance test in chapter 4.2 and the response of the interpolation methods when applied to the noise contaminated time series. (a) Noise-contaminated synthetic time series without gaps (green) and with gaps (blue). (b) Detrended time series. (c) Linear interpolated time series. (d) Nearest neighbour interpolated time series). (e) Piecewise cubic Hermite interpolated time series. (f) Piecewise cubic spline interpolated time series.

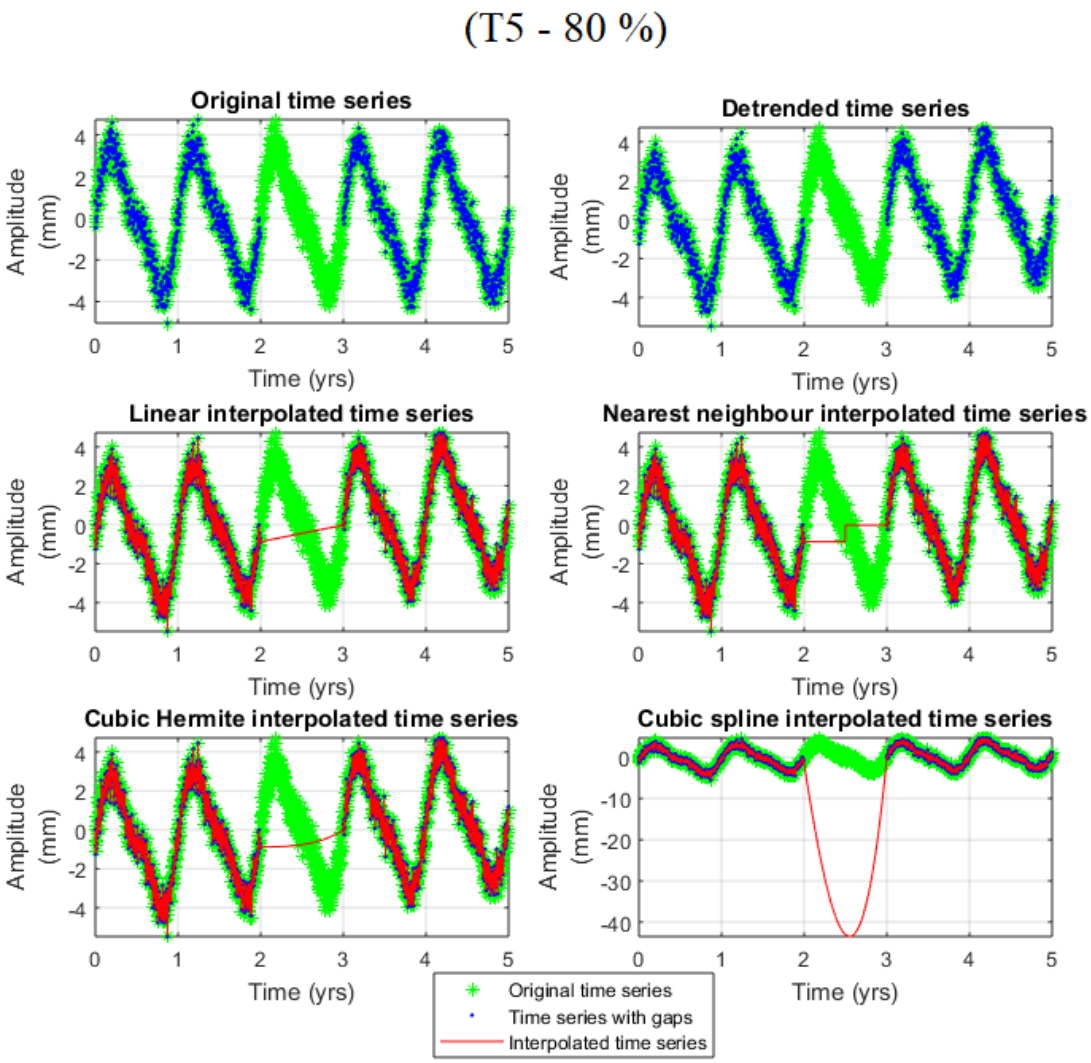


Figure 9.5: Synthetic time series T5 (with 20% missing data points), used in the variance test in chapter 4.2 and the response of the interpolation methods when applied to the noise contaminated time series. (a) Noise-contaminated synthetic time series without gaps (green) and with gaps (blue). (b) Detrended time series. (c) Linear interpolated time series. (d) Nearest neighbour interpolated time series). (e) Piecewise cubic Hermite interpolated time series. (f) Piecewise cubic spline interpolated time series.

Appendix B: Additional surface air temperature, pressure, rainfall and humidity cross-spectrum and coherence plots.

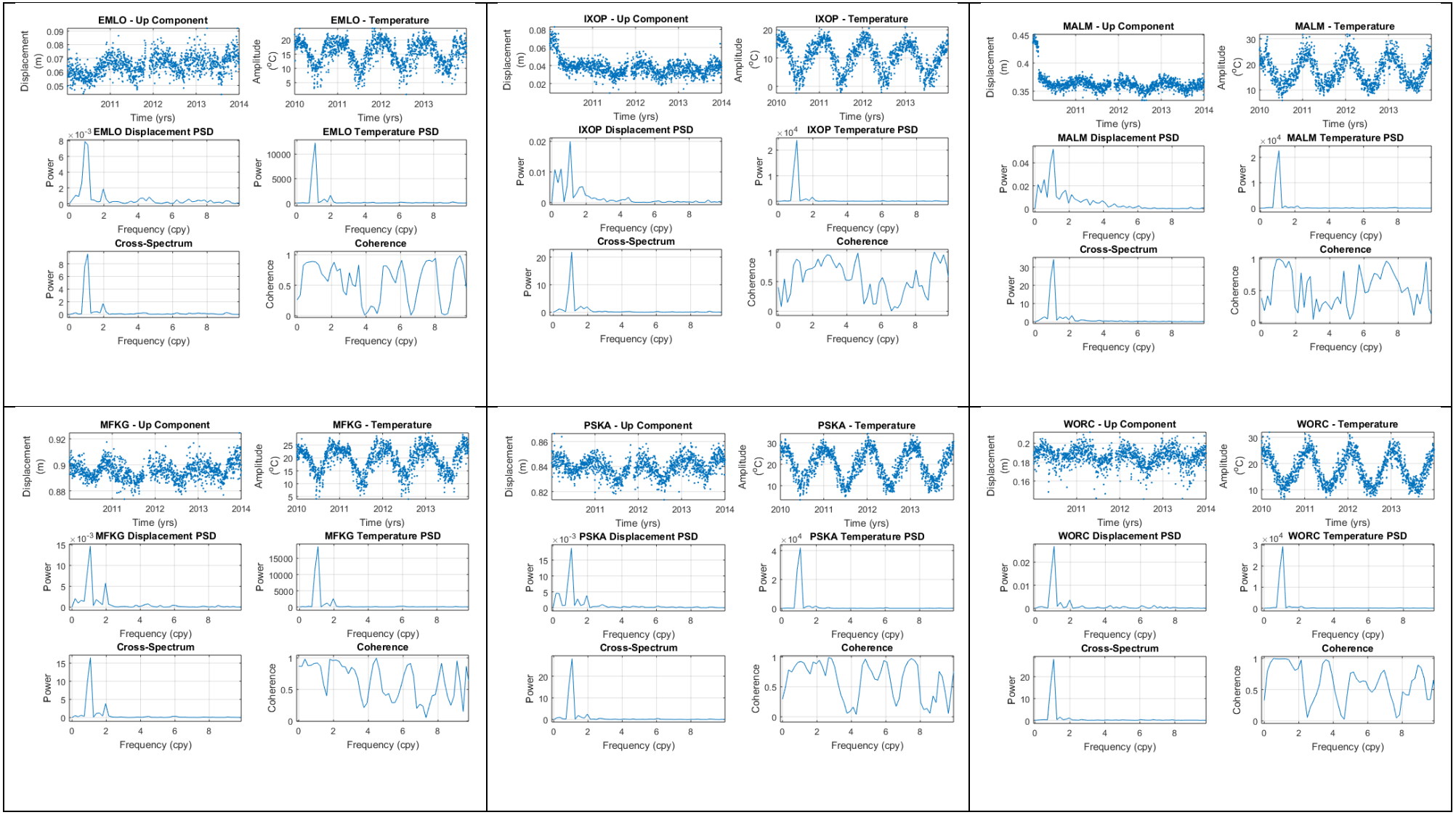


Figure 9.6: Additional Cross-spectrum and coherence correlation plots of cGPS displacement (m) vs average temperature (°C) time series.

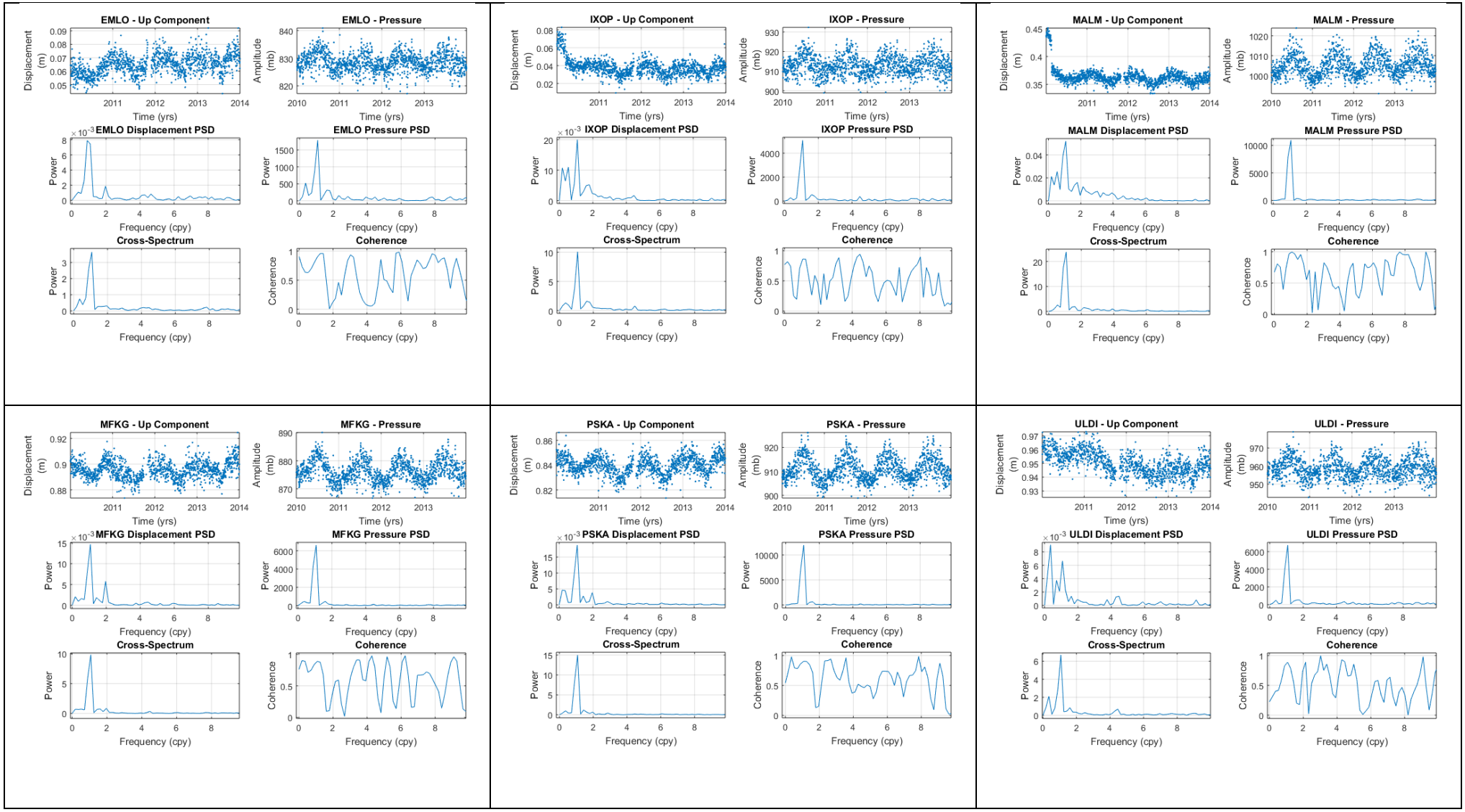


Figure 9.7: Additional cross-spectrum and coherence correlation plots of cGPS displacement (m) vs pressure (mbar) time series.

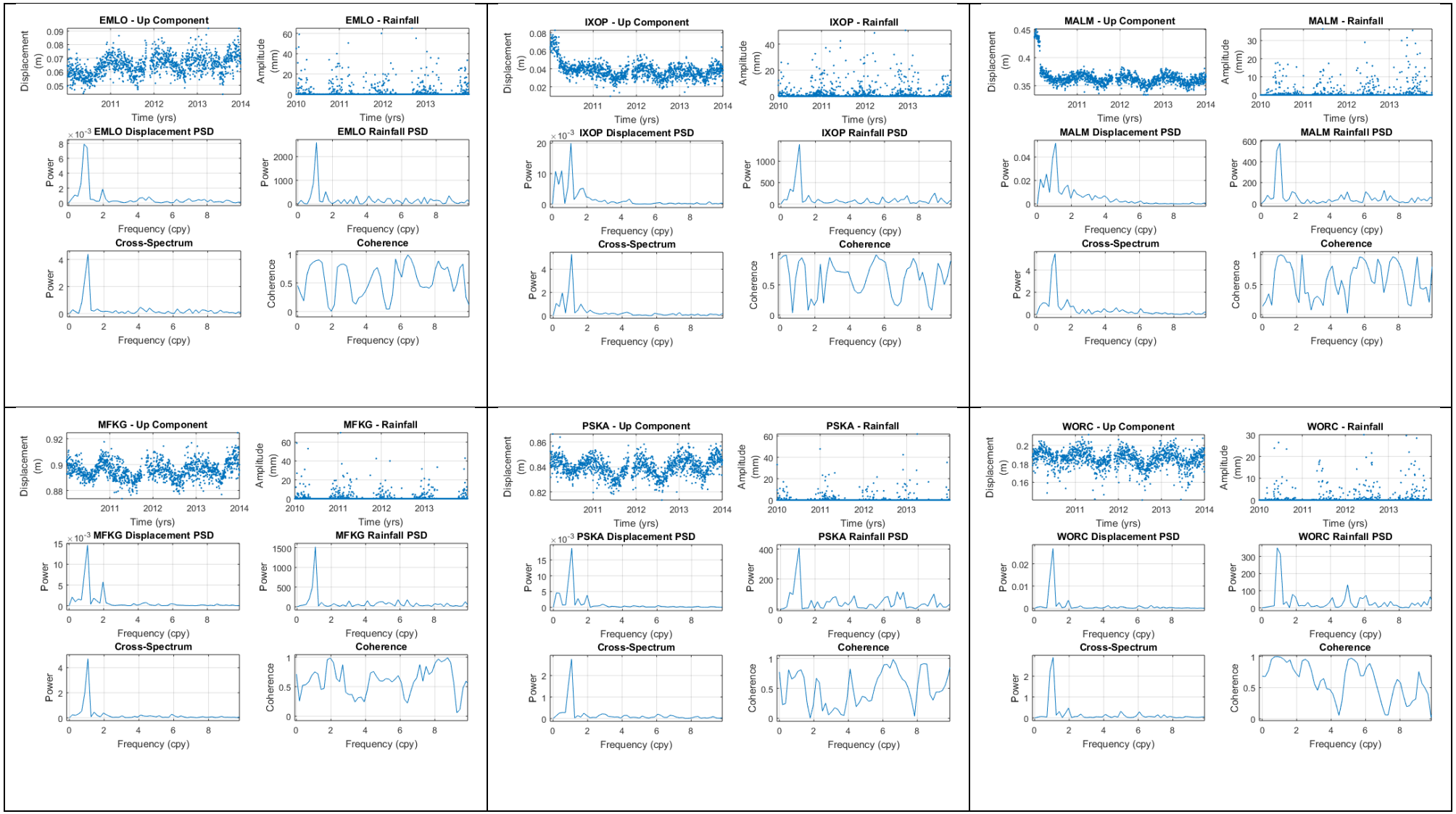


Figure 9.8: Additional cross-spectrum and coherence correlation plots of cGPS displacement (m) vs rainfall (mm) time series.

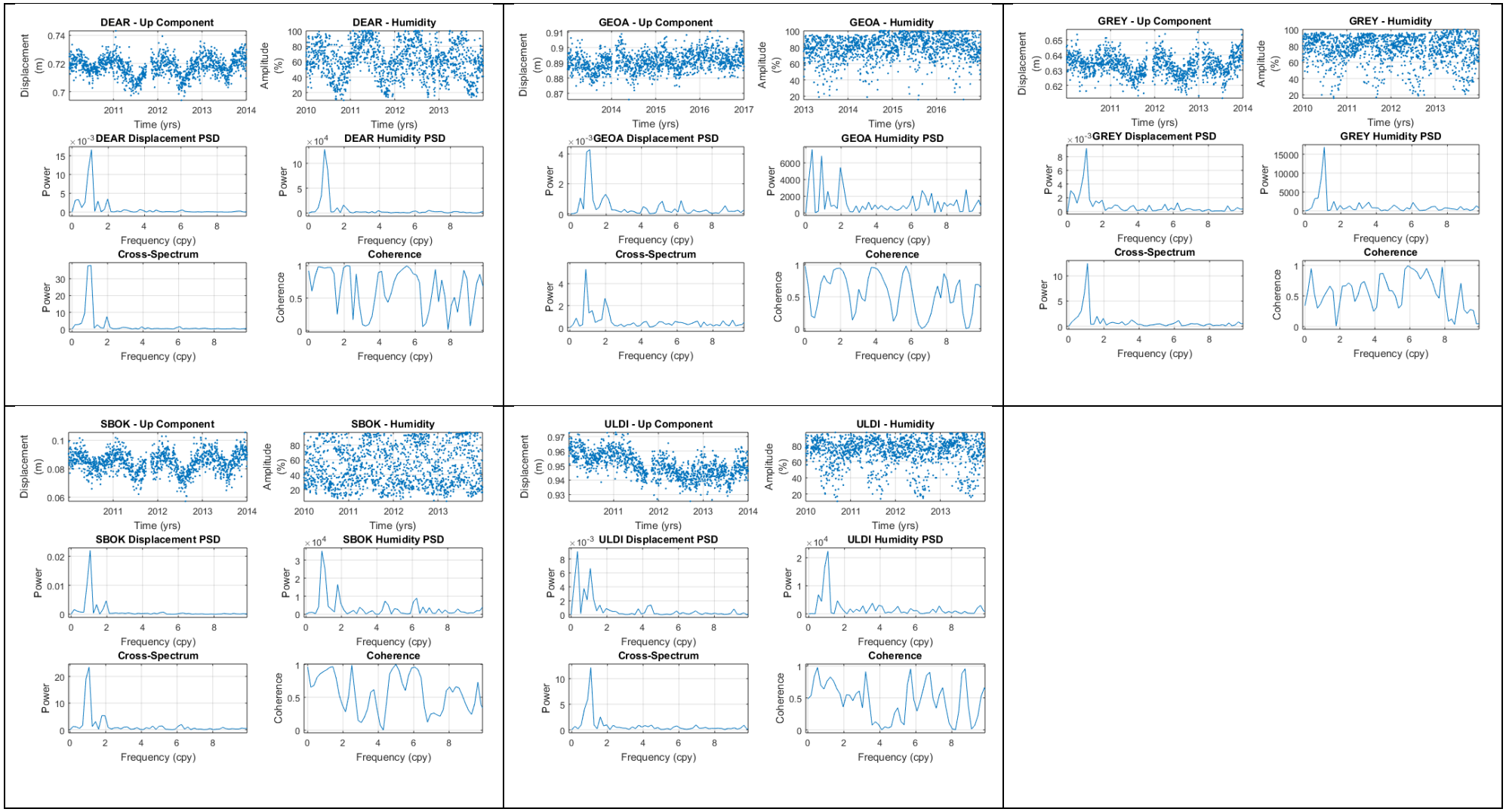


Figure 9.9: Additional cross-spectrum and coherence correlation plots of cGPS displacement (m) vs humidity (%) time series.

Appendix C: Additional surface air temperature, atmospheric pressure, rainfall, humidity and surface displacement semblance plots.

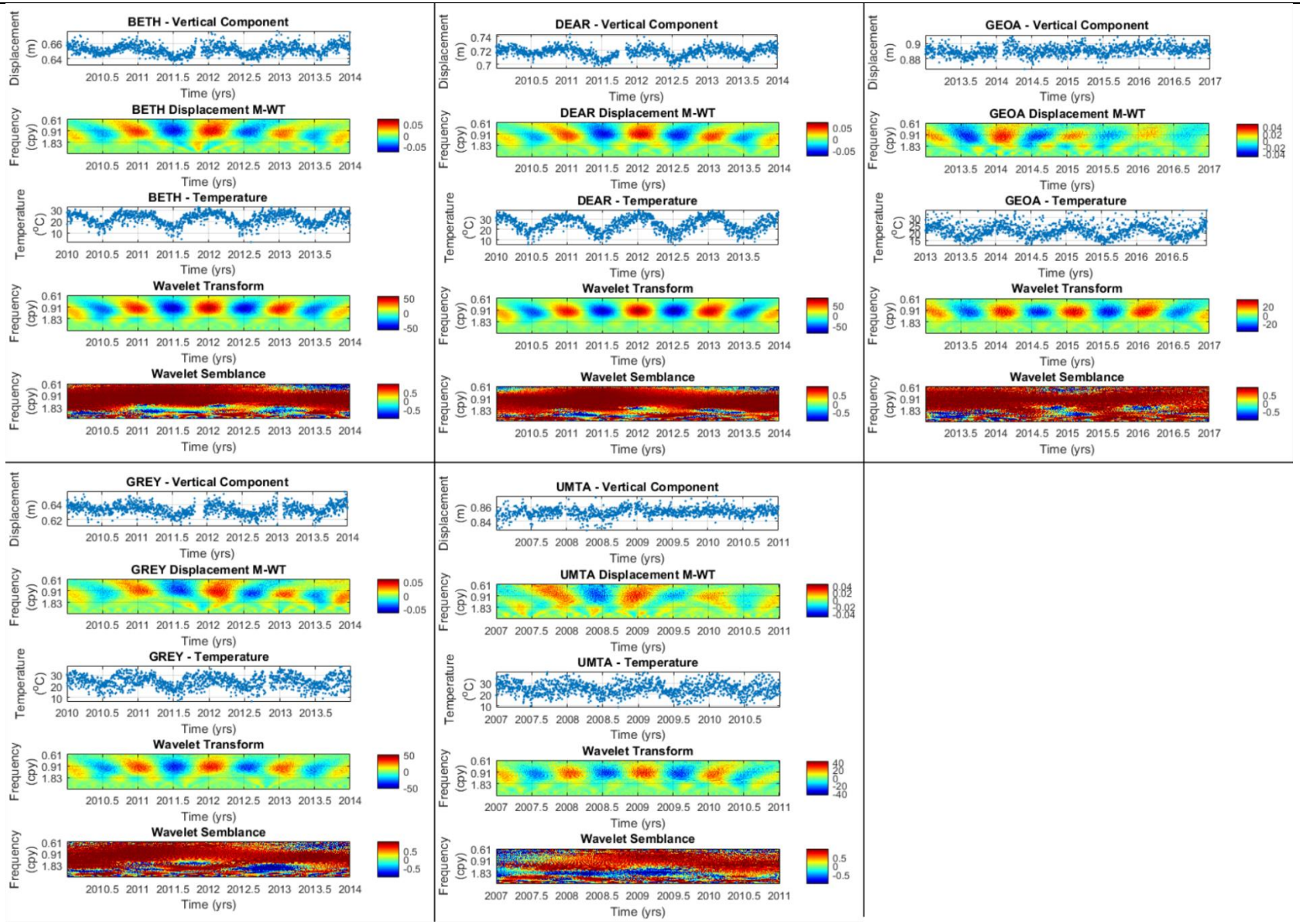


Figure 9.10: Additional semblance correlation plots of cGPS displacement time series (m) vs average temperature time series (°C).

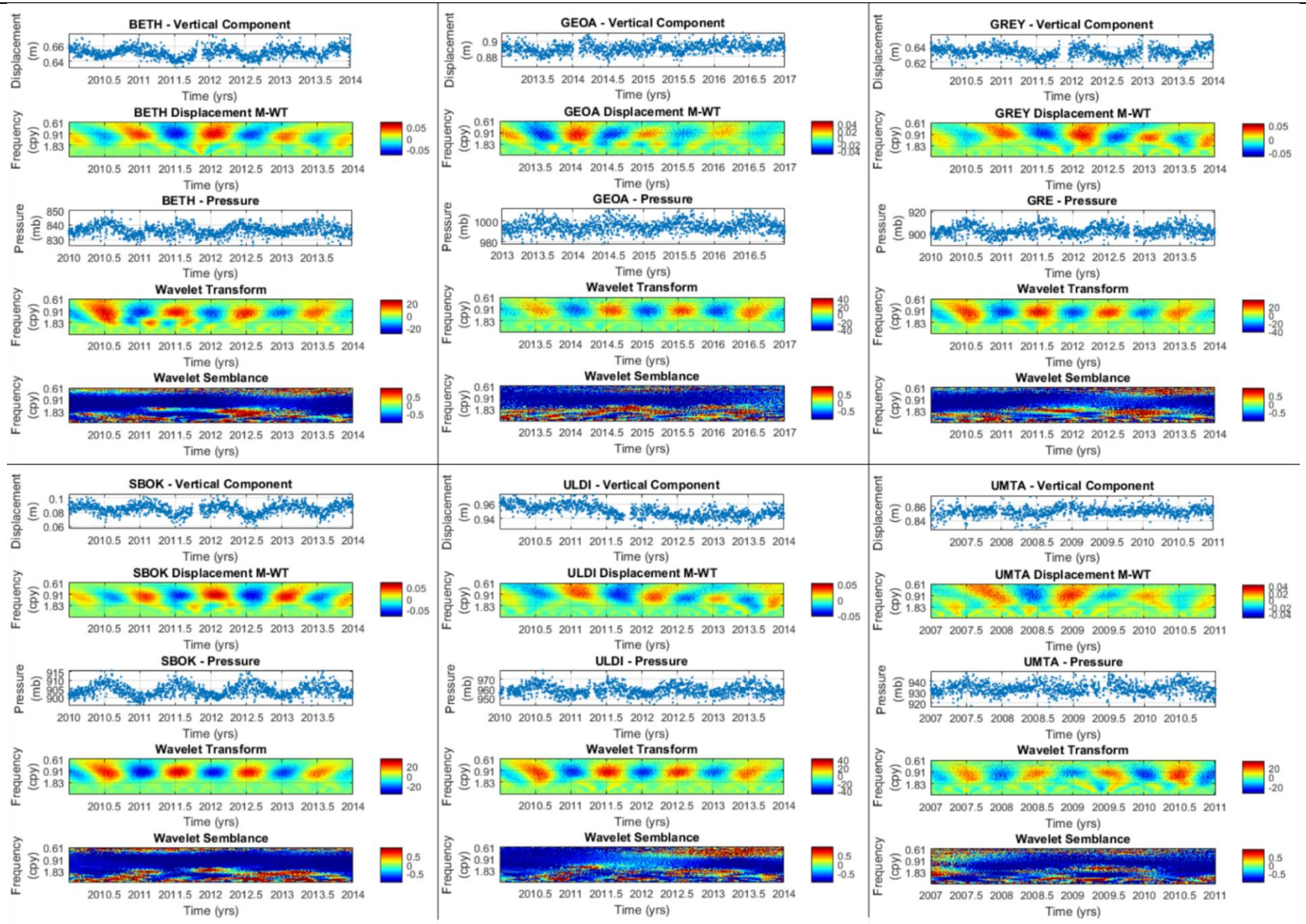


Figure 9.11: Additional semblance correlation plots of cGPS displacement time series (m) vs atmospheric pressure time series (mb).

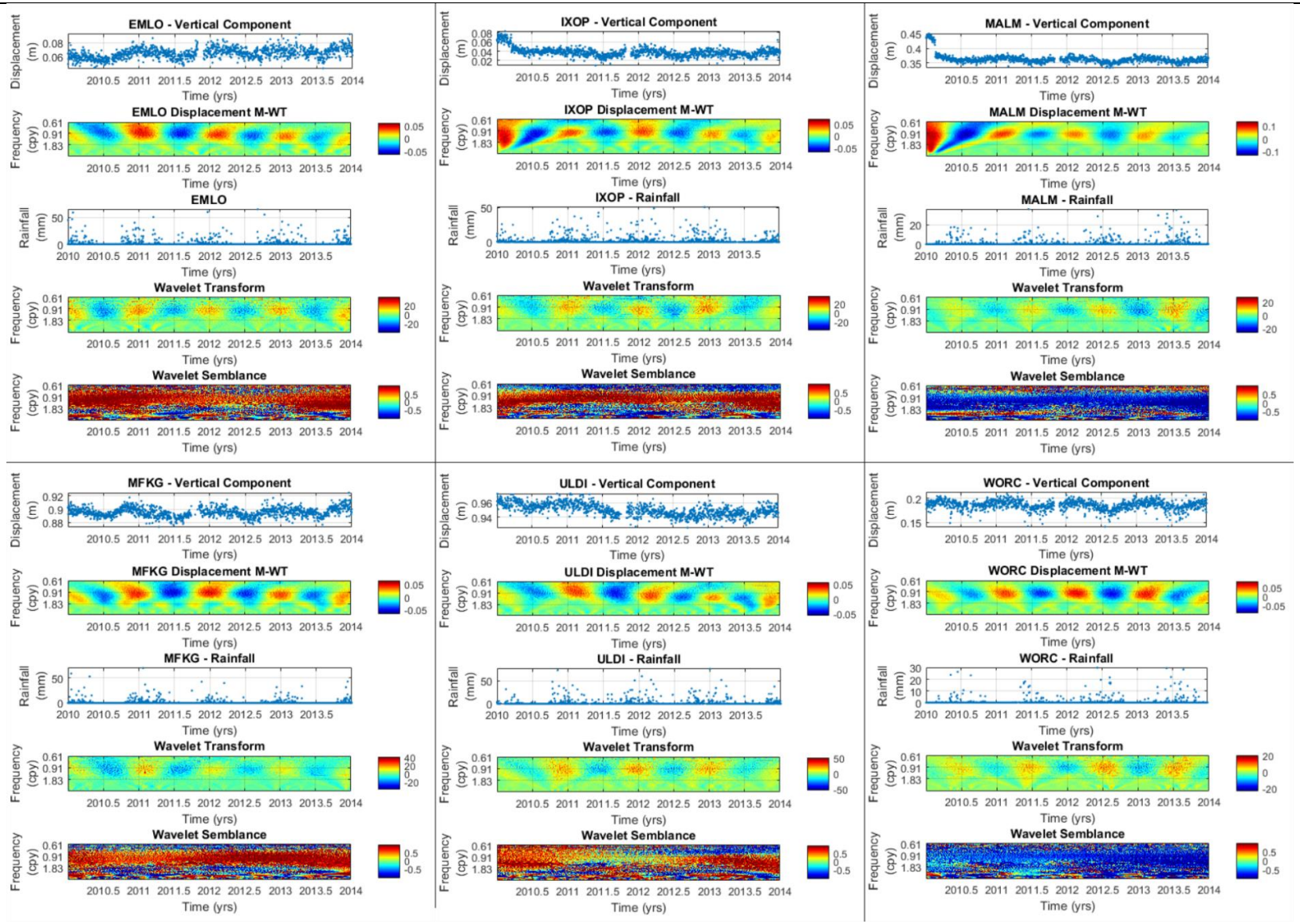


Figure 9.12: Additional semblance correlation plots of cGPS displacement time series (m) vs rainfall time series (mm).

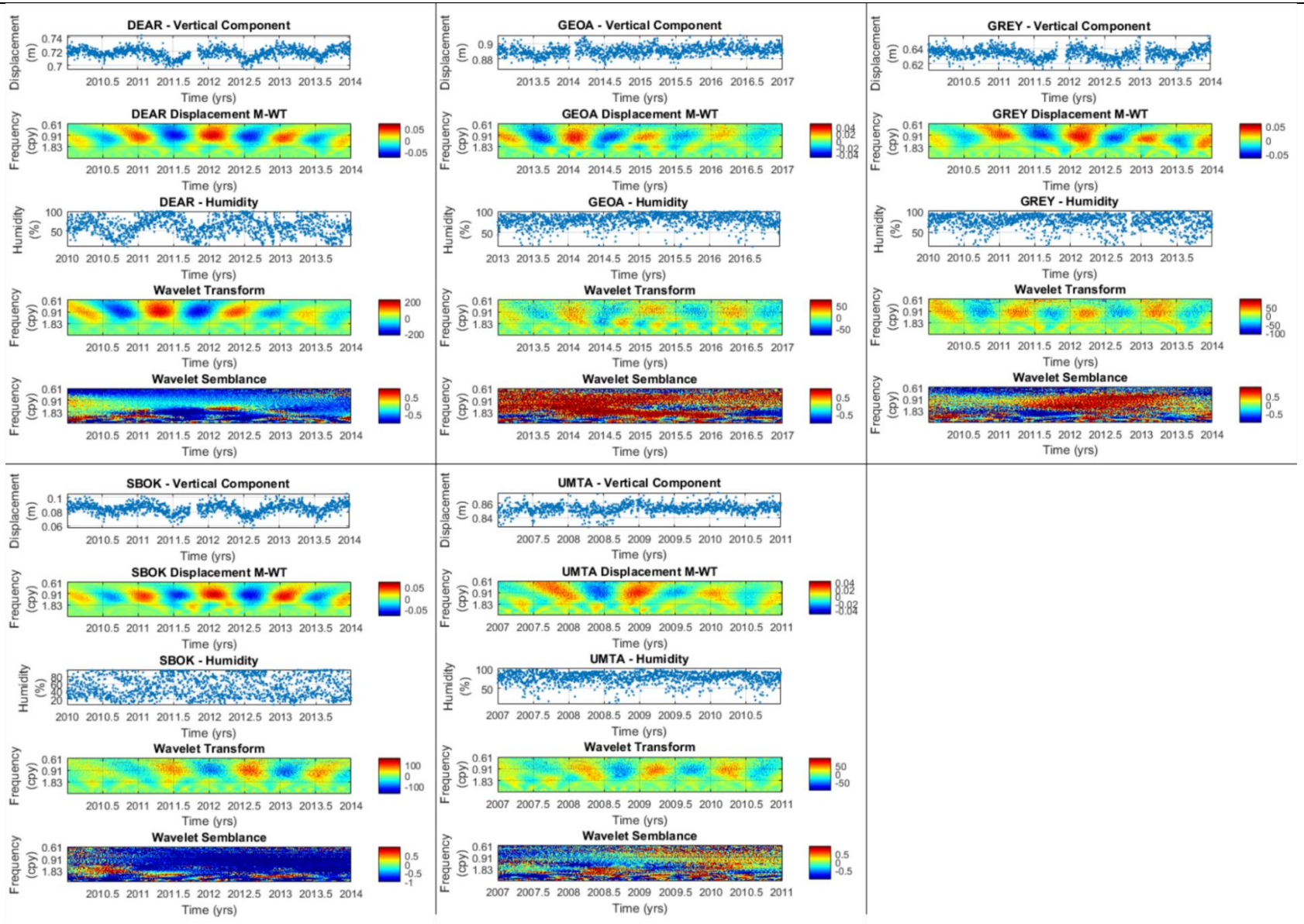


Figure 9.13: Additional semblance correlation plots of cGPS displacement time series (m) vs humidity time series (%).

Appendix D: Visual plots, FFT and WT plots of the additional time series

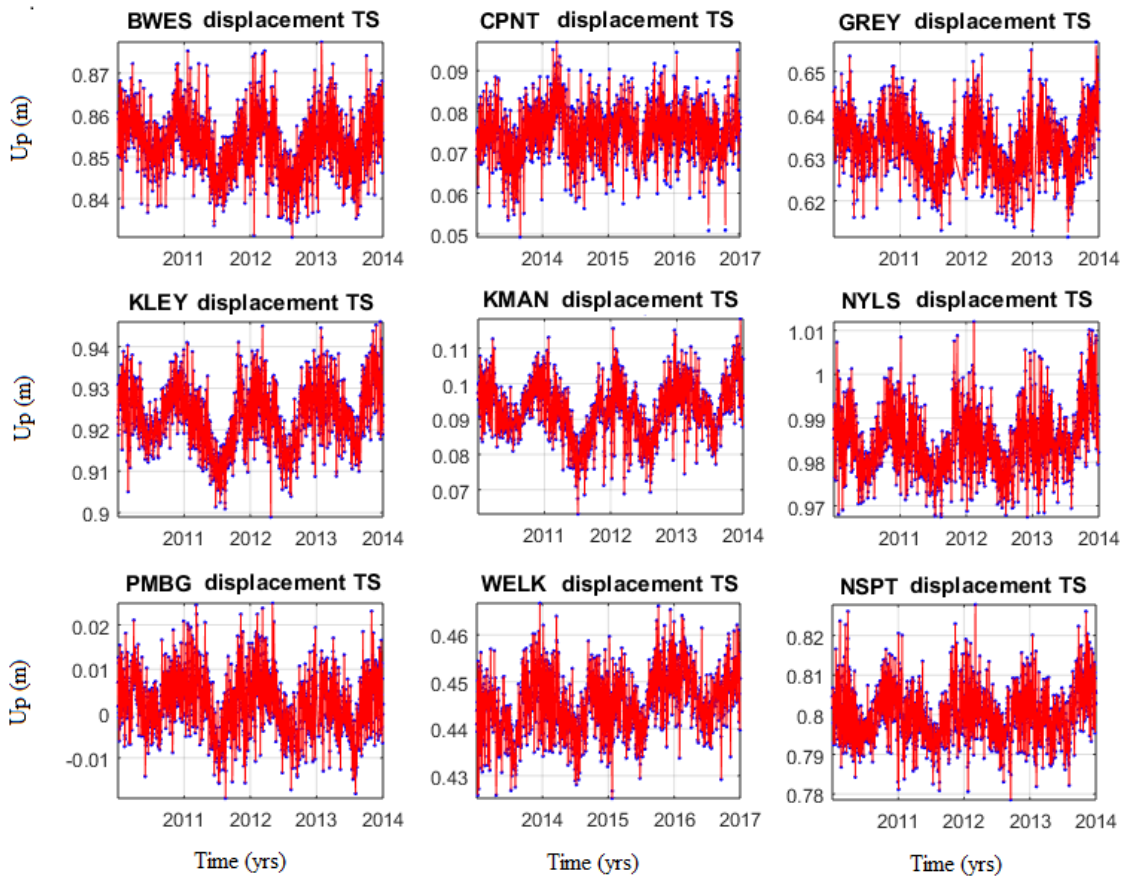


Figure 9.14: Time domain plots of the addition displacement time series

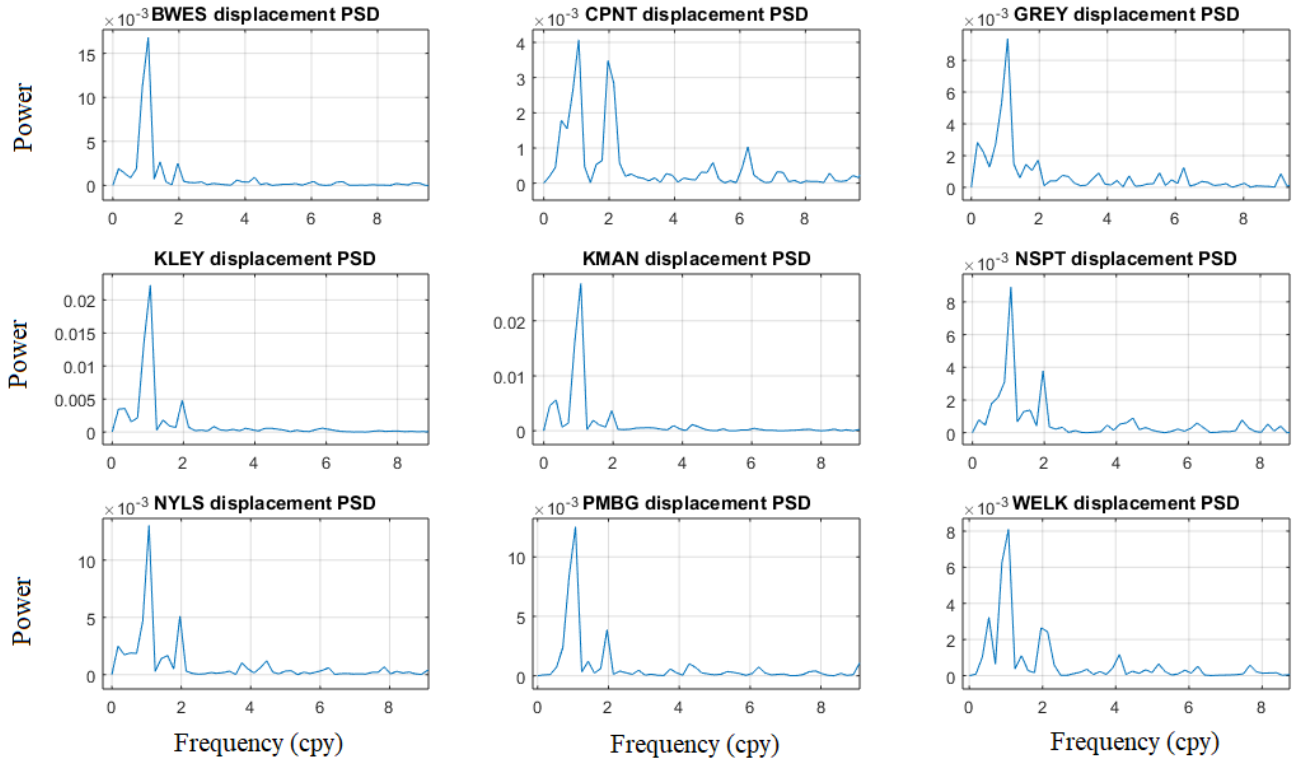


Figure 9.15: FFT transform of the addition displacement time series

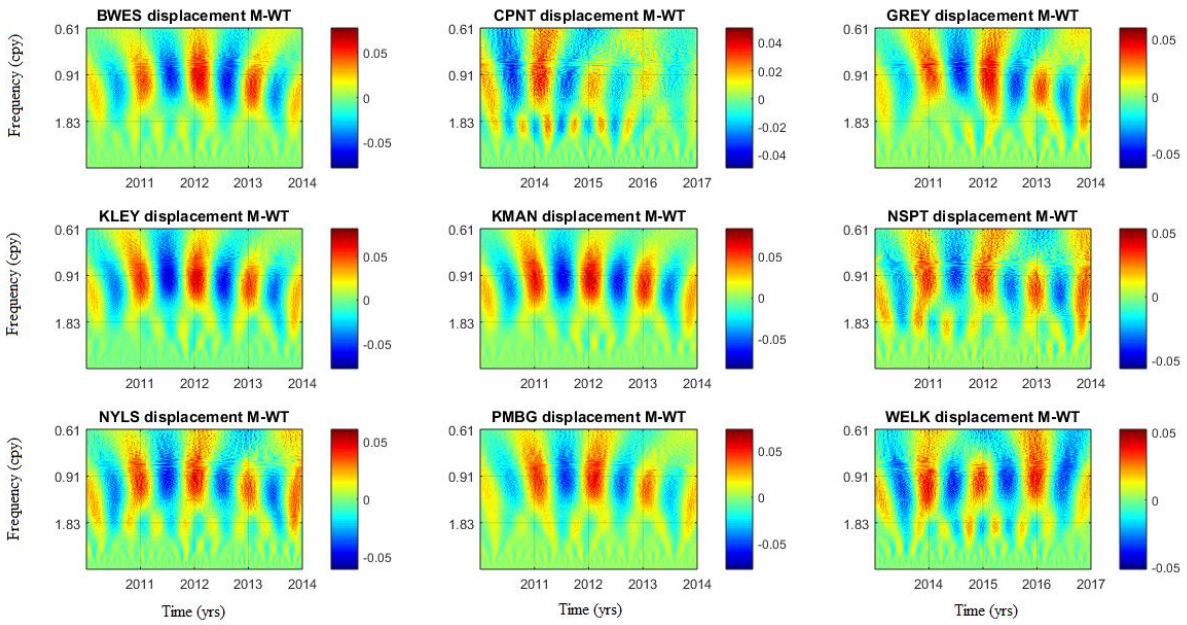


Figure 9.16: Morlet wavelet transform of the addition displacement time series.

Table 19: Additional information about the displacement time series

							Power	
Station name	Climatic zone	Latitude	Longitude	Percentage of missing data points (%)	interpolation technique	Variance (Time domain)	Annual component	Semi-annual component
KMAN	Desert	-27.461	23.432	98.4942	Cubic Hermite	0.0000594	0.0225	0.0029
PSKA	Desert	-29.668	22.749	93.0869	Linear	0.0000511	0.0155	0.0031
SBOK	Desert	-29.669	17.879	93.7714	Linear	0.0000504	0.0174	0.0036
PMBG	Wet tropical	-29.601	30.383	95.4141	Cubic Hermite	0.0000487	0.0109	0.0031
ULDI	Wet tropical	-28.293	31.421	89.5962	Linear	0.0000456	0.0049	0.0008
GREY	Wet tropical	-29.071	30.578	91.5127	Linear	0.0000468	0.0078	0.0014
IXOP	Wet tropical	-30.146	30.069	95.1403	Cubic Hermite	0.000074	0.0143	0.0023
UMTA	Wet tropical	-31.549	28.673	85.1472	Linear	0.0000363	0.0025	0.0011
KLEY	Sahelian	-28.743	24.806	98.6995	Cubic Hermite	0.0000564	0.0189	0.0039
DEAR	Sahelian	-30.665	23.993	92.8131	Linear	0.0000457	0.0146	0.0028
WELK	Sahelian	-27.978	26.738	98.5626	Cubic Hermite	0.0000398	0.0074	0.0026
MFKG	Sahelian	-25.805	25.540	93.2238	Linear	0.0000457	0.0121	0.0047
BWES	Sahelian	-33.347	22.574	97.5359	Cubic Hermite	0.0000539	0.0146	0.0021
EMLO	Dry tropical	-26.498	29.984	92.8131	Linear	0.0000421	0.0077	0.0018
BETH	Dry tropical/Sahelian	-28.250	28.334	95.6194	Cubic Hermite	0.0000455	0.0119	0.0033
NSPT	Dry tropical	-25.475	30.975	98.8364	Cubic Hermite	0.0000483	0.0066	0.0031
NYLS	Dry tropical	-24.703	28.406	98.3573	Cubic Hermite	0.000053	0.0098	0.0041
CPNT	Mediterranean	-34.353	18.490	97.1253	Cubic Hermite	0.0000426	0.0035	0.0033
MALM	Mediterranean	-33.464	18.731	96.0986	Cubic Hermite	0.0002089	0.0468	0.0063
GEOA	Mediterranean	-34.002	22.383	94.1821	Linear	0.000035	0.0041	0.0013
WORC	Mediterranean	-33.645	19.445	93.1554	Linear	0.0000803	0.0223	0.0029

Appendix E: Continuous GPS processing procedure

Table 20: Continuous GPS time series processing steps (As taken from the Nevada Geodetic Laboratory site: - http://geodesy.unr.edu/gps/ngl.acn.txt)

NGL/UNR GPS Data Analysis Strategy Summary	
Analysis centre	Nevada Geodetic Laboratory University of Nevada, Reno 1664. N. Virginia St. MS 178 Reno NV 89557 NV 89557 USA Data Archives: http://geodesy.unr.edu/
Contact person	Dr. Geoffrey Blewitt Email: gblewitt@unr.edu
Software used	GIPSY/OASIS-II Version 6.1.1 developed at JPL
Products used	Final, non-fiducial daily products from JPL archive: ftp://sideshow.jpl.nasa.gov/pub/JPL_GPS_Products/Final/ Including:
	GPS satellite orbit estimates
	GPS satellite clock estimates
	WLPB estimates (widelane & phase biases)
	Name of TRF (terrestrial reference frame)
	Transformation parameter estimates to named TRF
	Time-pole parameter estimates
	GPS satellite eclipse times
	Name of IGS ANTEX antenna calibration file
	Auxiliary data updated periodically from JPL:
	IGS ANTEX antenna calibration file
	JPL planetary ephemeris
	CODE CA-P DCB (differential code biases)
	GPS receiver type codes
	GPS constellation configuration history

	IERS/BIH leap seconds history
	IERS earth orientation parameters
	Auxiliary data updated from IGS Central Bureau:
	http://igscb.jpl.nasa.gov/
	IGS station receiver/antenna configuration history
	Auxiliary data from Chalmers University, Sweden:
	http://holt.oso.chalmers.se/loading/
	Ocean tidal loading coefficients for all stations
	Custom daily data (from NGL/UNR)
	Ftp://gneiss.nbmg.unr.edu/xfiles
	Transformation parameter estimates to frame NA12
	Ref: http://dx.doi.org/10.1016/j.jog.2013.08.004
GPS data used	RINEX files from various archives, including:
	UNAVCO ftp://data-out.unavco.org
	CDDIS ftp://cddis.gsfc.nasa.gov
	CORS ftp://cors.ngs.noaa.gov/cors
	SIO ftp://garner.ucsd.edu
	EUREF ftp://igs.bkg.bund.de/EUREF
	GEONET ftp://ftp.geonet.org.nz
	GREF ftp://igs.bkg.bund.de/GREF
	IGN ftp://rgpdata.ign.fr
	AUSTRALIA ftp://ftp.ga.gov.au
	GSI ftp://terras.gsi.go.jp
	SONEL ftp://ftp.sonel.org
Preparation date	October 15, 2013
Modification dates	October 15, 2013 Creation
Effective date for aata analysis	2011-12-17 onward using JPL version 2 reprocessing with IERS2010/IGS08 conventions
Measurement Models	

Preprocessing	RINEX header must be interpretable
	- approximate XYZ replaced with NGL database values
	- alias table replaces antenna type with IGS standard
	- fix obvious formatting errors
	- require antenna type has IGS ANTEX calibrations
	- non-calibrated radome set to "NONE" (IGS standard)
	Require minimum file size, typically ~18 hr/day
	Apply CA-P1 biases
	Fix non-compliant time-tags for older receiver types
	Remove non-GPS GNSS data (e.g., GLONASS)
	Remove L2C and C2 data
	Cycle slip detection
	Delete phase connected arcs < 20 minutes
	Carrier Phase: Decimated to 5 minutes
	Pseudorange: Carrier aided smoothing to 5 minutes
Basic observable	Undifferenced ionosphere-free carrier phase, LC Undifferenced ionosphere-free pseudorange, PC
	Elevation angle cutoff: 7 degrees Sampling rate: 5 minutes Data weight, LC: 1 cm Data weight, PC: 1 m
Modeled observable	Undifferenced LC and PC combinations CA-P1 biases from CODE applied
RHC phase rotation corr.	Applied
Marker -> antenna Arp eccentricity	dN, dE, dU eccentricities from RINEX header applied to compute station marker coordinates
Troposphere	A priori model: Pressure from GPT model
	(Boehm et al, 2007)
	Hydrostatic delay from Davis (1985)

	Wet delay 10 cm
	Mapping Function: Global Mapping Function (GMF)
	Estimation: Zenith delay and horizontal gradients
Ionosphere	1st order effect: Removed by LC and PC combinations
	2nd order effect: Not modeled
Plate motions	Not applied to apriori positions
Tidal	Solid earth tide: IERS 2010 Conventions
	Permanent tide: NOT removed from model, so NOT in estimated site coordinates
	Pole tide: IERS 2010 Conventions
	Ocean Tide Loading:
	Diurnal, Semidiurnal, MF, and MM Model: FES04
	Semiannual: Self-consistent equilibrium model
	hardisp.f from IERS2010
	Surface deformations computed with respect to instantaneous center of mass
	Ocean Pole Tide Loading: Not applied
Non-tidal loading	Atmospheric Pressure: Not applied
	Ocean Bottom Pressure: Not applied
	Surface Hydrology: Not applied
	Other Effects: None applied
Earth orientation parameter (EOP) model	IERS 2010 Conventions for diurnal, semidiurnal, and long period tidal effects on polar motion and UT1
Satellite centre of mass correction	Phase centers offsets from igs08_wwww.atx applied
Satellite antenna phase variations	PCV model w.r.t. phase center from igs08_www.at applied

Relativistic corrections	Periodic Clock Corrections, (-2*R*V/c): Applied Gravitational Bending (Shapiro Delay): Applied
GPS attitude model	GYM95 nominal yaw rate model from Bar-Sever (1996) and yaw rates estimated for Block II satellites
Orbit Models (JPL Orbit Products)	
Geopotential	EGM2008 12x12 C20, C30, C40, C21, S21 from IERS2010 standards
	GM = 398600.4415 km**3/sec**2
	AE = 6378.1363 km
Third-body	Sun, Moon, and All Planets
	Ephemeris: JPL DE421
Solar radiation pressure	Block II/IIA/IIR: JPL empirical SRP model, GSPM-10, Bar-Sever and Kuang, (2004), Sibthorpe et al, 2010
	Estimate GPS "Y-Bias" and solar radiation pressure(SRP) coefficient as constant with no a-priori constraint. Make small time-varying (stochastic) adjustments to SRP coefficients in spacecraft body-fixed X and Z directions (1% process noise sigma with 1 hr 11 sec updates and 4-hour correlation time.) Estimate tightly constrained time-varying empirical acceleration in
	spacecraft Y direction (0.01 nm/s^2 process noise sigma with 1 hr 11 sec updates and 4-hour correlation time.)
	Earth shadow model: conic model with oblate Earth, umbra and penumbra
	Earth albedo: applied
	Attitude Model: GYM95 yaw model from Bar-Sever (1996)
Tidal forces	Solid earth tides: IERS 2010 Conventions
	Ocean tides: FES2004 to degree and order 30 with convolution formalism of Desai and Yuan (2006)

	Solid Earth Pole tide: IERS 2010 conventions
	Ocean Pole tide: IERS 2010 conventions
Relativity	Applied Acceleration due to point mass of Earth Acceleration due to geodesic precession Acceleration due to Lense-Thirring precession
Numerical integration	Variable high order Adams predictor-corrector with direct integration of second-order equations
	Integration step: variable
	Starter procedure: RKF
	Arc length: 30 hours centered at 12:00 of each day
Estimated Parameters (Apriori Values & SIGMAS)	
Adjustment	Stochastic Kalman filter/smoother implemented as square root information filter with smoother
Station coordinates	Daily PPP estimates for all sites Apply daily transformation into IGS08 and NA12
Satellite clock	Fixed to JPL clock products, which are given every 5 minutes relative to reference clock (e.g. USN3/AMC2
Receiver clock	Estimate every 5 minutes relative to satellite clocks
Orbital	Fixed to JPL ECEF orbit products interpolated to 5 min
GPS attitude	Fixed to JPL products: yaw rates when in eclipse
Troposphere	Zenith delay: random walk 5.0d-8 km/sqrt(sec) Horizontal delay gradients: random walk 5.0e-9 km/sqrt(sec)
	Mapping function: GMF
Ionosphere	1st order effects removed by LC and PC combinations and 2nd order effects not modeled

Ambiguity	Resolve ambiguities using WLPB products from JPL
Earth orientation parameters	Fix to JPL products: polar motion, polar motion rate, and LOD, where UT1 is integrated from estimated LOD
Reference Frames	
Inertial	J2000 Geocentric
Terrestrial	Daily transformed coordinates into IGS08 and NA12
Interconnection	Precession: IAU 2006 Precession Theory
	Nutation: IAU 2006 Nutation Theory
	A priori EOPS: EOPC04 updated daily, with polar motion and length of day estimated daily
References	

Bar-Sever, Y. E. (1996), "A new model for GPS yaw attitude", Journal of Geodesy, 70:714-723

Bar-Sever, Y. E., and D. Kuang (2004), New empirically-derived solar radiation pressure model for GPS satellites, IPN Progress Reports 42-159, JPL. Available online: http://ipnpr.jpl.nasa.gov/progress_report/42-160/title.htm

Bassiri, S., and G. A. Hajj, (1993), Higher-order ionospheric effects on the global positioning systems observables and means of modelling them, Manuscripta Geodtica, 18, 280-289, 1993

Blewitt, G., (1990), An automatic editing algorithm for GPS data. Geophysical Research Letters, Vol. 17, No. 3, p. 199-202

Blewitt, G., C. Kreemer, W.C. Hammond, and J.M. Goldfarb (2013), "Terrestrial reference frame NA12 for crustal deformation studies in North America", J. Geodyn, http://dx.doi.org/10.1016/j.jog.2013.08.004

Boehm, J., A.E. Niell, P. Tregoning, H. Schuh (2006), "Global Mapping Functions (GMF): A new empirical mapping function based on numerical weather model data", Geophysical Research Letters, Vol. 33, L07304, DOI:10.1029/2005GL025545.
Boehm, J., R. Heinkelmann and H. Schuh (2007), "Short Note: A global model of pressure and temperature for geodetic applications", Journal of Geodesy, DOI: 10.1007/s00190-007-0135-3
IERS Conventions 2003, D.D. McCarthy & G. Petit (editors), IERS Technical Note 32, Frankfurt am Main: Verlag des Bundesamts fuer Kartographie und Geodaesie, 2004.
Kedar, S., G. Hajj, B. Wilson, and M. Heflin (2003), The effect of the second order GPS ionospheric correction on receiver positions, Geophys. Res. Lett., 30(16), 1829, doi:10.1029/2003GL017639
Moyer, T.D., (2000) Formulation of observed and computed values of deep space network data types for navigation, Deep Space Communications and Navigation Series, Jet Propulsion Laboratory, California Institute of Technology, Pasadena, CA, Chapter 4, pp, 19-28.
Sibthorpe, A., J. Weiss, N. Harvey, D. Kuang, and Y. Bar-Sever, Empirical modeling of solar radiation pressure forces affecting GPS satellites, AGU Fall Meeting, San Francisco, CA, 2010.

Appendix F: Codes used in this research

Appendix F1: Code used to generate the synthetic signals used this project

```
function SimpleSignalGeneration()
%Name: Sikelela  Gomo
%Purpose: To create a synthetic signal similar to that of cGPS and
%meteorology time series
%STEP 1: The following algorithm generates a four cycle sinusoidal wave.
%The wave is simulated to have been collected over five years,at a sampling
%frequency of 1 sample per day. Where Signalz is the generated sinusoidal
%signal.
fs=1/365;   %sampling frequency
f1=1;       %frequency of signal one
f2=2;       %frequency of signal two
t=0:fs:5;   %observation time
signal1=3*sin(2*pi*f1*t);       %Signal 1
signal2=sin(2*pi*f2*t);         %Signal 2
Resultant_signal=signal1+signal2;    %Signal one



%STEP 2:The algorithm below creates a random normally distributed noise
%data set. Where n is the standard deviation.
n=input('Enter standard deviation of the noise: ');
noise= n*randn(size(Resultant_signal));
%noise=noise.*exp(-1*t);

%STEP 3:The algorithm below adds the noise (in step 4) to the complex
%signal created in step 3
NoisyTimeSeries=noise+Resultant_signal;

%STEP 4: Adding a linear trend to the signal of with a slope of 2
Trend= 2*t;
CompleteSyntheticSignal=NoisyTimeSeries+Trend;

%STEP 5: Plots of all the signals
                                figure (1)
subplot(4,1,1)
plot(t,signal1,'.b',t,signal2,'.g'),axis tight, grid on;
title('Annual and semi-annual synthetic signals')
xlabel('Time (yrs)');
```

```
ylabel({'Amplitude';'(mm)'});

subplot(4,1,2)
plot(t,Resultant_signal,'.'), axis tight, grid on;
title('Resultant signal');
xlabel('Time (yrs)');
ylabel({'Amplitude';'(mm)'});

subplot(4,1,3)
plot(t,noise,'.b'),axis tight, grid on;
title('Gaussian white noise')
xlabel('Time (yrs)');
ylabel({'Distribution';'(STD=0.5 mm)'});

subplot(4,1,4)
plot(t,NoisyTimeSeries,'.'), axis tight, grid on;
title('Synthetic time series with noise');
xlabel('Time (yrs)');
ylabel({'Amplitude';'(mm)'});

figure (2)
subplot(2,1,1)
plot(t,Trend,'.b'),axis tight, grid on;
title('Trend with gradient of 2')
xlabel('Time (yrs)');
ylabel('Slope');

subplot(2,1,2)
plot(t,CompleteSyntheticSignal,'.'), axis tight, grid on;
title('Synthetic time series with noise and a trend')
xlabel('Time (yrs)');
ylabel({'Amplitude';'(mm)'});

% STEP 6: Importing the generated synthetic signal
A=zeros(length(t),2);
A(:,1)=t;
A(:,2)=CompleteSyntheticSignal;
FileName=input('Enter File name to be created, "add .xlsx" :','s');
xlswrite(FileName,A,'');
end
```

Appendix F2: Fast Fourier Transform code used on synthetic data

```
function FourierDecomTest()
%Purpose: To test frequency domain decomposition using the periodogram
%method and to check how noise affects the decomposition process
%Programmer: Sikelela Gomo

for LLn=1:3
%STEP ONE: Generation of the synthetic signals to be used
t=1:1/365.2422:4;
f=1;
f2=2;
if LLn==3
Trend=3*t;
elseif LLn==2
 noise= 3*randn(size(t));
else
 noise= 0*randn(size(t));
end
%Signal1=3*sin(2*pi*f2*t)+noise; % First time series
if LLn==3
    Signal2=3*sin((2*pi*f*t))+1*sin((2*pi*f2*t))+3*randn(size(t))+Trend;
else
Signal2=3*sin((2*pi*f*t))+1*sin((2*pi*f2*t))+noise;%Second time series
end

if LLn==3
    subplot(2,3,3)
    plot(t,Signal2,'.b'), grid on, axis tight;
    title('Time sereis with trend');
elseif LLn==2
    subplot(2,3,2)
    plot(t,Signal2,'.b'), grid on, axis tight;
    title('Time sereis with noise');
else
    subplot(2,3,1)
    plot(t,Signal2,'.b'), grid on, axis tight;
    title('Time series without noise');
end
```

```
xlabel('Time (yrs)');
ylabel({'Amplitude';'(mm)'});

%STEP TWO: reducing ringing using the hamming window
%WD=hamming(length(t));
%WD=blackmanharris(length(t),'periodic');
WD=kaiser(length(t));
%WD=[];
L=length(t);
NPL=nextpow2(L);                %Next power of 2 of the smaple number
n=2^NPL;
disp('Next Power of 2 of the sample number');
disp(n);

%STEP THREE: Computing the power spectral density of the test signals
[Pxx,f] = periodogram(Signal2,WD,n,1);
f=f*365.2422;
%magnitude = abs(Pxx);
if LLn==3
    subplot(2,3,6)
elseif LLn==2
    subplot(2,3,5)
else
    subplot(2,3,4)
end

plot(f,Pxx),grid on, axis tight;
title('Frequency spectrum')
ylabel('Power')
xlabel('Frequency (cpy)')
end
```

Appendix F3: Wavelet Transform code used on synthetic data

```
function DecompositionProgram()
%Programmer: Sikelela Gomo
%Purpose: To compute time-frequency domain decomposition using the wavelet
%transforms
%STEP 1: Importing data into MATLAB
%**************************Time series one*******************************
```

```
StationName=input('Enter file name containing signal 1 (add .txt): ','s');
data=load(StationName);
t1=data(:,1);                %Observation time of data
x1=data(:,2);                %Recorded data

%**************************Time series two*******************************
StationName=input('Enter file name containing signal 2 (add .txt): ','s');
data=load(StationName);
t2=data(:,1);                %Time series to recording time
x2=data(:,2);                %Recorded data

%****************Detrending Data Set 1*********************************
X1=detrend(x1,'linear');          %Detrending
%X1=x1;
%****************Detrending Data Set 2*********************************
X2=detrend(x2,'linear');          %Detrending
%X2=x2;

%STEP 2: Interpolation and detrending
%*******************Interpolation*************************************

%differenceT=diff(t);    %Determines sampling of the elements in a data set
InterpValue=1/365.2422;       %one divided by days in a year
%InterpValue=mode(differenceT);  %Determines a constant interpolation value
%IT1=t1(1):InterpValue:t1(length(t1)); %new equally spaced t1 time series
IT2=t2(2):InterpValue:t2(length(t2)); %new equally spaced t2 time series
%InterpMethod=input('Enter interpolation method: ','s');
%IX1=interp1(t1,X1,IT2,'linear');
IX2=interp1(t2,X2,IT2,'linear');
%IX1=detrend(IX1,'constant'); %To remove mean introduced by interpolation
IX1=X1;
IX2=detrend(IX2,'linear'); %To remove mean introduced by interpolation
%TitleName=input('Enter graph title: ','s');

%************************************************************************
%STEP 3: Computing the continuous morlet wavelet transforms of the datasets
%scales=input('Enter number of scales: ');
scales=1:600;
Xcoefs1=cwt(IX1,scales,'cmor1-1');   %CWT of dataset one
%Xcoefs1=cwt(X1,scales,'cmor1-1');     %CWT of raw dataset one
```

```
Xcoefs2=cwt(IX2,scales,'cmor1-1');   %CWT of dataset two
%Xcoefs2=cwt(IX1,scales,'cmor1-1');    %CWT of interpolated dataset


for n=1:2

       if n>1
            subplot(4,1,3);
            %plot(IT1,IX1,'.'),grid on, axis tight;
            plot(IT2,IX2,'.'),grid on, axis tight;
            title('Linear interpolated synthetic time series');
            xlabel('Time (yrs)');
            ylabel({'Amplitude';'(mm)'});

            subplot(4,1,4)
            imagesc(IT2,scales,real(Xcoefs2));axis xy tight;grid on;
colorbar; colormap (jet);
            title('Morlet wavelet transform');
            xlabel('Time (yrs)');
            ylabel({'Frequency';'(cpy)'});

            %COnverting scales to frequency
            ax = gca;
            tscl = get(ax,'YTick');
            %Rounding of tscl values to three decimals
            tscl=(1./tscl.')*365;
            tscl=(round(tscl./0.01)).*0.01;
            tfre=num2str(tscl);
            %tfre = num2str((1./tscl.')*365)
            set(ax,'YTickLabel',tfre);
            %End
       end

    subplot(4,1,1);
    plot(t2,X1,'.'),grid on, axis tight;
    title('linear detrended synthetic time series');
    xlabel('Time (yrs)');
    ylabel({'Amplitude';'(mm)'});
```

```
    subplot(4,1,2)
    imagesc(t1,scales,real(Xcoefs1));axis xy tight;grid on; colorbar;
colormap (jet);
    title('Morlet wavelet transform');
    xlabel('Time (yrs)');
    ylabel({'Frequency';'(cpy)'});

% STEP 4: Converting scales to frequency
    ax = gca;
    tscl = get(ax,'YTick');
    %Rounding of tscl values to three decimals
    tscl=(1./tscl.')*365;
    tscl=(round(tscl./0.01)).*0.01;
    tfre=num2str(tscl);
    %tfre = num2str((1./tscl.')*365)
    set(ax,'YTickLabel',tfre);
   %End
end
```

Appendix F4: Phase difference code applied in synthetic data to inspect the performance of the technique and the effect of noise on the algorithm.

```
function PhaseDifferenceTest()
%Programmer: Sikelela Gomo
%Purpose: To calculate the phase difference in the absence and presence
%of noise.

%STEP ONE: Generation of the synthetic signals to be used
for LLn=1:2
t=1:1/365.2422:4;
f=1;
f2=2;
if LLn==2
 noise= 3*randn(size(t));
else
 noise= 0*randn(size(t));
end
Signal1=3*sin(2*pi*f*t)+1*sin((2*pi*f2*t))+noise; % First time series
```

```
Signal2=3*sin((2*pi*f*t)+2.1)+1*sin((2*pi*f2*t)+2.1)+noise;%Second time
series

if LLn==2
    subplot(3,2,2)
    plot(t,Signal1,'b',t,Signal2,'r'), grid on, axis tight;
    title('Time series with noise');
else
    subplot(3,2,1)
    plot(t,Signal1,'.b',t,Signal2,'.r'), grid on, axis tight;
    title('Time series without noise');
end
xlabel('Time (yrs)');
ylabel({'Amplitude';'(mm)'});

% STEP TWO: reducing ringing using the hamming window
WD=kaiser(length(t));
L=length(t);
NPL=nextpow2(L);                %Next power of 2 of the smaple number
n=2^NPL;
disp('Next Power of 2 of the sample number');
disp(n);

%STEP THREE: Computing the cross-spectral density, coherence and phase
%shift of the two spectrums.
%    Crosspectral density
[Pxy,crrf]=cpsd(Signal1,Signal2,WD,n/4.5,n,1);
Cpsmagnitude=abs(Pxy);
crrf=crrf*365.2422;

if LLn==2
    subplot(3,2,4)
else
    subplot(3,2,3)
end
plot(crrf,Cpsmagnitude),grid on, axis tight;
title('Cross-spectrum')
ylabel('Power')
xlabel('Frequency (cpy)')
```

```
%STEP FOUR: Compoting the phase plot
PhasePxy=angle(Pxy);


if LLn==2
    subplot(3,2,6);
else
    subplot(3,2,5);
end
plot(crrf,PhasePxy), grid on, axis tight;
title('Phase spectrum')
xlabel('Frequency (cpy)')
ylabel('Phase angle')



%STEP FIVE: Computing the phase shift of the two imported signals
%Anual_Freq=1;
%SemiA_Freq=2;
%AnnualF=interp1(crrf,PhasePxy,Anual_Freq);
%F=AnnualF;
%disp(F);
%STEP FIVE: Phase shift
Anual_Freq=1;
SemiA_Freq=2;
AnnualF=interp1(crrf,PhasePxy,Anual_Freq);
SemiAF=interp1(crrf,PhasePxy,SemiA_Freq);
F= [AnnualF SemiAF];
disp('Annual Frequency    Semi annual frequency');
disp(F);
end
```

Appendix F6: Wavelet Transform code used to decompose real data

```
function MorletWaveletGapsTest()
%Name: Sikelela  Gomo
%Purpose of the program: to convert real data to the time-frequency domain
%using wavelet transforms
%STEP 1:Import data
for Ln=1:12
%                                PHASE ONE
StationName=input('Enter file name containing data (add .xlsx): ','s');
```

```
t=xlsread(StationName,1,'A:A');  x=xlsread(StationName,1,'D:D');

STEP 2: Removing Nans in the imported data
InTime=t;
InTime(isnan(x))=[];
x(isnan(x))=[];   %Removes nans in the imported data
%LI=length(InTime)
%LY=length(ATM)

%STEP 3: Interpolating the imported time series
  InterpValue=1/365.2422;
  t1_new=InTime(1):InterpValue:InTime(length(InTime));%new equally spaced
time axis
  x_new=interp1(InTime,x,t1_new,'pchip'); %Interpolating the easting data
  x_new=detrend(x_new,'linear');

%                                   PHASE TWO
scales=1:600;
Xcoefs=cwt(x_new,scales,'cmor1-1');

%Plot of the Wavelet Transform data
subplot(4,3,Ln)
imagesc(t1_new,scales,real(Xcoefs)),grid on,axis xy tight; colorbar,
colormap (jet);
GraphTitle2=input('Enter name station name: ','s');
title(GraphTitle2);

%STEP 4: Converting scale to frequency
 %Converting scales to frequency
    ax = gca;
    tscl = get(ax,'YTick');
    %Rounding of tscl values to three decimals
    tscl=(1./tscl.')*365;
    tscl=(round(tscl./0.01)).*0.01;
    tfre=num2str(tscl);
    %tfre = num2str((1./tscl.')*365)
    set(ax,'YTickLabel',tfre);
   %End
end
end
```

Appendix F7: Code used for converting real data into the frequency domain

```
function FourierTransform()
%Purpose: To convert time series to the frequency domain using the
%periodogram method
%STEP One: Importing data into MATLAB
for Ln=1:12
StationName=input('Enter file name containing data (add .xlsx): ','s');
t=xlsread(StationName,1,'A:A'); ATM=xlsread(StationName,1,'B:B');
% ATM = Atmospheric process
% GPS = Global Position System measured time series

%STEP TWO: Remove Nans from the time series
InTime=t;
InTime(isnan(ATM))=[];
ATM(isnan(ATM))=[];   %Removes nans in the imported data
%LI=length(InTime)
%LY=length(ATM)

%STEP THREE: Interpolating the data sets/time series
%The following statements interpolatet the atmospheric data of interest
  InterpValue=1/365.2422;
  t1_new=InTime(1):InterpValue:InTime(length(InTime));%new equally spaced
time axis
  ATM_y_new=interp1(InTime,ATM,t1_new,'pchip'); %Interpolating the easting
data

% subplot(3,3,Ln)
% plot(t1_new,ATM_y_new,'.'),grid on, axis tight;
% GraphTitle1=input('Enter station name: ','s');
% title(GraphTitle1);
% xlabel('Time (yrs)');
% Yaxis=input('Enter y-axis title of time series data: ','s');
% ylabel(Yaxis);
%********Detrending and removing mean to reduced ringing effects**********
xm=ATM_y_new-mean(ATM_y_new);
xmd=detrend(xm,'linear');
L=length(xmd);
disp(L)
```

```
%reducing ringing using the hamming window
WD=kaiser(L);
NPL=nextpow2(L);                %Next power of 2 of the smaple number
n=2^NPL;
disp('Next Power of 2 of the sample number');
disp(n);
%n=input('Enter the next power of 2 with respect to the samples number: ');
[Pxx,f] = periodogram(xmd,WD,n,1);
f=f*365.2422;
%magnitude = abs(Pxx);

subplot(4,3,Ln)
plot(f,Pxx),grid on,axis tight;
%xlabel('Frequency (cpy)')
%ylabel('Power')
GraphTitle2=input('Enter name station name: ','s');
title(GraphTitle2);

%STEP FOUR: determining the power annual and semi-annual power of the time
%series
VarianceT=var(xmd)
Anual_Freq=1;
SemiA_Freq=2;
AnnualF=interp1(f,Pxx,Anual_Freq);
SemiAF=interp1(f,Pxx,SemiA_Freq);
F= [AnnualF SemiAF];
disp('Annual Frequency    Semi annual frequency');
disp(F);
end
end
```

Appendix F8: Code used to compute the semblance spectrum of the cGPS and meteorology time series

```
function SemblanceSpectrum()
%Programmer: Sikelela Gomo
%Purpose: To compute wavelet transform and semblance correlation of two
%different time series
%STEP ONE: Import the first time series
```

```
%                                   PHASE ONE
StationName=input('Enter file name containing first data (add .xlsx):
','s');
t=xlsread(StationName,1,'A:A');  x=xlsread(StationName,1,'D:D');
                                        figure(1);

GraphTitleD=input('Enter GPS DISPLACEMENT time series graph title: ','s');
subplot(5,1,1);
plot(t,x,'.'), axis tight,grid on;
title(GraphTitleD)
%title('Synthetic time series');
xlabel('Time (yrs)');
ylabel({'Amplitude';'(mm)'});

%STEP TWO:Interpolation the imported data set
InterpValue=1/365.2422;   %one divided by days in a year
t_new=t(1):InterpValue:t(length(t)); %new equally spaced time axis
%InterpMethod=input('Enter interpolation method: ','s');
xn=x(find(~isnan(x)));  %Extracts all the x values that are not nan
tn=t(find(~isnan(x)));  %Extracts all the y values that correspond with
%values that are not nan in x
X_new=interp1(tn,xn,t_new,'linear');
LGPS=length(X_new);

%Detrending interpolated time series
x_new=detrend(X_new,'linear');  %Detrended time series

%Inserting the scale of the wavelet transform
%scales=input('Enter the range of scales (1:600): ');
scales=1:600;
CWT1=cwt(x_new,scales,'cmor1-1');

%Plot of the wavelet transform
%GraphTitleDM=input('Enter DISPLACEMENT WAVELET TRANSFORM graph title:
','s');
subplot(5,1,2)
imagesc(t,scales,real(CWT1));axis xy tight;grid on; colorbar; colormap
(jet);
%title(GraphTitleDM);
title('Morlet wavelet transform');
```

```
xlabel('Time (yrs)');
ylabel({'Frequency';'(cpy)'});

%***************Converting scales to frequency*************************
 %Converting scales to frequency
    ax = gca;
    tscl = get(ax,'YTick');
    %Rounding of tscl values to three decimals
    tscl=(1./tscl.')*365;
    tscl=(round(tscl./0.01)).*0.01;
    tfre=num2str(tscl);
    %tfre = num2str((1./tscl.')*365)
    set(ax,'YTickLabel',tfre);
 %End

%                                PHASE TWO
%STEP THREE: Importing the second data set
StationName=input('Enter file name containing second data (add .xlsx):
','s');
t2=xlsread(StationName,1,'A:A');  x2=xlsread(StationName,1,'B:B');

%Plotting the imported data
GraphTitleATM=input('Enter ATM process graph title: ','s');
GraphLabelX=input('Enter Y-axis LABEL of ATM time series: ','s');
ATMunits=input('Enter units of ATM process: ','s');
subplot(5,1,3);
plot(t2,x2,'.'), axis tight,grid on;
title(GraphTitleATM);
%title('Phase shifted synthetic time series');
xlabel('Time (yrs)');
ylabel({'Amplitude';'(mm)'});

%STEP FOUR: Interpolation the second data set
%InTime=(1:1461);  %x-axis value that will be used to interpolate the
                   %imported data
%InTime(isnan(x2))=[];
InTime=t2;
InTime(isnan(x2))=[];
x2(isnan(x2))=[];   %Removes nans in the imported data
InterpValue=1/365.2422;
```

```
%InterpValue=1;
InterpMethod=input('Enter interpolation method: ','s');
t1_new=InTime(1):InterpValue:InTime(length(InTime));%new equally spaced
%time axis
X_new=interp1(InTime,x2,t1_new,InterpMethod); %Interpolating the easting
%data

%Subtracting the meann and Detrending time series one
x_new=detrend(X_new,'linear');  %Detrended time series

%Computing the morlet wavelet transform
CWT2=cwt(x_new,scales,'cmor1-1');

%Plotting the Wavelet tranform results
subplot(5,1,4)
imagesc(t,scales,real(CWT2));axis xy tight;grid on; colorbar; colormap
(jet);
title('Wavelet Transform');
xlabel('Time (yrs)');
ylabel({'Frequency';'(cpy)'});
%Converting scales to frequency
  %Converting scales to frequency
    ax = gca;
    tscl = get(ax,'YTick');
    %Rounding of tscl values to three decimals
    tscl=(1./tscl.')*365;
    tscl=(round(tscl./0.01)).*0.01;
    tfre=num2str(tscl);
    %tfre = num2str((1./tscl.')*365)
    set(ax,'YTickLabel',tfre);
  %End

%                               PHASE THREE
%STEP FIVE: Computing the Cross-Wavelet transform and its amplitude
CWT3= CWT1.*(conj(CWT2));       %Cross wavelet transform
%A=abs(CWT3);                  %Amplitude of the Cross wavelet

%Computing the phase difference of the two signals
Phase=atan2(imag(CWT3),real(CWT3));
```

```
%                                PHASE FOUR
%STEP SIX:Computing the Wavelet Semblance
WS=cos(Phase);                   %Wavelet Semblance

%Plotting the Semblance results
subplot(5,1,5)
imagesc(t,scales,WS);axis xy tight;grid on; colorbar; colormap (jet);
title('Wavelet Semblance');
xlabel('Time (yrs)');
ylabel({'Frequency';'(cpy)'});

%Converting scales to frequency
set(gca,'YTickLabel',tfre);
end
```

Appendix F9: Code used to produce the Cross Spectral Density (CSD) and Coherence spectrum of the cGPS and meteorology time series.

```
function PhaseDifference()
%Programmer: Sikelela Gomo
%Purpose: To compute the phase difference, Cross Spectral Density and
%Coherence spectra of the cGPS and meteorology time series
%STEP ONE: Importing the surface displacement and atmospheric data
%   DISPLACEMENT DATA
StationName=input('Enter file name containing GPS data(add .xlsx): ','s');
t=xlsread(StationName,1,'A:A'); GPS=xlsread(StationName,1,'D:D');
%   ATMOSPHERIC DATA
StationName=input('Enter file name containing ATM data(add .xlsx): ','s');
ATM=xlsread(StationName,1,'B:B'); t2=xlsread(StationName,1,'A:A');

%STEP TWO: Removing nans from the imported data sets
%  Removing nans from the displacement data

t(isnan(GPS))=[];
GPS(isnan(GPS))=[];

%  Removing nans from the atmospheirc data
```

```
%InTime=(1:1461);  %x-axis value that will be used to interpolate the
                   %imported data
InTime=t2;
InTime(isnan(ATM))=[];
ATM(isnan(ATM))=[];   %Removes nans in the imported data
%LI=length(InTime)
%LY=length(ATM)

%STEP THREE: Interpolating the time series
%   Interpolating the displacement data
InterpValue=1/365.2422;   %one divided by days in a year
t1_new=t(1):InterpValue:t(length(t)); %new equally spaced time axis
InterpMethod=input('Enter interpolation method: ','s');
GPS_new=interp1(t,GPS,t1_new,InterpMethod); %Interpolating the easting data

%   Interpolating the atmospheirc data
InterpValue=1/365.2422;
%InterpMethod=input('Enter interpolation method: ','s');
t2_new=InTime(1):InterpValue:InTime(length(InTime));%new equally spaced
time axis
LT=length(InTime)
LATM=length(ATM)
ATM_new=interp1(InTime,ATM,t2_new,InterpMethod); %Interpolating the easting
data

%STEP FOUR: Detrending the time series to reduce rinking effects that will
%be introduced in the data when converting it ti the frequency domain
%   centering the time series to zero by removing mean
GPS_new=GPS_new-mean(GPS_new);
ATM_new=ATM_new-mean(ATM_new);

%   Detrending the time series
DGPS_new=detrend(GPS_new,'linear'); % assuming the trend is linear
DATM_new=detrend(ATM_new,'linear'); % assuming the trend is linear
L=length(DATM_new);

%  Plotting the prepared data sets
subplot(2,2,1)
GraphTitleGPS=input('Enter GPS Time Series title: ','s');
%plot(t1_new,DGPS_new,'.'),grid on, axis tight;
```

```
plot(t,GPS,'.'),grid on,axis tight;
title(GraphTitleGPS)
ylabel('Displacement (m)');
xlabel('Time (yrs)');

subplot(2,2,2)
GraphTitleATM=input('Enter ATM graph title: ','s');
GraphTitleATMY=input('Enter Y-axis label: ','s');
%plot(t1_new,DATM_new,'.'),grid on, axis tight;
plot(InTime,ATM,'.'),grid on, axis tight;
title(GraphTitleATM);
ylabel(GraphTitleATMY);
xlabel('Time (yrs)');

%STEP FIVE: Comverting the time series to the frequency domain using the
%periodogram method

%  reducing ringing using the hamming window
WD=blackman(length(t),'periodic');
NPL=nextpow2(L);                %Next power of 2 of the smaple number
n=2^NPL;
disp('Next Power of 2 of the sample number');
disp(n);

%STEP SIX: Computing the cross-spectral density, coherence and phase shift
of
%the two spectrums.
%    Crosspectral density
[Pxy,crrf]=cpsd(DGPS_new,DATM_new,WD,n/4.5,n,1);
Cpsmagnitude=abs(Pxy);
crrf=crrf*365.2422;

subplot(2,2,3)
plot(crrf,Cpsmagnitude),grid on, axis tight;
title('Cross-Spectrum')
ylabel('Power')
xlabel('Frequency (cpy)')

%STEP SEVEN: Compoting the phase plot
PhasePxy=angle(Pxy);
```

```
subplot(2,2,4);
plot(crrf,PhasePxy), grid on, axis tight;
title('Phase Spectrum')
xlabel('Frequency (cpy)')
ylabel('Phase angle')


%STEP EIGHT: Cumputing the phase shift of the two imported signals
Anual_Freq=1;
SemiA_Freq=2;
AnnualF=interp1(crrf,PhasePxy,Anual_Freq);
SemiAF=interp1(crrf,PhasePxy,SemiA_Freq);
F= [AnnualF SemiAF];
disp('Annual Frequency    Semi annual frequency');
disp(F);
end
```

Appendix F 10: Code used to calculate seasonal mean atmospheric pressure at local atmospheric pressure meteorology stations.

```
function APLoading()
%Purpose: to compute seasonal mean atmospheric pressure
%STEP ONE: Importing and segregating the atmospheric pressure time series
StationName=input('Enter file name containing data (add .xlsx): ','s');
t1=xlsread(StationName,1,'A:A');  y=xlsread(StationName,1,'B:B');
InTime=(1:1492);  %x-axis value that will be used to interpolate the
                  %imported data
InTime(isnan(y))=[];
y(isnan(y))=[];   %Removes nans in the imported data

%STEP 2: Interpolating the time series
InterpValue=1;
t1_new=InTime(1):InterpValue:InTime(length(InTime)); %new equally spaced
time axis
y_new=interp1(InTime,y,t1_new,'linear'); %Interpolating the easting data
ta1=t1(1:365);  ya1=y_new(1:365);
ta2=t1(366:730); ya2=y_new(366:730);
ta3=t1(731:1096); ya3=y_new(731:1096);
ta3(91)=[];  ya3(91)=[];
```

```
ta4=t1(1097:1461); ya4=y_new(1097:1461);
%ya1L=length(ya1);
%ya2L=length(ya2)
%ya3L=length(ya3)
%ya4L=length(ya4)
%[m,n]=size(ya1)
%[m,n]=size(ya2)
%[m,n]=size(ya3)
%[m,n]=size(ya4)
%f=[ya1,ya2,ya3,ya4]

%STEP TWO: Stacking the produced yearly time series
T=(1:365); Y=(ya1+ya2+ya3+ya4)./4;
F=[T Y];
figure
plot(T,Y)

%Step 3: breaking the annual series in terms of annual seasonal components
Summer=Y(1:90); Lsummer=length(Summer);
Autumn=Y(91:182);Lautumn=length(Autumn);
Winter=Y(183:274);Lwinter=length(Winter);
Spring=Y(275:365);Lspring=length(Spring);
figure
subplot(2,2,1)
plot(Summer);title('Summer');
subplot(2,2,2)
plot(Autumn);title('Autumn');
subplot(2,2,3)
plot(Winter);title('Winter');
subplot(2,2,4)
plot(Spring);title('Spring');

%*********Determining the MEAN CHANGE of each season*********************
Csummer=Summer-
Summer(1);SumSummer=sum(Csummer);MCsummer=SumSummer/length(Summer)
Cautumn=Autumn-
Autumn(1);SumAutumn=sum(Cautumn);MCautumn=SumAutumn/length(Autumn)
Cwinter=Winter-
Winter(1);SumWinter=sum(Cwinter);MCwinter=SumWinter/length(Winter)
```

```
Cspring=Spring-
Spring(1);SumSpring=sum(Cspring);MCspring=SumSpring/length(Spring)
end
```

The End